European Commission

JRC SCIENTIFIC AND POLICY REPORTS

Synthetic Amorphous Silicon Dioxide (NM-200, NM-201, NM-202, NM-203, NM-204): Characterisation and Physico-Chemical Properties

JRC Repository: NM-series of Representative Manufactured Nanomaterials

Kirsten Rasmussen, Agnieszka Mech, Jan Mast, Pieter-Jan De Temmerman, Nadia Waegeneers, Frederic Van Steen, Jean Christophe Pizzolon, Ludwig De Temmerman, Elke Van Doren, Keld Alstrup Jensen, Renie Birkedal, Marcus Levin, Signe Hjortkjær Nielsen, Ismo Kalevi Koponen, Per Axel Clausen, Yahia Kembouche, Nathalie Thieriet, Olivier Spalla, Camille Giuot, Davy Rousset, Olivier Witschger, Sebastian Bau, Bernard Bianchi, Boris Shivachev, Douglas Gilliland, Francesca Pianella, Giacomo Ceccone, Giulio Cotogno, Hubert Rauscher, Neil Gibson and Hermann Stamm

2013

NANOGENOTOX

Co-funded by the Health Programme of the European Union

Grant Agreement n°2009 21 01

Report EUR 26046

Joint Research Centre

European Commission
Joint Research Centre
Institute for Health and Consumer Protection

Contact information
IHCP Communication Office
Address: Joint Research Centre, Via Enrico Fermi 2749, 21027 Ispra (VA), Italy
E-mail: jrc-ihcp-communication@ec.europa.eu

http://ihcp.jrc.ec.europa.eu/
http://www.jrc.ec.europa.eu/

JRC 83506

EUR 26046 EN

ISBN 978-92-79-32323-2
ISSN 1831-9424

doi:10.2788/57989

Luxembourg: Publications Office of the European Union, 2013

JRC Repository: NM-Series of Representative Manufactured Nanomaterials

Synthetic Amorphous Silicon Dioxide (NM-200, NM-201, NM-202, NM-203, NM-204): Characterisation and Physico-Chemical Properties

Kirsten Rasmussen, Agnieszka Mech, Douglas Gilliland, Francesca Pianella, Giacomo Ceccone, Giulio Cotogno, Hubert Rauscher, Neil Gibson, Hermann Stamm
European Commission, Joint Research Centre, Institute for Health and Consumer Protection, Italy

Jan Mast, Pieter-Jan De Temmerman, Nadia Waegeneers, Frederic Van Steen, Jean Christophe Pizzolon, Ludwig De Temmerman, Elke Van Doren
Veterinary and Agrochemical Research Centre (CODA-CERVA), Belgium

Keld Alstrup Jensen, Renie Birkedal, Marcus Levin, Signe Hjortkjær Nielsen, Ismo Kalevi Koponen, Per Axel Clausen, Yahia Kembouche
National Research Centre for the Working Environment (NRCWE), Denmark

Nathalie Thieriet
L'Agence nationale de sécurité sanitaire de l'alimentation, de l'environnement et du travail (ANSES), France

Olivier Spalla, Camille Guiot
Commissariat à l'énergie atomique et aux énergies alternatives (CEA), France

Davy Rousset, Olivier Witschger, Sébastien Bau, Bernard Bianchi
Institut National de Recherche et de Sécurité (INRS), France

Boris Shichev
Institute of Mineralogy and Crystallography (IMC-BAS), Bulgaria

Abstract

The European Commission's Joint Research Centre (JRC) provides scientific support to European Union policy including nanotechnology. Within this context, the JRC launched, in February 2011, a repository for Representative Test Materials (RTMs), based on preparatory work started in 2008. It supports both EU and international research projects, and especially the OECD Working Party on Manufactured Nanomaterials (WPMN). The WPMN leads an exploratory testing programme "Testing a Representative set of Manufactured Nanomaterials" for the development and collection of data on characterisation, toxicological and ecotoxicological properties, as well as risk assessment and safety evaluation of nanomaterials. The purpose is to understand the applicability of the OECD Test Guidelines for the testing of nanomaterials as well as end-points relevant for such materials.

The Repository responds to a need for nanosafety research purposes: availability of nanomaterial from a single production batch to enhance the comparability of results between different research laboratories and projects. The availability of representative nanomaterials to the international scientific community furthermore enhances and enables development of safe materials and products.

The present report presents the physico-chemical characterisation of the synthetic amorphous silicon dioxide (SiO_2, SAS) from the JRC repository: NM-200, NM-201, NM-202, NM-203 and NM-204. NM-200 was selected as principal material for the OECD test programme "Testing a representative set of manufactured nanomaterials".

NM-200, NM-201 and NM-204 (precipitated SAS) are produced via the precipitation process, whereas NM-202 and NM-203 (fumed or pyrogenic SAS) are produced via a high temperature process. Each of these NMs originates from one respective batch of commercially manufactured SAS. They are nanostructured, i.e. they consist of aggregated primary particles. The SAS NMs may be used as a representative material in the measurement and testing with regard to hazard identification, risk and exposure assessment studies.

The results for more than 15 endpoints are addressed in the present report, including physical-chemical properties, such as size and size distribution, crystallite size and electron microscopy images. Sample and test item preparation procedures are addressed. The results are based on studies by several European laboratories participating to the NANOGENOTOX Joint Action, as well as the JRC.

Table of contents

List of abbreviations

2D	Two Dimensional
3D	Three Dimensional
ANOVA	Analysis of Variance
APS	Aerodynamic Particle Sizer
ASASP	Association of Synthetic Amorphous Silica Producers
BET	Brunauer, Emmet and Teller
BSA	Bovine Serum Albumin
CEA	Commissariat à l'énergie atomique et aux énergies alternatives
CEN	Comité Européen de Normalisation
CLS	Centrifugal Liquid Sedimentation
CODA-CERVA	Veterinary and Agrochemical Research Centre (Belgium)
CPC	Condensation Particle Counter
DLS	Dynamic Light Scattering
ELPI	Electrical Low Pressure Impactor
EM	Electron microscopy
EDX	Energy-Dispersive X-ray spectroscopy
Fh-IME	Fraunhofer Institute for Molecular Biology and Applied Ecology, Germany
FMPS	Fast Mobility Particle Sizer
FWHM	Full-Width Half-Maximum
GLP	Good Laboratory Practice
h	hours
HEPA filter	High-Efficiency Particulate Air filter
ICP-OES	Inductively Coupled Plasma – Optical Emission Spectrometry
IEP	Iso-Electric Point
IHCP	Institute for Health and Consumer Protection (JRC)
IMC-BAS	Institute of Mineralogy and Crystallography, Bulgaria
INRS	Institut National de Recherche et de Sécurite
ISO	International Organisation for Standardization
ISO/TC 229	ISO/Technical Committee on Nanotechnologies
IUPAC	International Union of Pure and Applied Chemistry
JRC	Joint Research Centre, European Commission
L or l	Litre
LNE	Laboratoire national de métrologie et d'essais, France
lpm	Litre per minute
ml / mL	Milli litre
MWCNT	Multi Walled Carbon Nano Tube

NIST	USA, National Institute of Standards and Technology
NM	Nanomaterial
NRCWE	National Research Centre for the Working Environment
OECD	Organisation for Economic Co-operation and Development
PSD	Particle Size Distribution
PBS	Phosphate Buffered Saline
PCS	Photon Correlation Spectroscopy
PdI	Poly Dispersion Index
pH	Acidity value
REACH	Registration, Evaluation, Authorisation and restriction of Chemicals
RH	Relative Humidity
RMN	Representative Manufactured Nanomaterial
rpm	Rounds Per Minute
RSD	Relative Standard Deviation
RTM	Representative Test Material
s	second
SAS	Synthetic Amorphous Silicon Dioxide
SAS NMs	All of NM-200, NM-201, NM-202, NM-203 and NM-204
SAXS	Small Angle X-ray Scattering
SD	Standard Deviation
SD	Small Rotating Drum
SDR	Sensor Disk Reader
SEM	Scanning Electron Microscopy
SEM-EDS	Scanning Electron Microscopy-Energy Dispersive Spectroscopy
SIRT	Simultaneous Iterative Reconstruction Technique
SOP	Standard Operating Procedure
SCENIHR	Scientific Committee for Emerging and Newly Identified Health Risks
TEM	Transmission Electron Microscopy
USA	United States of America
USA-EPA	USA Environmental Protection Agency
USAXS	Ultra Small Angle X-ray Scattering
VS	Vortex Shaker
WPMN	Working Party on Manufactured Nanomaterials
w/w%	weight percent
XPS	X-ray Photoelectron Spectrometry
XRD	X-ray Diffraction

1. Introduction

Over the past decade, nanomaterials have gained an increasing attention and they are subject to numerous international research projects aiming at both evaluating their potential for technological innovation and understanding possible adverse effects (Morris et al., 2011). It is of special interest to identify if the nanoform induces adverse effects (e.g. other effects, or different potency) different to non-nano forms of the same chemistry.

For nanosafety research purposes, availability of nanomaterial from a single batch is desirable to enhance the comparability of results between different laboratories and research projects. Such availability would overcome questions related to whether a nanomaterial tested in one project is the same or just similar to a nanomaterial tested in other project(s) and how results compare. In response to this need as well as supporting the OECD Working Party on Manufactured Nanomaterials (WPMN) programme for "Testing a Representative set of Manufactured Nanomaterials", the European Commission's Joint Research Centre (JRC) established a repository with Representative Test Materials (RTMs) hosting different types of nanomaterials. The role of Representative Test Materials is described in a recent publication (Roebben et al., 2013).

One of the nanomaterials tested by the OECD WPMN is silicon dioxide, for which synthetic amorphous silicon dioxide or SAS was selected and it widely used as an additive in broad variety of final products, e.g. as a functional filler in polymers, and to add strength to rubber (e.g. car tyres), paint and varnishes. Other examples are addition to paper to create different paper qualities, and to food as an anti-lumping agent. As the final products, e.g. car tyres, are available in very large quantities even a minor product content of SAS will add up to a large total volume. According to SRI Consulting precipitated SAS is the most abundant nanomaterial on the market in terms of quantity[1].

A substantial part of the information in this report come from a Joint Action, NANOGENOTOX, see http://www.nanogenotox.eu, which was co-financed by the Executive Agency of the Directorate General for Health and Consumers of the European Commission and 11 EU member states. In NANOGENOTOX characterisation and testing of SAS was an important task. In addition, results and data from the JRC laboratories are included. Another example of an EU project testing the materials from the Repository is MARINA (http://www.marina-fp7.eu/).

[1] http://www.ihs.com/products/chemical/planning/scup/nanoscale-chemicals.aspx?pu=1&rd=chemihs

1.1. Production of SAS

The SAS in the repository are produced industrially by two general methods: Wet route (precipitation) or Thermal route (pyrogenesis).

The Wet route production method for SAS involves steps in which a solution of alkali metal silicate is acidified to produce a gelatinous precipitate that is washed and then dehydrated to produce colourless microporous silica particles. In this method an alkali metal silicate dissolved in water, e.g. water glass ($Na_2O \cdot nSiO_2$; n = 2 – 4), reacts with sulphuric acid through a series of production steps that include raw material storage, synthesis, solid-liquid-filtration, drying and packaging. The synthesis can either be continuous or in batch. The SAS produced via this route is, among others, called precipitated SAS. NM-200, NM-201 and NM-204 in the JRC Nanomaterials Repository are produced with this method. The NM-nomenclature is explained in chapter 2.

SAS produced via the Thermal route is prepared by burning $SiCl_4$ in an oxygen rich hydrocarbon flame to produce a fume of SiO_2:

$$SiCl_4 + 2\ H_2 + O_2 \rightarrow SiO_2 + 4\ HCl$$

By varying e.g. the flame temperature, flame composition and feed stock, the physico-chemical properties of the product, e.g. the specific surface area and the particle size, can be controlled. The SAS produced via this route is also called pyrogenic SAS or fumed SAS. NM-202 and NM-203 in the JRC Nanomaterials Repository are produced using this method.

1.2. About this report

This report presents the characterisation data and methods for SAS from the JRC Nanomaterials Repository: NM-200, NM-201, NM-202, NM-203 and NM-204; when describing all 5 SAS the abbreviation "the SAS NMs" is used, otherwise a reference is made to which nanomaterials were investigated.

Chapter 2 introduces the JRC Repository for representative nanomaterials and the link to the OECD Working Party on Manufactured Nanomaterials (WPMN). Chapter 3 describes the materials, methods and end-points and presents an overview of the end-points tested and the methods applied for each end-point. Then homogeneity within and between vials is addressed in chapter 4.

The following chapters 5 to 13 describe in details the physico-chemical characteristics measured together with the applied methodology. The characterisation includes properties

such as hydrodynamic size and size distribution in aqueous suspensions, and zeta potential, and includes techniques such as dynamic light scattering (DLS), small-angle X-ray scattering (SAXS) and Ultra Small Angle X-ray Scattering (USAXS). The zeta potential as a function of pH was analysed to determine the stability properties of the aqueous suspensions over the pH range, and subsequently the iso-electric point (IEP, i.e. the pH at which the surface charge is globally neutral) was identified. In addition, the size distribution was analysed through Transmission Electron Microscopy (TEM) micrographs and Scanning Electron Microscopy (SEM) micrographs, and the specific surface area was measured by BET[2] and SAXS. Atomic Force Microscopy (AFM) was also applied to obtain information on particle size. The crystallinity was investigated by SAXS and XRD. For the dustiness testing NRCWE modified an ISO method, ISO EN 15051, and INRS used the vortex shaker method. Table 4 gives an overview of the end-points investigated, methods applied and the institutions involved.

The conclusions are presented in chapter 14, and include a summary of results for each of the SAS NMs.

A list of abbreviations has been included before the introduction. Furthermore, details on the methods applied are given in appendices A to D as available and relevant.

[2] Stephen Brunauer, Paul Hugh Emmett, and Edward Teller developed a theory that aims to explain the physical adsorption of gas molecules on a solid surface and serves as the basis for an important analysis technique, named after them by the initials of their last names, BET, for the measurement of the specific surface area of a material.

2. Overview of the JRC NM-Series of Representative Test Materials

The European Commission's Joint Research Centre (JRC) established the JRC Nanomaterials Repository for the NM-series of Representative Test Materials. The JRC Repository is hosted at the Institute for Health and Consumer Protection in Italy.

Table 1. List of representative Nanomaterials in the JRC NM Repository (2013).

NM code	Type of material*	Label name	Other information
NM-100	**Titanium Dioxide**	Titanium Dioxide	
NM-101	Titanium Dioxide	Titanium Dioxide	anatase
NM-102	Titanium Dioxide	Titanium Dioxide, anatase	anatase
NM-103	Titanium Dioxide	Titanium Dioxide thermal, hydrophobic	rutile
NM-104	Titanium Dioxide	Titanium Dioxide thermal, hydrophilic	rutile
NM-105	Titanium Dioxide	Titanium Dioxide rutile-anatase	anatase-rutile
NM-110	**Zinc Oxide, uncoated**	Zinc Oxide	
NM-111	Zinc Oxide, coated	Zinc Oxidecoatedtriethoxycaprylsilane	
NM-200	**Silicon Dioxide**	Synthetic Amorphous Silica PR-A-02	precipitated
NM-201	Silicon Dioxide	Synthetic Amorphous Silica PR-B-01	precipitated
NM-202	Silicon Dioxide	Synthetic Amorphous Silica PY-AB-03	thermal
NM-203	Silicon Dioxide	Synthetic Amorphous Silica PY-A-04	thermal
NM-204	Silicon Dioxide	Synthetic Amorphous Silica PR-A-05	precipitated
NM-211	**Cerium Dioxide**	Cerium (IV) Oxide precipitated, uncoated, cubic	
NM-212	Cerium Dioxide	Cerium (IV) Oxide precipitated, uncoated	
NM-300K	**Silver**	Silver<20 nm	
NM-300K DIS	Silver - dispersant	Ag - dispersant	
NM-330	**Gold**		
NM-330 DIS	Gold - dispersant	Gold - dispersant	
NM-400	**MWCNT**	Multi-walled Carbon Nanotubes	
NM-401	MWCNT	Multi-walled Carbon Nanotubes	
NM-402	MWCNT	Multi-walled Carbon Nanotubes	
NM-403	MWCNT	Multi-walled Carbon Nanotubes	
NM-600	**Nanoclay**	Bentonite	

* Nanomaterials, even of the same chemical composition, may be available e.g. in various sizes and/or shapes, which may influence their chemical and physical properties

Currently, the Repository contains eight chemical constituents of the nanomaterials tested within the OECD WPMN programme for "Testing a Representative set of Manufactured Nanomaterials". Each individual nanomaterial in the NM-series originates from one batch and has been allocated an identifying code with the following format: the letters "NM" followed by a dash and three digits (NM-XXX), therefore it is also called the NM-series. The Repository contains 22 representative nanomaterials of 8 different chemistries of the following chemical composition: titanium dioxide, zinc oxide, silicon dioxide, cerium dioxide, silver, gold, multi-

walled carbon nanotubes and bentonite (a nanoclay), see Table 1. Furthermore, the dispersants for silver and gold are also available from the repository. The sub-sampling was done in collaboration with the Fraunhofer Institute for Molecular Biology and Applied Ecology.

The NM-series are studied in national, European and global scientific projects. They are also used for testing models, and as performance standards and comparators. More than 10,000 individual samples have been distributed to research institutions, national authorities, industrial research laboratories and other scientific stakeholders in the EU, Switzerland, USA, Canada, Australia, China, Russia, Japan, and Korea. Several research projects have been undertaken to investigate properties of nanomaterials using the representative nanomaterials from the JRC repository.

Study results are collated in a JRC database, JRC NANOhub, and are made available to the OECD through dedicated data submissions to the JRC NANOhub. The combination of availability of representative test nanomaterials and JRC NANOhub reference data support innovation and competitiveness in Europe's growing nanotechnology industries by building foundations for research and product development.

2.1. Representativeness of the materials in the NM-series

To reliably address the scientific questions of nanomaterial induced effects for toxicity, ecotoxicity and environmental fate and behaviour, representative test nanomaterials are important, which are relevant for industrial application and commercial use, and for which a critical mass of study results are available. Representative test materials allow enhanced comparison of test results, robust assessment of data, and pave the way for appropriate test method optimization, harmonisation and validation and may finally serve as performance standards for testing.

In the following, the concept of Representative Test Material (RTM) is briefly outlined clarifying the difference to reference materials. Reference Material (RM) is the generic name for materials which have a proven and sufficient homogeneity and stability in terms of a defined intended use, and for certified reference materials there is a certified value for the property of interest. Reference Materials and Certified Reference Materials need to be produced and used applying the conditions and terms standardised and described in ISO Guides 30 to 35 relating to reference material production. Currently, only a small number of certified reference materials exist in the field of manufactured nanomaterials, for example gold nanoparticles (certified size) and single-wall carbon nanotube soot (certified

composition) from the USA National Institute of Standards and Technology (NIST) and colloid silica (certified size) from the European Commission (JRC-IRMM).

The nanomaterials in the JRC repository are representative test materials. For RTMs the following definition was proposed by Roebben et al. (2013):

> *A **representative test material (RTM)** is a material from a single batch, which is sufficiently homogeneous and stable with respect to one or more specified properties, and which implicitly is assumed to be fit for its intended use in the development of test methods which target properties other than the properties for which homogeneity and stability have been demonstrated.*

An RTM is not a reference material for the tests for which it is intended to be used, because homogeneity and stability are not demonstrated for the corresponding measurand. However, an RTM is more valuable than an ordinary test material, since it has been checked for homogeneity and stability in terms of one or more specified properties. RTMs are extremely useful tools in intra- or interlaboratory development of methods for which reference materials are not (yet) available. Thus, the NM-series of representative test materials are complementary to (certified) Reference Materials as illustrated in Table 2.

Table 2. Essential characteristics of the concept 'representative test material' compared to the existing concepts of reference material and certified reference material.

	Representative Test Material	**Reference Material**	
		Not certified	**Certified**
Parent material	Representative for a class of materials to be investigated with the target method(s)		
Homogeneity / stability	Assumed for the measurands of interest, demonstrated for other measurands	Demonstrated for the measurands of interest	Demonstrated for the measurands of interest
Assigned property value	None	None, or indicative only.	Certified for the measurand of interest

The OECD WPMN uses the term “Representative Manufactured Nanomaterial” for the nanomaterials selected for testing, which are assumed to be representative for a large fraction of nanomaterials on the market. The nanomaterials in the NM-series are a (random) sample from one industrial production batch, produced within industrial specifications. The NM-series ensures that the particular sample has been homogenised, and is sub-sampled into vials under reproducible (GLP) conditions, and the stability of the sub-samples is monitored. Thus, to the extent feasible for industrial materials, all sub-samples from one material should be identical and differences in test results between laboratories for the same end-point should not be attributed to differences in the material tested.

2.2. The OECD WPMN and Testing the NM-Series

In 2006 international recognition of the need of a deeper understanding of nanomaterials, including relevant characterisation information as well as hazard profiles of nanomaterials led to the establishment of the WPMN under the Chemicals Committee of the OECD. The WPMN leads one of the most comprehensive nanomaterial research programmes "Safety Testing of a Set of Representative Manufactured Nanomaterials", established in 2007.

The WPMN agreed on a list of Representative Manufactured Nanomaterials to be tested and relevant end-points to test for exploratory purposes. The nanomaterials listed in the testing programme are (2012): fullerenes, single-wall and multi-wall carbonnanotubes, cerium dioxide, zinc oxide, iron, gold, silver, titanium dioxide, silicon dioxide, nanoclay and dendrimers. Some of these materials are hosted in the JRC Repository.

For SiO_2 in the OECD testing programme, NM-200 was selected as the principal material, i.e. a full data set, as listed in Table 3, should be provided for this material; the other silicon dioxides, NM-201 to NM-204, are alternate materials and any data available on these materials will be submitted to the OECD testing programme as well.

Data in the OECD testing programme regarding characterisation, toxicological and eco-toxicological effects are generated in Phase 1 to understand the hazard profiles of the nanomaterials. A Phase 2 is planned and will start by evaluating the data received in Phase 1, and especially the test guidelines applied to identify their applicability and necessary modifications (if any). It may be considered if further testing is needed.

The endpoints addressed within Phase 1 are presented in Table 3. The Guidance Manual for the Testing of Manufactured Nanomaterials (OECD 2010) describes in detail the information expectations for each end-point and all end-points have to be addressed.

Table 3. Endpoints Agreed by the OECD WPMN for the Representative Manufactured Nanomaterials.

	Nanomaterial Information / Identification
1	Nano material name
2	CAS number
3	Structural formula / molecular structure
4	Composition of NM being tested (incl. degree of purity, known impurities or additives)
5	Basic Morphology
6	Description of surface chemistry (e.g. coating or modification)
7	Major commercial uses
8	Known catalytic activity
9	Method of production (e.g. precipitation, gas phase)

	Physical-chemical Properties and Material Characterization
10	Agglomeration / aggregation
11	Water solubility
12	Crystalline phase
13	Dustiness
14	Crystallite size
15	Representative TEM picture(s)
15	Particle size distribution
17	Specific surface area
18	Zeta potential (surface charge)
19	Surface chemistry (where appropriate)
20	Photo-catalytic activity
21	Pour density
22	Porosity
23	Octanol-water partition coefficient, where relevant
24	Redox potential
25	Radical formation
26	Other relevant information (where available)
	Environmental Fate
27	Dispersion stability in water
	Biotic degradability
28	- Ready biodegradability
29	- Simulation testing on ultimate degradation in surface water
30	- Soil simulation testing
31	- Sediment simulation testing
32	- Sewage treatment simulation testing
33	Identification of degradation product(s)
34	Further testing of degradation product(s) as required
	Abiotic degradability and fate
35	- Hydrolysis, for surface modified nanomaterials
36	Adsorption- desorption
37	Adsorption to soil or sediment
38	Bioaccumulation potential
39	Bioaccumulation in sediment
	Environmental Toxicology
40	Effects on pelagic species (short/ long term)
41	Effects on sediment species (short/ long term)
42	Effects on soil species (short/ long term)
43	Effect on terrestrial species
44	Effect on micro-organisms
45	Other relevant information
	Mammalian Toxicology
46	Pharmacokinetics (ADME)
47	Acute Toxicity
48	Repeated dose toxicity

	IF AVAILABLE
49	Chronic toxicity
50	Reproductive toxicity
51	Developmental toxicity
52	Genetic toxicity
53	Experience with human exposure
54	Other relevant test data
	Material Safety
55	Flammability
56	Explosivity
57	Incompatibility

In addition to the listed endpoints in the Guidance Manual for Sponsors (GMS), the GMS advises (p. 25): "To aid in assuring the identical nature of the sponsored MN, the material used in different tests should be obtained preferably in a single lot, and stored and manipulated in comparable, if not identical procedures." and further "Sponsors will identify the source of test nanomaterials, including all known aspects of material production, the manufacturer, facility location, lot number, and any other pertinent information as noted in Annex I "Nanomaterial Information/Identification"." Thus, the GMS recommends ensuring that, as far as possible, the testing of all endpoints is performed with a nanomaterial from one batch, and the JRC repository assists the WPMN in doing this.

The provision of the JRC NM-Series to the OECD WPMN test programme enables the development of the comprehensive data set on characterisation nanomaterial properties and toxicological and ecotoxicological behaviour, as described above. In June 2012 the OECD WPMN recommended the development of a risk assessment/safety evaluation methodology for nanomaterials, based on, among others, this data set.

2.3. Characterisation of the NM-series

For nanomaterials it is known that their hazardous properties can be affected by for example shape, size and surface area, because these parameters affect the transport properties of the particles (absorption, distribution, and excretion).

In addition, one of the issues raised consistently in the discussions under the OECD WPMN is the test item preparations and dispersion protocols for the nanomaterials. A "test item" is simply (the actual fraction of) the sample tested. This discussion is linked to the characterisation of the nanomaterials for which a number of relevant scenarios have been identified, and among these are:

Characterisation

I. as received
II. as dispersed
III. during testing

These scenarios reflect that many of the nanomaterials tested are insoluble (in water and other media) or only slightly soluble nanoparticles, and their physico-chemical properties as well as their (eco)toxicological effects are closely linked also to their physical surroundings. Thus, to acquire an in-depth understanding of the nanomaterials, material characterisation should be performed for a number of the different stages of the nanomaterials' use cycle. Table 3, sections "nanomaterial information" and "physico-chemical properties", list the characterisation end-points. Most of these may be measured both for the dry material and in dispersion; however, obviously some belong to a specific preparation form for the measurement: dustiness is a dry measurement whereas the water/octanol coefficient can be measured only in solution. Additional issues could be relevant, e.g. if the physical state and preparation of the material tested is representative for production and use, taking into account the chain of actors and life cycle.

Below is described a number of issues to consider for the characterisation.

I. "as received" is the characterisation of the properties of a RTM as received, and typical preparations are dry or aqueous.

II and III. "as dispersed" and **"during testing"** are for the nanomaterials undergoing further sample preparation steps, which should be assessed with regard to influence on measurement results, such as particle size determinations for the different scenarios: dry material, in aqueous or physiological media.

In addition to the physico-chemical characterisation also data relating to (eco)toxicological effects are requested in the OECD Test Programme. For this kind of testing, the test item preparation needs to be carefully considered. The characterisation of matrix-dependent properties of the prepared test item is an important issue for nanomaterials. Results are dependent on the matrix composition and protocols used.

For the testing, RTMs can best be used and brought into a matrix under defined conditions and applying defined procedures, and availability of protocols also for the matrices should minimise sources of uncertainties and methodological errors. Thus, dispersion protocols have been developed for test item preparation for use in test systems for (eco)toxicological testing or environmental fate analysis, comprising conditioning and choice of matrix

components. Hence, the prepared test item should fulfil the requirements of the test method under GLP conditions and be representative for the selected exposure route. Test items are prepared for environmental testing in the compartments soil, water, sediment, sewage treatment plants as well as for oral, dermal, (intravenous) and inhalation toxicity testing, in the form it is assumed to reach the biological entity in the test system.

Depending on the various protocols used, different results may be obtained for the same parameter measured. Also the effect of a particle's 'corona', the molecules surrounding it in a given medium has recently been acknowledged (Cedervall et al., 2007), emphasising that the constituents of the corona depend on the medium. Biophysical characterisation, such as corona composition, kinetics/exchange rates, corona structure and depletion effects/changes in matrix kinetics are therefore required in support of understanding of test items.

The determination of a property should be addressed by the selection of the appropriate measurand and the corresponding measurement method. For nanomaterials the "appropriate measurand" is not yet fully understood for all endpoints, and extensive discussion and guidance development take place in several international fora: the Scientific Committee on Emerging and Newly Identified Health Risks (SCENIHR 2010), the OECD WPMN, the Comité Européen de Normalisation Technical Committee 352 Nanotechnologies (CEN/TC 352), and the International Standardisation Organisation (ISO) under Technical Committee 229 Nanotechnologies (ISO/TC 229). In addition, for the measurements an uncertainty estimate should be described based on the Guide for Uncertainty in Measurements.

3. Materials, Methods and End-points

The synthetic amorphous silicon dioxides NM-200, NM-201, NM-202, NM-203 and NM-204 (all five together are described as 'SAS NMs') are available as white, fluffy powders in amber coloured vials containing either 500 mg, 1000 mg or 2000 mg under argon atmosphere. Each individual vial has a unique sample identification number.

This chapter gives an overview of institutions involved in the testing, the end-points tested and associated method(s), as well as the equipment used to characterise the SAS NMs.

The testing was performed by several European research institutes (alphabetical order):

CEA	Commissariat à l'énergie atomique et aux énergies alternatives, France
CODA-CERVA	Veterinary and Agrochemical Research Centre, Belgium
IMC-BAS	Institute of Mineralogy and Crystallography, Bulgaria
INRS	Institut National de Recherche et de Securité, France
JRC	Joint Research Centre, European Commission
NRCWE	National Research Centre for the Working Environment, Denmark

The data was generated in the context of several European projects, for example the Joint Action NANOGENOTOX, which was co-financed by DG SANCO and participating of EU member states, and research at the JRC. The NANOGENOTOX Joint Action was co-ordinated by L'Agence nationale de sécurité sanitaire de l'alimentation, de l'environnement et du travail (ANSES), France.

Table 4 lists the physico-chemical characterisation end-points suggested by the OECD WPMN and gives an overview for each SAS NM of the characterisation performed, methods used, and institution(s) involved. Some of the SAS NMs are tested more than others; the NM-204 was not part of some of the projects and therefore has less data. The experimental undertakings and results are described in chapter 4 and onwards.

As seen from Table 4, the following testing and measurements were performed: surface charge, hydrodynamic particle size and particle size distribution in aqueous suspensions by dynamic light scattering (DLS), small-angle X-ray scattering (SAXS) and Ultra Small Angle X-ray Scattering (USAXS). The surface charge as a function of pH was analysed to assess the stability properties of the aqueous suspensions over the pH range, and subsequently the iso-electric point (IEP), which is the pH value at which the surface charge is globally neutral, was

determined. The particle size distribution was analysed through TEM micrographs and SEM images, and the specific surface area was measured by BET, and SAXS and USAXS. For the dustiness testing NRCWE developed a dedicated method; the crystallinity was investigated by SAXS and XRD. The solubility was tested in three media, the NANOGENOTOX dilute BSA-water dispersion, Gambles solution and Caco 2 medium.

Table 4. SAS NMs: physico-chemical characterisation performed, and institutions involved.

Physico-chemical Properties and Material Characterization (from OECD list)	**NM characterised**					**Method**	**Institution(s)**	**Chapter**
	200	201	202	203	204			
Homogeneity	x			x		DLS	NRCWE, INRS, CEA	4
Agglomeration / aggregation	x	x	x	x		SAXS/USAXS	CEA	9
	x	x	x	x		DLS	CEA, NRCWE, INRS, JRC	7
	x	x	x	x		TEM	CODA-CERVA, IMC-BAS	12
Water solubility *)	x	x	x	x	x	SDR	NRCWE	6.3, 6.4
Crystalline phase	x	x	x	x	x	XRD	IMC-BAS, JRC,NRCWE	11
Dustiness	x	x	x	x	x	Small rotating drum	NRCWE	13.1.1
	x	x	x	x	x	Vortex shaker method	INRS	13.1.2
Crystallite size	x	x	x	x	x	SAXS/USAXS	CEA, NRCWE	9
	x	x	x	x	x	XRD	JRC, NRCWE, IMC-BAS	11
Representative TEM picture(s)	x	x	x	x	x	TEM	CODA-CERVA IMC-BAS	12
Particle size distribution	x	x	x	x	x	CLS	JRC	7.4
	x	x	x	x	x	TEM	CODA-CERVA IMC-BAS	12
	x	x	x	x		DLS	CEA, NRCWE, INRS, JRC	7
	x	x	x	x	x	AFM	CEA	12.10.212 .10.2
Specific surface area (SSA)	x	x	x x	x x	x x	BET	IMC-BAS, JRC	10
	x	x	x	x	x	SAXS/USAXS	CEA	9
Volume SSA	x			x		TEM tomography	CODA-CERVA	12.10
Zeta potential (surface charge)	x	x	x	x		Zeta-metry	CEA, NRCWE	8
Surface chemistry (where appropriate).	x			x		XPS	JRC	5.4
	x	x	x	x	x	TGA	NRCWE	5.2
	x	x	x	x	x	DTA	IMC-BAS	5.2
Presence of coating					x	GC-MS (TGA > 1 wt%)	NRCWE	5.3
Photo-catalytic activity	End-point not relevant for SAS							
Pour density	x	x	x	x	x	weighing	INRS	14
Porosity	x	x	x	x	x	BET	IMC-BAS	10
Octanol-water partition coefficient, where relevant	End-point not relevant							

Redox potential	x	x	x	x	x	SDR	NRCWE	6
OH radical formation, acellular	x	x	x	x	x	Benzoic acid probe to form hydroxybenzoic acid analysed by HPLC-UV	NRCWE	
Other relevant information (where available)								
Elemental analysis/impurities	x	x	x	x	x	Semiquantitaive ICP-OES	CODA-CERVA	5.1
Elemental analysis/impurities	x	x	x	x	x	Semiquantitaive EDS	IMC-BAS	5.1

*) the solubility was investigated in Gambles solution, Caco 2 medium, and the NANOGENOTOX dispersion medium

The institutes participating to the characterisation of the silicon dioxides used a number of different apparatus and equipment when performing the measurements. Table 5 gives an overview of equipment and conditions.

Table 5. Overview of apparatus used by the institutes for the testing.

Method	
Institution	Apparatus and methodology and descriptive text
AFM	
CEA	Atomic Force Microscope VEECO, Dimension V, in tapping mode, with standard silicon probe tip having Al backside coating [Mikromasch NSC15, 300kHz, 40 N/m, typical probe radius 10 nm. Nanoscope software v7.0. for image analysis.
BET	
IMC-BAS	High-speed surface area and pore size analyser NOVA 4200e (Quantachrome)
CLS	
JRC	CPS Instruments, INC. CPS disk centrifuge, Model DC24000UHR
DLS and Zeta potential	
CEA/LIONS	Zetasizer Nano ZS (Malvern Instruments), equipped with laser 633 nm, computer controlled by Malvern software (DTS 5.03 or higher), samples inserted in DLS cuvettes of clear disposable polymer (optical path length 1 cm) or glass cells or folded capillary zeta cells (Malvern Instruments) volume 0.75 to 1 mL, DTS1061, with gold electrodes
INRS	VASCO™ particle size analyzer (VASCO-2 Cordouan Technologies, France) with a 65 mW fiber semiconductor laser at the wave length 635 nm. Data collection and analysis is provided by the proprietary software nanoQ™ 1.2.0.4. The sample is dropped directly with a pipette (volume ≈ 2 µl) in the center of the cell. The cell bottom formed by the upper surface of the glass prism guiding the laser beam.
JRC	Zetasizer NanoZS from Malvern Instruments
NRCWE	Zetasizer Nano ZS (Malvern Instruments), equipped with laser 633 nm, computer controlled by Malvern software (DTS 5.03 or higher), samples inserted in DLS cuvettes of clear disposable polymer (optical path length 1 cm) or glass cells or folded capillary zeta cells.
DTA	
IMC-BAS	A STA781 and DTA 675 from Stanton Redcroft was used for the differential thermal analysis (DTA). The heating rate was 10 °C /Min.
EDS	
IMC-BAS	Philips TEM420 at 120 kV acceleration voltage
GC-MS	

NRCWE	On-column GC-MS equipped with FactorFour™ 30 m VF-5ms capillary column with a diameter of 0.25 mm and 0.25 µm stationary phase containing 5 % phenyl poly dimethylsiloxane (Varian). The MS was run in positive mode using EI (electron ionization).
ICP-OES	
CODA-CERVA	Inductively coupled plasma-optical emission spectrometry using a Varian 720-ES, Agilent Technologies
SAXS and USAXS	
CEA/LIONS	The main set up components used for SAXS and USAXS experiments are: ▪ X-ray generator : Rigaku generator RUH3000 with copper rotating anode (λ= 1.54 Å), 3kW ▪ Home made optic pathways and sample holders (with two channel-cut Ge (111) crystals in Bonse/Hart geometry for USAXS set up, cf Lambard (1992). ▪ Flux measurement for SAXS set up : pico amperemeter Keithley 615 ▪ Flux measurement for USAXS set up : DonPhysik ionization chamber ▪ Detector for SAXS set up : 2D image plate detector MAR300 ▪ Detector for USAXS set up: 1D high count rate CyberStar X200 associated to a scintillator/ photomultiplier detector. All experimental parameters are monitored by computer by a centralized control-command system based on TANGO, and interfaced by Python programming. 2D images are treated using the software *ImageJ* supplemented with specific plug-ins developed at CEA/LIONS, see O. Taché, 2006.
SDR	
NRCWE	24-well Sensor Disc Reader (SDR) system from PreSens Precision Sensing GmbH, Germany
Small rotating drum	
NRCWE	Small (5.9 L) rotating drum system modified and optimized by NRCWE with online measurement of size-distribution using Fast Mobility Particle Sizer, Aerodynamic Particles Sizer, particle number concentration using Condensation Particle Sizer and filter sampling of either respirable or inhalable dust for calm air.
Sonication	
CEA	Ultrasonic probe equipped with a standard 13 mm disruptor horn: Sonics & Materials, VCX500-220V, 500 W, 20 kHz
CODA-CERVA	Vibracell™ 75041 ultrasonifier (750 W, 20 kHZ, Fisher Bioblock Scientific, Aalst, Belgium). 13 mm horn (CV33)
INRS	Ultrasonic probe equipped with a 14 mm Ti disruptor horn: Heilscher UP200H (200W)
JRC	Tweeter sonicator from Hielscher., Ultrasound technology, vial tweeter UIS250v, 250 watt; 24 kHz. The tweeter sonicator does not have a horn.
NRCWE	Ultrasonic probe equipped with a standard 13 mm disruptor horn: Branson Bransonic 400W
TEM	
CODA-CERVA	Tecnai™ G2 Spirit microscope (FEI, Eindhoven, The Netherlands) with biotwin lens configuration operating at 120 kV
IMC-BAS	Philips TEM420 at 120 kV acceleration voltage
TEM tomography	
CODA-CERVA	Tecnai™ G2 Spirit microscope (FEI, Eindhoven, The Netherlands) with biotwin lens configuration operating at 120 kV
TGA	
NRCWE	A Mettler Toledo TGA/SDTA 851e was used with oxygen atmosphere. The heating rate was 10 K/min and the temperature range was from 25 °C to 1000 °C. The sample holders

	used for the TGA measurements were made of alumina and had a volume of 70 µL or 150 µL.
Vortex Shaker Method	
INRS	Vortex dustiness test system modified and optimized at INRS. CPC: Model 3785 Water-based Condensation Particle Counter (TSI, USA)
XPS	
JRC	AXIS ULTRA Spectrometer (KRATOS Analytical, UK).
XRD	
IMC-BAS	Bruker D2 Phaser diffractometer in reflection mode with theta-theta geometry. Cu X-rays were generated by a sealed Cu X-ray tube run at 30 kV and 10 mA and focused using a Ni filter and a fixed 0.2° divergence slit. Data generated with a step size of 0.02 degree 2theta and with a step time of 10 s and collected scintillation detector with opening angle 0.2°. Since the instrument does not use a monochromator, the raw data contains reflections from both Kα1 and Kα2 rays. For data comparison, the Kα2 contribution was therefore stripped from the data using the EVA software (Bruker).
JRC	In-house constructed glancing-angle X-ray diffractometer. Variable incident angle and incident beam slit width, with laser sample alignment system. Ka radiation, with tube operating at 1kW. Germanium solid state detector for background reduction and elimination of Kb radiation. Instrumental resolution with diffracted beam Soller slit approximately 0.15°–0.2°, depending on incident beam slit width.
NRCWE	Bruker D8 Advanced diffractometer in reflection mode with Bragg-Brentano geometry. The analysis were made using CuKα1 X-rays (1.5406 Å) generated using a sealed Cu X-ray tube run at 40 kV and 40 mA. The x-ray beam was filtered for CuKα2 and focused using a primary beam Ge monochromator and fixed divergence slit 0.2°. The analyses were made in the stepping mode stepping 0.02 degree 2theta per second and data were collected using a linear PSD detector (Lynx-eye) with opening angle 3.3°.

The NANOGENOTOX sample preparation protocol was developed by CEA, INRS and NRCWE and the final dispersion protocol is published on the project's web page at http://www.nanogenotox.eu/files/PDF/web%20nanogenotox%20dispersion%20protocol.pdf Briefly, the final dispersion following the protocol has a concentration of 2.56mg/mL and sterile-filtered 0.05% w/v BSA-ultrapure water. The samples are sonicated (probe sonicator) for 16 minutes, placed in an ice bath. The energy input should be calibrated to be in the order of 3,136 MJ/m^3.

4. Homogeneity within and between vials. Reproducibility of sample preparation among laboratories

4.1. Procedure and sample preparation

Samples are provided in vials. The homogeneity both within vials and between vials was assessed by DLS measurements on aqueous suspensions in the best dispersed state after probe sonication. The DLS technique is further detailed in chapter 7 and in Appendix A. It should be noted that this type of analysis give information on the spherical equivalent hydrodynamic aggregate size.

The main technical difference, which could lead to interlaboratory variability in the analytical results on the suspended particles may come from the different sonicators used in the different laboratories as well as differences due to the different DLS equipments used. The comparison of measurements and data treatment procedures between the different DLS apparatus, i.e. Zetasizer NanoZS from Malvern Instrument for CEA and NRCWE, and Vasco Cordouan for INRS are discussed in Appendix C. For the comparison NM-200 and NM-203 were selected.

Three laboratories each assessed the **homogeneity within (intra) a vial** by DLS measurements; NM-200 and NM-203 were evaluated. Each laboratory performed measurements on a series of independent samples from one vial particular to the laboratory. Within a laboratory the samples were prepared by the same operator, under the same conditions and from the same vial, and thus illustrate both the homogeneity within one vial and the reproducibility of the sample preparation by a given operator.

The **homogeneity between (inter) vials** was evaluated by measuring on a series of samples from different vials of a given NM, prepared by the different laboratories. The results from the "homogeneity within a vial" were included in this analysis, thus quantifying both the variability between vials of the given NM, and between sample preparations from the different laboratories.

The main results are reported below in sections 4.2 (NM-200) and 4.3 (NM-203). When several samples from one vial were tested, mean values with standard deviations are reported. The data reported are Z-average particle diameter (Nobbmann et al., 2007) and polydispersity index (PdI), calculated using the cumulant method both for Malvern and Vasco Cordouan apparatus. The position of the main peak of the intensity size distribution was modelled with a multimodal analysis. For the Malvern apparatus, the CONTIN method was

used and the width of the main intensity peak (FWHM) is also reported. For the measurements with the Cordouan apparatus, this peak corresponds to the position of the main mode obtained with the Padé-Laplace method (see Appendix A).

4.2. Homogeneity Results for NM-200

Results by two laboratories for repeated DLS measurements on NM-200 are reported in Table 6; each laboratory measured on independent samples from one vial particular to the laboratory. DLS results on NM-200 obtained from different vials and three different laboratories are gathered in Table 7.

Table 6. DLS main size parameters (Z-average, polydispersity index, width and position of main peak in intensity distribution) obtained from independent suspensions of NM-200 prepared from the same vial under the same conditions.

NM	Lab.	vial n°	repetition /date	Z-Average	PdI	Intensity distribution main peak	FWHM peak width
NM-200	CEA	50	20101005	222	0.435	244.4	158.8
			20110202	198.5	0.371	218.1	115.3
			20110922	195.6	0.343	226.7	134.9
			20111116	212.4	0.412	262.9	230
intra vial				**207.1 ±12.3**	**0.390 ±0.041**	**238.0 ±19.9**	**159.8 ±50.1**
NM-200	INRS	109	N1	238.5	0.246	338.9	
			N2	243.0	0.244	281.9	
			N3	240.0	0.255	257.1	
intra vial				**240.5 ±2.3**	**0.248 ±0.006**	**292.7 ±42.0**	

Table 7. DLS main size parameters (Z-average, polydispersity index, width and position of the main peak in intensity distribution) obtained from independent suspensions of NM-200 prepared from different vials.

NM	Lab.	vial n°	Z-Average	PdI	Intensity distribution main peak	FWHM peak width
NM-200	CEA	50 (4)	207.1 ±12.3	0.390 ± 0.041	238.0 ±19.9	159.8 ±50.1
NM-200	CEA	95	195.3	0.378	222.4	163.1
NM-200	INRS	109 (3)	240.5 ±2.3	0.248 ±0.006	292.7 ±42.0	
NM-200	NRCWE	279	183.2	0.244	215.0	109.6
NM-200	NRCWE	494	184.8	0.237	226.3	125.8
NM-200	NRCWE	372	176.6	0.232	215.9	114.6
Average 3 vials NRCWE			**181.5 (±4.3)**	**0.238 (±0.006)**	**219.1 (±6.3)**	**116.7 (±8.3)**
Average over the 6 vials			**197.9 ±23.4**	**0.288 ±-0.075**	**235.0 ±29.4**	

The intra-vial reproducibility seems to be very dependent both on the mesurand and the laboratory. At INRS, the variability of data from the cumulant analysis (Z-average and PdI) is only a few percent, whereas it is much higher for the position of the peak obtained from Padé-Laplace analysis. At CEA, the observed intra-vial variability is about 6 to 10 percent. When comparing the 3 vials tested at NRCWE, the inter vial homogeneity seems very good (2-3%) with slightly higher intra-vial homogeneity than observed at CEA.

However, the size of NM-200 particles measured by each institution is quite different, so when comparing the 6 vials from the 3 institutions, the variability is higher than 10%. Given the consistency of the results obtained from each institution, the vials are thought to be rather homogeneous and the variations may originate from a systematic difference of sample preparation caused e.g. by the different types of sonicator and handling, including time-lapse from preparation to measurement etc.

4.3. Homogeneity Results for NM-203

Results from repeated DLS measurements on NM-203 dispersions made by two laboratories are reported in Table 8. Each laboratory used independent samples from one vial particular to the laboratory for the measurements. DLS results on NM-203 obtained from different vials and three different laboratories are gathered in Table 9.

Table 8. DLS main size parameters (Z-average, polydispersity index, width and position of main peak in intensity distribution) obtained from independent suspensions of NM-203 prepared from the same vial under the same conditions.

NM	Lab.	vial n°	repetition /date	Z-Average	PdI	Intensity distribution main peak	FWHM peak width
NM-203	INRS	227	N1	218.9	0.290	141.3	
			N2	288.2	0.327	154.9	
			N3	230.1	0.281	148.0	
intra vial				**245.7 ±37.2**	**0.299 ±0.024**	**148.1 ±6.8**	
NM-203	NRCWE	169	1	142.2	0.219	169.7	77.5
			2	149.9	0.247	189.6	99.1
			3	152.4	0.259	181.3	84.7
			4	145.6	0.250	171.6	76.5
intra vial				**147.5 ±4.5**	**0.244 ±0.017**	**178.1 ±9.2**	**84.4 ±10.4**

Table 9. DLS main size parameters (Z-average, polydispersity index, width and position of the main peak in intensity distribution) obtained from independent suspensions of NM-203 prepared from different vials.

NM	Lab.	vial n°	Z-Average	PdI	Intensity distribution main peak	FWHM peak width
NM-203	CEA	207 (2)	172.9 ±9.2	0.427 ± 0.025	181.0 ±4.0	82.5 ± 11.3
NM-203	CEA	118	179.2	0.375	154.5	63.9
NM-203	INRS	227 (3)	245.7 ±37.2	0.299 ± 0.024	148.1 ±6.8	
NM-203	NRCWE	169 (4)	147.5 ±4.5	0.244 ±-0.017	178.1 ±-9.2	84.4 ±10.4
NM-203	NRCWE	294	146.3	0.214	183.1	83.6
NM-203	NRCWE	212	146.6	0.229	181.7	83.4
Average 3 vials NRCWE			**146.8 (±0.6)**	**0.229 (±0.015)**	**181.0 (±-2.6)**	**83.8 (±0.6)**
Average over the 6 vials			**173.0 ±38.4**	**0.298 ±0.086**	**171.1 ±15.5**	

As also observed for NM-200, the sizes of NM-203 particles measured by the three institutions are relatively different, i.e. the variability in particle size between the 6 vials tested by the 3 institutions is quite high (20%). However, the reproducibility intra-vial obtained from CEA and from INRS is reasonable (a few to ten percent). The inter-vial variability from the three vials tested at NRCWE is even lower than the intra-vial variability. Therefore, the aggregated sizes in the vials are considered rather homogeneous and the variations observed may originate from a systematic difference in sample preparation caused e.g. by the different types of sonicator and handling, including time-lapse from preparation to measurement etc. However, as the average zeta-size, which was used for the comparison, does not give detailed information on the physical size-distribution of particles, especially not for polydisperse particles, this comparison should still be considered indicative. Due to the measurement principle, the DLS size is not the physical size of the primary nano-objects and may not always reflect the underlying number size distribution of the dispersed particles (Calzolai et al., 2011). Further detailed variability analysis is necessary using other methods such as TEM and BET to address detailed nano- and bulk-scale measurements, respectively.

5. Chemical composition

5.1. Elemental Composition by EDS and ICP-OES

The elemental composition of any nanomaterial is essential information for its chemical categorization; the observed toxicity of a nanomaterial may also be linked to the presence of coatings, catalysts and impurities. The elemental composition may be analysed using a range of different techniques. Depending on the technique used, the elemental analysis will range qualitative to a fully quantitative

The composition of the SAS NMs was analysed using semi-quantitative energy dispersive X-ray spectroscopy (EDS or EDX) on powder tablets by IMC-BAS. Additional analyses were performed using semiquantitative inductive coupled plasma (ICP) with optical emission spectrometry (OES) for detection and semiquantitative determination on extracted elements. Where EDS is suitable for major and minor elements, ICP techniques are generally most suitable for detecting and quantification of trace elements in the ppt to ppm levels. The applied techniques are described below.

Energy dispersive X-ray spectroscopy

EDS is short for Energy-dispersive X-ray spectroscopy and is available as an analytical tool in some electron microscopes.

In the present analysis, elements from Na and up were analysed using semi-quantitative analyses, which is an analysis based on factory-defined calibration curves with theoretical corrections for matrix effects etc. Oxygen was calculated by difference (assumed to be the residual un-quantified part of the sample). Therefore the sum of all elements adds up to 100 wt%. Due to current quality of detectors and instrument stability, semiquantitative analyses are relatively reliable for major and minor elements if the samples are of sufficient thickness and have low roughness.

Samples were prepared by pelletizing a known amount of powder, and the results are given in wt% and mass-based parts per million (ppm) depending on the absolute concentrations in the sample.

Table 10 list the elemental composition determined on the SAS NMs. All NMs only contain minor elemental impurities. The content of Na is 0.18 to 0.88 wt%, or 1800 to 8800 ppm, (NM-200, NM-201 and NM-204), whereas the content of Al is ca. 0.43 to 0.74 wt%, or 4300 to 7400 ppm, (all SAS NMs) and the content of S is 0.04 to 0.87 wt%, or 400 to 8700 ppm, (all NMs except NM-202). Ca was only observed in NM-203 (0.18 wt% or 1800 ppm). Based

on the weight percent of Si, the purity was also calculated assuming the ideal stoichiometric composition SiO_2.

Table 10. Elemental concentrations by EDS measurements on SAS performed at IMC-BAS.

Material	Si (wt.%)	Na* (ppm)	Al* (ppm)	S* (ppm)	Ca* (ppm)	O calculated[#] (wt.%),	Calculated[@] indicative content of SiO_2 (%wt)
NM-200	44.77	8800	4600	8700		53.02	96
NM-201	45.27	4400	7400	4600		53.08	97
NM-202	46.23		4500		1800	53.14	99
NM-203	46.32		4300	400		53.21	99
NM-204	45.96	1800	4800	2100		53.17	98

* ppm by weight [#] calculated by difference
[@] formula used: wt% SiO_2 = wt% Si x (1 + {molar weight O_2/molar weight Si})

Inductively coupled plasma-optical emission spectrometry

All ICP-OES measurements (inductively coupled plasma-optical emission spectrometry) were carried out by CODA-CERVA using a Varian 720-ES (Agilent Technologies). The analyses were performed using the SemiQuant feature, which is designed to provide a fast estimate of the concentration of non-calibrated compounds in samples. The samples were screened for 68 elements: Ag, Al, As, Au, B, Ba, Be, Bi, Ca, Cd, Ce, Co, Cr, Cu, Dy, Er, Eu, Fe, Ga, Gd, Ge, Hf, Hg, Ho, In, Ir, K, La, Li, Lu, Mg, Mn, Mo, Na, Nb, Nd, Ni, P, Pb, Pd, Pr, Pt, Rb, Re, Rh, Ru, S, Sb, Sc, Se, Si, Sm, Sn, Sr, Ta, Tb, Te, Th, Ti, Tl, Tm, U, V, W, Y, Yb, Zn and Zr.

Samples were prepared for analysis by dissolving the SAS NM in hydrofluoric acid. 0.1 g was weighed in a 50 ml DigiPREP HT tube (SCP SCIENCE) for each sample and 2 ml of concentrated hydrofluoric acid was added. The mixture was heated overnight at 80°C in a DigiPREP MS (SCP SCIENCE). After cooling double distilled water was added until the volume was 10 ml.

Table 11 presents the major impurities found in the SAS NMs: Na (> 0.1% in NM-200, NM-201 and NM-204), S (> 0.1% in NM-200) and Al (> 0.1% in NM-201). Calcium was found at > 0.01% in NM-200 and NM-201. Sulphur was found at >0.01% in NM-201 and NM-204. Smaller amounts of Fe, K, Zr and Mg were found in NM-200, NM-201 and NM-204. NM-202 and NM-203 contained no detectable impurities, except NM-203 (vial 0244) where almost 0.01% of Na was found while in NM-203 (vial 0239) Na was not detectable.

Table 11. Overview of impurities detected in SAS by semi-quantitative ICP-OES.

Material	Impurities > 0.01%	Impurities 0.005 – 0.01%	Impurities 0.001 – 0.005%
NM-200	Al, Ca, Na (>0.1%), S (>0.1%)	Fe, K	Mg, Zr
NM-201	Al (>0.1%) Ca, Na (>0.1%), S	Zr	Fe, K, Mg
NM-202	-	-	-
NM-203	-	Na (in one of the two vials tested)	-
NM-204	Al, Na (>0.1%), S	Ca	Fe, Zr

NM-200, NM-201 and NM-204 are produced by the precipitation process, and in that process Na_2SO_4 is a by-product when the starting materials are water glass ($Na_2O{\cdot}nSiO_2$, n=2-4) and sulphuric acid. In addition, the observed presence of calc-alkali elements, S and Al in the elemental analyses, is consistent with the XRD data with occasional observation of Na sulfate and böhmite, see chapter 11.

5.2. Presence of associated organic matter by TGA and DTA

Identification of potential presence of organic coating was assessed by sample mass-loss during heating using thermograviometric analysis (TGA) at NRCWE and differential thermal analysis (DTA) at IMC-BAS. Materials with with more than 1 wt% mass-losses above the dehydration temperatures were subject to extraction thermally or with organic solvents and analyses by gas chromatography and mass spectrometry (GC-MS).

In a TGA measurement a sample is heated in a gas (usually air, O_2 or N_2) and the weight of the sample is measured as a function of the temperature. The decomposition temperature and loss of mass may give information about the sample, e.g. water adsorbed to the surface of particles will evaporate around 100 °C, whereas most other added organic matter will evaporate or combust at higher temperature.

In DTA, the reference and the sample undergo identical thermal cycles; they are either heated or cooled with the same rate. The temperature is measured for both sample and reference, and the difference is calculated. Most transformations such as phase transitions, melting, crystallization, decomposition etc. are either endothermic or exothermic; that is they either require or release energy. Thus, when such a transformation takes place the temperature of the material will deviate from a reference, which is what is seen by DTA.

Figure 1 and Figure 2 show the results from thermogravimetric analyses of the SAS NMs. Weight losses below 100 °C for NM-200, NM-201, and NM-204 suggests that these samples

contain adsorbed water. The same samples also have a gradual mass-loss up to ca. 200 °C. This suggests presence of an organic compound, which may be functional coatings or associated organic compounds. NM-202 and NM-203 do not react thermograviometrically in the oxygen atmosphere.

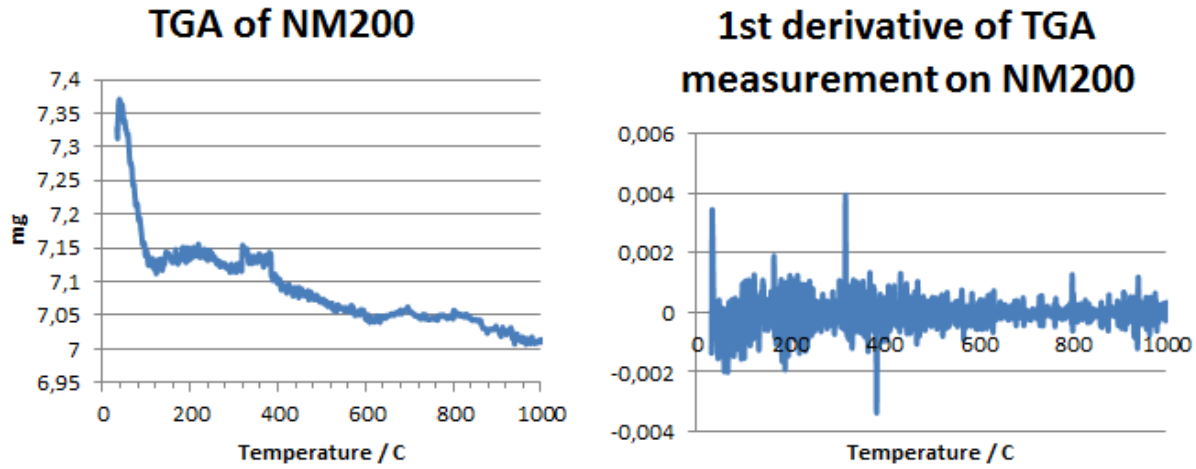

Figure 1. Results from TGA measurement on NM-200.The first and most pronounced weight loss is below 100 °C. It may be water attached to the surface. There is a second more gradual weight loss, possibly a coating.

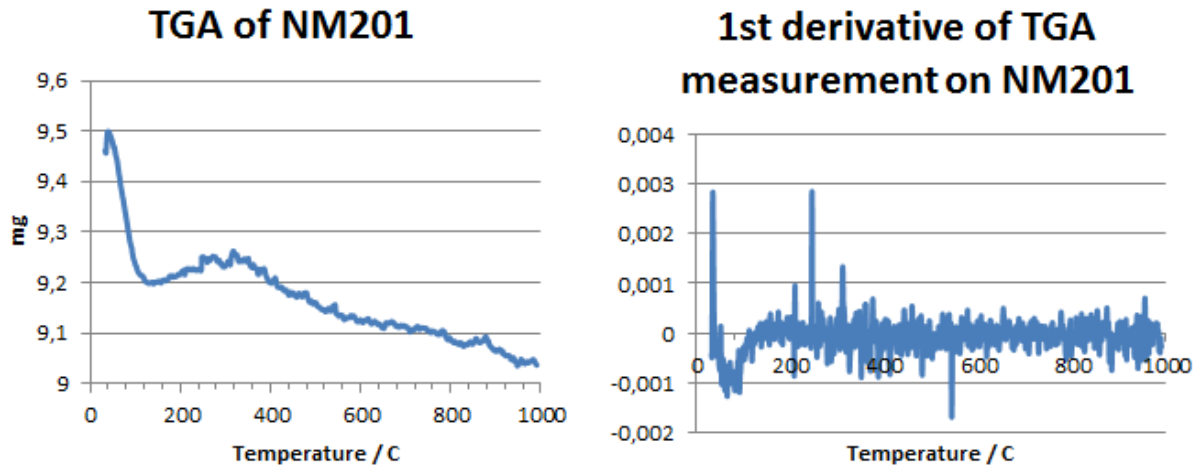

Figure 2. Results from TGA measurement on NM-201. The first weight loss occurs below 100 °C. It may be water attached to the surface. There is a second, more gradual weight loss, possibly a coating.

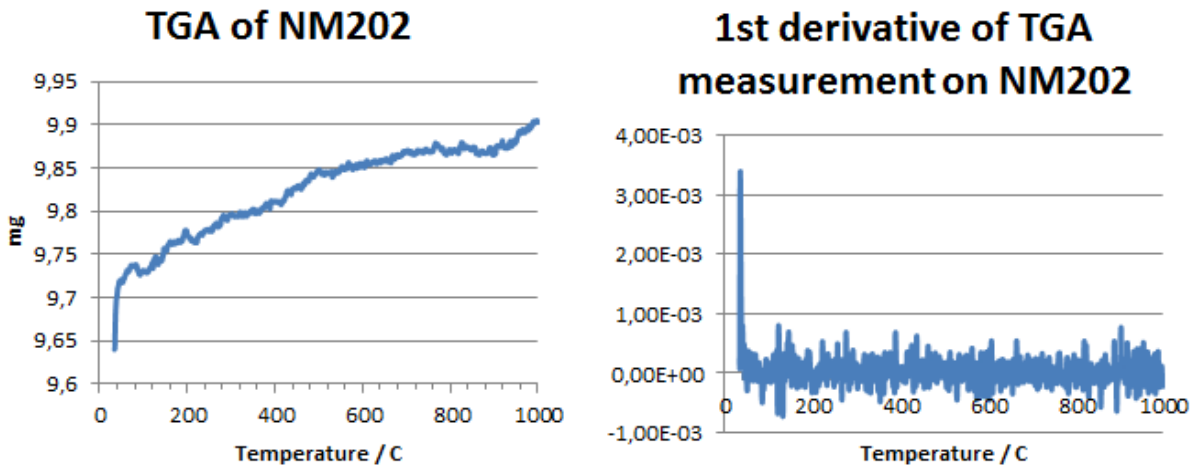

Figure 3. Results from TGA measurement on NM-202. The change in weight is due to buoyancy[3].

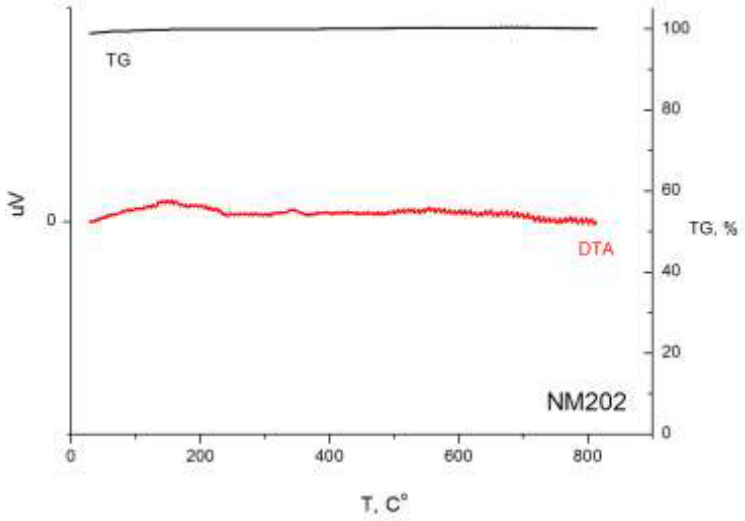

Figure 4. DTA (red curve, unit (left) is µV [Thermocouple electromotive force]) /TG (black curve, remaining mass in percent (right)) results for NM-202 showing no indication of any phase transformations.

[3] Buoyancy: During an experiment, the gas in the system is heated, primarily by conduction at low temperatures and by radiation at higher temperatures. In the initial stage the gas temperature is in advance of the sample/crucible temperature. The buoyancy of the gas itself decreases and therefore the sample/crucible appears to gain weight. This is, in part, due to the differences in thermal conductivity, density, and heat capacity for the gas and the sample/crucible.

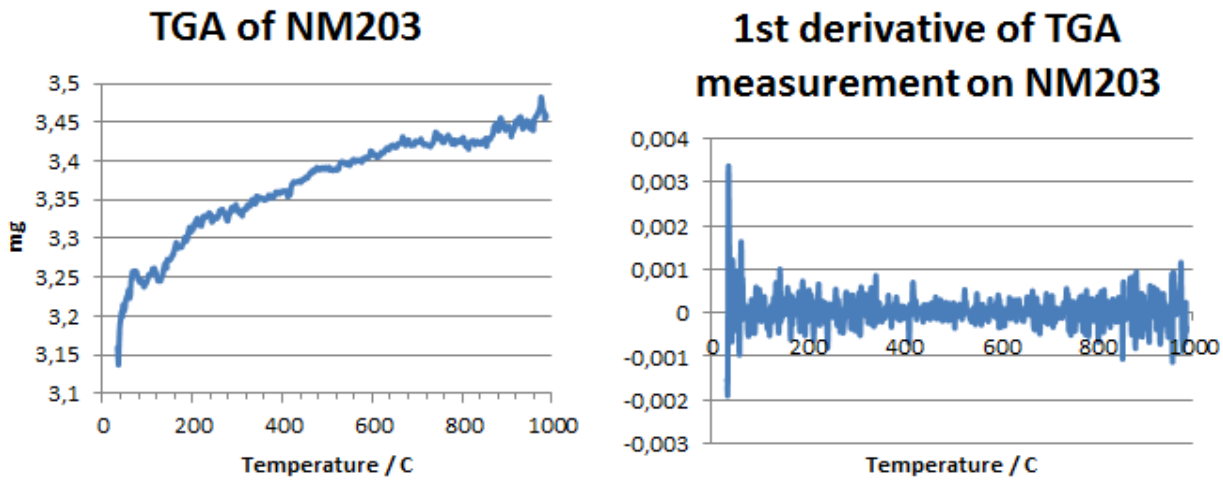

Figure 5. Results from TGA measurement on NM-203. The weight change is due to buoyancy[3].

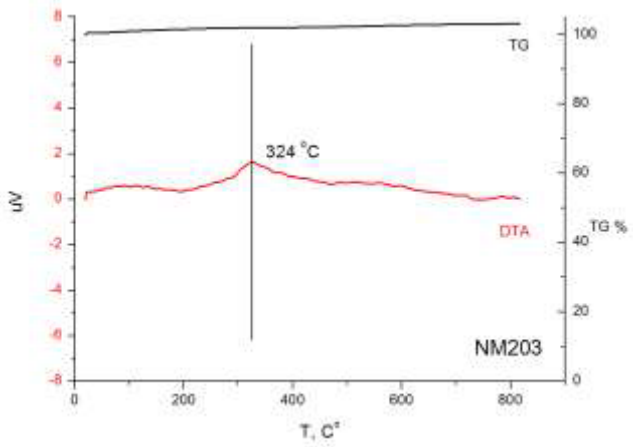

Figure 6. DTA (red curve, unit (left) is µV [Thermocouple electromotive force]) /TG (black curve, remaining mass in percent (right)) results for sample NM-203. There is a phase transformation at 324 °C.

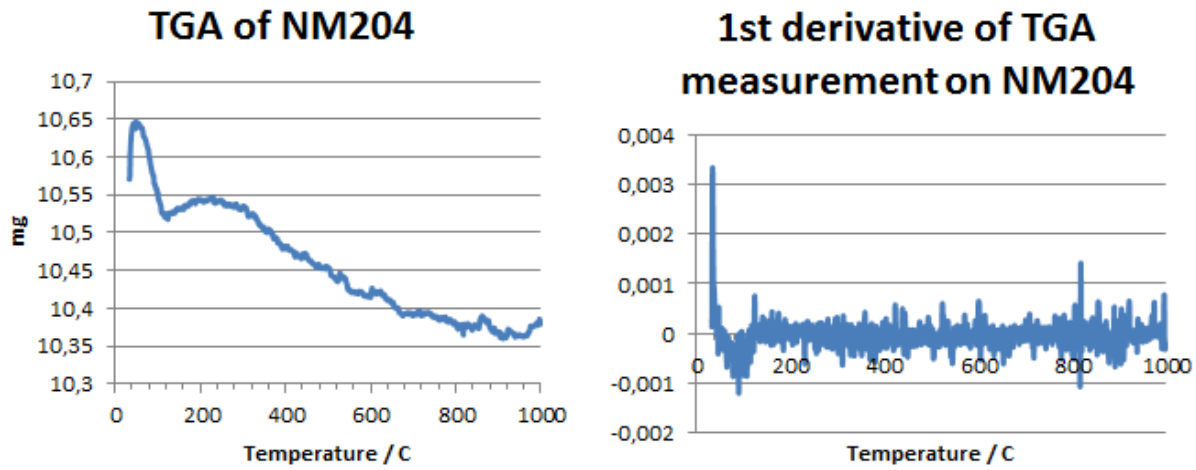

Figure 7. Results from TGA measurement on NM-204 showing a first weight loss below 100 °C. It may be water attached to the surface. There is a second more gradual weight loss, possibly a coating.

5.3. Analysis of associated organic matter

Analysis of the chemical composition of the organic matter coating or associated with the SAS NM was made at NRCWE. Samples that had a weight-loss of 1 wt% or more above 110°C were analysed. For SAS, this only included NM-204. In the general analysis, organic compounds were either extracted using ASE (Accelerated Solvent Extraction) or desorbed by TD (Thermal Desorption). The solvent extraction can be used for several chromatographic and mass spectrometric techniques and enable quantitative determination, but it has been found that TD combined with gas chromatography – mass spectrometry (GC-MS) generally is suitable for screening of the samples for up to medium molecular weights of the organic coatings. However, the thermal stability and solubility of a coating must be considered before extraction or desorption. If e.g. the organic coating material consists of high molecular weight component(s), MALDI-TOF-MS (Matrix Assisted Laser Desorption Ionization Time Of Flight) or ESI-MS (Electrospray Ionization) would be good choices instead of GC-MS.

For NM-204, approximately 300 mg of NM was extracted in methanol using ASE and analyzed using on-column GC-MS. The extract was injected directly (1 µl) into the on-column-GC-MS (Perkin Elmer Turbomass) which was equipped with a FactorFour™ 30 m VF-5ms capillary column with a diameter of 0.25 mm and 0.25 µm stationary phase containing 5 % phenyl poly dimethylsiloxane (Varian). The column flow was 1 ml/min helium and the injector temperature at 50°C was held for 2 min and then heated to 250°C at a rate of 50°C/min. The GC oven program was 50° for 4 min increased by 4°/min to 120° and 8°/min to 250° and held for 10 min. The transfer-line temperature was 275°C. The MS was run in positive mode using EI (electron ionization). Scanning mass range was from 50 to 500

m/z. Identification of the organic compounds was performed by AMDIS version 2.65 June 26, 2008 and NIST/EPA/NIH Mass Spectral Library Version 2.0f, 23 June 25, 2008 (NIST, USA). Compounds for which authentic standards were used and matched both retention time and spectrum were considered as clearly identified. The following GC-MS properties of the authentic standards were used for identification: Retention time (tR), mass spectrum (MS spectrum), fragmentation pattern and peak shape.

5.3.1 Results

The results from the GC-MS analysis at NRCWE are listed in Table 12 and as seen, four organic compounds were identified: tetramethyl silicate; Hexadecanoic acid, methyl ester; Hexadecanoic acid and Octadecanoic acid. The content of tetramethyl silicate in the extracts was surprising due to its relative high chemical reactivity (hydrolysis). However, indirect proof of the presence in the extracts was the observation that the peaks of tetramethyl silicate disappeared few days after extraction. This was also the case for the authentic tetramethyl silicate standards. Water vapour from the laboratory air will undoubtedly be taken up by the extracts and standard solutions and degrade tetramethyl silicate by hydrolysis. Tetramethyl silicate may have been produced during the extraction process which uses relatively harsh extraction conditions (150 °C and 140 bar) and methanol, either directly through reaction of SiO_2 with methanol or from tetraalkoxy silanes with other chain lengths in the samples, which in excess alcohol and basic conditions may produce tetramethyl silicate. It was not possible to confirm or reject these hypotheses at this point in time.

Table 12. Results for NM-204 of the GC-MS measurements performed at NRCWE.

Organic Compounds in the order of retention time On-Column-GC-MS	**Retention time (min)**	**Relative amount** (x= minor; xxx=major)
Tetramethyl silicate?	4.9	xxx
Hexadecanoic acid, methyl ester	33.4	x
Hexadecanoic acid	33.9	x
Octadecanoic acid	35.8	x

5.4. Surface composition by XPS

JRC performed XPS analyses on the SAS NMs. Compressed, dry pellets of sample were mounted on the sample holder using a double sided ultra high vacuum compatible (Si free) copper adhesive tape. All sample handling was done using nitrile powder free gloves. Nanomaterial was deposited onto the tape and then pressed with a clean Al foil to form a

uniform and continuous film. The XPS analysis provides information on the surface composition (down to a depth of 10 nanometres) of the analysed material. The detection limit of the method is about 0.1% percent of the atoms (at%).

XPS measurements were performed using an AXIS ULTRA Spectrometer (KRATOS Analytical, UK). Instrument calibration was performed using a clean, pure Au/Cu sample and pure Ag sample (99.99%). Measured values for electron binding energies (BE) were 84.00+/-0.02 eV, and 932.00+/-0.05eV (Briggs and Seah, 1983).

The samples were irradiated with monochromatic AlK α X-rays ($h\nu$=1486.6eV) using X-ray spot size of 400x700μm^2 and a take-off angle of 90° with respect to the sample surface. The base pressure of the instrument was better than $1x10^{-8}$ Torr and the operating pressure better than $3x10^{-8}$ Torr. A filament (I=1.9A) was used to compensate for surface charging and all spectra were corrected by setting hydrocarbon to 285.00eV.

For each sample, a survey spectrum (0 - 1110eV), from which the surface chemical compositions (at%) were determined, was recorded at pass energy of 160eV. In addition one set of high-resolution spectra (PE=20eV) was also recorded on each sample. The data were processed using the Vision2 software (Kratos, UK). Sample compositions were obtained from the survey spectra after linear background subtraction and using the Relative Sensitivity Factors included in the software derived from Scofield cross-sections. This method is estimated to give an accuracy of 10% in the measurement of elemental compositions. Curve fitting of core level peaks was carried out using the same initial parameters and inter-peak constrains to reduce scattering. The core level envelopes were fitted with Gaussian-Lorentian function (G/L=30) and variable full width half maximum.

Results and discussion

The surface composition of the SAS-NMs is reported in Table 13 where the values reported are the average of three measurements. Figure 8 show the survey spectra for the SAS NMs.

Table 13. Surface composition (at%) obtained from XPS survey spectra. Standard Deviation in brackets.

Material	at% **C**	at% **O**	at% **Si**	at% **S**	at% **Na**
NM-200	4.1 (0.9)	70.8 (0.6)	24.1 (0.5)	0.06 (0.04)	1.0 (0.2)
NM-201	4.5 (0.5)	70.3 (0.1)	23.6 (0.6)	0.01 (0.01)	1.5 (0.2)
NM-202	2.9 (0.6)	72.1 (0.4)	25.0 (0.3)	0	0
NM-203	2.3 (0.7)	71.7 (0.3)	26.0 (0.5)	0	0
NM-204	4.3 (2.6)	71.9 (2)	23.2 (1.0)	0	0.5 (0.1)

The composition of the nanomaterials is similar. Beside the expected presence of Si and O, a hydrocarbon contamination is observed which is attributed to adsorbed carbon on the surface. Also Na was detected in NM-200, NM-201 and NM-204 which have all been synthesized by the precipitation process where Na_2SO_4 will be present as an impurity in the final product.

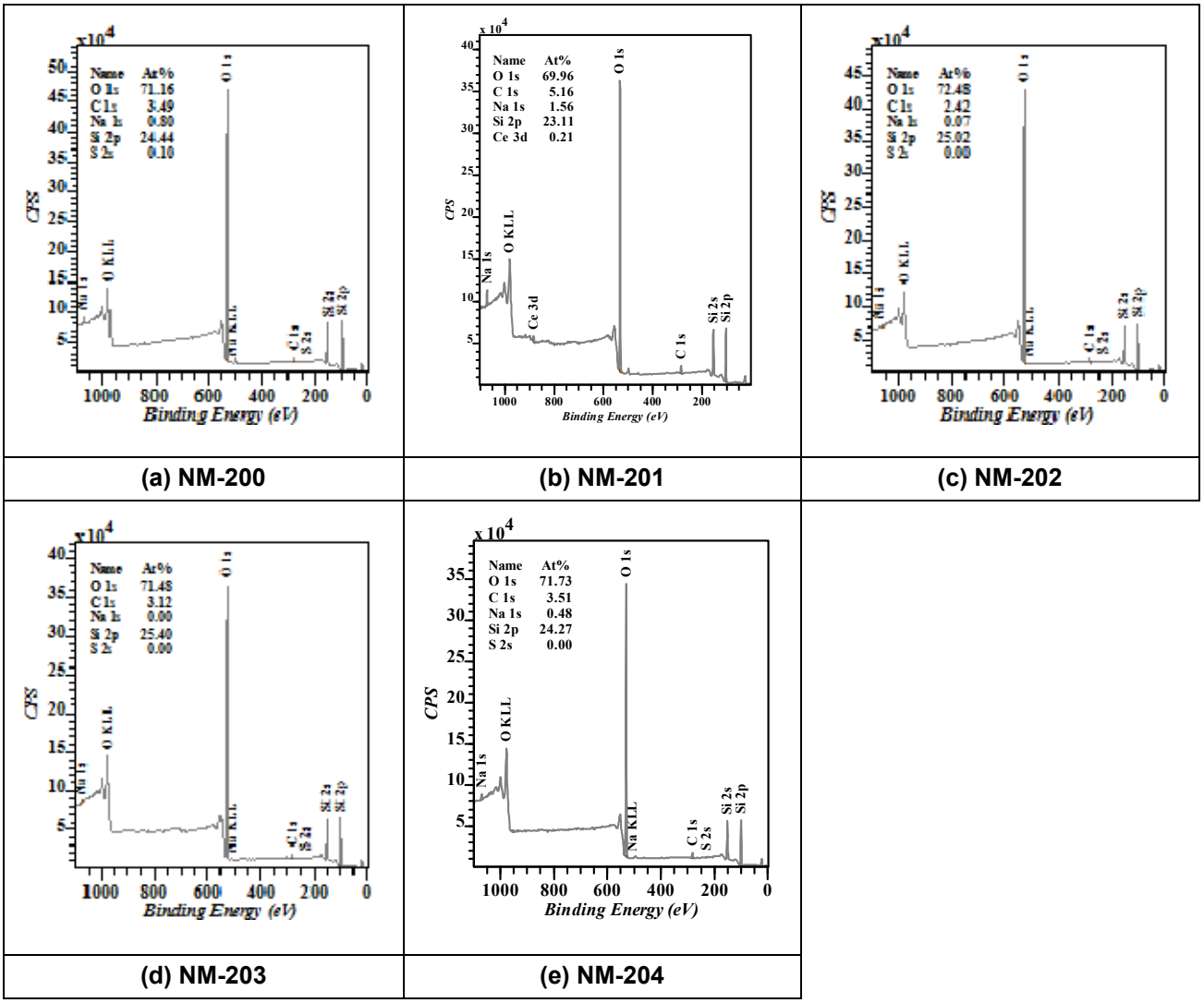

Figure 8(a) to (e). Survey spectra of the SAS NMs.

No other elements were detected at the surface of the samples, except for NM-201 for which Ce was detected. This indicates that the presence of Al observed by XRD could be related to crystalline phases formed within the nanoparticles during the growth process and not to post process contamination. Moreover, after 2 minutes of etching with Ar^+ ions at 3keV the Na and S signals disappeared indicating that those elements are present as surface contaminants. The carbon and oxygen levels are slightly decreasing in all samples after Ar etching, whilst the Si2p intensity increases. An interesting finding is the appearance of the Ce 3d signal at

about 880eV in sample NM-201. The amount of Ce is quite low (about 0.25±0.1 at%), but it increases at about 0.80at% after ion etching.

The ratio Si/O is below the theoretical value of 0.5 for all samples. This can be explained by the possible surface contamination with Carbon-Oxygen compounds. The analysis of C1 high resolution peaks reveals the presence of three components at 285eV, 286.7eV and 288.6eV that can be ascribed to CC/CH, C-O and C=O bonds, respectively, see Figure 9.

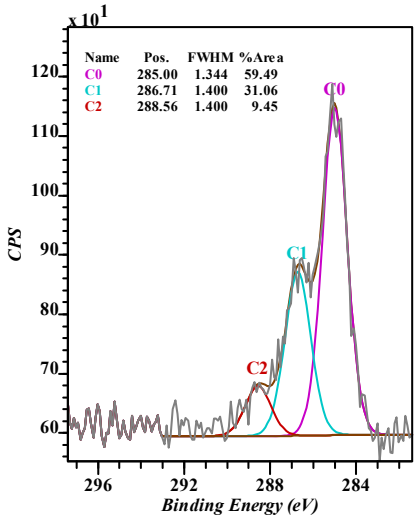

Figure 9. C1s high resolution core level spectrum of sample NM200.

5.5. Observations and conclusions for chemical composition

As expected, all the analytical methods used indicate that the SAS NMs main elemental components are Si and O, and impurities are only a minor part. Depending on analytical technique, several additional elements and compounds were attributed to the different SAS NMs, see Table 14, which report only the impurities, as all methods agreed on the main components Si and O. The ICP-OES analysis identified a number of impurities below 0.01% for NM-200, NM-201 and NM-204 and these are reported in Table 11. In addition to the information from this chapter 5 also the information from the XRD analysis (chapter 11) is included, as it suggests presence of identified crystalline impurities. Also the results from the biodurability study (chapter 6.4) are reported as Al was detected in all the SAS NMs. Furthermore, the TGA analysis of the SAS NMs indicated that NM-204 had an organic coating in abundance greater than 1 wt% (see chapter 5.2).

Table 14. Elements (impurities) detected in the SAS NMs according to analytical method.

Material	EDS*	ICP-OES*	XPS	XRD[$]	Biodurability information[&]
NM-200	Na, Al, S	Na, Al, S, Ca (above 0.01%)	Na, C	Na, Al, S	Al
NM-201	Na, Al, S	Na, Al, S, Ca	Na, C	Na, Al, S	Al
NM-202	Al, Ca	-	Na, C	Al, S	Al
NM-203	Al, S	-	C	Al	Al
NM-204	Na, Al, S	Na, Al, S	Na, C	No impurities detected	Al

* Semi-quantitative [&] Determined by ICP-MS

[$] The XRD analysis was performed by three laboratories, and only one of them detected Al as böhmite.

As seen from Table 14, the different techniques applied for analysis of the composition of the materials indicate that different impurities are present in the SAS-NMs. The results of these analyses agree to a certain degree (between laboratories and between methods). The exact nature and amount of all impurities is not fully understood. The different methods applied have different detection limits, resolution and detection abilities. Thus, the precise composition of the different SAS NMs and their impurities and surface chemistry is still somewhat inconclusive. More detailed quantitative bulk elemental, organic and surface chemical analyses are required for full assessment of the chemical composition. A detailed analytical electron microscopy analysis could be a solution for detailed characterization of impurity phases.

6. Hydrochemical reactivity, solubility and biodurability

The 24-hour hydrochemical reactivity, solubility and inferred biodurability of the SAS MN were investigated by NRCWE. The tests were completed in the NANOGENOTOX 0.5% BSA batch dispersion medium and two synthetic biological media relevant for assessing the NM behavior in the lung-lining fluid (low-Ca Gambles solution) and the intestinal system (Caco 2 cell medium).

Data on the hydrochemical reactivity of NMs and their biodurability may be important to better understand the biochemical reactivity of nanoparticles and dissolution in contact with specific biofluids. When particles come in contact with biofluids, reactions may take place that cause e.g. changes in pH, adsorption of ions or biomolecules, dissolution, and electron loss or gain, which can result in formation of reactive oxygen species (ROS). ROS are often considered as being one of the most important parameters of hydrochemical reactivity (e.g., Dick et al., 2003; Xia et al., 2006).

Biodurability is another classical test, originally established to analyse the degradation (dissolution) rate of asbestos, minerals and man-made fibres in synthetic lung-fluids (e.g., Forster and Tiesler, 1993; Christensen et al., 1994; Sebastian et al., 2002). Recently, the development of biodurability testing has gained new interest (Wiecinski et al., 2009; Xinyuan et al., 2010; Osmond-McCloud et al., 2011; Cho et al., 2011). Quantification of biodurability is usually done by weighing residual particles on a filter sample and/or measurement of specific constituent elements. However, representative retrieval of NMs from small volume dispersions, may be associated with some difficulty.

In this analysis, we performed a batch dissolution test of the hydrochemical reactivity and solubility under external environmental control mimicking in vitro toxicological test conditions. For the experiments, we used a commercial 24-well pH and O_2 Sensor Dish Reader (SDR) system (PreSens GmbH; Germany). Dispersions were prepared as described in the generic NANOGENOTOX dispersion protocol to mimic the treatment used for toxicological studies

The SDR system enables simultaneous measurement in 24 wells at one second resolution and therefore ability to establish a variety of data as function of dose and time. The test conditions using the SDR system are maintained by a cell-incubator and consequently directly corresponds to the conditions of a given *in vitro* exposure event (here 37°C and 5% CO_2 for lung conditions). However, one drawback is that the measurable pH-range is limited to pH 5 to 9. The range in O_2 concentrations is wide and vary from 0 to 250% O_2 saturation (0 to 707.6 µmol/l). Due to the principle link between electron activity and oxygen fugacity

(e.g., Nordstöm and Munoz, 1994), the variation in O_2 may correspond to values obtained by direct redox potential measurement.

As a final output from the SDR studies, the measured amount of soluble NM (concentrations of dissolved elements) after the 24-hour incubation in each of the three incubation media is reported. For this, liquid samples were carefully extracted, filtered and centrifuged to remove dispersed NM in the liquid sample. Quantification was done as a commercial service by ICP-OES (Si) and ICP-MS (Al) without further acid treatment other than stabilization. The concentrations of dissolved elements give indication on the durable fraction (total – the dissolved amount) in the three media. However, the values are still indicative as high-precision analysis was not performed on the starting materials.

6.1. Results, Hydrochemical pH reactivity

As explained in Appendix B, four concentrations and six dose response measurements are made in one test round. Figure 10 to Figure 14 show the temporal pH evolution in each of the tested NM incubations considering the highest dose experiments compared to the reference (zero-dose). The results show that most of the NM has negligible to minor influence on the pH-evolution in the three test media. If there is a pH reaction, this normally occurs within the first few hours. It is particularly noteworthy that pH-evolution paths are mostly controlled by the different test media.

The pH in the 0.05% BSA water batch dispersion medium typically increases from near or below the pH 5 lower detection limit to between pH 5 and 6 within the first hour. Addition of nanomaterial to the BSA water appears generally to cause a small elevation in the pH as compared to the reference medium.

The Gambles solution medium has slightly basic pH values, typically starting between pH 8 and 9. In a few cases, the pH even exceeds the pH 9 upper detection limit of the SDR (e.g. Figure 10 center). This demonstrates clearly that there may be a need to perform accurate online pH control to avoid episodes with unrealistic biological simulation or test conditions. Moreover, the protocol should ensure that pH adjustment in this type of static experiment without online pH control at least make proper pH adjustment in the initial step of the test. By deviation from protocol, this was not done in these tests.

The Caco 2 cell medium normally has an initial pH around 7.5 to 8 and the pH usually drops slightly during the 24-hour experiment. In the test with NM-200 (Figure 10, bottom), the pH increases dramatically in all wells from about half an hour to almost 2 hours. This was also seen for the Gambles solution (Figure 10, centre) and for BSA/water (Figure 10, top) though

less pronounced in the latter case and suggests that a loss of CO_2 control may have occurred. The notable increase at the last few hours of testing NM-202, see Figure 12, may be due to similar events. Further information cannot be given at this point due to lack of additional experiments.

Due to the presence of Na_2SO_4 in some of the SAS samples, some lowering of the pH could be expected for NM-200, NM-201 and NM-204. However, this was not observed.

As a general conclusion, it is found that the selected incubation media and the incubator atmosphere are the primary controllers of the temporal pH evolution for the nanomaterials.

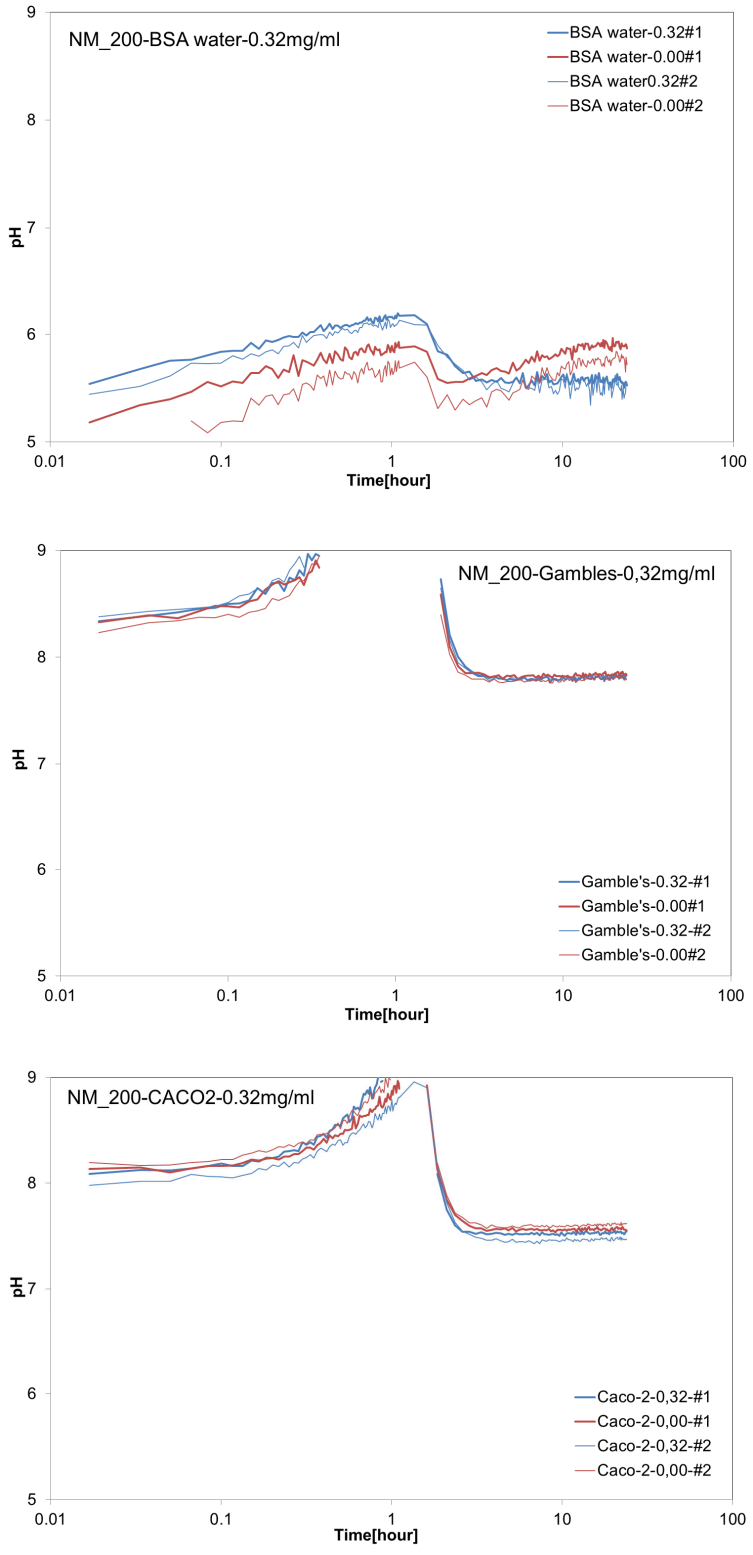

Figure 10. pH-evolution during 24-hour incubation of NM-200 in 0.05% BSA water NANOGENOTOX batch dispersion (top); Gambles solution (centre); and Caco2 cell medium (bottom). The particle concentrations in the Gambles solution and Caco2 cell medium were dosed from the batch dispersion tested in (top).

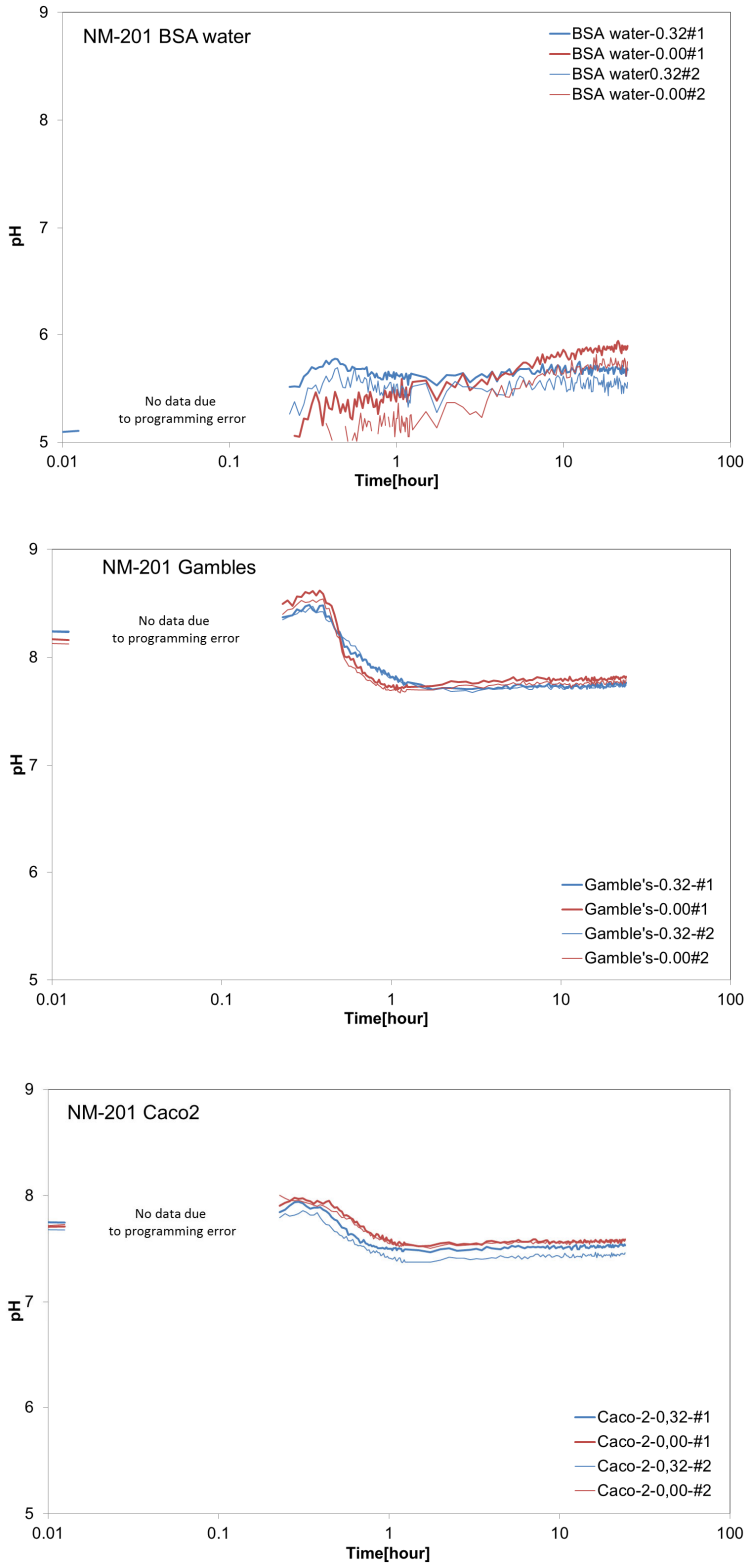

Figure 11. pH-evolution during 24-hour incubation of NM-201 in 0.05% BSA water NANOGENOTOX batch dispersion (top); Gambles solution (centre); and Caco2 cell medium (bottom). The particle concentrations in the Gambles solution and Caco2 cell medium were dosed from the batch dispersion tested in (top).

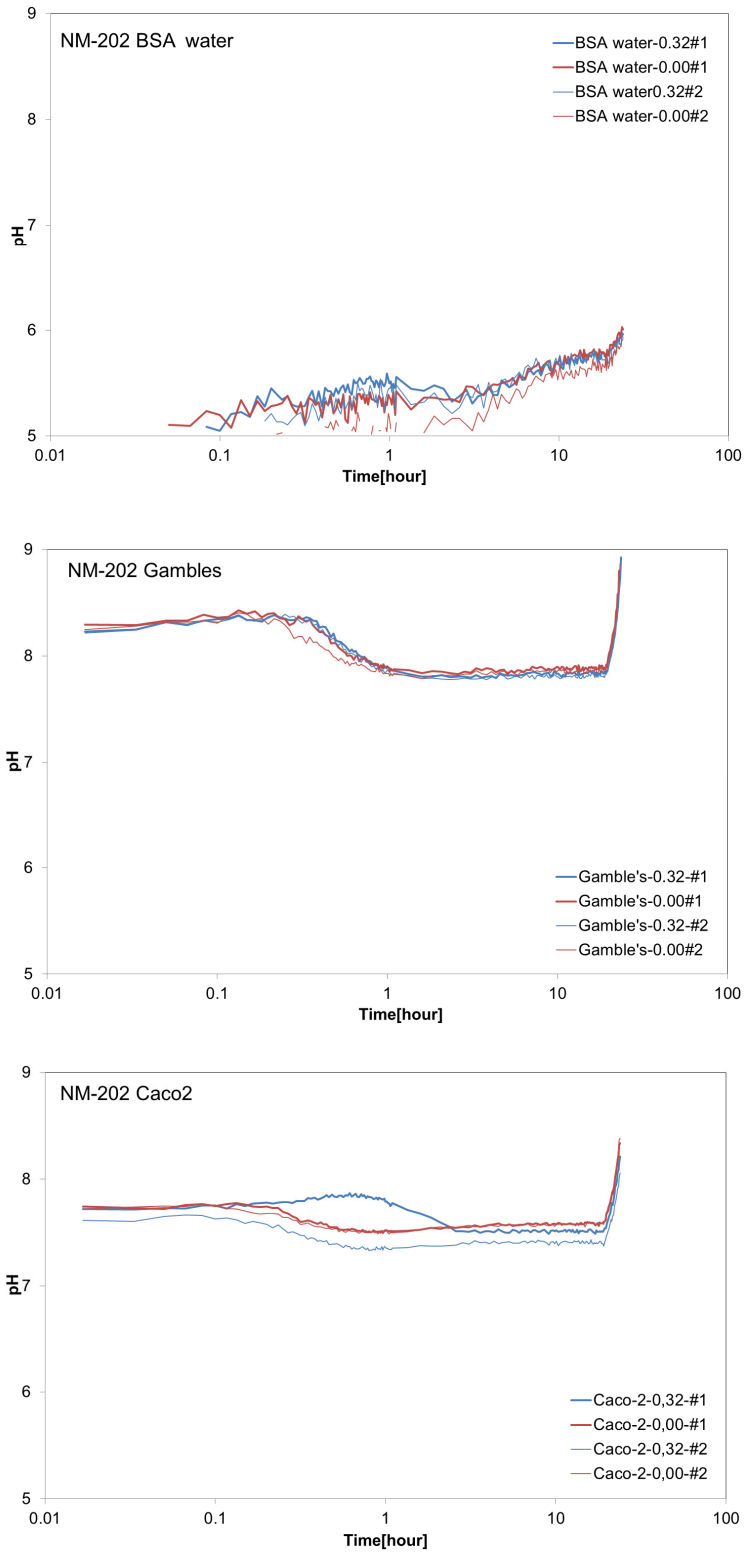

Figure 12. pH-evolution during 24-hour incubation of NM-202 in 0.05% BSA water NANOGENOTOX batch dispersion (top); Gambles solution (centre); and Caco2 cell medium (bottom). The particle concentrations in the Gambles solution and Caco2 cell medium were dosed from the batch dispersion tested in (top).

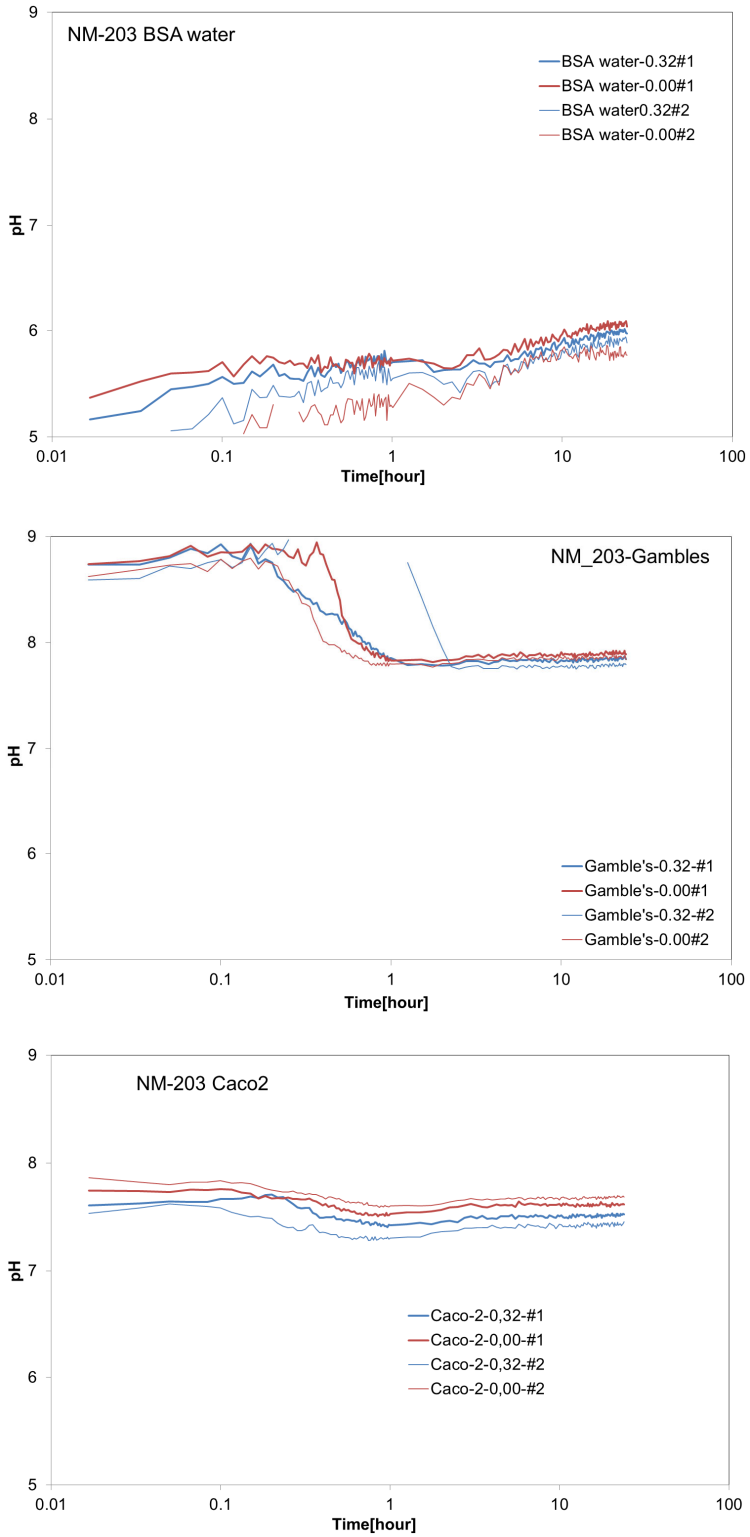

Figure 13. pH-evolution during 24-hour incubation of NM-203 in 0.05% BSA water NANOGENOTOX batch dispersion (top); Gambles solution (centre); and Caco2 cell medium (bottom). The particle concentrations in the Gambles solution and Caco2 cell medium were dosed from the batch dispersion tested in (top).

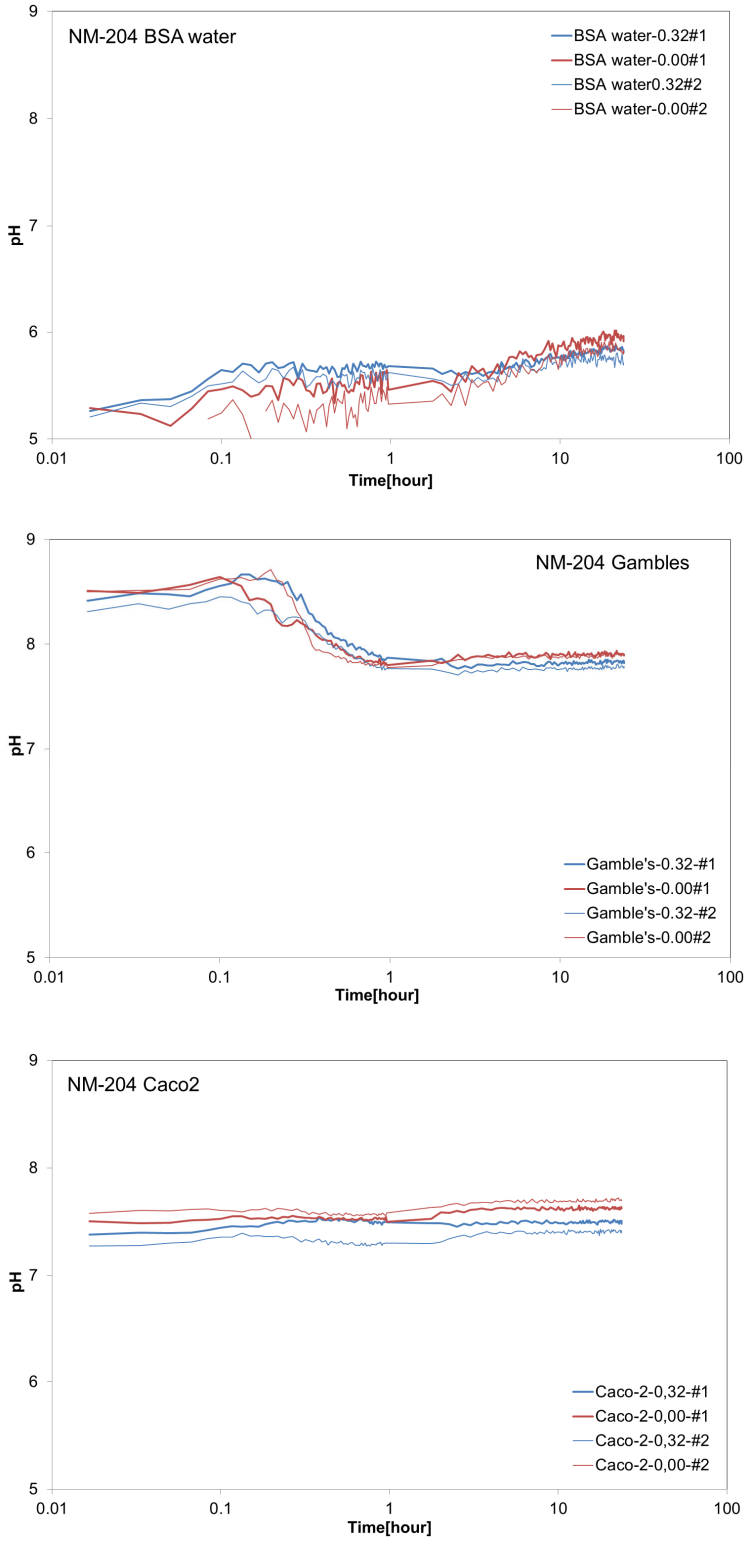

Figure 14. pH-evolution during 24-hour incubation of NM-204 in 0.05% BSA water NANOGENOTOX batch dispersion (top); Gambles solution (centre); and Caco2 cell medium (bottom). The particle concentrations in the Gambles solution and Caco2 cell medium were dosed from the batch dispersion tested in (top).

6.2. Hydrochemical O_2 Activity

In the O_2 analyses the temporal evolution of O_2 was expressed as $dO_2 = O_{2,\ dose} - O_{2\ medium\ control}$, where $O_{2\ medium\ control}$ is the O_2 from the control, which is medium without any NM added, and $O_{2,\ dose}$ is the O_2 from the dispersed sample. Figure 15 to Figure 19 show the temporal variation in dO_2 (average of two experiments) and show that the SAS NMs have a wide range of reactivity. Interestingly, the reactivity may not be exerted to similar degree in the different media. It appears as though the reactivity for the SAS NMs often is less pronounced in the BSA medium than in the Gambles solution and Caco 2 media.

For SAS NMs, increased dO_2 levels were, to some extent, observed in all three media for NM-200 (not Caco 2 medium), NM-201, NM-202, and NM-203, whereas NM204 is only slightly reactive. The maximum dO_2 change is on the order of 40 µmol/ml. Considering the applied doses, this suggest that the particle reactivity easily can exceed 1 µmol O_2/mg.

This type of analysis is still in development and a clear data interpretation is not possible at this point in time. It is, however, evident that the SAS NMs do react and have influence on the O_2 concentrations in the dispersions. Currently, the interpretations of the dO_2 variations are as a strong indication of the SAS NMs to be redox-active due to direct electron transfer processes or to cause changes in the O_2 concentration due to dissolution-related reactions.

6.3. In vitro dissolution and solubility

Table 15 present the elemental analysis of the carefully centrifuged and filtered particle-free media, which show that the three media give only minor background concentrations of Ti, Si, Al, and Fe, Co, and Ni, which were the key target elements for assessing the 24-hour NM dissolution ratios (see also Table 16).

Table 15. Elemental concentrations in the investigated incubation media (n=2).

MDL[€]	Element	unit	BSA	σ	Gambles	σ	Caco2	σ
1	K	mg/l	<	<	<	<	160	<
1	Si		<	<	<	<	<	<
0.05	Fe		<	<	<	<	0.31	0.36
30	Al	µg/l	<	<	<	<	<	<
5	Ti		7.6	1.0	10.2	1.4	11.5	1.3
1	Cr		0.9	0.7	1.3	0.4	1.8	0.6
5	Co		<	<	<	<	<	<
1	Ni		1.8	0.8	1.97	0.33	2.4	1.5
5	Zn		22.3	11.5	11.0	3.8	88	7

[€] MDL = Minimum detection limit; < = not detected or below MDL. Measurements were performed twice, i.e. n=2

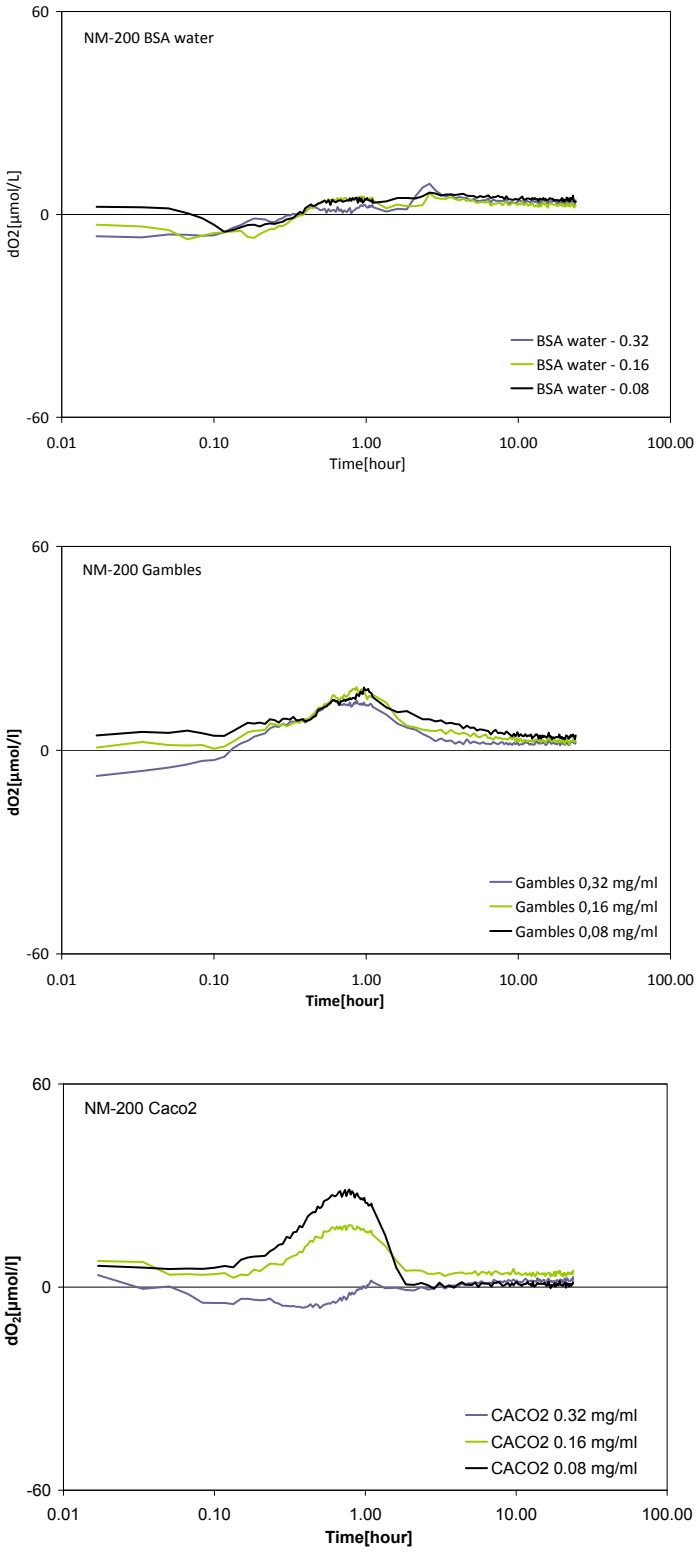

Figure 15. O_2-evolution during 24-hour incubation of NM-200 in 0.05% BSA water NANOGENOTOX batch dispersion (top); Gambles solution (centre); and Caco2 cell medium (bottom). The particle concentrations in the Gambles solution and Caco2 cell medium were dosed from the batch dispersion tested in (top).

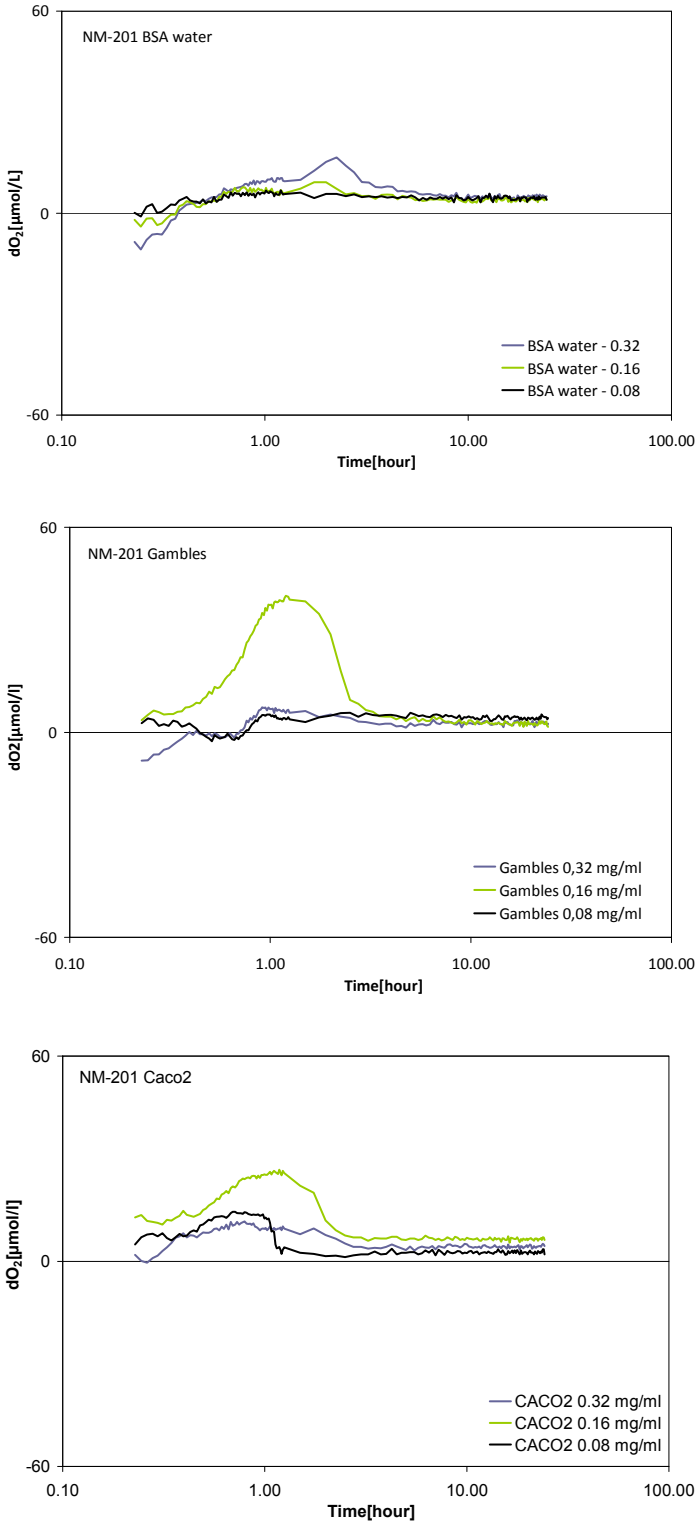

Figure 16. O_2-evolution during 24-hour incubation of NM-201 in 0.05% BSA water NANOGENOTOX batch dispersion (top); Gambles solution (centre); and Caco2 cell medium (bottom). The particle concentrations in the Gambles solution and Caco2 cell medium were dosed from the batch dispersion tested in (top).

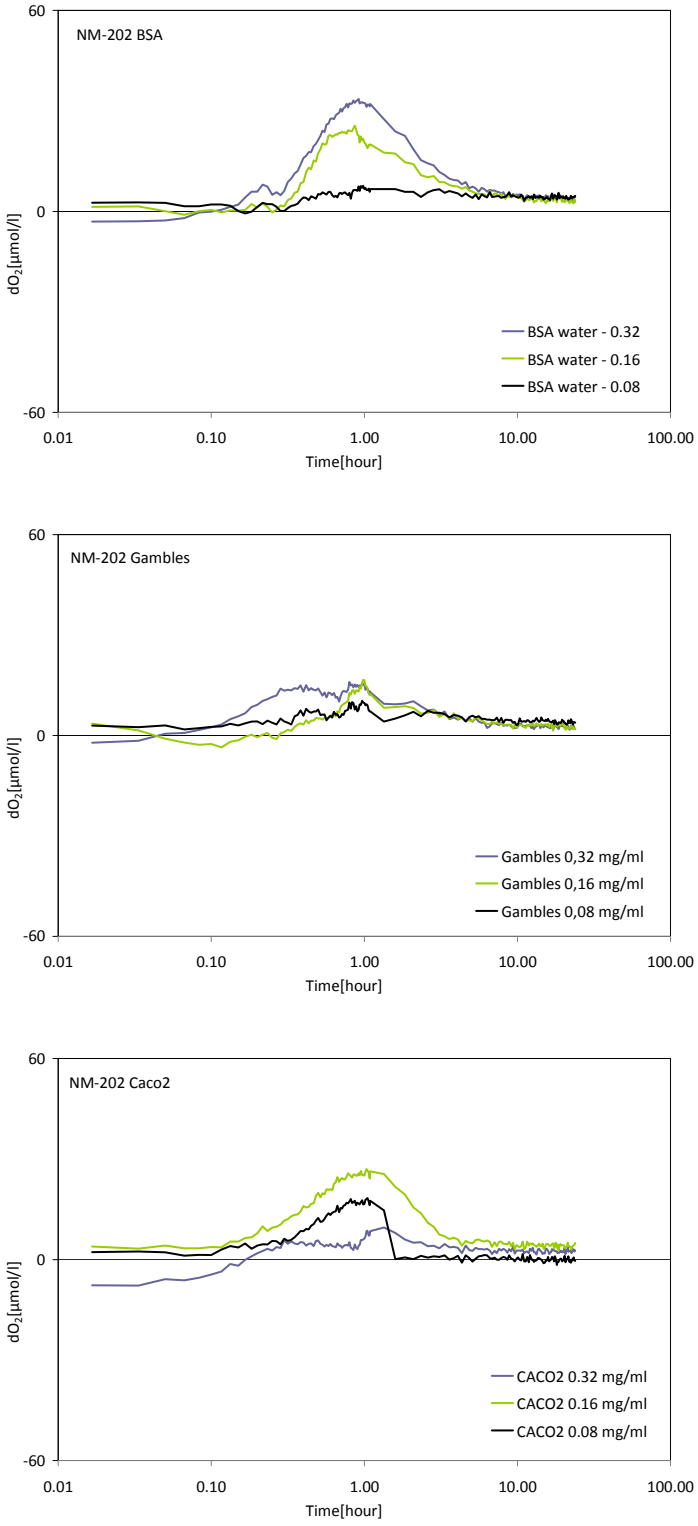

Figure 17. O_2-evolution during 24-hour incubation of NM-202 in 0.05% BSA water NANOGENOTOX batch dispersion (top); Gambles solution (centre); and Caco2 cell medium (bottom). The particle concentrations in the Gambles solution and Caco2 cell medium were dosed from the batch dispersion tested in (top).

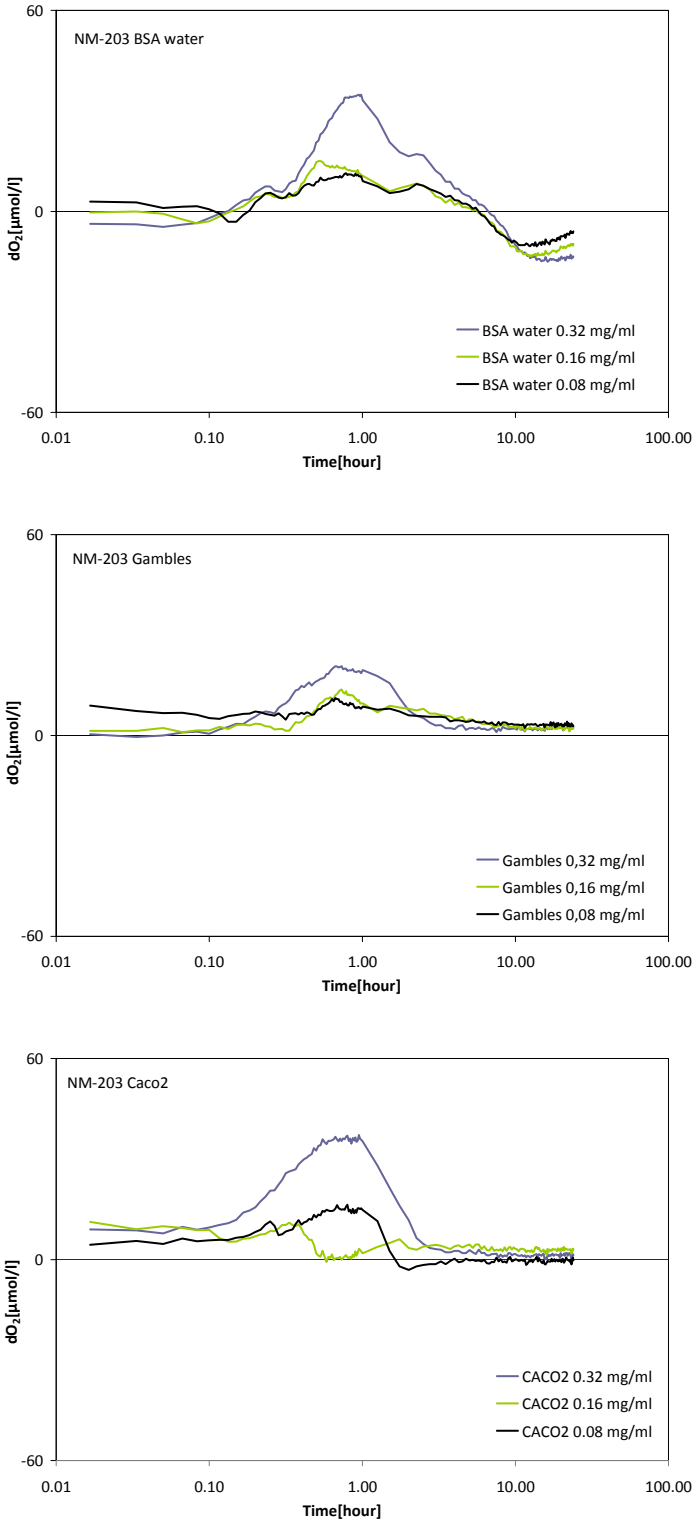

Figure 18. O_2-evolution during 24-hour incubation of NM-203 in 0.05% BSA water NANOGENOTOX batch dispersion (top); Gambles solution (centre); and Caco2 cell medium (bottom). The particle concentrations in the Gambles solution and Caco2 cell medium were dosed from the batch dispersion tested in (top).

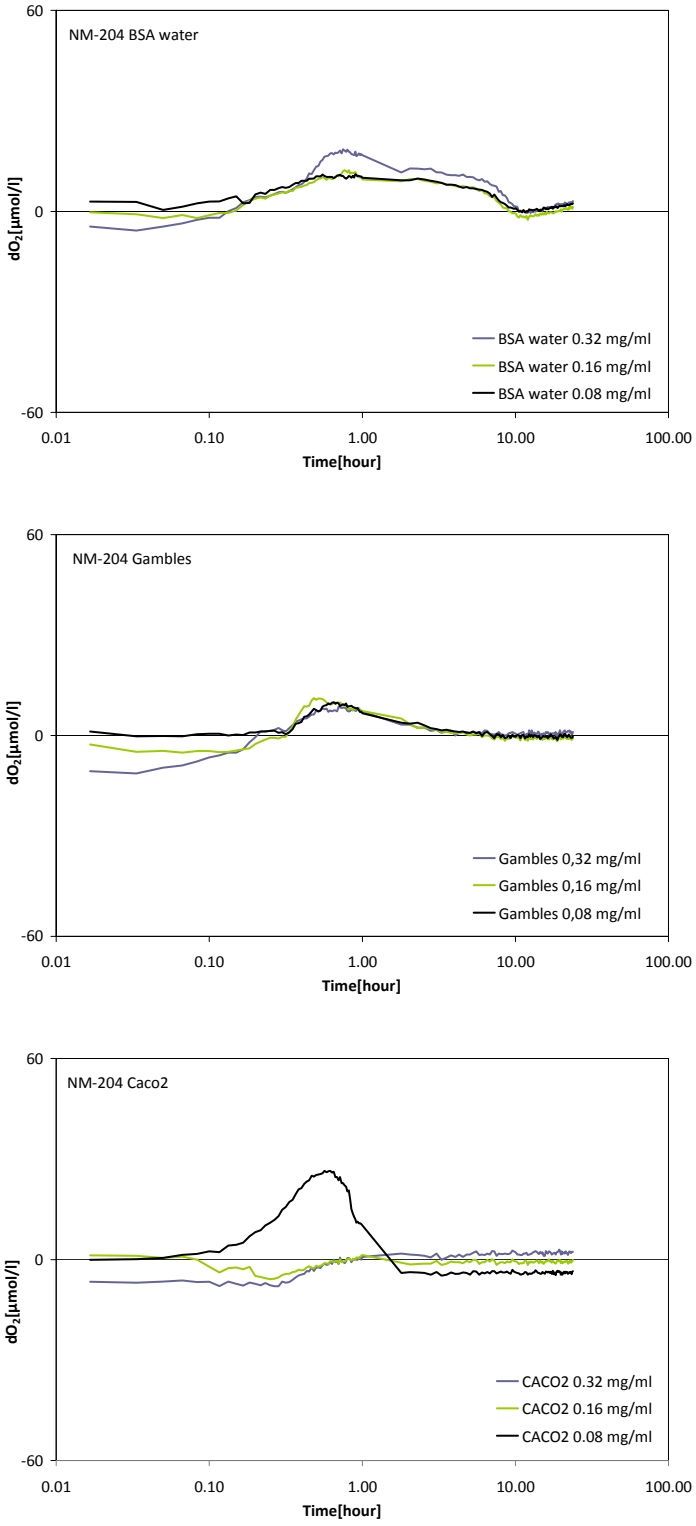

Figure 19. O_2-evolution during 24-hour incubation of NM-204 in 0.05% BSA water NANOGENOTOX batch dispersion (top); Gambles solution (centre); and Caco2 cell medium (bottom). The particle concentrations in the Gambles solution and Caco2 cell medium were dosed from the batch dispersion tested in (top).

Table 16 lists the elemental concentrations used for the assessment of NMs' solubility and biodurability. As mentioned in Chapter 5, only semi-quantitative analyses were made on the SAS NMS. Therefore, the assessment of 24-hour solubility limits and biodurable fraction must be considered approximate.

Table 16. Elemental concentrations (µg/g) in the NM samples used for assessment of dissolved fraction and particle biodurability.

Sample	Si*	Al*
NM-200	447,700	4,600
NM-201	452,700	7,400
NM-202	462,300	4,500
NM-203	463,200	4,300
NM-204	459,600	4,800

*From EDS measurements in Chapter 5

Table 17 lists the elemental compositions in the three incubation media corrected for the background concentrations in the incubation media. It is clear that most elements are present in relatively low concentrations. However, for proper assessment of the amount of dissolved matter, the calculation must be made using the applied elemental dose in the experiments. For this analysis, 0.32 mg/ml NM powder was dosed into each incubation media.

Table 17. Background-corrected elemental concentration in the test mediums after 24-hour dissolution tests with SAS NM (n=2).

MDL			NM-200	σ	NM-201	σ	NM-202	σ	NM-203	σ	NM-204	σ
0.05% BSA												
1	**mg/l**	**Si**	2.1	0.2	-	-	7.1	0.1	7.4	0.2	2.0	0.2
30	**µg/l**	**Al**	105	16	231	148	145	92	90	6	84	55
Gambles solution												
1	**mg/l**	**Si**	47.6	<	15.4	<	46.2	<	47.6	<	34.3	1.0
30	**µg/l**	**Al**	71	8	178	65	73	12	238	79	-	-
Caco2												
1	**mg/l**	**Si**	39.9	1.0	10.5	<	38.5	1.0	39.9	1.0	23.8	<
30	**µg/l**	**Al**	301	10	217	30	72	3	104	43	224	40

MDL: Minimum detection limit in the raw analysis; - denotes not detected; < denotes background corrected concentration lower than 0.1 x MDL. Measurements were performed twice, i.e. n=2

The elemental dose concentration was determined by simple multiplication of element concentration (Table 16) in µg/mg with the applied dose 0.32 mg sample/ml medium. These concentration data were used to calculate the weight percent of dissolved element using the background-corrected elemental concentrations in the three incubation media after 24-hour incubation (Table 17). The results from these calculations are shown in Figure 20, which shows the elemental dose and the percent dissolved Si and Al in the three incubation media.

Naturally, the elemental dose is heavily dominated by Si, but the concentration of the Al impurities appear to be relevant as well. The highest Al-content was found in NM-201 (0.74 wt%) and it was in the order of 0.4 to 0.5 wt% in the other SAS samples (Figure 20 and Table 16). The presence of Al is, at least in some samples, due to associated böhmite found by XRD in NM-200, NM-201, NM-202, and NM-203. But from the XRD analyses, it cannot be excluded to occur also in NM-204.

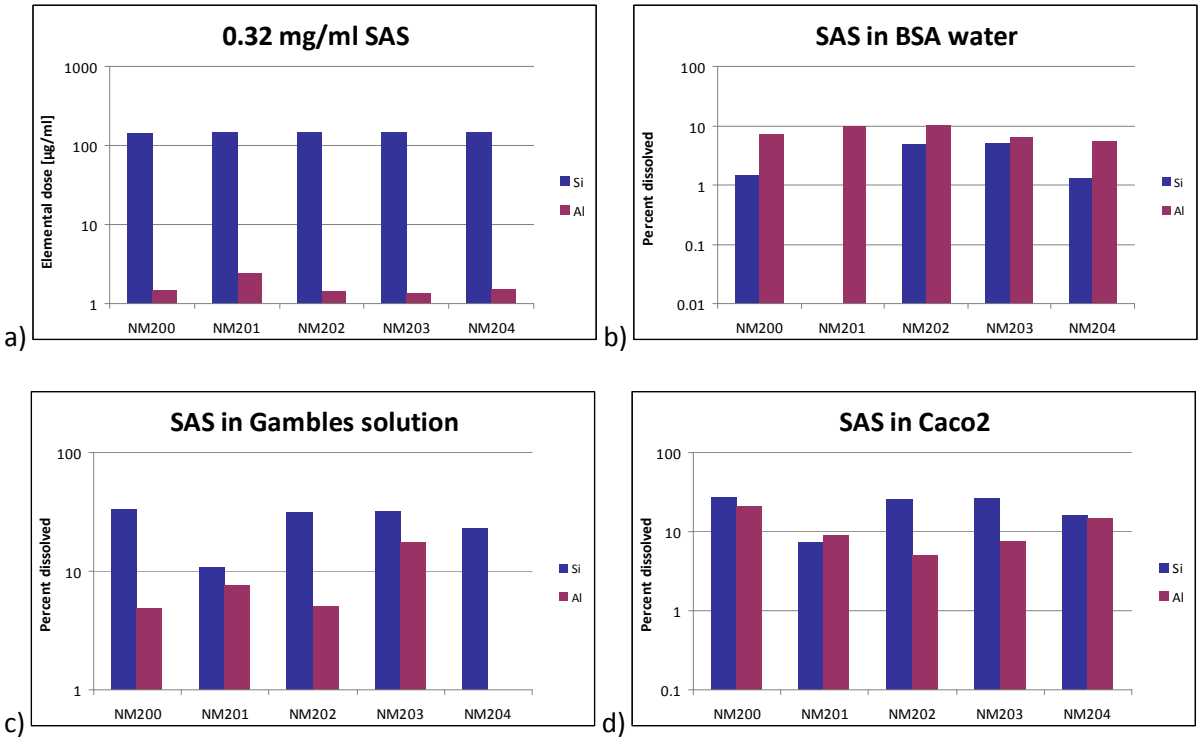

Figure 20. a) Elemental dose for most abundant elements in the SAS NM. Percent dissolved element in b) BSA water; c) Gambles solution; and d) Caco 2 cell medium.

As seen from Figure 20, the fraction of dissolved impurity Al (phase) and Si rarely match completely, suggesting that the SAS and Al impurity behave differently in the different media. In BSA-water, the fraction of dissolved Al exceed the fraction of dissolved Si, but this relationship is opposite in Gambles solution and the Caco 2 media. The amount of dissolved Al varies from 7.8 to 10.5 wt% in the BSA-water, <MDL to 17 wt% in Gambles solution, and 5 to 20 wt% in Caco 2 cell medium (Figure 20). Si was not detected for NM-201 in BSA. Al was not detected for NM-204 in Gambles solution. Note that the most reliable Al dissolution data are probably from the relatively high concentrations in NM-201. Inferred from the Si-concentrations, the fraction of dissolved SAS vary from <MDL to 5 wt% in BSA-water, 10 to 33 wt% in Gambles solution, and 7 to 28 wt% in Caco 2 cell medium. From the current dissolution data, the SAS and associated Al-phase appears to be least soluble in the BSA

water used for the generic batch dispersion protocol, and the SAS solubility in the Gambles solution may be slightly higher than in Caco 2 cell medium.

6.4. Estimation of biodurability

The results from the 24-hour reactivity and dissolution tests can give some indication on the biodurability of the nanomaterials. It is interesting to note that the elemental analysis have shown different behavior of the different elements in SAS, Al was present due to impurity phases of böhmite. The SAS and associated böhmite were, with a few exceptions, partially dissolved in all incubation media. Based on measured Si-concentrations, the average 24-hour SAS dissolution is about 3.2 wt% in BSA water and 20 to 26 wt% in Gambles solution and the Caco 2 media and the large difference in solubility is ascribed to the influence of the medium. On average 8 and 11 wt% of the associated Al is dissolved in the three different media. Based on these observations, it is concluded that the SAS NM have moderate biodurability in lung lining fluids and the intestine. The apparently higher biodurability in the BSA-water, is advantageous from experimental points of view, because less SAS is expected to degrade before onset of actual exposure.

6.5. Conclusions

Under in vitro test conditions, pH reactivity tests revealed negligible to moderate effects on pH of the tested NMs in 0.05% w/v BSA-water, Gambles solution, and Caco 2 cell medium. However, relatively great variations could occur during the course of the experiment, which are tentatively assumed to be due to small fluctuations in CO_2 concentrations delivered from external pressure tanks.

O_2 reactivity tests showed some material and media-dependent effects on dO_2 (difference between O_2 concentration in dosed and reference vials). Increased dO_2 values were observed for the following SAS NMs in all test media: NM-200 (not Caco 2 medium), NM-201, NM-202 and NM-203, whereas a slight reduction was observed with NM-204.

The SAS dissolution and biodurability revealed material-dependent behaviour, partially linked to presence of associated impurity phases in SAS. The NMs are partially dissolved in all three media. However, Si was not detected for NM-201 in incubation with BSA water and Al was not detected for NM-204 incubated in Gambles solution. The relative fraction of dissolved Si (average = 3 wt%) is lower than for Al (average = 8 wt%) in BSA-water, but similar (average 21 to 26 wt%) or higher than for Al in Gambles solution (9 wt%) and Caco 2 cell medium (11 wt%). Consequently, SAS and the associated Al, of which some is present as böhmite, are considered to have moderate biodurability.

7. DLS measurements for size distributions, mean aggregate size and structure

Dynamic Light Scattering (DLS) is a technique to characterise colloidal systems based on the scattering of visible light resulting from the difference in refractive index between the dispersed colloids and the dispersion medium. DLS may be applied for sizing particles in the range from ca. 0.6 nm to ca. 6 μm depending on the optical properties of the material and medium. In DLS the transmitted or back-scattered light from a laser diode is measured as function of time. A photo-detector collects the signal, which will fluctuate with time depending on the level of Brownian motion of the suspended nm- to μm-size objects in liquid suspension. The Brownian motion is caused by collision between the particle and the molecules of the medium and varies as a function of particle size and causes variation in the intensity of transmitted or scattered light as function of time. A correlator compares the signal measured at a time t_0 with different, very short time delays *dt* (autocorrelation). As the particles move, the correlation between t_0 and subsequent *dt* signals decreases with time, from a perfect correlation at t_0, to a complete decorrelation at infinite time (in practice order of milliseconds). For big particles, the signal changes slowly and the correlation persists for a long time, whereas small particles have high Brownian movement causing rapid decorrelation. Details are given in Appendix A, which also describes the equipment used, measurements performed and algorithms used for data analysis.

For DLS measurement results, care should be taken regarding their interpretation, as the performance of the DLS method and instrumentation may be limited for measurements on mixtures of particles of different sizes. DLS measurements on the single components of one well defined size gave results corresponding to the findings obtained by using TEM, however the measurement results regarding the size distribution of mixtures of such components showed significant limitations, e.g. the smaller particles were not identified by the measured distribution (Calzolai et al., 2011, Linsinger et al. 2012).

DLS characterisation was performed by CEA, NRCWE, INRS and JRC, and the results from these institutes are described in the following. The apparatus used are listed in Table 5.

7.1. DLS measurements and data treatment

7.1.1. Sample preparation

For the characterisation of the SAS-NMs, CEA developed a dispersion protocol to achieve conditions giving the best dispersion state of the NM in order to assess the size of the

smallest aggregates, which was dispersion in pure water with a pH value around 7 and lowest ionic strength. The dispersion medium must be filtrated before use to avoid any dust contamination. Suspensions were sonicated under conditions where the SAS NMs have a high surface charge to prevent subsequent agglomeration, i.e. sonication of 6.82 mg/mL SAS NM suspension was performed at 40% amplitude for 20 min in ice-water cooling bath. The dispersion prepared for these DLS measurements were also used for SAXS measurements performed by CEA. The measurements and data analysis are explained in Appendix A.

7.1.2. Suspension Stability over time followed by DLS

The stability of SAS NM suspensions was also tested by CEA using DLS to follow the evolution of Z-average and mean count rate over 17 hours, see Figure 21.

In general, for NM-200, NM-201, NM-202 and NM-203 a slight sedimentation was observed during the first hour and then for the next 16 hours the samples were very stable, i.e. the values of the Z-average and mean count rate were unchanged.

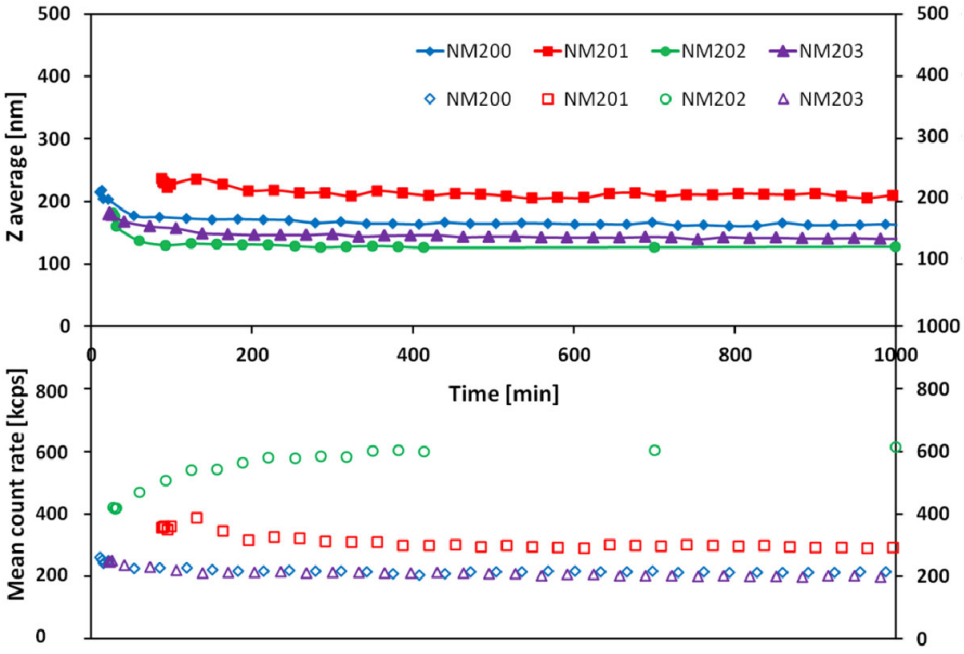

Figure 21. Evolution of DLS representative quantities (Top: Z-average mean size. Bottom: mean count rate) with residence time over 17 hours for SiO_2 suspensions ultrasonicated (20 min at 40 % amplitude) in pure water.

7.1.3. DLS results: size distribution and intensity averaged mean size of aggregates

Intensity size distributions for NM-200, NM-201, NM-202 and NM-203 studied by CEA are shown in Figure 22, left (average of 3 measurements).

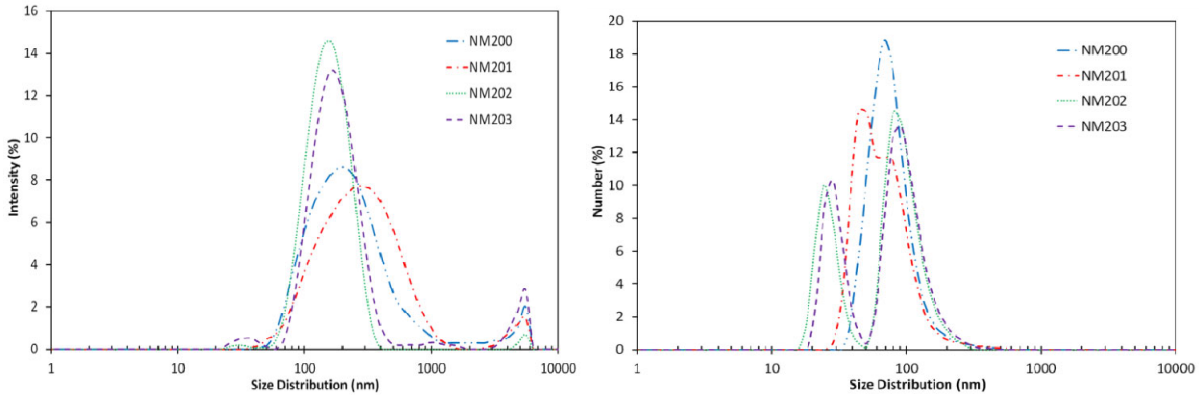

Figure 22. DLS intensity size distributions (left) and number size distributions (right) for suspensions of SiO_2 nanomaterials dispersed by ultrasonication (20 min at 40 % amplitude) in ultrapure water.

The corresponding number size distributions are also displayed, see Figure 22, right, to illustrate the size range and proportions in number. The high polydispersity and the presence of large particle aggregates of several µm size result in an intensity signal weighing towards the bigger aggregates. Conversion to the number distribution weighs the intensity distribution with the size-intensity relationship. The dispersions analysed by number distribution have a high frequency of occurrence of small-size particles. Due to the wide size-distribution and presence of large aggregates, the smallest particles may not be resolved well and the true sizes may be smaller than derived from these DLS measurements. NM-202 and NM-203 display more narrow size distributions centred around slightly smaller values than NM-200 and NM-201; the pairs of nanomaterial are synthesized using the same process (NM-200 & 201: precipitated; NM-202 & 203: thermal).

DLS measurements were repeated with dispersions prepared with different samples from the same vial and with samples from different vials to obtain mean values and standard deviation of size parameters. An overview of the results of Z-average, polydispersity index, position and width (FWHM) of the main peak in intensity size distribution is given for NM-200, NM-201, NM-202 and NM-203 in Table 18.

The previous observations are confirmed. However, the polydispersity indices are all above 0.25 indicating that the DLS data should not be analysed using the model for multimodal analysis. The values of Table 18 can be used for comparative purposes, e.g. for the homogeneity analysis, see section 5.1.

Table 18. Size parameters and standard deviations from DLS measurements by CEA averaged on a given number of SiO_2 samples prepared by ultrasonication (20 min at 40 % amplitude) in ultrapure water. Z-average, polydispersity index, position and width (FHWM) of the main peak in intensity size distribution.

Material (total number of samples)	Size parameters from DLS (intensity averaged)			
	Z-Average (nm)	**PdI**	**Intensity distribution main peak (nm)**	**FWHM peak with (nm)**
NM-200 (5)	207.8 ± 11.9	0.388± 0.036	234.9 ± 18.6	160.4 ± 43.4
NM-201 (3)	200.7 ± 27.6	0.342 ± 0.026	224.2 ± 79.0	117.2 ± 84.9
NM-202 (2)	175.9 ± 4.5	0.355 ± 0.001	159.9 ± 1.8	56.2 ± 2.9
NM-203 (3)	175.0 ± 7.4	0.409 ± 0.035	172.1 ± 15.5	76.3 ± 13.4

Also NRCWE and INRS performed DLS measurements to confirm the protocol and to perform an interlaboratory comparison of results which are shown in Table 20.

7.2. JRC DLS measurements and data treatment

7.2.1. Sample preparation

JRC used a dispersion protocol for dispersion in water in which 45 mg of SAS NM was added to the 15 mL of milliQ water. This was sonicated for 5 minutes in the probe sonicator (UP200S sonicator by Hielscher fitted with a 3mm probe 200W, 24kHz) and subsequently vortex was applied for 10 s, the probe sonication and vortex was repeated once.

7.2.2. Measurement results

When dispersed in Milli-Q® water, after the double sonication and vortex step, all samples presented some large sediments of size > 1 µm, which were impossible to disperse and they did not disappear even after prolonged sonication. DLS measurements are highly affected by the presence of large particles[4] (here particles > 1 µm) whose scattering of the light covers the signal of smaller particles. Therefore, no small particles (< 100 nm) could be identified, even if present in the particle size distribution. Most of the samples had a PdI > 0.3 clearly indicating a high poly-dispersivity. Table 19 gives an overview of the Particle Size Distribution (PSD) range observed from the measurements.

When dispersed in PBS, the PdI of NM-200 remained quite high (> 0.3) still with the presence of large aggregates, while for the NM-203 no big aggregates were seen. When

[4]For two particles with a size ratio of 10, the large particle contributes 1000 times more than the small one to the volume distribution, and 1,000,000 times more to the distribution by intensity. DLS measurements are based on intensity, and the light scattered by a few large particles may totally cover the signal from smaller ones.

NM-200 and NM-203 were dispersed in culture media without serum protein, NM-200 presented some turbidity as in water and a high PdI (≈ 0.5), while NM-203 was well dispersed with a relatively low PdI (≈ 0.2). When NM-200 and NM-203 were dispersed in culture media with serum proteins, an increased diameter of the particles was observed in both cases, even if NM-203 remained rather well dispersed (PdI < 0.2).

Finally, the Zeta potential values measured in pure water had a nominal value larger than 30 mV, indicating a good stability of the suspension.

Table 19. Size parameters from DLS measurements by the JRC (average of measurements on three samples) prepared by ultrasonication in ultrapure water. Z-average, PdI, position and width of the main peak in intensity size distribution and zeta potential.

NM-20X	Dispersant	Concentration (mg/mL)	Mean size (nm)		PdI	Zeta Potential (mV)	pH
			Peak 1	Peak 2			
NM-200	milliQ water	3.0	136	376	0.524	-47.5	7.0
NM-201	milliQ water	2.9	161	968	0.420	-51.7	6.9
NM-202	milliQ water	3.1	156	200	0.160	-43.7	6.5
NM-203	milliQ water	3.0	133	221	0.490	-46.1	6.6
NM-204	milliQ water	3.0	147	474	0.470	-45.1	6.9
NM-200	culture media	3.0	144.4	2611	0.492		
NM-203	culture media	3.0	94.5		0.123		
NM-200	PBS	5.0	187.2	712.7	0.532	-18	7.1
NM-203	PBS	5.0	170.3		0.202	-18	7.1

Figure 23 to Figure 26 show the outcomes of the DLS measurements performed by the JRC. Figure 23 and Figure 24 show the size distributions by intensity measured for NM-200 and NM-203 samples dispersed in Milli-Q® water, while the size distributions in cell culture growth medium without serum proteins is shown on the Figure 25 and Figure 26. For both NMs the DLS curves obtained for different dispersion media vary: for NM-200 differences in the intensities of the two peaks present in the profile of a size distribution were observed, whereas for NM-203 (Figure 26) dispersed in cell culture growth medium without serum proteins it seems that the second peak disappears.

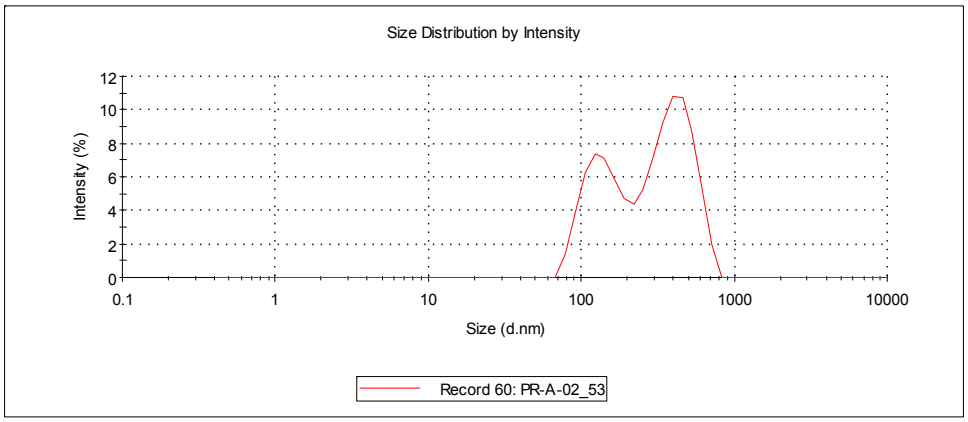

Figure 23. DLS size distribution by intensity for NM-200 dispersed in Milli-Q® water. PdI = 0.529, peak 1 = 143 nm, peak 2 = 411 nm.

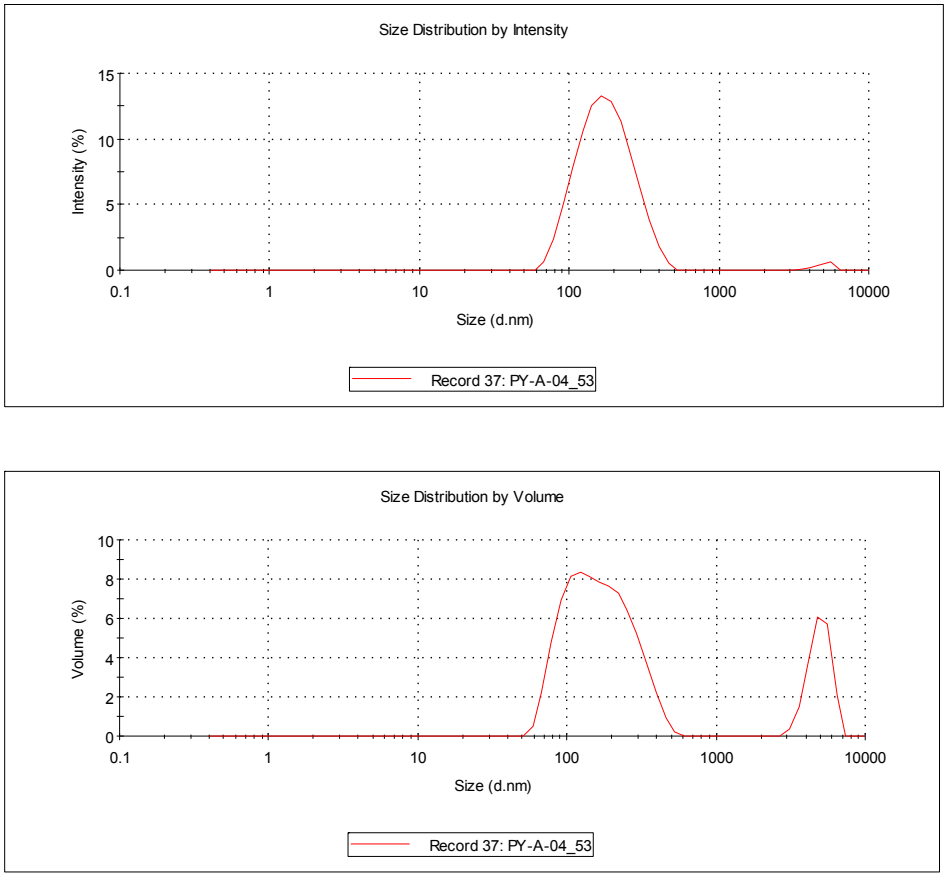

Figure 24. DLS size distributions for NM-203 dispersed in Milli-Q® water. Both the distribution by intensity (top) and the distribution by volume (bottom) are shown. PdI = 0.184, peak 1 = 186 nm, peak 2 = ~ 2000 nm.

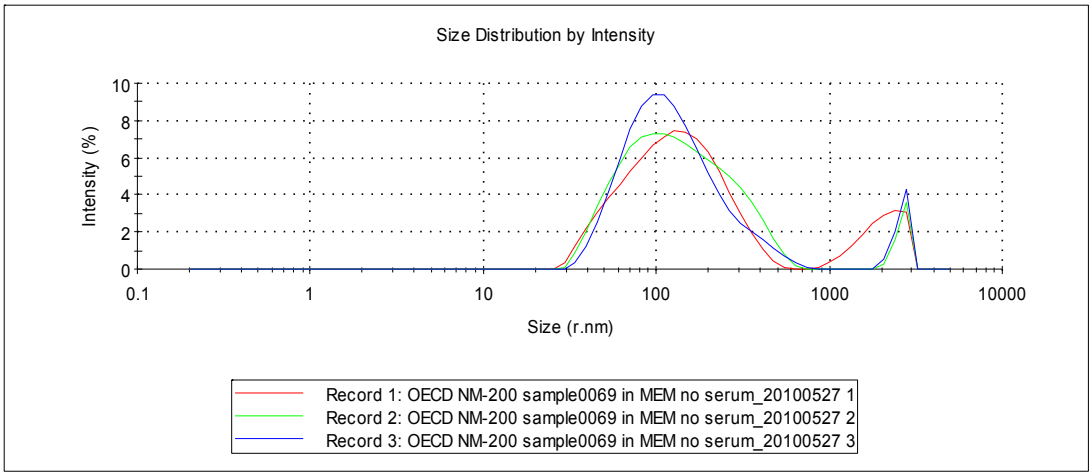

Figure 25. NM-200 dispersed in cell culture growth medium without serum protein. PdI = 0.492, peak 1 = 144.4 nm, peak 2 = 2611 nm.

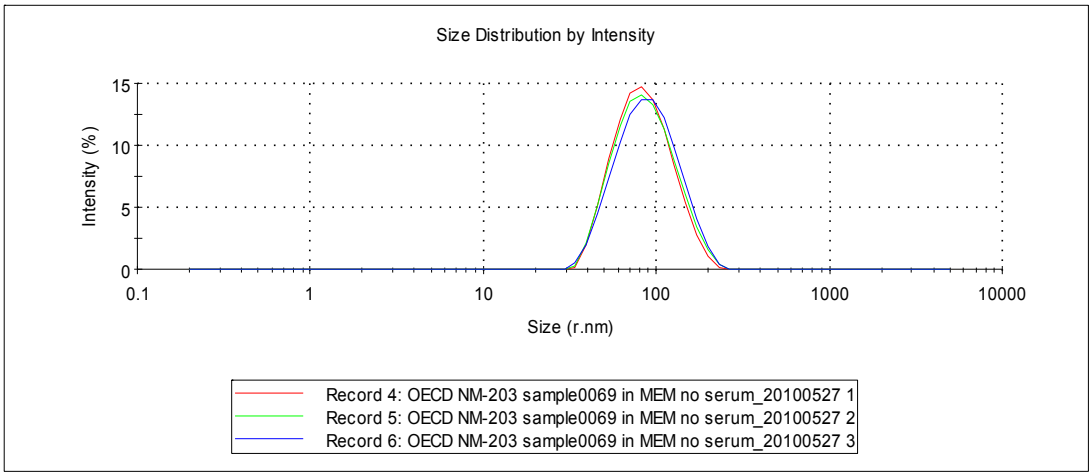

Figure 26. NM-203 dispersed in cell culture growth medium without serum proteins. PdI = 0.123, peak 1 = 94.46 nm, peak 2 = - .

7.3. Conclusions on DLS measurements

Table 20, from NANOGENOTOX, gives an overview of the DLS measurement results of particle size distribution in ultra-pure water. The DLS results all indicate that the SAS NMs are polydisperse. Measurements performed applying the same dispersion protocol by different institutions give similar results.

The JRC results displayed in Table 19 are DLS measurements for same NMs but using different dispersion protocols. The JRC measurements also indicate that the NMs are polydisperse, however the peaks are at different positions depending on the protocol used. As such this is not surprising, due to the use of a procedure at JRC that was not harmonized with respect to sonication power and media as used in NANOGENOTOX. Moreover, the use

of different media inevitably influences on the measured size. Depending on ionic strength, pH and presence of proteins etc., a corona of specific thickness is formed around the nanoparticles influencing their hydrodynamic size. In addition, different media have different viscosities, which may also contribute to shifting of hydrodynamic particle size-distributions away from true values if not corrected in the calculations.

Table 20. Size parameters and SD of DLS measurements on SiO_2 NMs prepared by ultra-sonication (20 min at 40 % amplitude) in ultrapure water. Z-average, polydispersity index, position and width of the main peak in intensity size distribution are shown.

Institu-tion	Vial no.	Repetition/ date	Z-averag e	(SD)	PdI	(SD)	Intensity distribution main peak	(SD)	FWHM peak width	(SD)
RESULTS for NM-200										
CEA	50	20101005	222		0.435		244.4		158.8	
CEA	50	20110202	198.5		0.371		218.1		115.3	
CEA	50	20110922	195.6		0.343		226.7		134.9	
CEA	50	20111116	212.4		0.412		262.9		230	
Intra vial			**207.1**	**12.3**	**0.390**	**0.041**	**238.0**	**19.9**	**159.8**	**50.1**
CEA	**95**	**20111129**	**195.3**		**0.378**		**222.4**		**163.1**	
INRS	109	N1	238.54		0.246		338.93			
INRS	109	N2	243.04		0.244		281.91			
INRS	109	N3	239.9		0.255		257.11			
Intra vial			**240.5**	**2.3**	**0.248**	**0.006**	**292.7**	**42.0**		
NRCWE	279		183.2		0.244		215		109.6	
NRCWE	494		184.8		0.237		226.3		125.8	
NRCWE	372		176.6		0.232		215.9		114.6	
inter vial (3-NRCWE)			**181.5**	**4.3**	**0.238**	**0.006**	**219. 1**	**6.3**	**116.7**	**8.3**
inter vial all (6)			**197.9**	**23.4**	**0.288**	**0.075**	**235.0**	**29.4**	**134.6**	**25.2**
all			**208.2**	**24.4**	**0.309**	**0.079**	**246.3**	**37.8**	**144.0**	**40.1**
RESULTS for NM-201										
CEA	48	20110922	232.5		0.371		315.3		215.2	
CEA	48	20110202	183.7		0.332		173.7		65.69	
intra vial			**208.1**	**34.5**	**0.352**	**0.028**	**244.5**	**100.1**	**140.4**	**105.7**
CEA	39	20111129	185.9		0.323		183.7		70.73	
inter vial			**197.0**	**15.7**	**0.337**	**0.020**	**214.1**	**43.0**	**105.6**	**49.3**
all			**200.7**	**27.6**	**0.342**	**0.026**	**224.2**	**79.0**	**117.2**	**84.9**
RESULTS for NM-202										
CEA	1	20110202	179.1		0.356		158.6		54.1	
CEA	1	20111115	172.7		0.354		161.1		58.2	
intra vial/all			**175.9**	**4.5**	**0.355**	**0.001**	**159.9**	**1.8**	**56.2**	**2.9**
RESULTS for NM-203										
CEA	207	20110720	166.4		0.409		178.1		90.51	
CEA	207	20111115	179.4		0.444		183.8		74.52	
intra vial			**172.9**	**9.2**	**0.427**	**0.025**	**181.0**	**4.0**	**82.5**	**11.3**
CEA	118	20110202	179.2		0.375		154.5		63.88	
INRS	227	N1	218.93		0.29		141.29			
INRS	227	N2	288.17		0.327		154.92			
INRS	227	N3	230.05		0.281		147.95			
intra vial			**245.7**	**37.2**	**0.299**	**0.024**	**148.1**	**6.8**		

NRCWE	294		146.3		0.214		183.1		83.6	
NRCWE	212		146.6		0.229		181.7		83.36	
NRCWE	169	-1	142.2		0.219		169.7		77.46	
NRCWE	169	-2	149.9		0.247		189.6		99.09	
NRCWE	169	-3	152.4		0.259		181.3		84.68	
NRCWE	169	-4	145.6		0.25		171.6		76.53	
intra vial			**147.5**	**4.5**	**0.244**	**0.017**	**178.1**	**9.2**	**84.4**	**10.4**
inter vial (3-NRCWE)			**146.8**	**0.6**	**0.229**	**0.015**	**181.0**	**2.6**	**83.8**	**0.6**
inter vial all (6)			**173.0**	**38.4**	**0.298**	**0.086**	**171.1**	**15.5**	**79.6**	**8.8**
all			**178.8**	**45.1**	**0.295**	**0.077**	**169.8**	**16.1**	**81.5**	**10.1**

7.4. Centrifugal Liquid Sedimentation size analysis

As the DLS technique may have limitations (Calzolai et al., 2011) the JRC measured the hydrodynamic size-distribution using the Centrifugal Liquid Sedimentation (CLS) technique. CLS is a gravimetricallty forced sedimentation for measuring particle sizes. Like in DLS, a particle may be a single particle, an aggregate or an agglomerate, as the technique does not distinguish this. As the centrifugation force separates the particles according to their size and density, the size distribution can be investigated. The technique is further explained at http://www.cpsinstruments.eu/centrifuge.html. The nanomaterials were dispersed as described in Table 21. The CLS technique has a good reproducibility and each curve shown represents one measurement.

Table 21. JRC dispersion protocol for CLS.

JRC dispersion protocol	
1) Weigh 50-100 mg of NM into 15 ml centrifuge tube 2) Add MQ water to make a 10 mg/ml solution (solution A). Vortex 2-3 min 3) make a 1mg/ml solution for the materials diluting either with MQ or Surfactant (*). This is called solution B. 4) Prepare aliquots of 2 ml each in centrifuge tubes to be sonicated	
Sonication methods and timing:	
Ultrasonic bath (T is 35 °C)	5 minutes
	30 minutes
Ultrasonic Tweeter (Amplitude 75%. Cycle 35%)	1 minute
	5 minutes
	15 minutes
After sonication immediately measure dispersion using CLS and DLS	
(*) surfactant: 0.1% solution of sodium hexametaphosphate (CAS 68915-31-1), Calcon	

Normalised graphs showing the "relative weight" (y-axis) against the particles diameter (x-axis) for the SAS NMs are given in Figure 27 to Figure 31. The graphs are normalised to their maximum value so the particle diameter that has the highest weight fraction was set to

100% and weight fractions of the other particles diameters are given relative to the highest fraction. Table 22 summaries the results, i.e. mean size, CLS derived polydispersity index and half width from the blue curves on the graphs, see Figure 27 to Figure 31.

Ideally the curve should include a relative weight fraction of zero for large diameter particles to ensure that all particles have been measured. This is so for NM-202 and NM-203. For NM-200, NM-201 and NM-204 the graphs indicate that particles larger than 1 micron passed the detector before the measurements started. As sonication was done with a tweeter sonicator, which is not in direct contact with the system, these larger particles are not probe debris.

Figure 27 for NM-200 shows the CLS measurement curve of the same vial (no. 4230) using the dispersion protocol described in Table 21 at two dates (11 July 2012 and 23 Nov. 2012). The two measurements are essentially identical, so the material was stable over time between the two measurements with regard to particle size distribution. The measured curve is somewhat rough due to a high instrument signal to noise ratio as SiO_2 has low scattering and absorption giving a low signal. For high particle diameter, where the measuring starts, the value of the relative weight is above zero indicating that particles bigger than 1 micron have passed by the detector before measurements began. The size distribution is rather broad and the particle size is centred around a value of about 90 nm. It is not possible from these graphs to estimate the smallest detected particle size. The other peak around 200 nm is most like an artefact related to the injection of the sample.

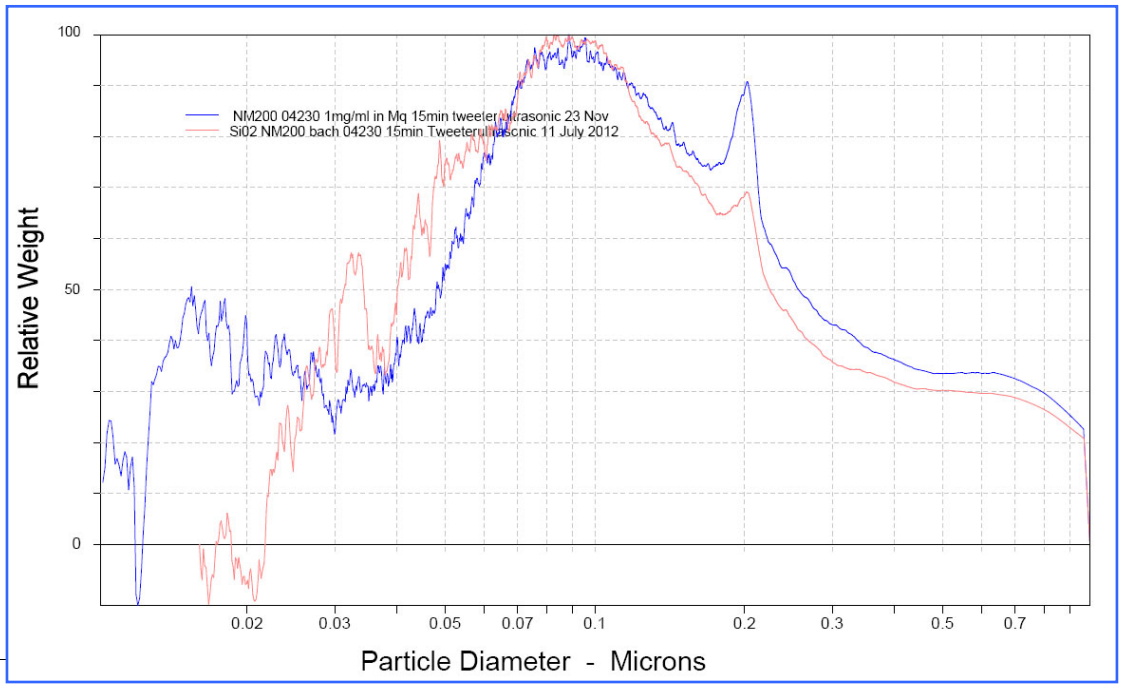

Figure 27. CLS particle size distribution graph for NM-200.

Figure 28 show the CLS scan on NM-201 using the JRC protocol (Table 21, Figure 28 blue curve) as well as the NANOGENOTOX protocol (Figure 28 red curve). As seen the sample contained particles larger than 1 micron that passed the detector before measurements started; as mentioned above the tweeter sonicator is not in direct contact with the test system so it is not probe debris. The NANOGENOTOX dispersed material seems to have a higher number of large particles, which could be due to associated BSA. Both size distributions are rather broad and the particle size appears to be distributed around the same value of about 90 nm for both dispersions, and the smallest detected particle size is ca. 30 nm.

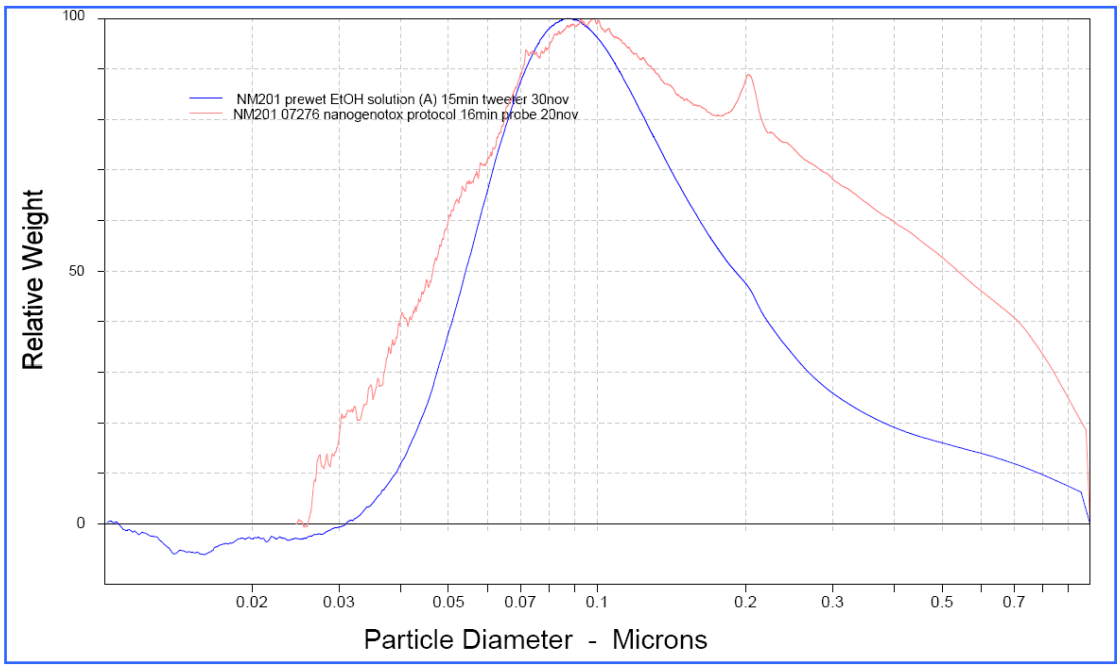

Figure 28. CLS particle size distribution graph for NM-201.

The CLS measurement or NM-202 is shown on Figure 29 for measurements at two different dates and there are no significant differences between the two graphs. As seen, the size distribution is narrower compared to NM-200 and NM-201 and no reading was detected above ca. 300 nm, indicating that particles/aggregates/agglomerates are smaller than 300 nm. The particle size is centred around 73 nm and the smallest detected size is about 35 nm.

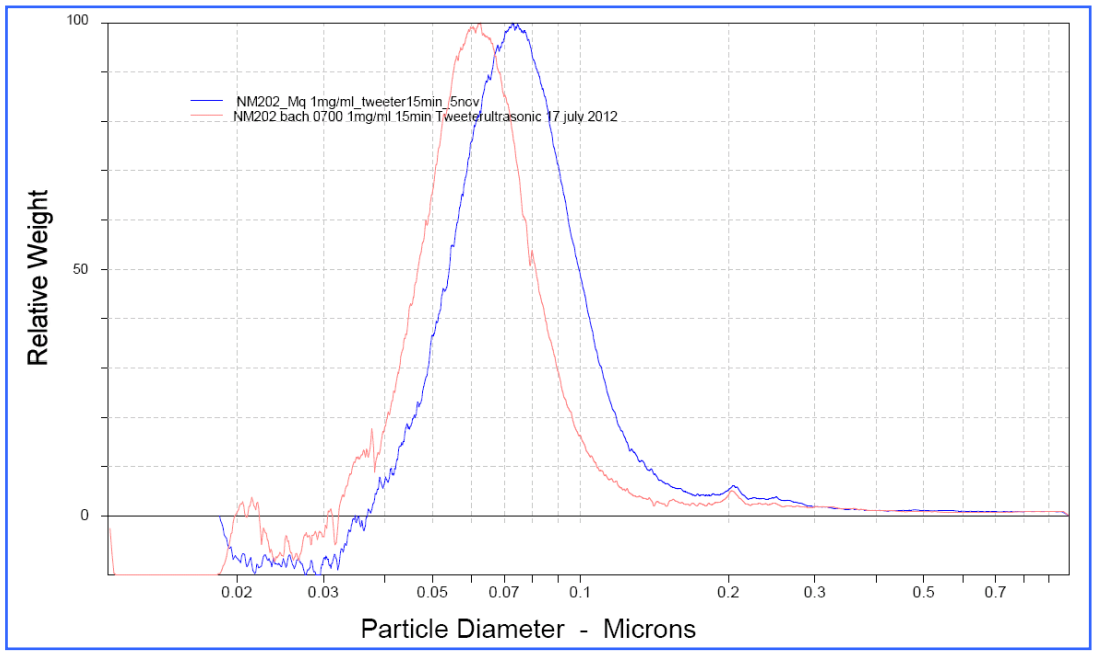

Figure 29. CLS particle size distribution graph for NM-202.

Figure 30 shows the CLS curve for NM-203, and it indicates that the particle size of NM-203 is slightly larger than NM-202, but otherwise the two CLS curves are similar. The particle size distribution is centred around 64 nm and the smallest detected particle size is ca. 35 nm.

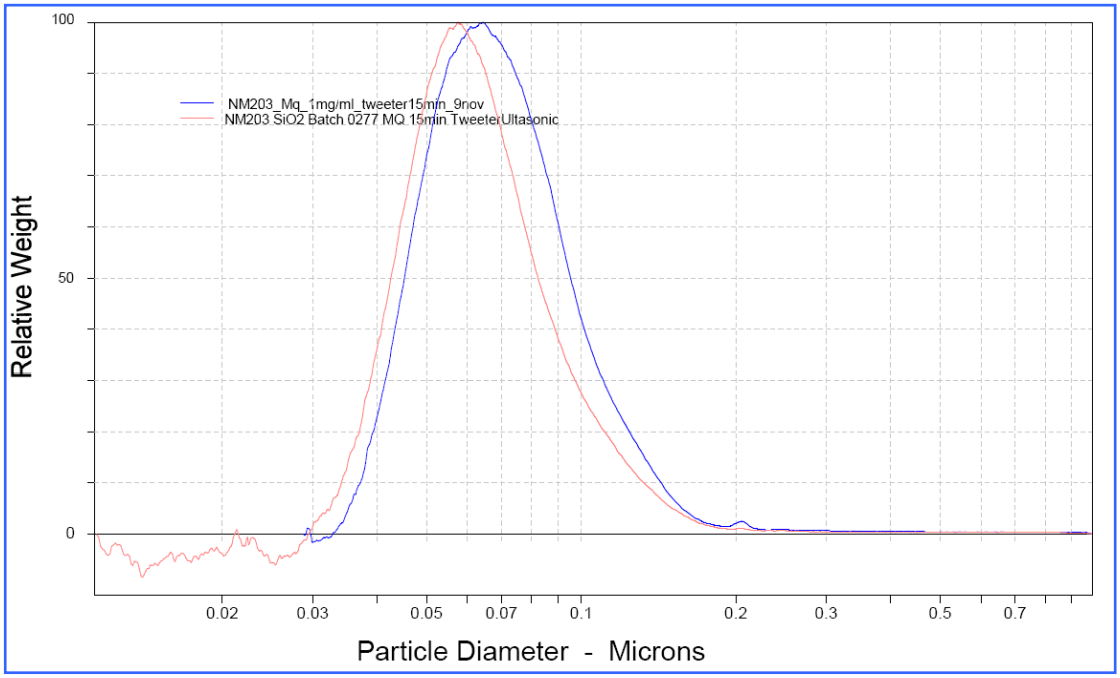

Figure 30. CLS particle size distribution graph for NM-203.

Figure 31 shows the CLS particle size measurement for NM-204, which is similar to the curves for NM-200 and NM-201. The particle size distribution is centred at 98 nm and the smallest size detected is around 30 nm-size.

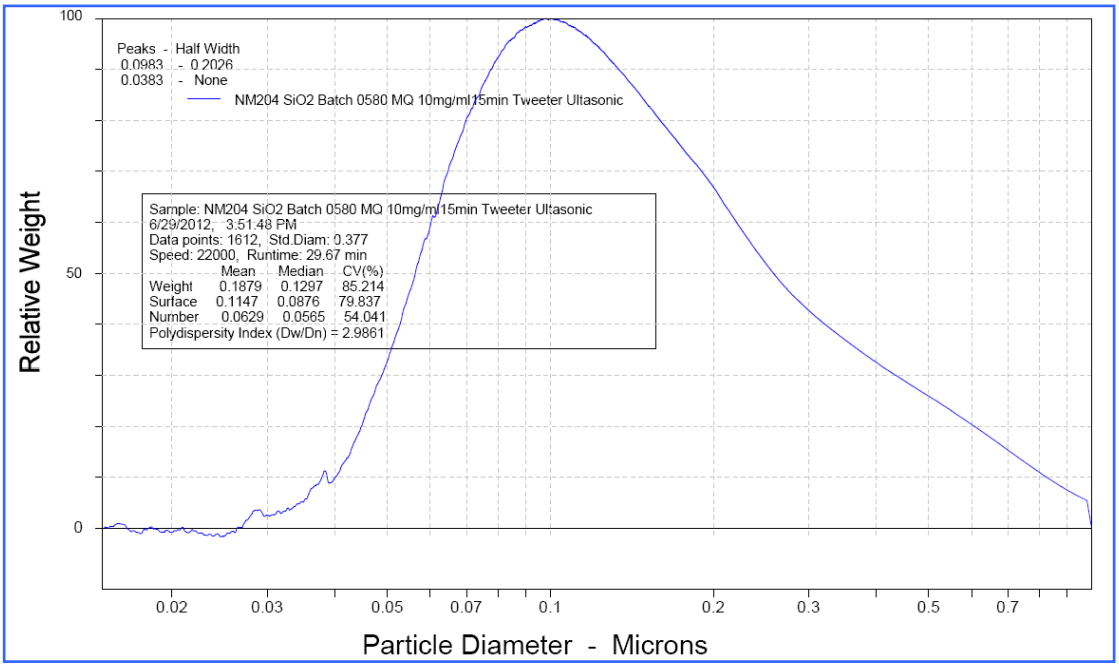

Figure 31. CLS particle size distribution graph for NM-204.

The CLS measurements indicate that the precipitated NMs, NM-200 NM-201 and NM-204 have a broader size distribution and contain a fraction of very large particles, whereas the pyrogenic NM-202 and NM-203 have a narrower particle size distribution and do not contain very large agglomerates/aggregates.

Based on the CLS measurements, the size (position of the peak), the CLS derived polydispersity index (D_n/D_w, i.e. the diameter calculated based on number divided by the diameter based on weight) and the half width were estimated, see Table 22. The results presented in the table are in all cases based on the blue curves in the figures.

Table 22. Summary of results of the CLS measurements.

Material	Peak (nm)	Half width	CLS Polydispersity index
NM-200*	75-95	-	10.18
NM-201	88	136	2.65
NM-202	73	45	1.43
NM-203	64	50	1.35
NM-204	98	203	2.99

* For NM-200 the output was very rough and machine reading not possible; the value is visual estimation

CLS measurements cannot distinguish between individual particles and aggregates. The particle size measured by CLS is consistently smaller than the particle size measured by DLS (nor this technique can distinguish individual particles and aggregates) which may be due to the CLS separation of particles according to sizes that promotes a better visibility of smaller particles. However, sample preparation steps for both DLS and CLS involve sonication which probably produces true breaking of aggregates due to the brittle nature of amorphous silicon dioxide. This could be investigated further by performing both types of measurements on the same prepared sample to investigate the influence from the sonication step on the two particle size distributions. Also TEM or SEM micrographs could give information on the true particle size distribution.

8. Zeta potential

Appendix B gives the detailed procedures for the measurements performed. Samples for zeta potential measurements were prepared by CEA as aqueous suspensions of 1 g/L SAS NMs with a constant ionic strength of 0.036 mol/L (monovalent salt) and controlled pH. Concentrated sonicated stock suspensions of 10 g/L in pure water was diluted into pH and ionic strength controlled “buffers” prepared by addition of HNO_3, NaOH and $NaNO_3$ in various proportions. For each suspension of known pH, fixed ionic strength and fixed NM concentration, a "general purpose mode" was used for the zeta potential measurements with automatic determination of measurement parameters (position of the laser focus, attenuator, number and duration of runs). For each data point three measurements were performed and the average value was reported. Zeta potentials were then plotted against pH to determine the stability domains and isoelectric point (IEP). Figure 32 shows the results of zeta potential vs. pH for NM-200, NM-201, NM-202 and NM-203, and includes also the corresponding IEP.

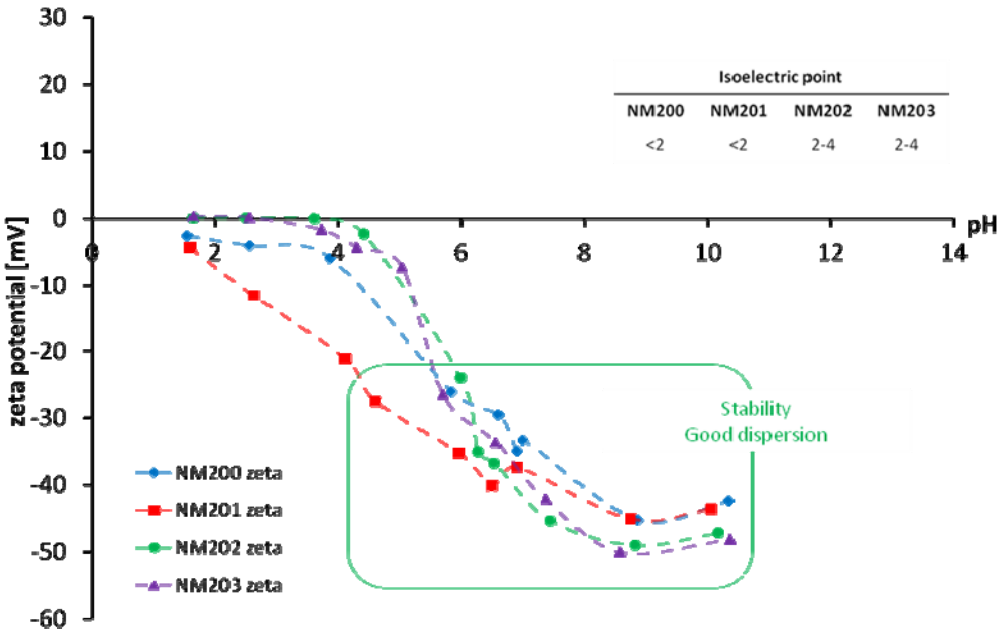

Figure 32. Zeta potential as a function of pH for SiO_2 NM suspensions (1 g/L) in constant ionic strength aqueous media (0.036 mol/L HNO_3/NaOH), highlighting the domain of higher stability for pH higher than 5; the IEP values are also reported on the figure.

All dispersions were stable and during zeta potential measurements no sedimentation occurred. The average aggregate sizes measured by DLS were roughly constant over the pH range (results not presented here).The zeta potential varied greatly with pH and reached -40 mV around pH 7 or higher; this variation was slightly different for NM-201, which has an IEP lower than 2.

The JRC measured the zeta potential, see Table 19, in connection with the JRC DLS measurements in pure water at a concentration around 3.0 mg/mL for the SAS NMs. In addition, for NM-200 and NM-203 PBS was added as dispersant and the concentration was around 5.0 mg/mL. For pure water the zeta potential for the SAS NMs was between -43.7 and -51.7 mV. For NM-200 and NM-203 with PBS as dispersant and at higher concentration the zeta potential was -18 mV.

The measurement results obtained by the JRC for pure water (assumed pH value is 7) and by the NRCWE and CEA for a pH value around 7 have very similar values, as expected.

9. SAXS and USAXS measurements and data treatment

Small-angle X-ray scattering (SAXS) is a technique based on the interaction between X-rays and matter to probe the structure of materials. The processed data are the intensity, ***I***, of X-ray scattered by a sample as a function of angular position of a detector, see Figure 33.

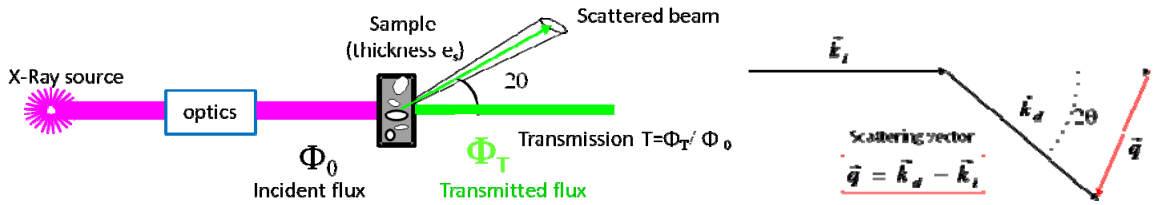

Figure 33. Schematic set up for SAXS and physical quantities.

The intensity is expressed in absolute scale, cm^{-1}, independent from test parameters such as X-ray wavelength, experimental background, time of acquisition and sample thickness. 2D raw data images are converted into diffractograms displaying the scattered intensity ***I*** as a function of scattering vector *q* defined by:

$$q = \frac{4\pi \sin\theta}{\lambda}$$

λ : X-ray wavelength

Ultra small angle X-ray scattering (USAXS) measurements give access to X-ray scattering data for a smaller range of *q* and then complement the SAXS diffractograms. It requires a specific and very precise set-up, usually different from the one used for SAXS.General theorems of experimental physics have been developed for the interpretation of the diffractograms to extract different properties of nanostructured materials, such as shape of nanoparticles, surface area, interactions occurring, etc.

In the high q range, diffractograms display an intensity decrease in a q^{-4} trend, called the "Porod region", corresponding to the "real space" to the scale of the interfaces (for smooth interfaces). Therefore, for a sample with two phases, the asymptotic limit of the "Porod's plateau", when data are represented as $Iq^4=f(q)$, is related to the total quantity of interface Σ (in m^2/m^3) between the two phases, as follows (Porod's law):

$$\Sigma\,[m^{-1}] = \frac{\lim_{\text{plateau}} (I.q^4)}{2\pi(\Delta\rho)^2}$$

$\Delta\rho$ is the difference in scattering length density between the two phases.

To treat raw SAXS data and obtain absolute intensities, the intensity by the thickness of the scattering material need to be normalised. For powder samples where sample thickness has no real meaning, a model system is used, in which the effective thickness of material crossed by X-rays, e_B, is considered and it corresponds to a thickness equivalent to the material arranged in a fully dense (no inner or outer porosity) and uniform layer. The sample transmission is related to this equivalent thickness by the following equation:

$$e_B = -\frac{1}{\mu}\ln\left(T_{exp}\right)$$

where μ: material absorption coefficient for X-rays (μ_{SiO2} = 77cm^{-1}) and *Texp* is the experimental transmission (transmitted flux Φ_T/incident flux Φ_0), i.e. transmission of the sample plus cell with regard to the transmission of the empty cell (kapton alone, empty capillary, etc).

The intensity scaled by this thickness e_B is called I_1. Porod's law can then be applied for I_1 to calculate the specific surface area of the powder. The optimum parameters for measurements are given in Table 23.

Table 23. Material properties considered and corresponding calculated optimum thickness of dense material for a sample transmission of 0.3.

Material	Density	Scattering length density	Absorption coefficient (μ)	Optimum thickness (e_B)
SiO_2	2.196 g/cm^3	1.862 · 10^{11} cm^{-2}	77 cm^{-1}	150 µm

SAXS measurements were performed by CEA using kapton capillaries of internal thickness 1.425 mm and run for 3600s. USAXS measurements were performed in 1 mm or 1.5 mm non-sticky double kapton cells. A measurement is considered optimal for a transmission around 0.3 and the optimum thicknesses e_B for the SAS NMs are gathered in Table 24.

Table 24. Experimental parameters for SiO_2 powder samples.

	Cell	e_B	*Texp*
NM-200	1.5 mm glass capillary	115 µm	0.41
NM-201	1.5 mm glass capillary	187 µm	0.24
NM-202	1.5 mm glass capillary	106 µm	0.44
NM-203	double sticky kapton cell	40 µm	0.73
NM-204	1.5 mm glass capillary	153 µm	0.31

For each SAS NM, two SAXS measurements were performed, one with a short acquisition time to prevent saturation of the detector, typically 200 s or 150 s, and one with a long-time acquisition of 1800 s to lower the signal/noise ratio at high q.

Image treatment and calculations on radial averaged data are described in Appendix D for SAXS and USAXS data. It includes normalization of the intensity by the parameters of the experiments, e.g. acquisition time, sample thickness, calibration constants determined using reference samples and background subtraction. SAXS data obtained for short time and long-time and USAXS data are merged to get continuous diffractograms for the whole q range.

All specific surface area results, together with their uncertainty calculations are presented below. Errors on the Porod's plateaus have been determined manually for each diffractogram, and the uncertainty on the material density is considered to be about 5%.

The specific surface areas of powders are determined on the Porod plateau, see Appendix D. More details on the general principles of measurement and the measurement technique as well as the data treatment are described in Appendix D.

9.1. Size and structure of fractal aggregates by SAXS

All SAXS diffractograms and the corresponding representations in I(q)q4 for SiO_2 powders are displayed in Figure 34, Figure 35 and Figure 36. The diffractograms for the different NMs are very similar indicating that NMs have very similar size and shape of the nanostructure.

On the NM-204 curve, some oscillations appear, indicating that this material is less polydisperse than the others. A general rule specify that for spherical particles of radius R, the first oscillation appears at $qR = 4.5$. For estimated radius of 21 nm, this corresponds to q=0.043 Å, which is indeed the position of the first oscillation observed on NM-204 curve.

The calculation results for specific surface area of SiO_2 powders, expressed in m^{-1} and in m^2/g, together with uncertainty estimations, are reported in Table 25. The diameter calculated in the last column corresponds to the size of dense, perfectly monodisperse and spherical SiO_2 nanoparticles that would exhibit the same mean surface area.

Table 25. Specific surface area measured by SAXS for the SAS NMs.

	Lim Iq^4 (10^{-3} cm^{-1} A^{-4})	**Σ** (m^{-1})	**Specific surface area** (m^2/g)	**Error on plateau** (m^2/g)	**+ 5% error on density** (m^2/g)	**Equivalent diameter for spheres** (nm)
NM-200	5.6	2.71E+08	123.3	± 4.9	± 17.3	22
NM-201	5.2	2.71E+08	123.3	± 8.3	± 20.6	22
NM-202	7.8	4.04E+08	184.0	± 17.8	± 36.2	15
NM-203	8.0	3.67E+08	167.2	± 13.4	± 20.6	16
NM-204	6.3	2.89E+08	131.7	± 22.9		21

The structure and main size parameters determined by the model, i.e. radius of gyration of primary particles (Rg_1), radius of gyration of aggregates (Rg_2) fractal dimension (D_f) and average number of primaries per aggregates ($N_{part/agg}$) are reported in Appendix D. The full sets of parameters used for the fit of experimental curves with the unified model are gathered in Appendix D. Table 26 gives an overview of the parameters.

Table 26. Structure and size parameters extracted from SAXS data fitting by the unified model from SiO_2 suspensions ultrasonicated (20 min at 40 % amplitude) in pure water. Gyration diameter of primary particles (2 Rg_1) and aggregates (2 Rg_2), fractal dimension D_f and number $N_{part/agg}$ of particles per aggregate.

	Main size and structure parameters from SAXS unified fit model			
	2 Rg_1 (nm)	**2 Rg_2 (nm)**	**D_f**	**$N_{part/agg}$**
NM-200	18	440	2.45	3600
NM-201	20	180	2.45	457
NM-202	16	100	2.5	200
NM-203*	-	-	-	-

*NM-203 measurements cannot be fitted to the model at low q, and very different values of the parameters would lead to the same (bad) fit. Therefore, no parameters are reported.

The increase of intensity observed at low q for NM-203 cannot be fitted by the model, and parameters extracted from such a poor fit are unreliable and thus not reported here.

The tested SAS NMs exhibit roughly the same fractal structure, with slight differences in primary particle size and aggregate size. NM-202 display smaller aggregate size than NM-201 and NM-200. NM-200 and NM-201 are both produced by precipitation whereas NM-202 is produced by thermal route, and this may explain the observed similarities and differences.

The real concentrations of nanoparticles obtained through the invariant theorem and the specific surface areas corresponding to Porod's plateau were consistent with theoretical concentrations and specific surface areas of dry materials determined by SAXS, see also the measurement of specific surface area by BET.

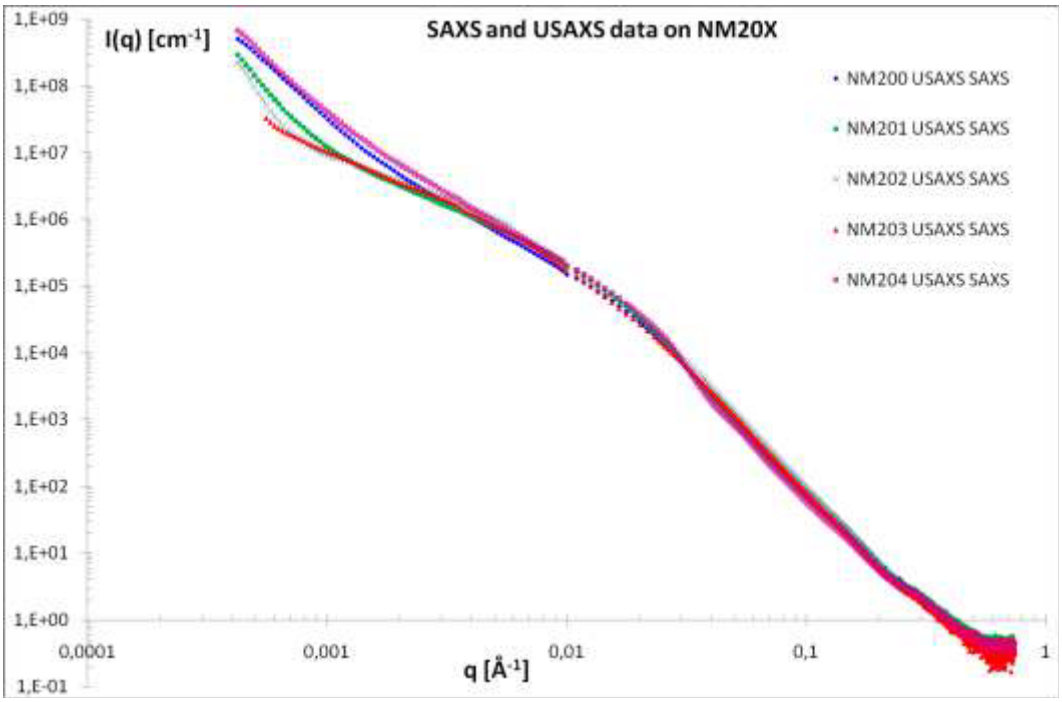

Figure 34. SAXS and USAXS results for SiO_2 raw powders NM-200 (blue), NM-201 (green), NM-202 (dark blue), NM-203 (red) and NM-204 (pink).

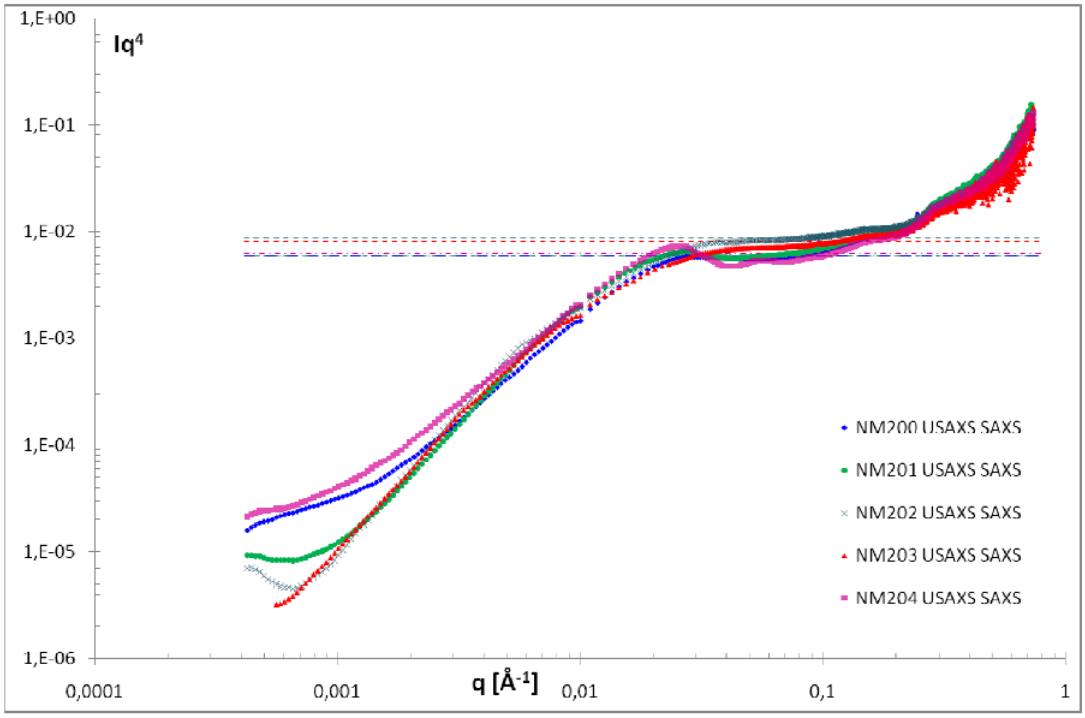

Figure 35. Representation in Iq4 of SAXS and USAXS results of NM-200 (blue), NM-201 (green), NM-202 (dark blue), NM-203 (red) and NM-204 (pink). The dotted lines are the corresponding Porod's plateaus.

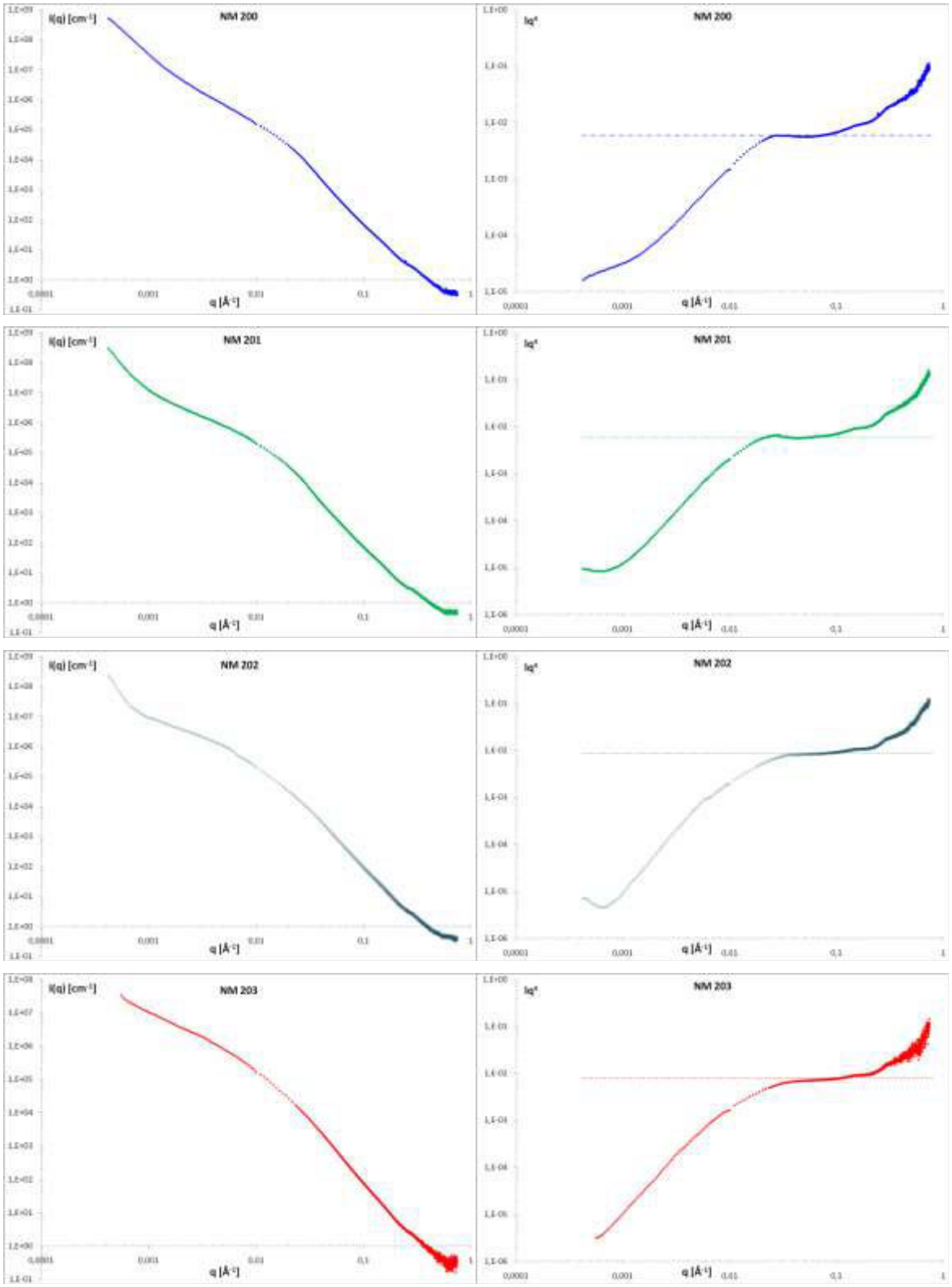

(figure continued)

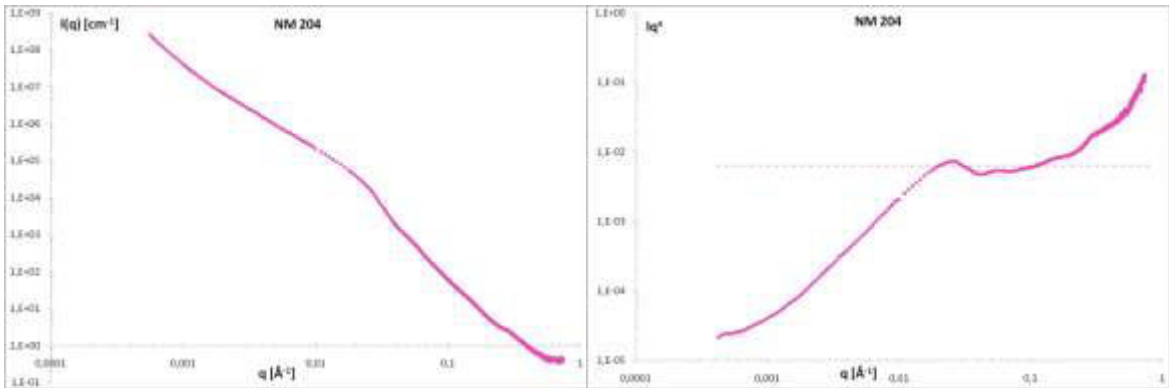

Figure 36. SAXS and USAXS results for raw powders of a) NM-200; b) NM-201; c) NM-202, d) NM-203 and e) NM-204; I(q) representations on the left; $I(q)^4$ presentations q4 representation revealing Porod's plateaus on the right.

10. Brünauer, Emmett and Teller (BET) measurements

The most widely used technique for estimating surface area and porosity is the BET method (Brünauer, Emmett and Teller, 1938). The concept of the theory is an extension of the Langmuir theory for monolayer molecular adsorption to multilayer adsorption with the following hypotheses: (a) gas molecules physically adsorb on a solid in layers infinitely; (b) there is no interaction between each adsorption layer; and (c) the Langmuir theory can be applied to each layer. The BET equation is

$$\frac{1}{v[(p_0/p)-1]} = \frac{c-1}{v_m c}\left(\frac{p}{p_0}\right) + \frac{1}{v_m c}$$

where p and p_0 are the equlibrium and the saturation pressure of adsorbates at the temperature of adsorption, v is the adsorbed gas quantity (for example, in volume units), and v_m is the monolayer adsorbed gas quantity. c is the BET constant.

$$c = \exp\left(\frac{E_1 - E_{L1}}{RT}\right)$$

where E_1 is the heat of adsorption for the first layer, and E_L is that for the second and higher layers and is equal to the heat of liquefaction.

The equation is an adsorption isotherm and can be plotted as a straight line with the y-axis showing $1/v[(P_0/P)-1]$ and $\varphi = P/P_0$ on the x-axis according to experimental results (BET plot). P is the equilibrium pressure and P_0 is the saturation pressure. The value of the slope, A, and the y-intercept, I, of the line are used to calculate the monolayer adsorbed gas quantity Vm and the BET constant c. The following equations are used:

$$v_m = \frac{1}{A+I} \quad and \quad c = 1 + \frac{A}{I}$$

A total surface area $S_{BET,total}$ and a specific surface area S_{BET} are estimated by the following equations:

$$S_{BET,Total} = \frac{v_m N s}{V} \quad and \quad S_{BET} = \frac{S_{Total}}{a}$$

where Vm is in units of volume which are also the units of the molar volume of the adsorbate gas, N is Avogadro's number, S is the adsorption cross section of the adsorbing species, V is the molar volume of adsorbate gas, α is the mass of adsorbent (in g).

10.1. BET results

The results for the specific surface area, pore volume and microporosity of the SAS NMs obtained by IMC-BAS are summarised in Table 27.

The nitrogen adsorption isotherms for the SAS NMs are shown on Figure 37 and the curves are very similar in shape suggesting that the SAS NMs have the same comportment.

Table 27. Results of the IMC-BAS BET measurements on the SAS NMs.

	BET surface m^2/g	**Total pore volume** mL/g	**Micro surface area** m^2/g	**Micropore volume** mL/g
NM-200	189.16	0.7905	30.044	0.01181
NM-201	140.46	0.5815	23.144	0.00916
NM-202	204.11	0.5136	8.268	0.00084
NM-203	203.92	0.4991	5.332	0.0
NM-204	136.60	0.5057	17.485	0.00666

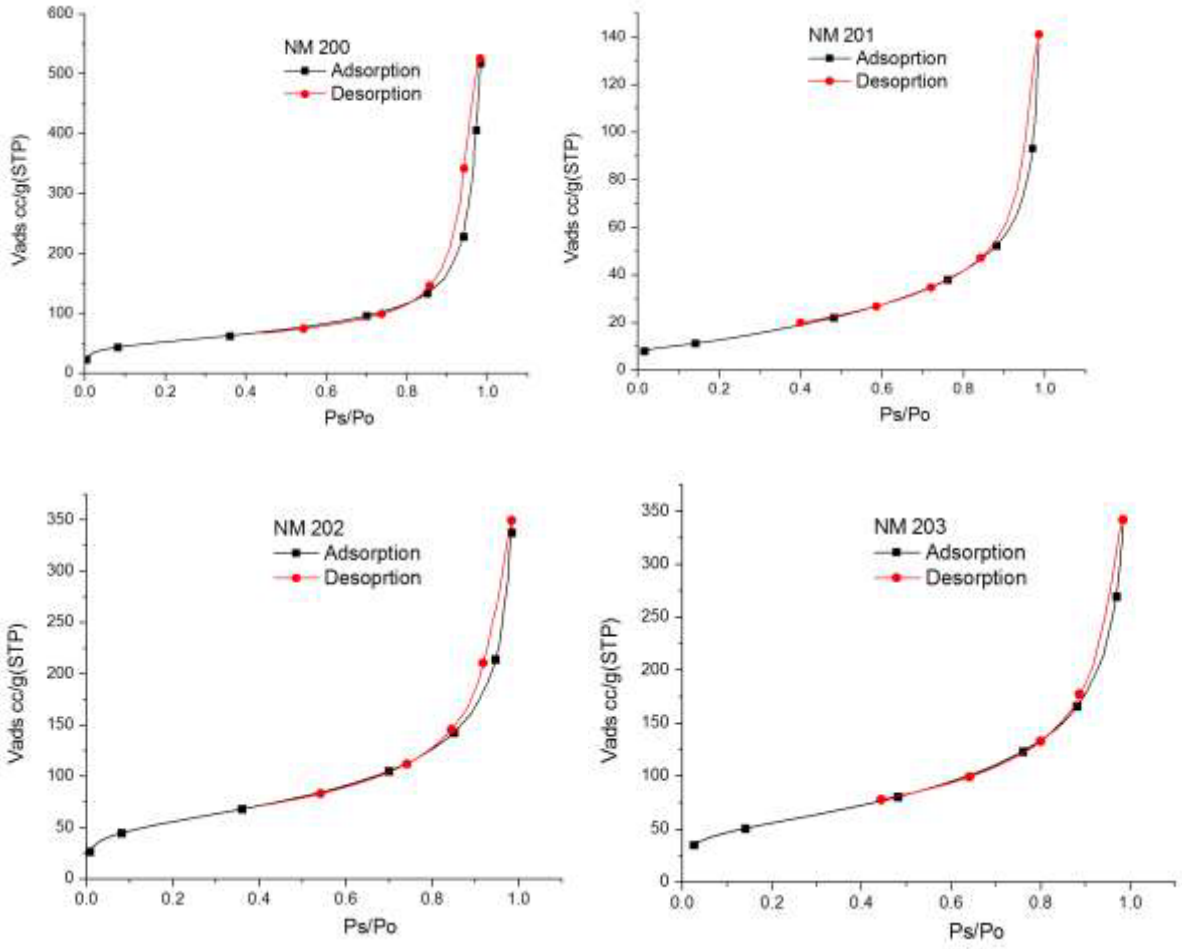

figure continued

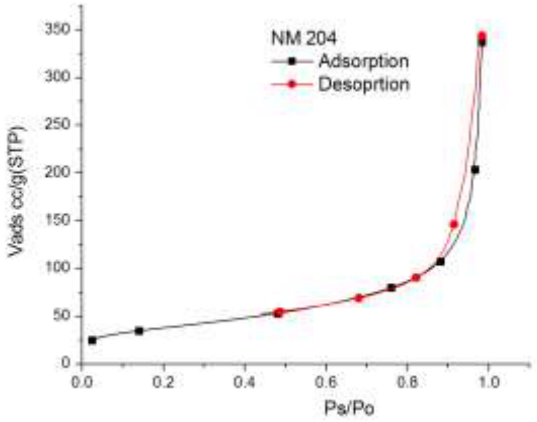

Figure 37. Isotherms of nitrogen sorption experiments by IMC-BAS at 77K for SAS NMs giving the adsorbed volume (Vads) in cm^3 per gram (cc/g) [y-axis] and P/P_0 on the x-axis The NM-numbers are mentioned in the title of each plot.

The results for the specific surface area of the NM-202, NM-203 and NM-204 obtained by JRC are summarised in Table 28; the measurements of NM-200 and NM-201 are on-going. The JRC measurements were done according to both single point and multipoint BET measurements. The single point measurement can be applied when the BET constant c >>1, and it can be assumed that the plot passes through the origin.

Table 28. Results of the JRC BET measurements on NM-202, NM-203 and NM-204.

	BET surface. Sample stored at 40 °C m^2/g		**BET surface. Sample stored at low temperature[5]** m^2/g	
	Single point	**Multipoint**	**Single point**	**Multipoint**
NM-202	186.5392	191.9871	187.4781	192.9282
NM-203	192.4628	198.0809	189.8376	195.4241
NM-204	131.7462	134.3128	132.057	134.6187

10.2. Comparison between BET data from research laboratories and producers

In Table 29 the results from the BET analyses in the project are compared with data provided by manufacturers of the industrial materials. Despite clear differences in absolute numbers, it is evident that there is an overall, and possibly as good as possible, comparability between the three data sets. The results suggest reasonable material homogeneity and/or that both the NANOGENOTOX project and producer instrumental capacity and the SOPs for making BET analysis are of similar quality. However, a final conclusion cannot be made on

[5] low temperature: -80 °C or colder

comparability as the results were not produced using traceable standards for calibration or benchmarking.

Table 29. Comparison of BET data by the manufacturers and measured in the NANOGENOTOX project, and SAXS data.

NM-20x	BET surface Producer m^2/g	BET surface IMC-BAS m^2/g	BET surface JRC (range)* m^2/g	SAXS surface CEA m^2/g
NM-200	220	189.16		123.30(+/-4.9)
NM-201	160	140.46		123.3(+/-8.3)
NM-202	170-230	204.11	186.5 to 192.9	184(+/-17.8)
NM-203	200(+/-25)	203.92	189.8 to 198.1	167.2(+/-13.4)
NM-204	140	136.60	131.7 to 134.6	131(+/-22.9)

*the JRC measurements reflect samples stored at two different temperatures and two different BET measurements, see Table 28.

10.3. Comparison of SAXS and BET data

The SAS NMs were analysed with regard to specific surface area using BET and SAXS and comparison between the data, see Table 29, shows a relatively large difference for some of SAS NM materials and the biggest discrepancy was observed for the sample NM-200.

Considering the few data points, no overall linear correlation between SAXS and BET data for SAS alone (Figure 39) is seen.

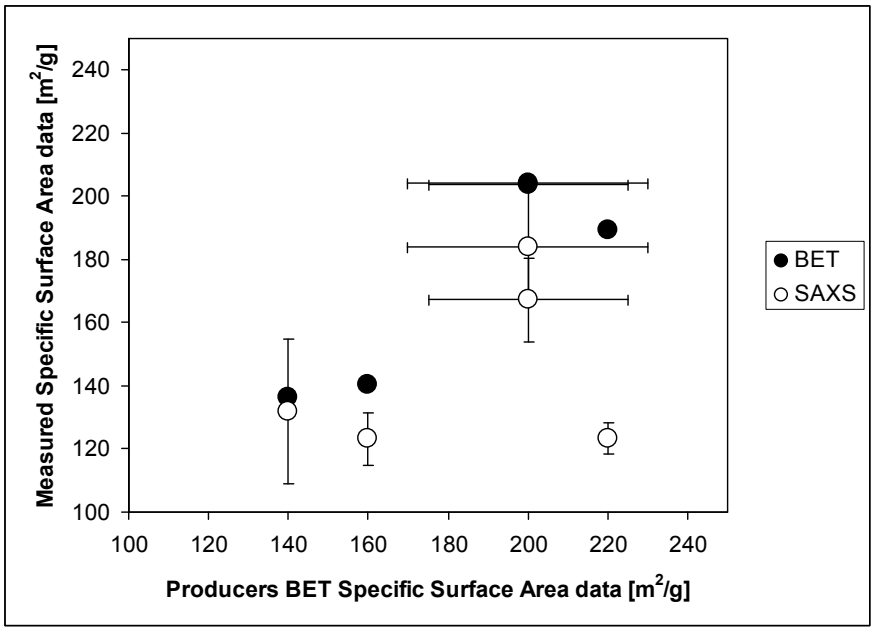

Figure 38. Plot of measured BET (filled spheres) and SAXS (open spheres) specific surface area data plotted against the BET specific surface area data reported by the producers. Generally, good agreement is observed between measured and producer data. SAXS data appears to underscore the BET surface areas at high surface area values.

In the Specific Surface Area assessment, differences and limitations of the methods also need to be considered. Assessed from the methodology, most of the differences in the obtained results may be explained by the combined errors in density and placement of plateau. Other explanations may come from the difference in thermal treatment and outgassing of the powders before BET analysis. Indeed, thermogravimetric analysis showed a two main weight losses regions in the analysis of NM-200, which could come from organic coating and water, “wrapping” the nanoparticles and therefore responsible for a decrease of the X-ray contrast and subsequently of the specific surface area seen by SAXS.

It should also be mentioned that the Porod plateau is determined in a q range up to 0.3 $Å^{-1}$, which corresponds in the direct space to dimensions down to 2 nm. This means that it is very difficult to estimate a roughness smaller than 2 nm under these conditions (leading to an additional surface area). This could explain why, in BET measurements, N_2 molecules, smaller than 2 nm, might in general “see” more surface; therefore the determination of surface area for very small and bigger (>200 nm) particles needs more attention. Both of these issues could be of great importance for the SSA measurements of high-surface area nanomaterials.

11. XRD measurements

X-Ray Diffraction (XRD) analysis is based on the principle that crystalline materials diffract X-rays in a characteristic pattern, which is unique for each material. XRD is a method of determining the atomic and molecular structure of a crystal in which the regular atomic lattice causes a beam of X-rays to diffract into many specific directions. XRD can therefore be used to identify different polymorphs, such as typical TiO_2 polymorphs rutile, brookite and anatase. The width of the reflections can also give information about the size of the diffracting domains (crystallites), which for nanoparticles may often (but not always) correspond to particle size.

A low concentration of crystalline impurities (~1%) in amorphous materials can also be detected with XRD. For the SAS NMs, the material is a powder, and the crystallites and particles are randomly oriented, hence all the peaks reported for a phase in the XRD pattern database should be present, and all laboratories should see quite similar XRD peak ratios from the different phases. If all peaks for a specific phase are not present, then they do not come from a randomly oriented fine-grained powder. Of course minor peaks may be lost in noise, but major peaks should all be there in the correct intensity ratios. If one laboratory sees one or more prominent 'extra' peaks and all others do not, then it has to be carefully checked if those peaks arise from some non-sample effect; it should also be checked that the different XRD patterns have comparable quality of the noise-signal ratio as this has a bearing on the level of impurities that are detectable. Furthermore, the type of sample mounting may have a significant influence on what is seen from the XRD data. With the sample holder used by IMC-BAS no impurities are detected in the SAS NMs. NRCWE used small samples on low background Si-sample holders and mounted the samples using vacuum grease, giving scans that show impurities which could not be ascribed to the vacuum grease used to mount the samples. It should be noted that for certain X-ray detectors, geometries and monochromator arrangements, single crystal silicon substrates can give rise to ‘spurious’ sharp peaks in XRD patterns, though this is not necessarily the case here; the JRC instrument occasionally give raise to such peaks.

XRD was carried out on the samples by several laboratories: IMC-BAS, NRCWE and JRC and Table 30 gives an overview of the results of the XRD measurements on the SAS NMs.

11.1. XRD results

XRD can be measured in different setups and the use of different wavelengths is possible, but for standard measurements this is less important, as long as it is taken into account. Most databases are based on irradiation using Cu Kα X-rays.

All data presented in this report were recorded in reflection mode (either in θ-2θ or glancing angle geometries) using Cu Kα radiation. Reflection mode analysis has the advantage that very small samples can be used (though more material is recommended) and as the scatter is usually detectable until high values of 2θ, unit cells can be determined with high accuracy. Ideally, internal standards are used to control for differences between instruments, but this was not done here.

A priori, it was expected that the SAS NMs are amorphous and XRD analysis confirmed this, as seen from the very broad peak at ca. 22.5° 2θ in the XRD scans. As the samples mainly contain amorphous material quantitative analysis is impossible with XRD.

Table 30. XRD measurements on SAS NMs. Phases and impurities detected.

Sample	Vial no.	Institution	Phase and Impurities Measured	Times measured
NM-200	0072	NRCWE	Amorphous (A)	0
			A+ Na_2SO_4	2
			A+ Na_2SO_4 + Böhmite*	3
			A+ Na_2SO_4 + one extra reflection^{++}	1
	0441		A+ Na_2SO_4	1
			A+ Na_2SO_4 + Böhmite	1
	0156	IMC-BAS	A + no impurities detected	
	0157		A + no impurities detected	
	4230	JRC	A + crystalline impurities consistent with $Na_2SO_4$$^{\$}$	
NM-201	0022	NRCWE	A+ Na_2SO_4	2
			A+ Na_2SO_4 + Böhmite	3
	0444		A+ Na_2SO_4	1
			A+ Na_2SO_4 + Böhmite	3
	0100	IMC-BAS	A + no impurities detected	
	0102		A + no impurities detected	
	2628	JRC	A + crystalline impurities consistent with $Na_2SO_4$$^{\$}$	
NM-202	0027	NRCWE	A+ Böhmite	3
	0486		A+ Böhmite	2
	0104	IMC-BAS	A + no impurities detected	
	0108		A + no impurities detected	
	0528	JRC	A + no impurities detected	
NM-203	0152		Amorphous (A)	2

		NRCWE	A+ Böhmite	1
	0363		Amorphous (A) A+ Böhmite	1 2
	0280	IMC-BAS	A + no impurities detected	
	0282		A + no impurities detected	
	0480	JRC	A + no impurities detected	
NM-204	0006	NRCWE	A + no impurities detected	
	0098	IMC-BAS	A + no impurities detected	
	0102		A + no impurities detected	
	0580	JRC	A + no impurities detected	

* Böhmite is an aluminium oxide hydroxide (γ-AlO(OH)) mineral.
$ The JRC itself did not identify the crystalline impurities, but the scan has peaks consistent with the NRCWE observations regarding two main peaks that can be associated with Na_2SO_4.
++ The reflection was consistent with one of the reflections seen in the reflection library for cristobalite; however, positive identification of cristobalite could not be made from this peak alone and the reflection was seen only in this specific subsample from this vial.

Table 14 gives an overview of the elemental impurities detected by various methods, and regarding the crystalline nature of these impurities the XRD scan parameters would influence what can be detected, as described at the start of chapter 11.

NRCWE identified two reflections consistent with presence of Na_2SO_4 in NM-200 and NM-201; however the XRD spectrum database at NRCWE does not allow a positive identification of Na_2SO_4. The presence of Na_2SO_4 in NM-200 and NM-201 is due to the production process based on precipitation. In addition, NRCWE suggested the presence of Böhmite (AlO(OH)) in NM-200, NM-201, NM-202 and NM-203. The suggested impurities and their phases are based on knowledge of elements present (from EDX) and possible crystalline materials containing one or more of these elements. Presence of an Al-rich phase is additionally supported by results from chemical results of dissolved elements in the dissolution studies, where Al was observed in all samples.

The JRC also measured the SAS NMs using XRD, see Figure 42 and the JRC results confirm that the material is amorphous. The peaks at near 32 and 34 degrees suggest the presence of some crystalline material in NM-200 and NM-201, consistent with the presence of Na_2SO_4. However, on the basis of the two peaks only, positive identification was not made. The XRD scans for NM-202, NM-203 and NM-204 by the JRC did not have any peaks near 32 and 34 degrees, i.e. the crystalline impurities seen for NM-200 and NM-201 were absent for the other NMs.

Results from the elemental analyses, presented in chapter 5, further support the findings from the XRD analyses.

The SAS NMs are amorphous, and thus XRD measurements cannot be used to determine the crystallite size.

The graphs of some of the XRD measurements are presented in Figure 39 to Figure 42.

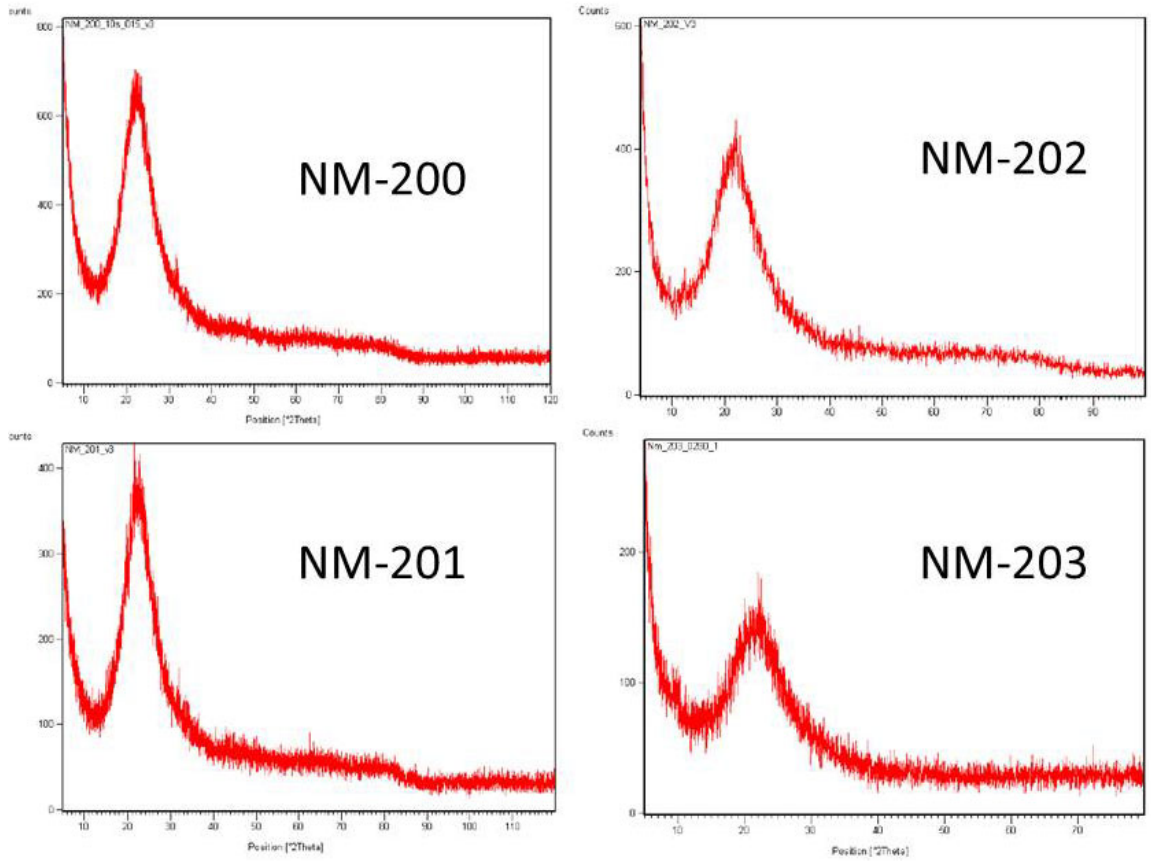

Figure 39. XRD scan on NM-200, NM-201, NM-202 and NM-203 by IMC-BAS.

Figure 41 shows three XRD scans of NM-200, illustrating the care taken also in confirming observations.

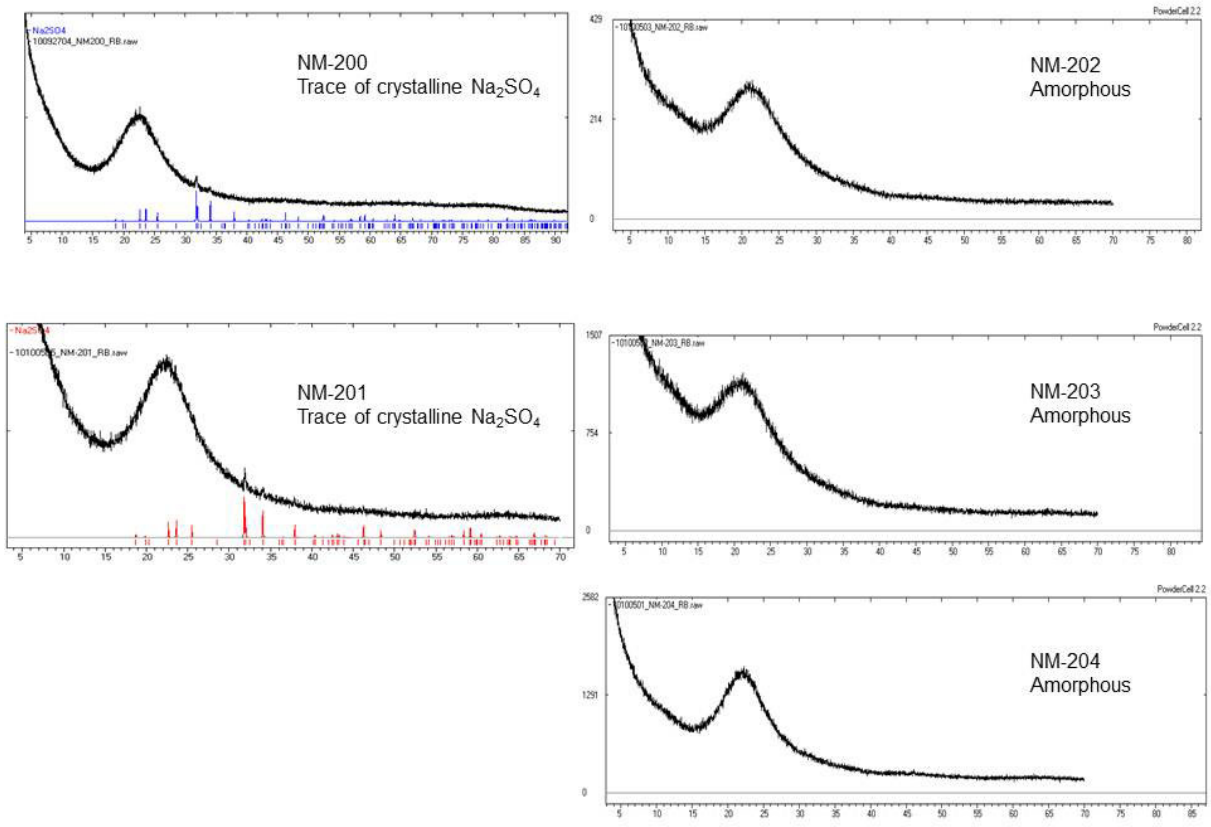

Figure 40. XRD scans of the SAS NMs by NRCWE. The SAS NMs are all amorphous, and for NM-200 and NM-201 a trace of Na_2SO_4 is seen.

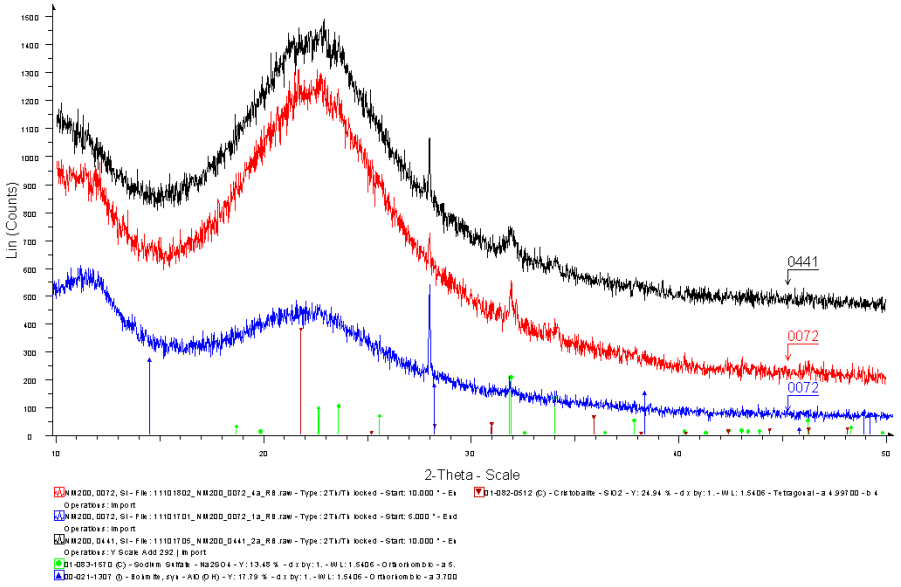

Figure 41. Three XRD scans of NM-200 by NRCWE suggesting presence of Böhmite and Na_2SO_4. Colour code for the <u>X-axis</u>: Böhmite is blue and Na_2SO_4 is green. The numbers 0441 and 0072 refer to the vial numbers.

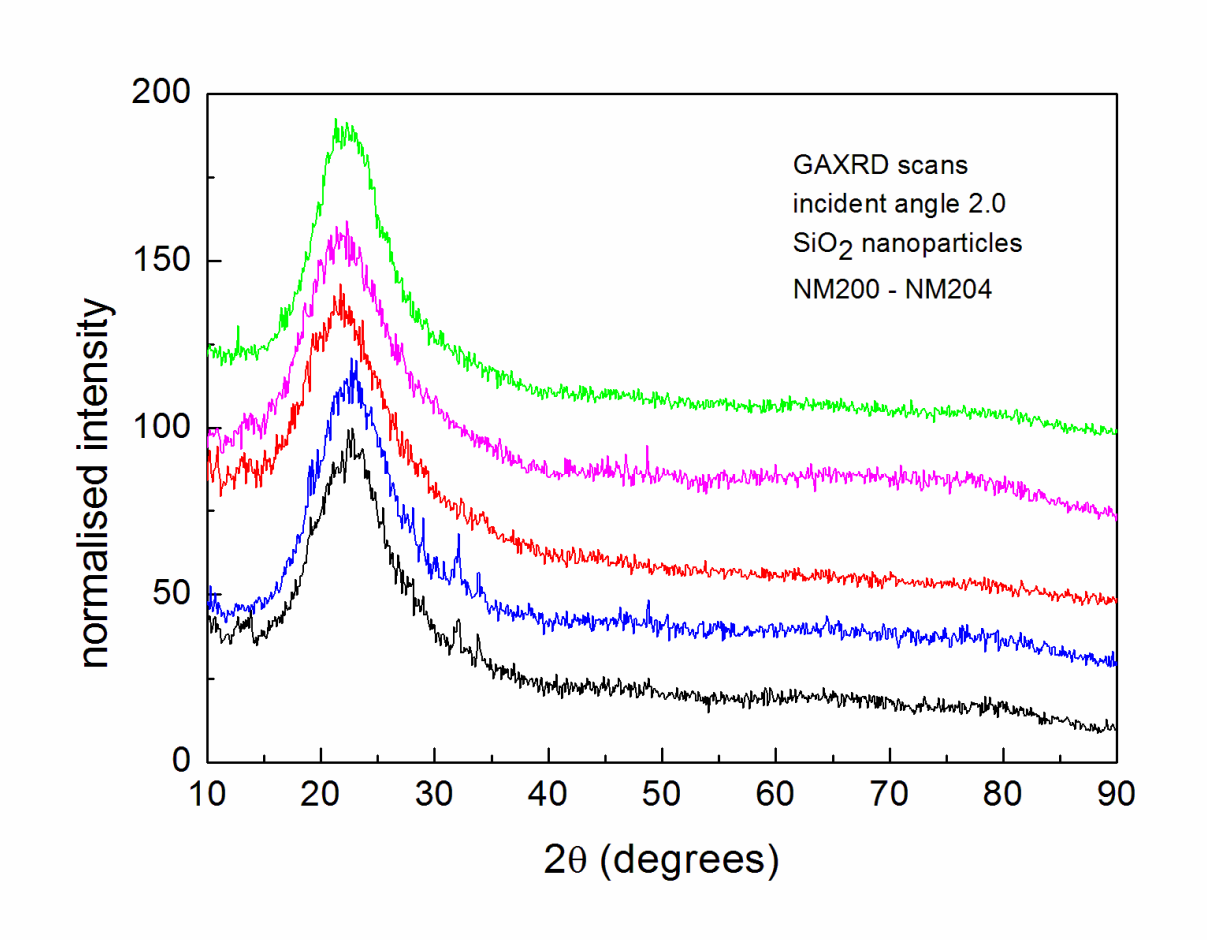

Figure 42. JRC XRD of NM-200 to 204, amorphous. Black: NM-200, blue: NM-201, red: NM-202, pink: NM-203, green: NM-204.

The XRD scans by the different laboratories all agree that the SAS NMs are amorphous. In addition, one of the laboratories suggested that the SAS NMs, except NM-204, contain just detectable concentrations of böhmite,. The suggested presence of Na_2SO_4 in NM-200 and NM-201 is supported by the scans by the NRCWE and the JRC as well as the results from elemental analysis and was confirmed by the industrial synthetic silica group, Association of Synthetic. Amorphous Silica Producers (ASASP). The presence of böhmite is only found at NRCWE and based on one clear peak and 2 very weak peaks in the background profile (Figure 42). The possible presence of böhmite in the SAS samples was later confirmed by ASASP. Furthermore uncertain presence of cristobalite was suggested for one of the NMs based on a single peak observed in one of the subsamples in a scans. From comparative analysis in NANOGENOTOX, the ability of detecting impurity phases appears to depend on equipment and the samples mounts.

12. Transmission Electron Microscopy (TEM)

The TEM experiments were performed by CODA-CERVA and IMC-BAS. Given that a sub-1-nm-resolution is the aim for NM characterisation, TEM is one of the few techniques, in addition to SEM and in specific cases AFM, with sufficient resolution. TEM yields number-based results, allows size measurements but also specific shape measurements and characterization of surface topologies on a number basis (per particle). It allows distinguishing between characterization of primary particles and aggregates/agglomerates and was successfully applied to the SAS NMs.

The TEM results give both a qualitative and a quantitative description. A qualitative description of the NM is provided based on conventional BF electron microscopy. This description includes (i) representative and calibrated micrographs, (ii) the agglomeration and aggregation status, (iii) the general morphology, (iv) the surface topology, (v) the structure (crystalline, amorphous, …) and (vi) the presence of contaminants and aberrant particles. To measure the characteristics of primary particles of the SAS NMs, the Feret Min and Feret Max were measured in CODA-CERVA following a systematic random sampling based on stereology at appropriate magnifications. CODA-CERVA developed a standardised procedure for performing a quantitative analysis of the TEM micrographs applying the above mentioned systematic random sampling. This sampling procedure is described in section 12.2 . The method is described in detail in De Temmerman et al., 2012.

12.1. TEM measurements and sample preparation

12.1.1. Sample preparation

The obtained powders were brought in suspension according to the NANOGENOTOX protocol for producing suitable manufactured nanomaterial exposure media.

In CODA-CERVA, the NMs were brought in the dispersion medium of choice at a suitable concentration: 2.56 mg/ml for SAS and sonicated for 16 minutes using a Vibracell™ 75041 ultrasonifier (750 W, 20 kHZ, Fisher Bioblock Scientific, Aalst, Belgium) equipped with a 13 mm horn (CV33) at 40% amplitude. This setup resulted in an average horn power of about 26 W and a sample specific energy of 2530 ± 20 MJ/m³. During sonication the samples were cooled in ice water to prevent excessive heating. After sonication, the samples were diluted to a concentration of 0.512 mg/ml. The suspended NM were brought on pioloform- and carbon coated, 400 mesh copper grids (Agar Scientific, Essex, England) that were pretreated with 1% Alcian blue (Fluka, Buchs, Switzerland) to increase hydrophilicity.

In IMC-BAS, the NMs were transferred onto carbon-coated copper grids without Alcian blue pre-treatment using a special tool, a platinum (Pt) wire loop (0.2 mm Pt wire, one end of

which is bent as loop with external diameter of 2.5-3.0 mm). The following operations were carried out during the transfer of suspension onto EM grids: (i) catching a grid by tweezers with reverse action; (ii) disposing the tweezers on a table surface in a way ensuring direct contact of the grid and the filter paper; (iii) careful sinking and extracting the Pt loop in/from the vessel with suspension of nanoparticles (here, a thin film of nanoparticles suspension is formed in the loop space due to the surface tension); (iv) careful touching the Cu grid placed on the filter paper by the Pt loop (in this operation, the whole surface of Cu grid in contact with the Pt loop is covered by nanoparticles while liquid media is absorbed by the filter paper); (iii-iv) operation can be performed 1 or 2 times (the Cu grid covered by nanoparticles is ready for observation immediately or after drying a few seconds at ambient temperature).

12.1.2. Recording of the electron micrographs

In IMC-BAS, well-contrasted bright field (BF) images of NM were obtained using: (i) a Philips TEM420 at 120 kV acceleration voltage; (ii) EM grids with holey carbon support film; (iii) well calibrated regimes in EM for recording images on photo plates (Kodak electron image film SO-163); (iv) appropriate developing of EM films; (v) high-resolution scanner technique for transferring the image from EM film into digital file, (vi) image processing.

In CODA-CERVA, the samples were also imaged in BF mode using a Tecnai™ G2 Spirit microscope (FEI, Eindhoven, The Netherlands) with Biotwin lens configuration operating at 120 kV at spot size 3. The condenser lens current was chosen so that the beam was parallel and images were taken approximately 500 nm below minimal contrast conditions, where Fresnel fringes were minimal and contrast was judged to be optimal. Micrograph were recorded using a 4*4 K CCD camera (Eagle, FEI).To achieve maximal traceability of information, each micrograph was stored together with its administrative and sample preparation information and the information related to its imaging conditions in a dedicated database integrated in the iTEM software (Olympus, Münster, Germany). Modifications of the TIA image acquisition software (FEI) and of the iTEM software were made to transfer the micrographs and their associated information efficiently in the iTEM database. (i) The TIA protocol for batch conversion of the software-specific SER- and EMI-formats was adjusted to avoid too long file names. (ii) An imaging C- and libtiff library-based module, referred to as the TIA-TAG module, was developed in iTEM. This module reads the information relevant for image analysis and quality control in the private tags of the TIF image files and renders it accessible in a new information tab of the iTem software. In addition, the TIA TAG module facilitates calibration of images by automatically converting the pixel size from mm scale to nm scale. (iii) New fields were defined in the iTEM database specifying the sample and its preparation characteristics. Where applicable, drop lists were foreseen to avoid typing errors.

12.2. Systematic Random Sampling and data analysis

To avoid microscopist subjectivity in the selection of particles, the positions on the EM grid where micrographs were taken, were selected randomly and systematically, see Figure 43. The grid was placed randomly into the holder and positions distributed evenly over the entire area were predefined by the microscope stage. When the field of view was obscured, e.g. by a grid bar or an artifact, the stage was moved sideways to the nearest suitable field of view. For each NM three independent samples were analysed and per sample, five micrographs were made with a 4*4 k Eagle CCD camera (FEI) at a magnification of 18500 times. For the given microscope and camera configuration, this magnification corresponds with a pixel size of 0.60 nm and a field of view of 2.45 µm by 2.45 µm implying a lower particle size detection limit of approximately 6 nm, supporting on the criterion of Merkus (2009) that large, systematic size deviations can be avoided if the particle area is at least hundred pixels. The field of view limits the upper size detection limit to 245 nm, one tenth of the image size as recommended, ISO (2004). To estimate the number of particles required for the estimation of the mean particle diameter with a confidence level, it is assumed that the size distribution can be approximated by a log-normal distribution. The minimal number of particles can then be calculated according to Masuda and Gotoh (1999).

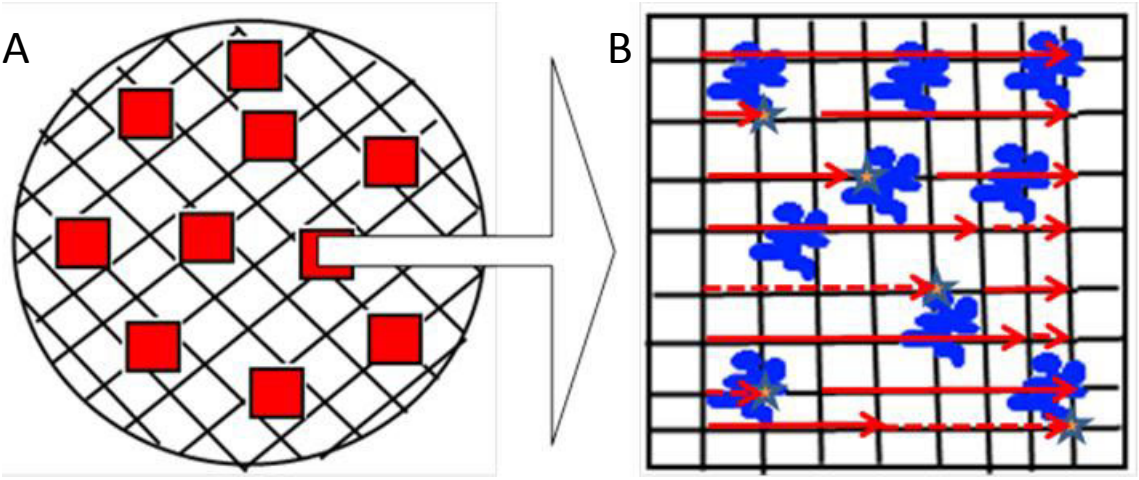

Figure 43. Schematic overview of the systematic random sampling. A) TEM grid with 10 fixed positions indicated by red squares. B) TEM micrograph with a 100 X 100 nm mesh grid. Primary particles on the intersections of the grid were measured. The stars indicate the measured primary particles, full red lines: Counting procedure from left to right until each 10th intersection. Dashed red line: the horizontal grid lines were followed until a primary particle was located on an intersection.

The Feret Min and Feret Max were measured as indicated in Figure 44. The Feret Mean was calculated as the mean of Feret Min and Feret Max. The aspect ratio was calculated as the ratio of Feret Max and Feret Min.

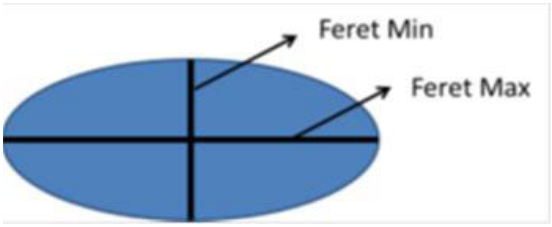

Figure 44. Schematic view of the Feret Min and Feret Max measurements on a primary particle.

The 'Detection module' of iTEM was used for threshold-based detection of the NM. Briefly, the contrast and brightness of the micrographs were optimized, the particles were enclosed in a pre-defined frame or region of interest and thresholds were set to separate particles from the background based on their electron density and size. Particles consisting of less than fifty pixels and particles on the border of the frame were omitted from the analysis.

The semi-automatic detection and measurement of SAS NMs based on mass thickness contrast is relatively straightforward. In 10 micrographs, a number of particles are detected. Figure 46 illustrates the detection methodology using iTEM software. The nanoparticles that are detected on the TEM image, in this case 4997 particles, shown in Figure 46A are given in colour in Figure 46B, where the different colours are related to the size of the detected nanoparticles.

For each particle, twenty-three quantitative parameters, described in Table 31, are measured and considered relevant for its characterization. Each particle detected in a micrograph was identified by a unique number, written in the overlay of the image. This allowed the selection of data of individual particles and the post-analysis deletion of erroneously detected particles. Artifacts were characterized by their morphology and a grey value lower than the mean grey value of the background plus three times its standard deviation. Particles fulfilling this criteria were identified and deleted automatically. Particles with an unusual morphology, judged to be artifacts after visual inspection of the micrographs, were omitted manually from analysis.

Sigmaplot (Systat, Cosinus computing, Drunen, the Netherlands) was used to calculate statistics and histograms. The normality of the distributions of the measured parameters was tested with the Shapiro-Wilk and Kolmogorov-Smirnov tests, while the homogeneity of variances was tested with Spearman rank correlation test. Since these assumptions were not met, the non-parametric Kruskal-Wallis one way ANOVA was performed and data were compared pairwise with Dunn's Method to determine the micrograph and sample effects, and to determine the effect of sonication on the number of particles per grid area.

Table 31. Quantitative parameters and their description as described in the iTEM software.

Measured parameter[1]	Description
Area[4,3] (nm²)	Projection area
Convex Area[3] (nm²)	The area of the convex hull (envelope) bounding the measured object.
Rectangle Max (nm²)	The area of the biggest rectangle whose sides consist of tangents to the measured object borders.
Rectangle Mean (nm²)	The area of the mean rectangle whose sides consist of tangents to the measured object borders.
Rectangle Min[5] (nm²)	The area of the smallest rectangle whose sides consist of tangents to the measured object borders.
ECD[6] (nm)	The equivalence refers to the area of the measured object. The ECD is the diameter of a circle that has an area equal to the area of the measured object.
Feret Max[4] (nm)	The maximum distance of parallel tangents at opposing measured object borders.
Feret Mean[7] (nm)	The mean distance of parallel tangents at opposing measured object borders.
Feret Min[4] (nm)	The minimum distance of parallel tangents at opposing measured object borders.
Radius of Inner Circle (nm)	Radius of the maximal circle inside the measured object.
Central Distance Max (nm)	The maximum distance between the center and the border of a measured object.
Central Distance Mean (nm)	The mean distance between the center and the border of a measured object.
Central Distance Min (nm)	The minimum distance between the center and the border of a measured object.
Diameter Max (nm)	The maximum diameter of a measured object (for angles in the range 0° through 179° with step width 1°).
Diameter Mean (nm)	The mean diameter of a measured object (for angles in the range 0° through 179° with step width 1°).
Diameter Min (nm)	The minimum diameter of a measured object (for angles in the range 0° through 179° with step width 1°).
Convex Perimeter[3] (nm)	The length of the perimeter of the convex hull (envelope) bounding the particle.
Perimeter[3] (nm)	The sum of the pixel distances along the closed boundary.
Aspect Ratio [8]	The maximum ratio of width and height of a bounding rectangle for the measured object.
Convexity [9]	The fraction of the measured object's area and the area of its convex hull.
Elongation	The elongation of the measured object can be considered as lack of roundness. It results from the sphericity.
Shape Factor [10]	The shape factor provides information about the "roundness" of the measured object. For a spherical measured object the shape factor is 1; for all other measured objects it is smaller than 1.
Sphericity	Describes the sphericity or 'roundness' of the measured object by using central moments.

1 These parameters are used in the iTEM software and are described in the iTEM help files
2 The descriptor between brackets gives the synonym for the iTEM parameter as described in ISO
3 As described in ISO 9276-6:2008
4 As described in ISO 13322-1:2004
5 Feret box area[3]
6 Area equivalent diameter[4]
7 Angle-average Feret diameter
8 Shape factor[4,3]
9 Solidity[3]
10 Form Factor[3]

The normality of the distributions and the homogeneity of variances were met for the mean values of the median mean diameter, the median sphericity and the median shape factor of the different SAS NM that were obtained in independent analyses.

Hence, a one way analysis of variance (ANOVA) was performed and data were compared pairwise with the Tukey test. The measured parameters were classified by principle component analysis using the SAS statistical software (SAS Institute Inc., Cary, NC, USA).

12.2.1. Results for Transmission Electron Microscopy

In a preliminary experiment, for the effects of sonication, the number of particles of a representative SAS (NM-201) per grid area increased proportionally with sonication time, see Figure 45. For 8 and 16 minutes of sonication of NM-201, the total number of detected aggregates was 1564 and 1674, respectively. This was higher than 1366, the number of particles allowing an estimation of the geometric mean particle size with an error of maximum five percent [Masuda and Gotoh (1999); ISO (2004)]. The corresponding median mean particle diameters were 40 and 39 nm, respectively, and did not differ significantly. For zero, two and four minutes of sonication, the total number of detected aggregates was too low (17, 905 and 1220, respectively), and the median mean diameter for these sonication times could not be evaluated reliably.

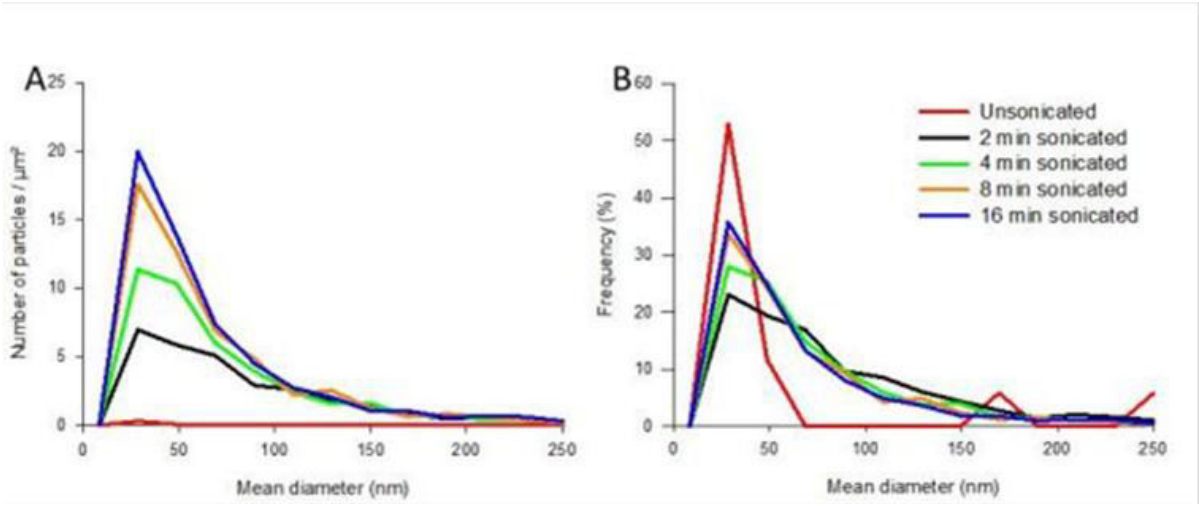

Figure 45. Effect of sonication on the size distribution of NM-201 (precipitated). The number of particles per µm² of grid area for a concentration of 0.512 mg/ml (A) and the corresponding frequencies (B) are represented as a function of their mean diameter.

To examine the intrinsic properties of SAS NMs, samples were diluted in double distilled water because this medium allowed maximal adsorption of the fraction of nano-sized particles to the grid surface. Fifteen to thirty percent of the grid surface was covered by the

SAS NMs, and the particles were homogenously distributed over the grid surface and were well separated with only occasional overlap, see Figure 46.

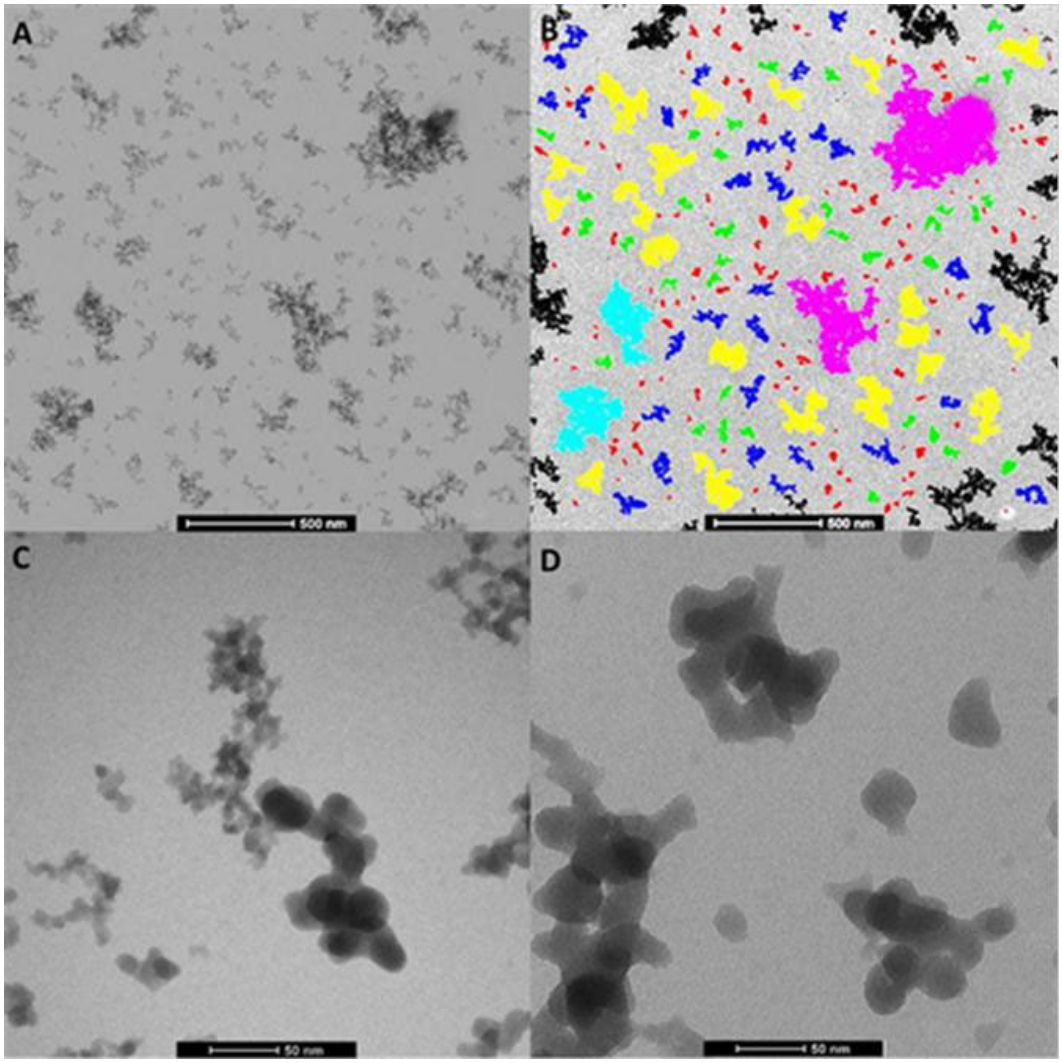

Figure 46. Illustration of the detection of NM-201 based on electron density and detail of the primary particles of NM-201 and NM-203. The figure also illustrates particle detection using iTEM software: the NM in the TEM micrograph (A) are detected, classified by mean diameter and falsely colour-coded in the corresponding annotated image (B). Red: <50 nm, green: 50 - 70 nm, blue: 70 - 100 nm, yellow: 100 - 200 nm, cyan: 200 – 300 nm, pink: 300 -500 nm and brown: >500 nm. Particles at the borders of the detection region (black) are omitted from analysis. Bar 500 nm. The TEM micrographs C and D illustrate the primary particles of NM-203 (C) and NM-201 (D); bar 50 nm.

Using other media with moderate salt concentrations, like 10 mM phosphate and 137 mM NaCl in PBS, as well as proteins, provided as 0.05 % BSA or 10 % fetal calf serum, resulted in a reduced number of particles per surface area (Figure 47A), although the size distributions remained unchanged (Figure 47B). This possibly results from the formation of agglomerates that precipitate.

Using this methodology a stable dispersion of SAS NMs could be obtained in water, in water & 0.05 % BSA, and water & 0.05 % BSA & ethanol.

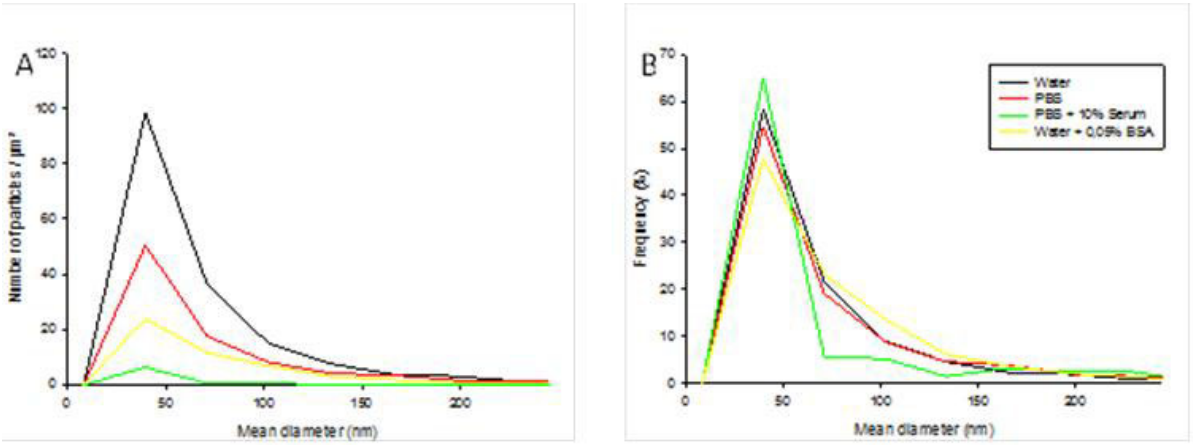

Figure 47. Effect of medium on the size distribution of NM-200. The number of particles per µm² of grid area for a concentration of 0.512 mg/ml (A) and corresponding frequencies (B) are represented as a function of their mean diameter.

12.3. Results for NM-200

12.3.1. Qualitative analysis of NM-200

In general, NM-200 particles, dispersed into double distilled water, are evenly distributed over the grid surface. As illustrated by Figure 48, the specimen consists mainly of aggregates and only a few, if any, primary particles are detected. In addition, the existence of larger agglomerates of aggregates is very rarely detected, which could be due to sonication as part of the dispersion process.

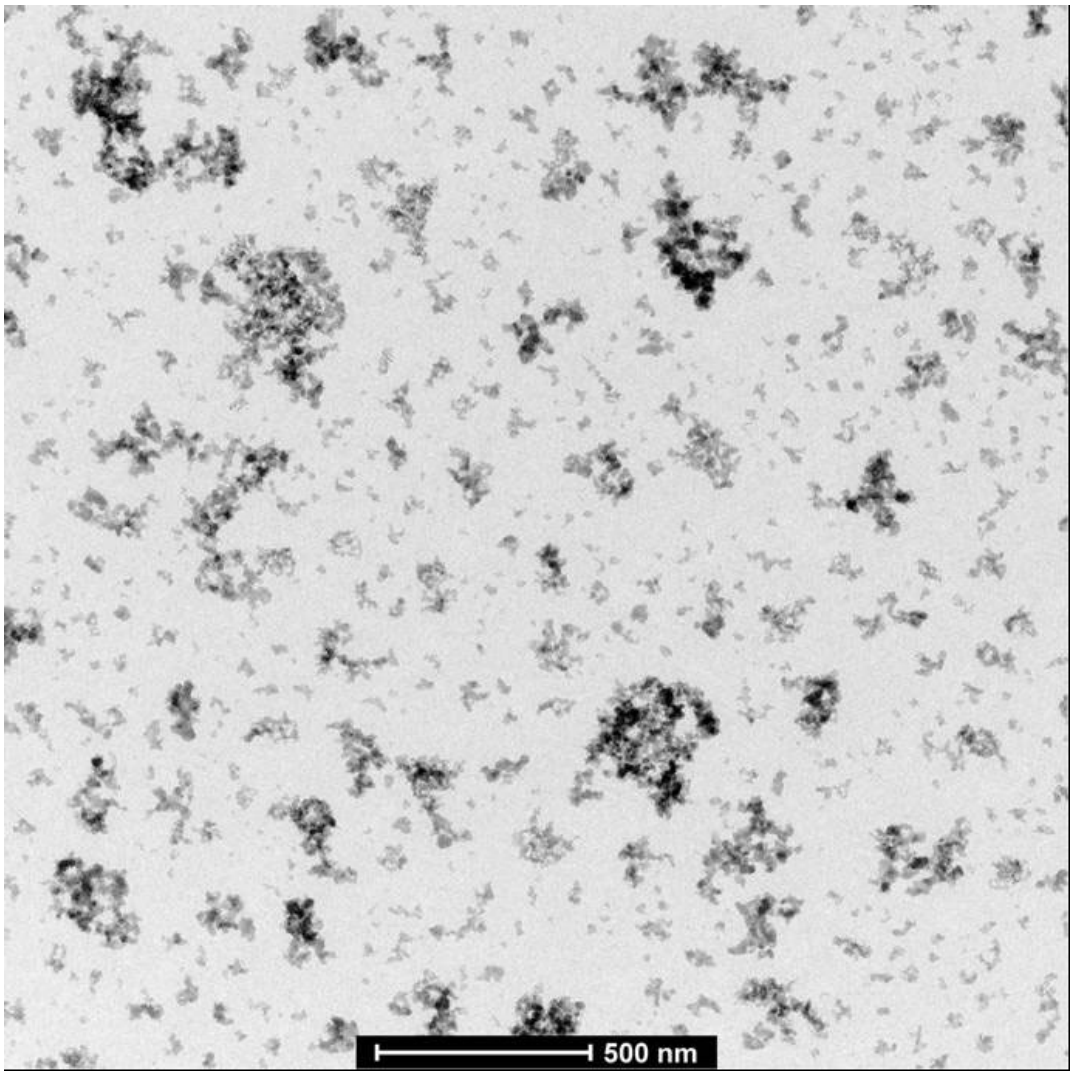

Figure 48. Representative micrograph of NM-200 dispersed into double distilled water. The presence of larger aggregates is clearly seen.

The micrograph shown in Figure 49 illustrates the occurrence of larger agglomerates.

A representative TEM micrograph of NM-200 showing the complex structure of silicon dioxide aggregates is given in Figure 50. The general morphology of the primary sub-units of NM-200 is equi-axed and rounded, or slightly elongated with a suggested spherical or ellipsoidal 3D structure. The aggregates and agglomerates tend to be more or less equi-axed, possibly due to steric preference, but often dendritic outliers are observed.

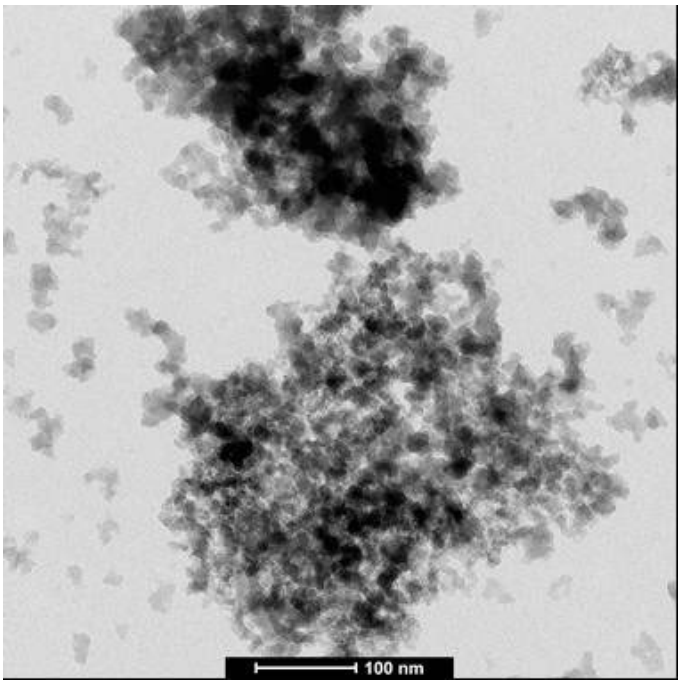

Figure 49. Micrograph of NM-200, illustrating the occurrence of large agglomerates of aggregates.

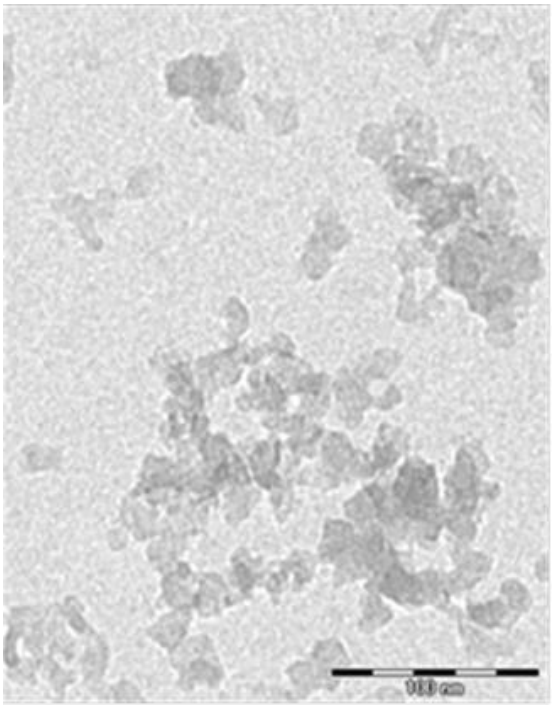

Figure 50. NM-200: selected TEM micrograph showing the complex structure of the aggregates; scale bar is 100nm.

12.3.2. Quantitative analysis of sample NM-200

The descriptive statistics are summarized in Table 32 for NM-200. The average value (Mean), the standard deviation (Std Dev), the standard error on the mean (Std Err), and the

smallest (Min) and largest (Max) observation, are presented. The primary particles of the nanomaterial are homogenous in size and primary particle sizes of about 10-20 nm are measured on the TEM images. The aggregates have a size ranging from 15 nm to 650 nm. However, since for all measured parameters, the Kolmogorov-Smirnov and the Shapiro-Wilk probabilities are smaller than 0.001 (not shown), none of these parameters can be assumed to be normally distributed. Hence, non-parametric estimates of these parameters describe the sample better. These include the median and the 25 and 75 percentiles.

Table 32. Descriptive statistics of NM-200 (for 4997 particles).

Column	Mean	Std Dev	Std Err	Max	Min	Median	25%	75%
Diameter Mean (nm)	50.0	55.0	0.8	656.3	8.8	32.0	18.7	58.3
Diameter Max (nm)	56.2	61.9	0.9	726.3	9.6	36.0	21.0	65.4
Diameter Min (nm)	36.7	40.4	0.6	502.2	5.1	23.5	13.6	43.1
ECD (nm)	36.9	37.0	0.5	506.7	8.3	25.1	15.2	43.8
Feret Mean (nm)	47.2	51.4	0.7	628.9	8.9	30.4	17.8	54.6
Feret Max (nm)	56.3	61.9	0.9	727.2	9.5	36.1	21.1	65.6
Feret Min (nm)	35.5	38.9	0.6	497.3	5.6	22.7	13.5	41.6
Central Distance Mean (nm)	19.1	19.7	0.3	252.6	3.9	12.8	7.6	22.5
Central Distance Max (nm)	30.1	33.8	0.5	384.3	4.6	19.1	10.9	35.1
Central Distance Min (nm)	7.2	7.5	0.1	140.1	0.1	5.2	3.2	8.6
Radius of Inner Circle (nm)	254.8	147.9	2.1	555.0	1.0	252.0	127.0	378.0
Next Neighbour Distance (nm)	60.1	25.5	0.4	245.3	9.9	56.3	41.9	73.5
Perimeter (nm)	211.4	354.8	5.0	6141.4	26.8	103.7	58.3	208.6
Area (nm²)	2148	6986	99	201642	54	496	181	1510
Convex Area (nm²)	3159	10730	152	280010	57	605	209	1938
Convex Perimeter (nm)	153.6	170.2	2.4	2048.5	26.9	97.9	56.2	178.1
Rectangle Mean (nm²)	4758	15914	225	390026	79	909	310	2905
Rectangle Max (nm²)	5242	17482	247	412536	84	984	341	3208
Rectangle Min (nm²)	4142	13959	197	350642	70	792	269	2538
Aspect Ratio	1.567	0.353	0.005	4.243	1.026	1.495	1.307	1.744
Convexity	0.814	0.109	0.002	0.985	0.386	0.833	0.743	0.905
Elongation	1.731	0.516	0.007	5.208	1.005	1.608	1.357	1.984
Shape Factor	0.557	0.218	0.003	1.004	0.033	0.569	0.390	0.741
Sphericity	0.411	0.197	0.003	0.990	0.037	0.387	0.254	0.543

Table 33 summarizes the number of particles smaller than 100nm, 50nm and 10nm. The amount of particles smaller than 100 nm is 88.7% based on number. The sphericity of the particles is larger than 0.33 for 60.7% of the particles. According to Krumbein and Sloss (1963), a value larger than 0.33 corresponds with medium sphericity and a value larger than 0.67 corresponds with high sphericity.

Table 33. Number (expressed in %) of NM-200 particles smaller than 100 nm, 50 nm and 10 nm.

	< 100 nm (%)	< 50 nm (%)	< 10 nm (%)
NM-200	88.7	69.8	1.7

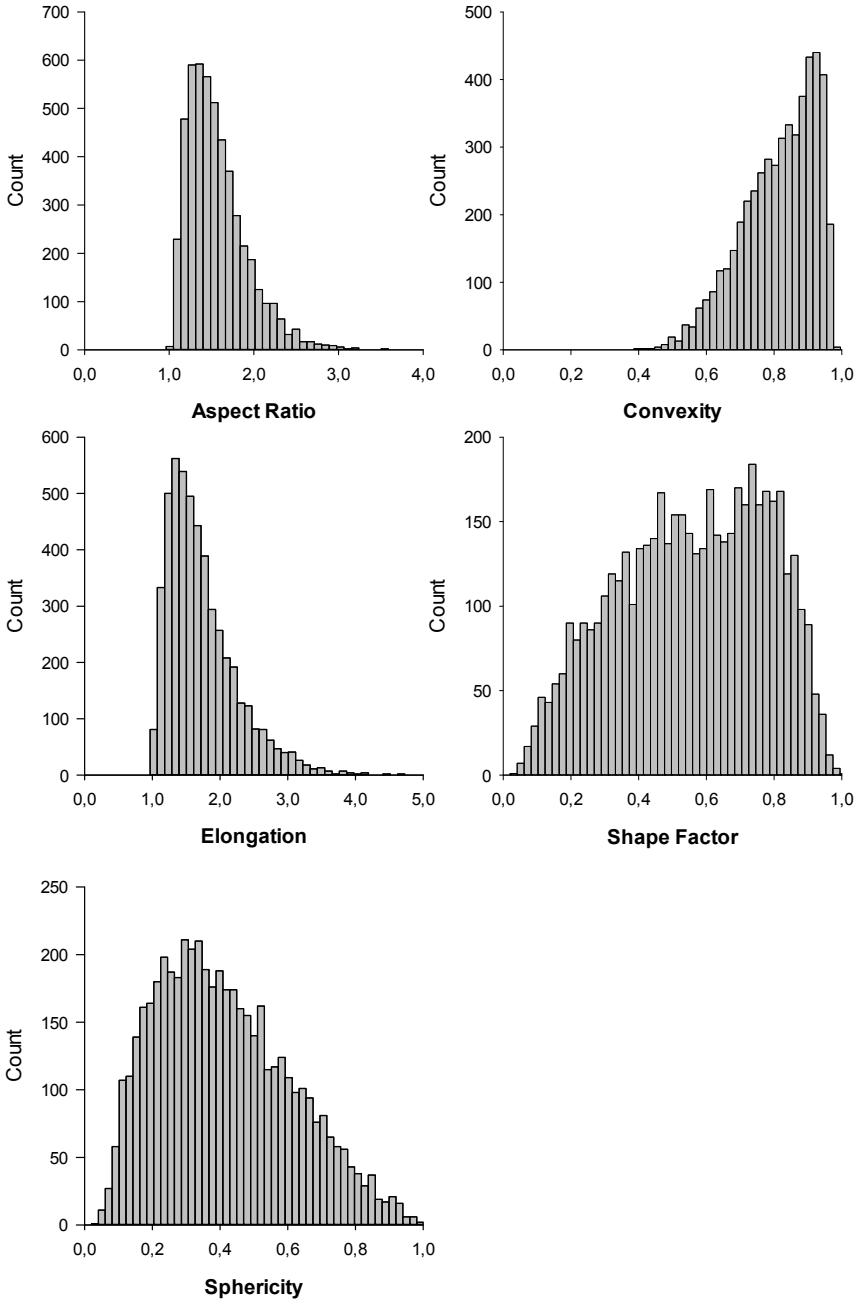

Figure 51. Histograms showing the number-based 'Shape' distributions of NM-200.

Figure 51 illustrates that 40.0% of the particles have a shape factor smaller than 0.5.

12.4. Results for NM-201

12.4.1. Qualitative analysis of NM-201

NM-201 dispersed into double distilled water, consists of individual particles, aggregates and agglomerates, as illustrated by Figure 52A and only a few individual particles are detected. The existence of larger agglomerates of aggregates is very rarely detected. In general, the particles are evenly distributed over the grid surface.

Figure 52B shows a higher resolution image of the NM illustrating the complex open network structure. The primary particles of the nanomaterial are homogeneous and have a size of about 10-20 nm, measured on the TEM images. The aggregates have a size ranging from 15nm to 600nm. The general morphology of the primary subunits of the NM is equi-axed and rounded, or slightly elongated. Their suggested 3D structure is spherical or ellipsoidal. The aggregates and agglomerates tend to be more or less equi-axed, possibly due to steric preference, or have a more dendritic structure.

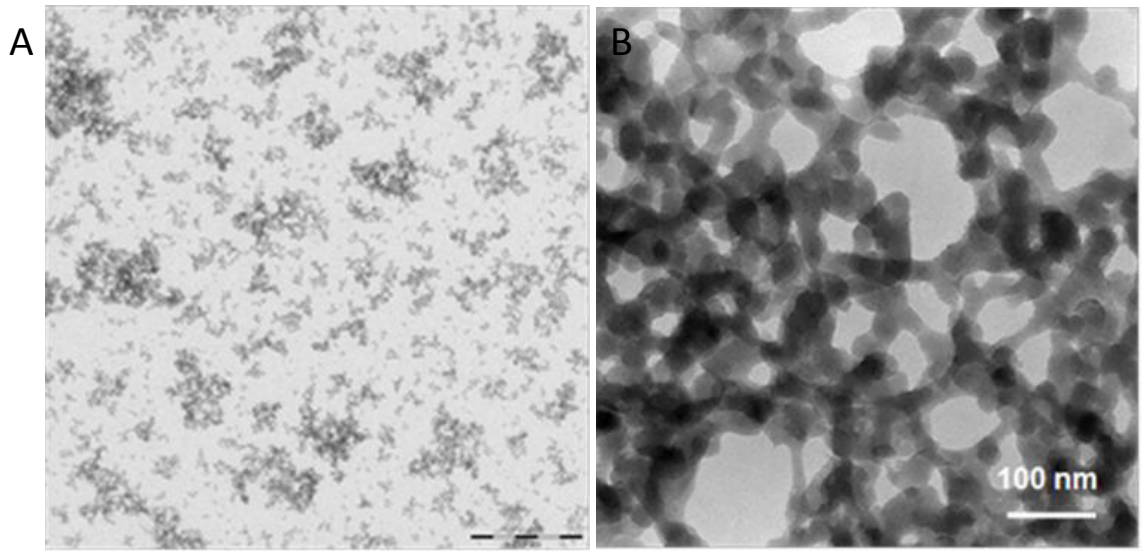

Figure 52. NM-201: A) Representative TEM micrograph of well-dispersed sample taken for quantitative TEM-analysis; scale bar is 500nm. B) TEM micrograph showing the complex open network structure in the silicon dioxide aggregates; scale bar is 100nm.

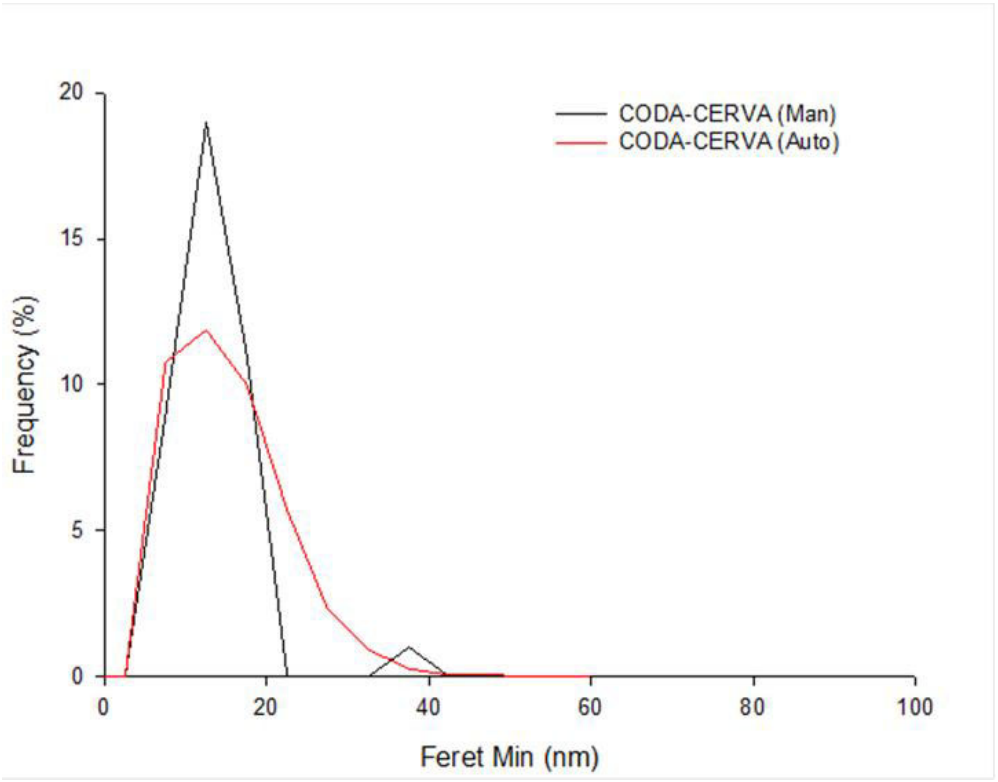

Figure 53. Qualitative TEM image analysis of NM-201. The graph illustrates the primary particle Feret Min size distribution as a function of the frequency. The manual (CODA-CERVA (Man)) and semi-automatic measurement (CODA-CERVA (Auto)) are given.

12.4.2. Quantitative analysis of sample NM-201

The semi-automatic detection and measurement of NM-201, based on mass thickness contrast, included 10 micrographs, in which 2464 particles were detected; the method is described earlier. NM-201 contains small ellipsoidal primary particles with an aspect ratio of 1.4 and a size of 13-14 nm, depending on the used methodology. All analysed primary particles were smaller than 100nm (Table 34). The Feret Min (Figure 53), Feret Mean, Feret Max and Aspect Ratio of these particles were lognormal distributed for manual measurements but not for semi-automatic measurements. No significant ($p < 0.05$) differences were found between manual and semi-automatic measurements.

Table 34. Primary particle, Feret Min, Feret Max, Feret Mean, percentage of particles with a Feret Min lower than 100 nm and Aspect ratio for NM-201.

Lab	Feret Min ± SD (nm)	Feret max ± SD (nm)	Feret mean ± SD (nm)	< 100 nm	Aspect ratio	n
CODA-CERVA (Man)	12,7 ± 1,3[a]	17,9 ± 1,4[a]	15,4 ± 1,3[a]	100 %	1,4 ± 1,3[a]	42
CODA-CERVA (Auto)	13,9 ± 1,5[a]	19,4 ± 1,6[a]	17,0 ± 1,6[a]	100 %	1,4 ± 1,2[a]	1726

* Geometric mean ± the geometric standard deviation (SD) [15]

[a, b] Different letters indicate significantly different mean values by Kruskal-Wallis One Way Analysis of Variance on Ranks ($p < 0,05$)

In analogy with the results reported for NM-200, the amount of particles smaller than 100 nm is 81.5%. Table 36 summarizes the number of particles smaller than 100nm, 50nm and 10nm. Furthermore, the sphericity of the particles is larger than 0.33 for 63.5% of the particles, i.e. between medium (value larger than 0.33) and high (value larger than 0.67) sphericity according to Krumbein and Sloss (1963). The descriptive statistics are given in Table 35. A graphical representation of some of the information is given in Figure 54.

Table 35. Descriptive statistics for NM-201 (based on 2464 particles).

Column	Mean	Std Dev	Std Err	Max	Min	Median	25%	75%
Diameter Mean (nm)	64.88	62.22	1.25	549.97	8.79	43.70	24.95	82.17
Diameter Max (nm)	72.67	69.67	1.40	603.13	9.65	49.31	27.75	91.46
Diameter Min (nm)	48.17	46.49	0.94	424.56	5.38	32.35	18.63	60.68
ECD (nm)	48.53	41.90	0.84	360.57	8.29	35.07	21.10	60.96
Feret Mean (nm)	61.32	58.30	1.17	518.48	8.94	41.50	24.04	77.60
Feret Max (nm)	72.81	69.69	1.40	603.03	9.52	49.39	27.86	91.75
Feret Min (nm)	46.49	44.46	0.90	408.63	6.21	31.10	18.38	58.63
Central Distance Mean (nm)	24.99	22.14	0.45	186.76	3.91	17.85	10.57	31.42
Central Distance Max (nm)	38.86	37.85	0.76	329.81	4.50	26.15	14.53	49.21
Central Distance Min (nm)	9.60	8.28	0.17	74.58	0.18	7.40	4.65	11.60
Radius of Inner Circle (nm)	13.72	8.38	0.17	92.42	2.69	11.66	8.08	17.65
Next Neighbour Distance (nm)	93.21	35.97	0.73	352.63	15.10	89.78	67.84	113.44
Perimeter (nm)	268.38	375.29	7.56	4712.05	27.46	141.40	77.51	301.73
Area (nm²)	3227.42	7100.53	143.04	102111.46	54.03	966.10	349.76	2919.05
Convex Area (nm²)	4666.80	11480.56	231.28	171295.47	56.89	1143.04	387.87	3872.08
Convex Perimeter (nm)	200.35	193.03	3.89	1706.75	26.70	134.51	76.79	253.74
Rectangle Mean (nm²)	7010.79	17214.87	346.80	264862.69	79.79	1687.14	564.88	5838.90
Rectangle Max (nm²)	7720.37	18940.02	381.56	294685.48	83.20	1849.63	607.92	6525.19
Rectangle Min (nm²)	6099.90	15065.28	303.50	236951.69	69.77	1482.54	504.16	4985.47
Aspect Ratio	1.55	0.34	0.01	3.93	1.04	1.47	1.30	1.71
Convexity	0.83	0.11	0.01	0.99	0.41	0.85	0.76	0.92
Elongation	1.70	0.49	0.01	5.50	1.02	1.57	1.34	1.94
Shape Factor	0.57	0.23	0.00	1.00	0.05	0.59	0.39	0.76
Sphericity	0.42	0.19	0.00	0.97	0.03	0.40	0.27	0.56

Table 36. Number (expressed in %) of NM-201 particles smaller than 100 nm, 50 nm and 10 nm.

	< 100 nm (%)	< 50 nm (%)	< 10 nm (%)
NM-201	81.5	55.3	1.1

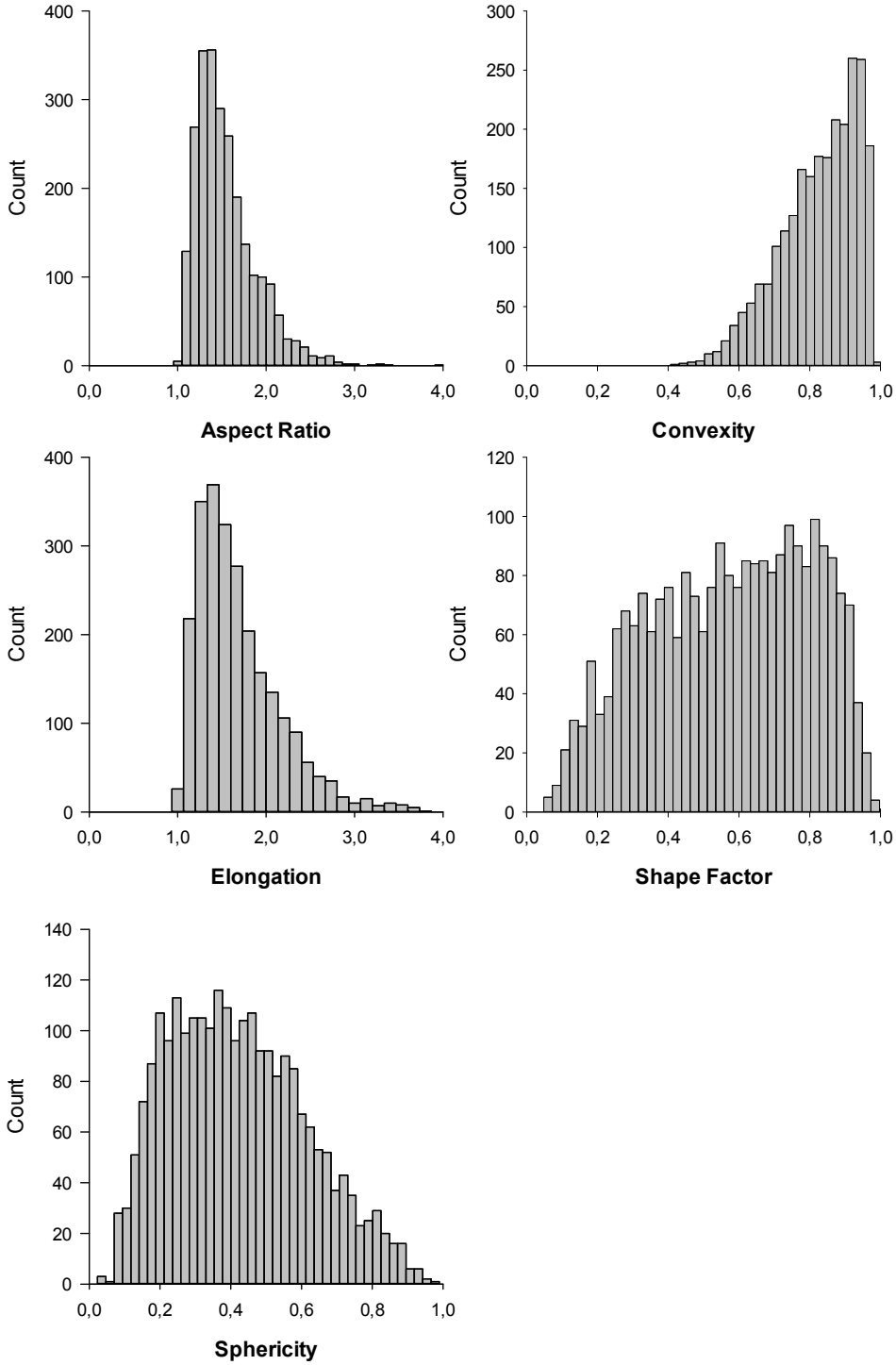

Figure 54. Histograms showing the number-based 'Shape' distributions of NM-201.

12.5. Results for NM-202

12.5.1. Qualitative analysis of NM-202

NM-202 dispersed into double distilled water, consists mainly of aggregates and agglomerates of aggregates, as illustrated by Figure 55. Primary particles are only very rarely observed.

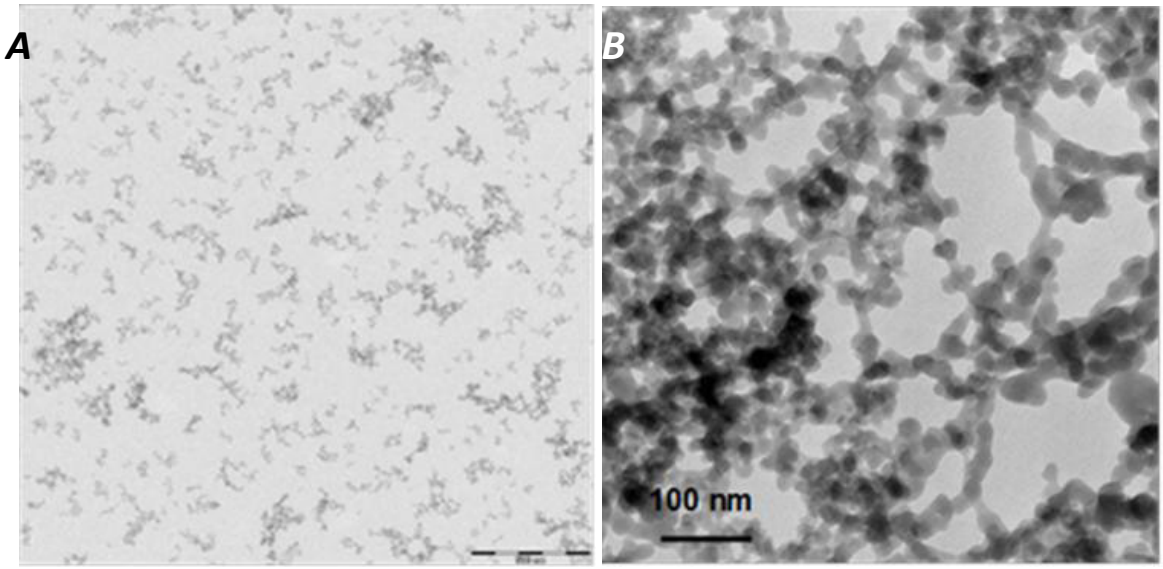

Figure 55. NM-202: A) Representative TEM micrograph of well-dispersed sample taken for quantitative TEM-analysis; scale bar is 500nm. B) TEM micrograph showing the complex open network structure in the silicon dioxide aggregates; scale bar is 100nm.

The selected micrograph shown in Figure 56 illustrates the occurrence of larger agglomerates. In general, the particles are evenly distributed over the grid surface.

The primary particles of the nanomaterial are heterogeneous in size, as illustrated by Figure 56. Particle sizes ranging from 5 nm to 30 nm are measured on the TEM images. The aggregates have a size ranging from 10 nm up to 600 nm. The general morphology of the primary subunits of the NM is equi-axed and rounded, or slightly elongated. Their suggested 3D structure is spherical or ellipsoidal. The aggregates and agglomerates tend to be more or less equi-axed, possibly due to steric preference, or have a more dendritic structure.

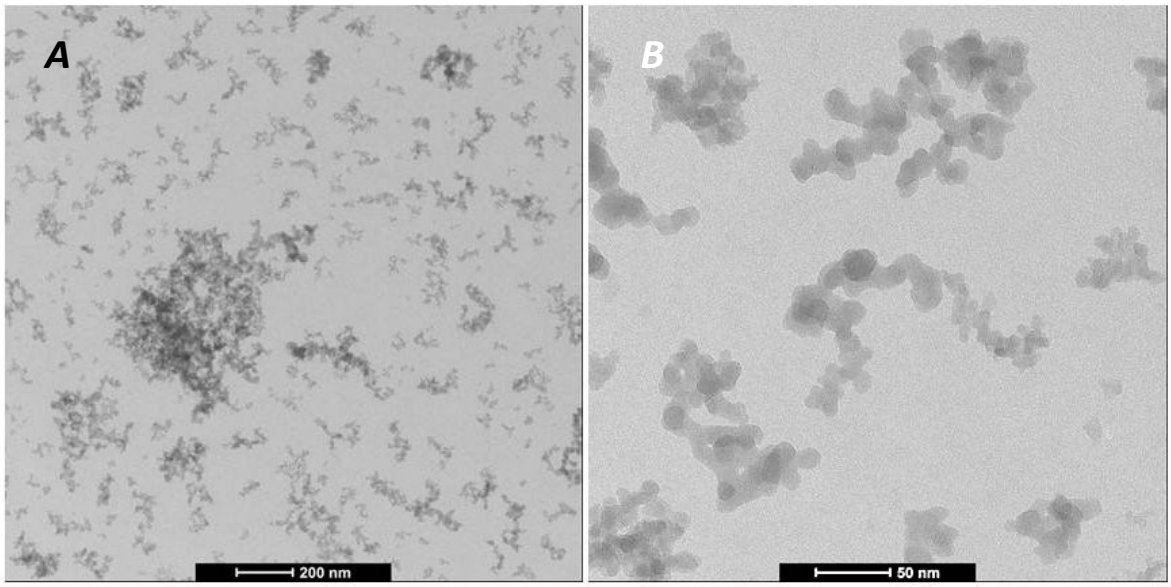

Figure 56. Micrograph of NM-202, illustrating the occurrence of agglomerates or aggregates (A) and the difference in primary particle size (B).

12.5.2. Quantitative analysis of sample NM-202

The semi-automatic detection and measurement of NM-202, based on mass thickness contrast, included 10 micrographs, in which 3484 particles were detected; the method is described earlier. The descriptive statistics are summarized in Table 37.

Table 37. Descriptive statistics for NM-202 (based on 3284 particles).

Column	Mean	Std Dev	Std Err	Max	Min	Median	25%	75%
Diameter Mean (nm)	68.60	70.43	1.19	1031.87	9.03	44.32	26.08	83.07
Diameter Max (nm)	77.13	79.72	1.35	1200.26	9.46	49.94	29.06	93.99
Diameter Min (nm)	49.45	48.67	0.83	631.23	5.52	32.50	19.09	59.96
ECD (nm)	46.36	40.10	0.68	552.57	8.29	33.11	20.36	57.33
Feret Mean (nm)	64.22	64.42	1.09	912.89	9.05	41.88	24.81	77.98
Feret Max (nm)	77.26	79.73	1.35	1200.30	9.77	49.92	29.25	93.98
Feret Min (nm)	47.31	45.88	0.78	555.97	6.04	31.49	18.53	57.77
Central Distance Mean (nm)	24.68	23.15	0.39	340.54	3.94	16.94	10.37	30.24
Central Distance Max (nm)	41.47	43.40	0.74	661.24	4.73	26.54	15.36	50.38
Central Distance Min (nm)	6.45	5.92	0.10	55.15	0.03	4.94	2.85	7.97
Radius of Inner Circle (nm)	10.68	5.63	0.10	43.97	2.69	9.27	6.28	13.46
Next Neighbour Distance (nm)	72.58	32.18	0.55	278.75	12.84	67.28	49.43	91.24
Perimeter (nm)	352.93	590.58	10.01	15015.98	27.32	159.76	84.61	359.63
Area (nm^2)	2950.26	7085.86	120.05	239806.43	54.03	861.08	325.61	2581.09
Convex Area (nm^2)	5183.82	14496.49	245.60	475501.93	56.89	1138.56	400.75	3861.53
Convex Perimeter (nm)	210.05	213.55	3.62	3034.31	27.54	136.28	79.66	255.41
Rectangle Mean (nm^2)	8036.58	23254.98	393.98	782285.74	80.65	1723.00	601.70	5953.72
Rectangle Max (nm^2)	8955.29	26258.01	444.86	879729.87	83.82	1899.88	663.75	6529.02

Rectangle Min (nm²)	6857.69	19556.31	331.32	666566.74	70.43	1505.31	533.31	5190.77
Aspect Ratio	1.60	0.37	0.01	3.41	1.05	1.53	1.32	1.79
Convexity	0.74	0.13	0.01	0.98	0.33	0.75	0.65	0.85
Elongation	1.81	0.55	0.01	4.92	1.01	1.68	1.40	2.08
Shape Factor	0.43	0.24	0.01	1.00	0.01	0.41	0.24	0.62
Sphericity	0.39	0.20	0.01	0.98	0.04	0.35	0.23	0.51

The average value (Mean), the standard deviation (Std Dev), the standard error on the mean (Std Err), and the smallest (Min) and largest (Max) observation, are presented. However, since for all measured parameters, the Kolmogorov-Smirnov and the Shapiro-Wilk probabilities are smaller than 0.001 (not shown), none of these parameters can be assumed to be normally distributed. Hence, non-parametric estimates of these parameters describe the sample better. These include the median and the 25 and 75 percentiles.

The amount of particles smaller than 100 nm is 80.4%. Table 38 summarizes the number of particles smaller than 100 nm, 50 nm and 10 nm. Furthermore, the sphericity of the particles is larger than 0.33 for 54.1% of the particles. According to Krumbein and Sloss (1963), a value larger than 0.33 corresponds with medium sphericity and a value larger than 0.67 corresponds with high sphericity. In Figure 57 it can be observed that 62.0% of the particles have a shape factor smaller than 0.5.

Table 38. Number (expressed in %) of NM-202 particles smaller than 100 nm, 50 nm and 10 nm.

	< 100 nm (%)	< 50 nm (%)	< 10 nm (%)
NM-202	80.4	55.0	0.9

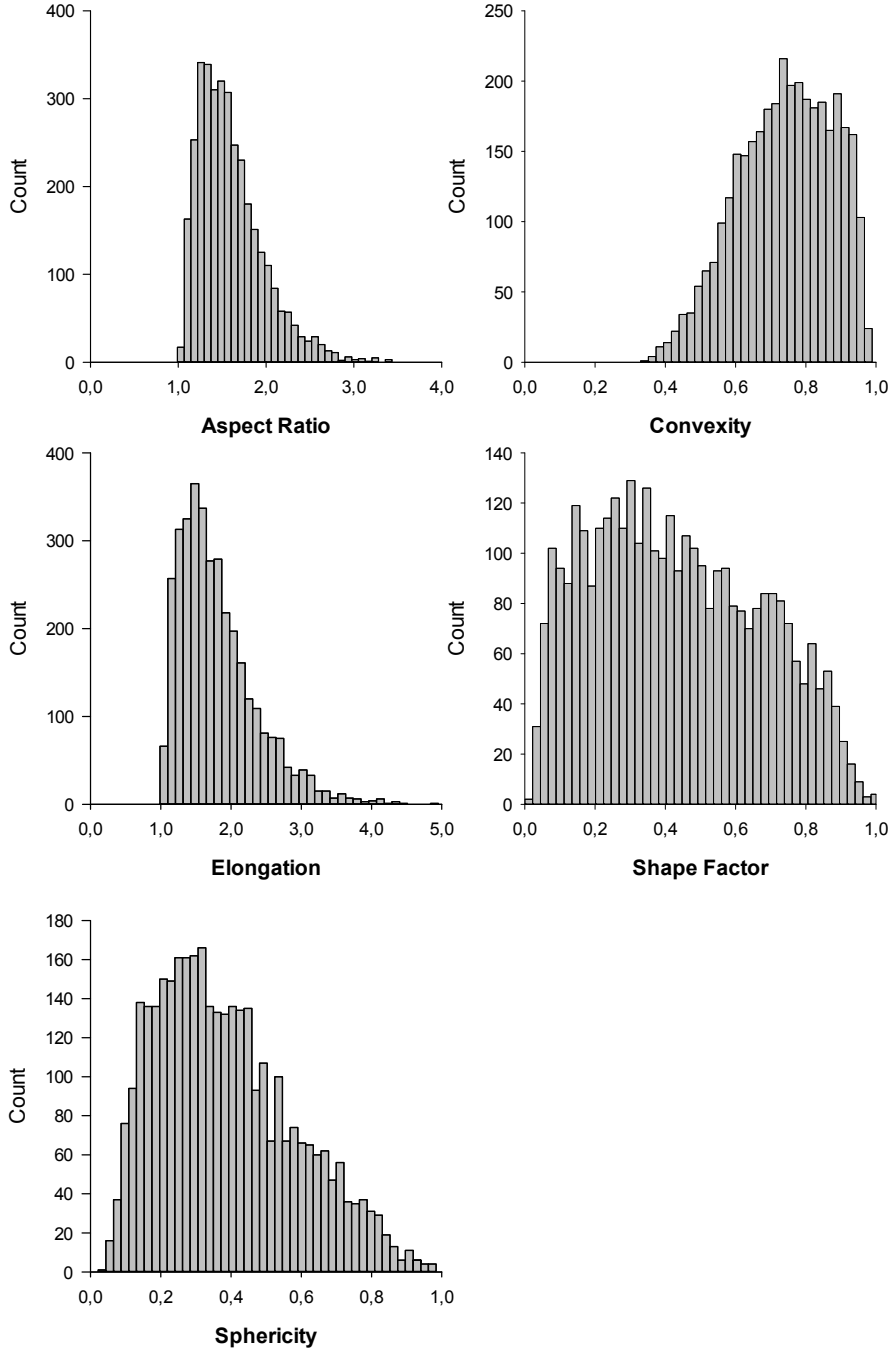

Figure 57. Histograms showing the number-based 'Shape' distributions of NM-202.

12.6. Results for NM-203

12.6.1. Qualitative analysis of NM-203

NM-203 dispersed into double distilled water consists mainly agglomerates of aggregates and of aggregates, as illustrated by Figure 58A. Single particles are only very rarely observed. In general, the particles are evenly distributed over the grid surface. The primary particles of the nanomaterial are heterogeneous in size, as illustrated by Figure 58. Primary particle sizes ranging from 5 to 30 nm are measured on the TEM images. The aggregates have a size ranging from 10 up to 600 nm. The general morphology of the primary subunits of the NM is equi-axed and rounded, or slightly elongated. Their suggested 3D structure is spherical or ellipsoidal. The aggregates and agglomerates tend to be more or less equi-axed, possibly due to steric preference, or have a more dendritic structure.

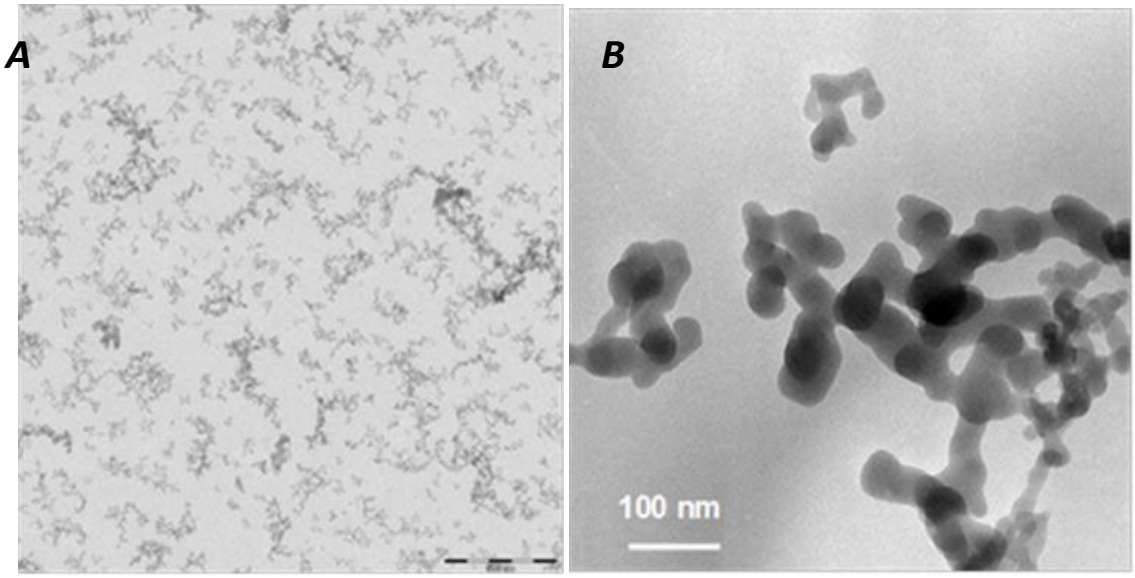

Figure 58. NM-203: A) Representative TEM micrograph of well-dispersed sample taken for quantitative TEM-analysis; scale bar is 500nm. B) TEM micrograph showing the complex open network structure in the silicon dioxide aggregates; scale bar is 100nm.

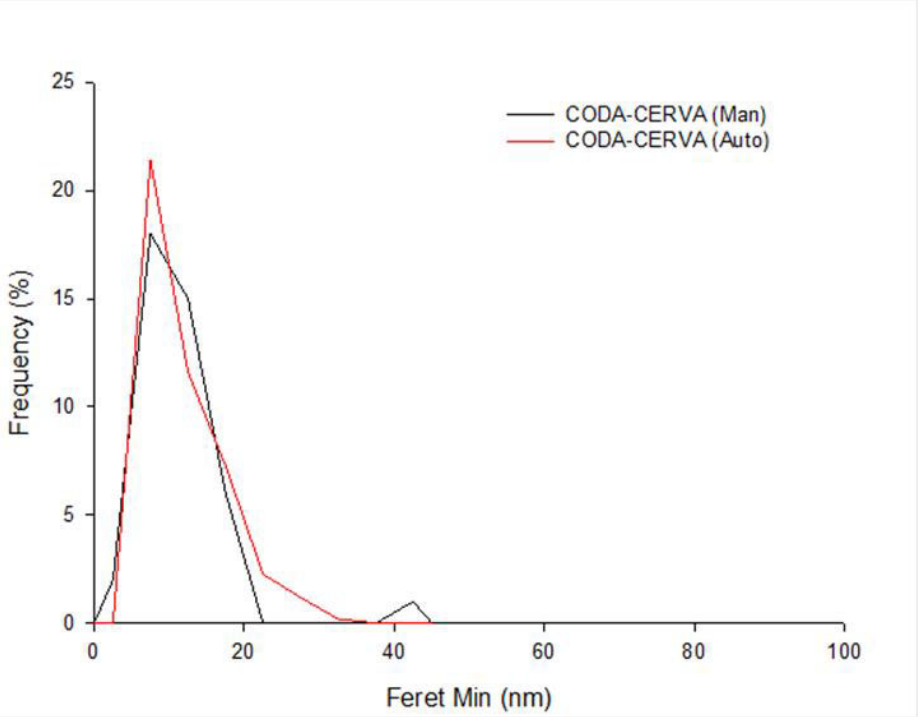

Figure 59. Qualitative TEM image analysis of NM-203 illustrating the primary particle Feret Min size distribution as a function of the frequency. The manual (CODA-CERVA (Man)) and semi-automatic measurements (CODA-CERVA (Auto)) are given.

12.6.2. Quantitative analysis of sample of NM-203

NM-203 contains small ellipsoidal primary particles with an aspect ratio of 1.4 – 1.5 and a size of 10-11 nm, depending on the used methodology. All analysed primary particles were smaller than 100 nm (Table 39). The Feret Min (Figure 59), Feret Mean, Feret Max and Aspect Ratio of these particles were lognormal distributed for manual measurements but not for semi-automatic measurements. No significant ($p < 0.05$) differences were found between manual and semi-automatic measurements.

Table 39. Primary particle, Feret Min, Feret Max, Feret Mean, percentage of particles with a Feret Min lower than 100 nm and Aspect ratio of NM-203.

Laboratory	Feret Min ± SD (nm)	Feret max ± SD (nm)	Feret mean ± SD (nm)	< 100 nm	Aspect ratio	n
CODA-CERVA (Man)	10,4 ± 1,5 [a]	16,3 ± 1,5 [a]	13,5 ± 1,5 [a]	100 %	1,5 ± 1,4 [a]	44
CODA-CERVA (Auto)	10,8 ± 1,5 [a]	15,6 ± 1,5 [a]	13,5 ± 1,5 [a]	100 %	1,4 ± 1,2 [a]	448

* Geometric mean ± the geometric standard deviation (SD) [15]

[a, b] Different letters indicate significantly different mean values by Kruskal-Wallis One Way Analysis of Variance on Ranks ($p < 0,05$)

The semi-automatic detection and measurement of NM-203, based on mass thickness contrast, included 10 micrographs, in which 3213 particles were detected; the method is

described earlier and Table 40 gives the descriptive statistics. The average value (Mean), the standard deviation (Std Dev), the standard error on the mean (Std Err), and the smallest (Min) and largest (Max) observation, are presented. However, since for all measured parameters, the Kolmogorov-Smirnov and the Shapiro-Wilk probabilities are smaller than 0.001 (not shown), none of these parameters can be assumed to be normally distributed. Hence, non-parametric estimates of these parameters describe the sample better. These include the median and the 25 and 75 percentiles.

The amount of particles smaller than 100 nm is 77.5%. Table 41 summarizes the number of particles smaller than 100nm, 50nm and 10nm. Furthermore, the sphericity of the particles is larger than 0.33 for 49.1% of the particles. According to Krumbein and Sloss (1963), a value larger than 0.33 corresponds with medium sphericity and a value larger than 0.67 corresponds with high sphericity. By comparing the shape factor of the specimens in Figure 60, it can be observed that 72.6% of the particles have a shape factor smaller than 0.5.

Table 40. Descriptive statistics for NM-203 (based on 3213 particles).

Column	Mean	Std Dev	Std Err	Max	Min	Median	25%	75%
Diameter Mean (nm)	73.61	66.04	1.17	704.18	8.77	51.78	30.18	92.57
Diameter Max (nm)	82.90	74.79	1.32	814.33	9.29	57.96	33.94	104.55
Diameter Min (nm)	52.28	45.46	0.80	384.44	5.35	37.55	21.93	66.94
ECD (nm)	48.25	36.73	0.65	300.14	8.27	36.63	23.05	61.47
Feret Mean (nm)	68.64	60.27	1.06	589.75	8.88	48.72	28.82	86.78
Feret Max (nm)	83.03	74.80	1.32	814.28	9.74	58.14	34.12	104.69
Feret Min (nm)	50.00	43.02	0.76	369.45	5.75	35.99	21.26	64.27
Central Distance Mean (nm)	26.10	21.55	0.38	219.61	3.89	19.15	11.75	32.93
Central Distance Max (nm)	44.68	40.74	0.72	421.81	4.68	31.45	17.96	56.06
Central Distance Min (nm)	6.25	5.76	0.10	64.07	0.05	4.76	2.47	8.21
Radius of Inner Circle (nm)	10.53	5.15	0.09	45.16	2.09	9.27	6.88	12.86
Next Neighbour Distance (nm)	76.98	32.35	0.57	230.40	12.91	72.20	53.92	95.86
Perimeter (nm)	386.49	515.23	9.09	5825.08	26.76	198.36	100.84	450.02
Area (nm^2)	2887.29	5149.95	90.86	70753.02	53.67	1053.76	417.12	2967.98
Convex Area (nm^2)	5197.13	11036.72	194.71	177816.27	56.89	1518.92	540.93	4816.17
Convex Perimeter (nm)	224.77	199.77	3.52	1958.56	26.55	158.33	92.69	284.45
Rectangle Mean (nm^2)	8096.06	17677.23	311.86	316758.35	78.46	2324.58	803.69	7340.19
Rectangle Max (nm^2)	9033.75	20189.26	356.18	384567.87	85.70	2574.55	887.38	8192.07
Rectangle Min (nm^2)	6911.42	14735.72	259.97	239648.27	69.77	2012.18	710.59	6264.29
Aspect Ratio	1.64	0.39	0.01	3.56	1.04	1.56	1.35	1.84
Convexity	0.70	0.14	0.00	0.98	0.29	0.70	0.60	0.81
Elongation	1.88	0.59	0.01	5.17	1.00	1.75	1.43	2.18
Shape Factor	0.37	0.22	0.00	0.96	0.02	0.33	0.18	0.52
Sphericity	0.36	0.19	0.00	1.00	0.04	0.33	0.21	0.49

Table 41. Number (expressed in %) of NM-203 particles smaller than 100 nm, 50 nm and 10 nm.

	< 100 nm (%)	< 50 nm (%)	< 10 nm (%)
NM-203	77.5	48.4	0.3

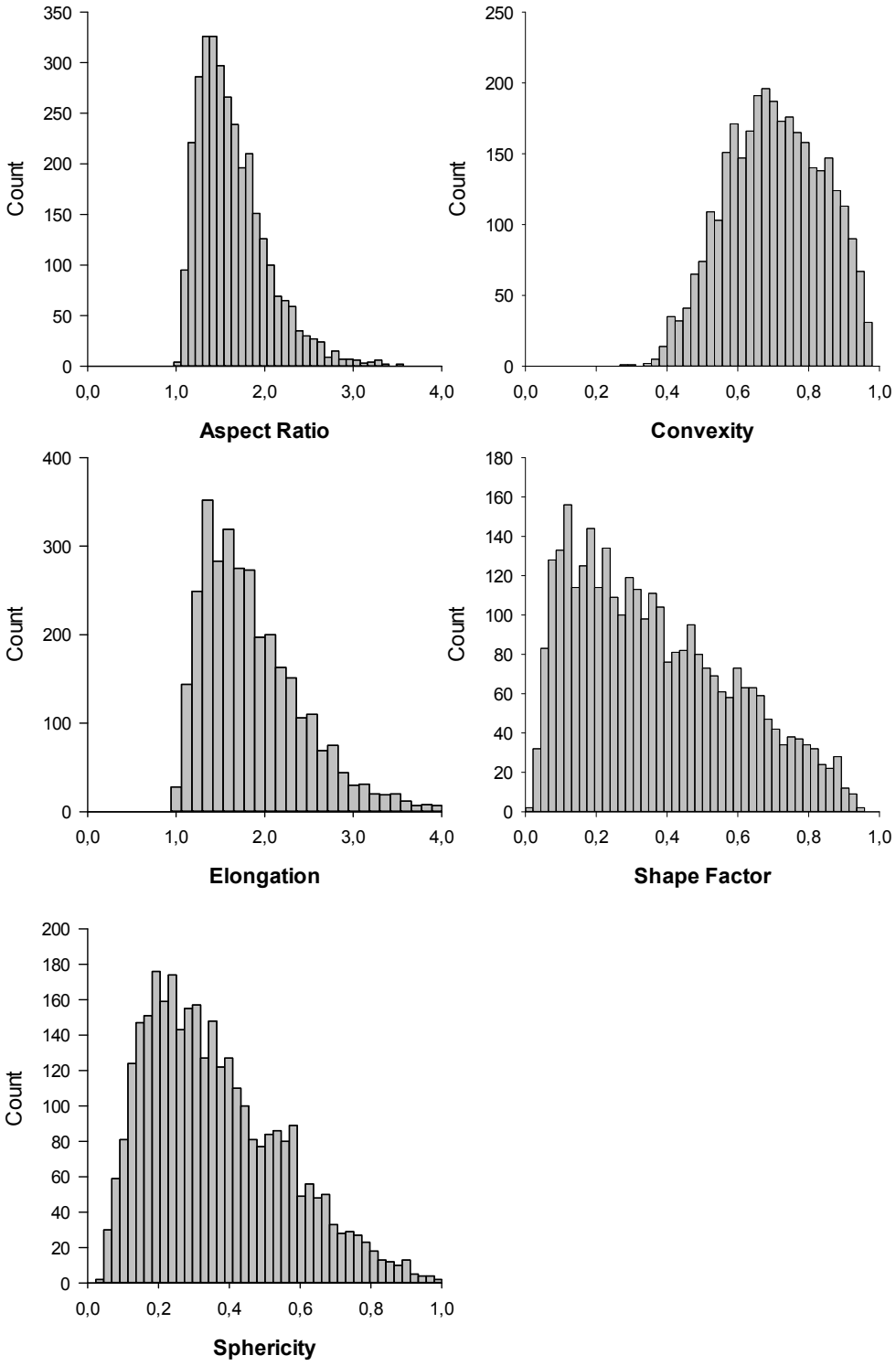

Figure 60. Histograms showing the number-based 'Shape' distributions of NM-203.

12.7. Results for NM-204

12.7.1. Qualitative analysis of NM-204

NM-204 dispersed into double distilled water, consists of individual particles, aggregates and agglomerates of aggregates. In general, these particles are evenly distributed over the grid surface. As illustrated by Figure 61A the specimen consists mainly of aggregates, and only a few Individual particles are detected. In addition, the existence of larger agglomerates of aggregates is very rarely detected.

The primary particles of the nanomaterial are homogenenous in size. The selected micrograph in Figure 61B shows an image of the NM-204 at higher magnification. Primary particle sizes of about 10-20 nm are measured on the TEM images.

The aggregates have a size ranging from 15 nm to 650 nm. The general morphology of the primary subunits of the NM is equi-axed and rounded, or slightly elongated. Their suggested 3D structure is spherical or ellipsoidal. The aggregates and agglomerates tend to be more or less equi-axed, possibly due to steric preference, but also dendritic outliers are often observed.

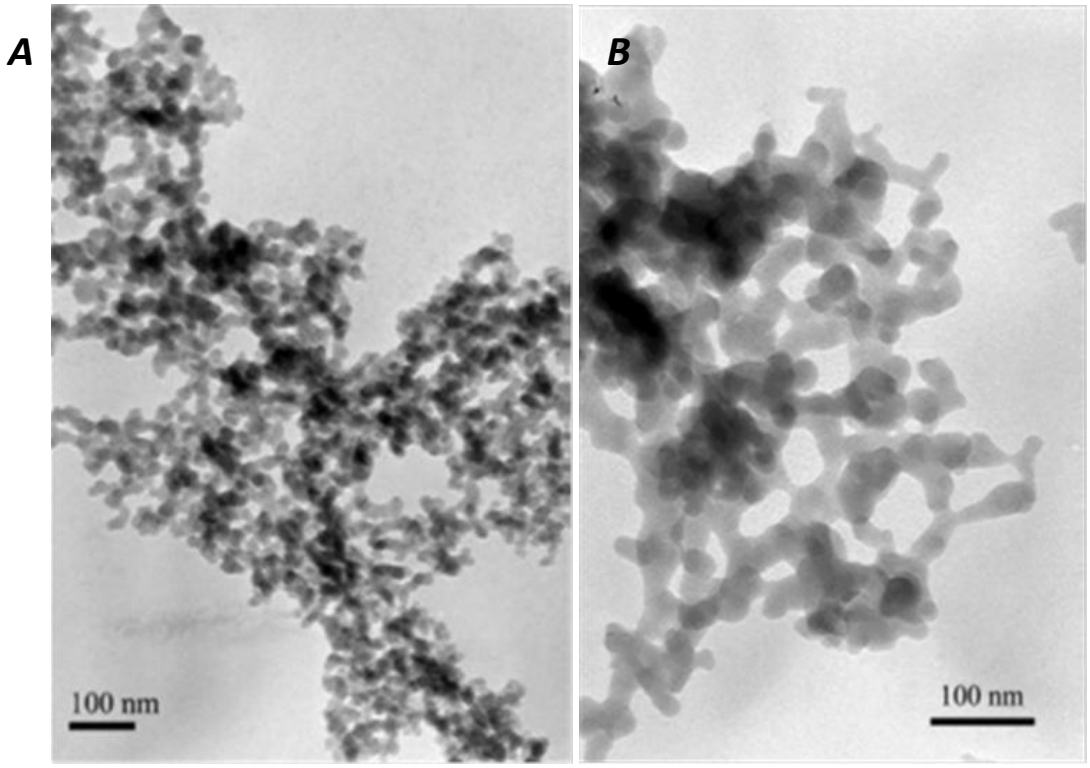

Figure 61. A) Representative TEM micrograph of typical NM-204 aggregate; B) TEM micrograph showing the complex open structure of NM-204.

12.7.2. Quantitative analysis of sample NM-204

The semi-automatic detection and measurement of NM-204, based on mass thickness contrast, included 10 micrographs, in which 1466 particles were detected; the method is described earlier. The descriptive statistics are summarized in Table 42, presenting the average value (Mean), the standard deviation (Std Dev), the standard error on the mean (Std Err), and the smallest (Min) and largest (Max) observation. The Kolmogorov-Smirnov and the Shapiro-Wilk probabilities are smaller than 0.001 (not shown) for all measured parameters, meaning that the parameters cannot be assumed to be normally distributed, and non-parametric estimates of the parameters describe the sample better. These include the median and the 25 and 75 percentiles.

Furthermore, the sphericity of the particles is larger than 0.33 for 59.9% of the particles. According to Krumbein and Sloss (1963), a value larger than 0.33 corresponds with medium sphericity and a value larger than 0.67 corresponds with high sphericity.

Table 42. Descriptive statistics for NM-204 (based on 1466 particles).

Column	Mean	Std Dev	Std Err	Max	Min	Median	25%	75%
Diameter Mean (nm)	88.19	75.48	1.97	926.48	9.19	66.66	39.19	110.76
Diameter Max (nm)	98.83	84.59	2.21	1013.37	10.45	74.28	43.91	124.16
Diameter Min (nm)	65.11	56.57	1.48	784.99	4.79	48.44	28.59	81.49
ECD (nm)	64.27	50.37	1.32	682.09	8.29	50.27	32.33	80.85
Feret Mean (nm)	83.17	70.69	1.85	897.44	9.28	62.43	37.48	104.46
Feret Max (nm)	98.98	84.61	2.21	1013.24	10.35	74.41	44.13	124.15
Feret Min (nm)	62.76	54.40	1.42	770.25	5.93	46.88	27.26	79.87
Central Distance Mean (nm)	33.17	26.57	0.69	342.87	3.98	25.43	16.29	41.38
Central Distance Max (nm)	52.89	45.84	1.20	557.63	5.19	39.59	23.03	66.83
Central Distance Min (nm)	10.98	10.74	0.28	169.04	0.03	8.37	5.26	12.61
Radius of Inner Circle (nm)	15.94	8.05	0.21	72.68	2.69	14.36	11.07	18.84
Next Neighbour Distance (nm)	116.49	51.28	1.34	597.37	25.45	108.43	79.69	141.91
Perimeter (nm)	411.22	636.11	16.61	15365.08	28.48	227.14	123.43	463.62
Area (nm²)	5235.48	13257.92	346.27	365401.21	54.03	1984.44	820.83	5134.27
Convex Area (nm²)	7757.88	21049.81	549.77	580301.29	60.83	2542.80	940.69	6975.94
Convex Perimeter (nm)	272.85	234.47	6.12	2993.43	28.39	204.26	121.49	342.64
Rectangle Mean (nm²)	11657.26	30409.40	794.22	800904.92	85.64	3819.71	1379.27	10641.11
Rectangle Max (nm²)	12842.63	33307.28	869.91	864589.72	87.65	4159.87	1477.95	11816.23
Rectangle Min (nm²)	10181.44	27338.01	714.00	747618.37	78.34	3355.93	1212.24	9165.36
Aspect Ratio	1.56	0.33	0.01	3.00	1.05	1.50	1.31	1.72
Convexity	0.79	0.11	0.00	0.98	0.44	0.79	0.71	0.88
Elongation	1.73	0.48	0.01	4.17	1.03	1.63	1.38	1.97
Shape Factor	0.48	0.23	0.01	0.96	0.02	0.46	0.29	0.67
Sphericity	0.40	0.19	0.00	0.95	0.06	0.38	0.26	0.53

By comparing the shape factor of these specimens in Figure 62, it can be observed that 55.8% of the particles have a shape factor smaller than 0.5.

Table 43. Number (expressed in %) of NM-204 particles smaller than 100 nm, 50 nm and 10 nm.

	< 100 nm (%)	< 50 nm (%)	< 10 nm (%)
NM-204	71.2	36.4	0.3

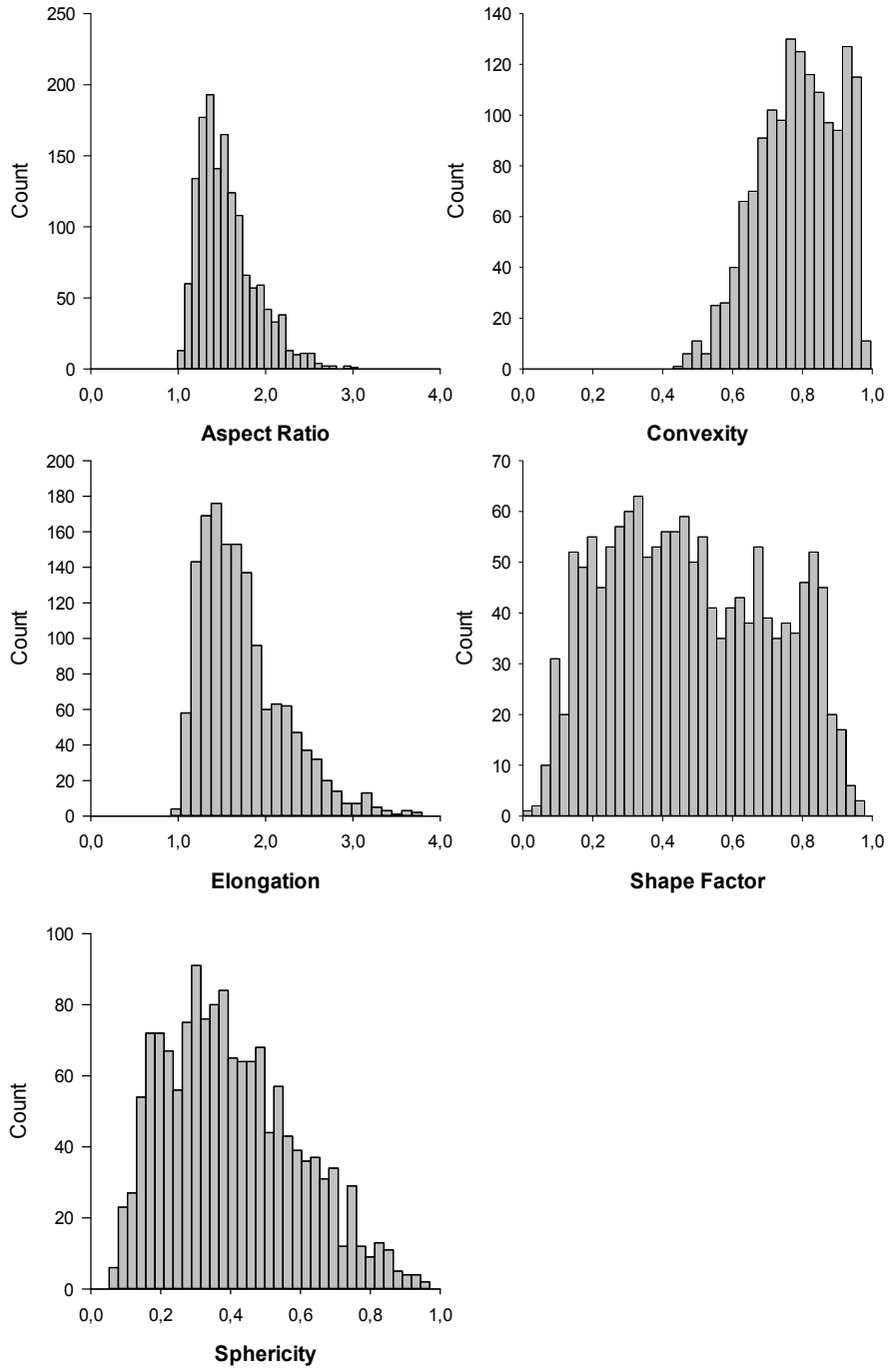

Figure 62. Histograms showing the number-based 'Shape' distributions of NM-204.

The amount of particles smaller than 100 nm is 71.2% for NM-204. Table 43 summarizes the number of particles smaller than 100nm, 50nm and 10nm.

12.8. Primary particle measurements for the SAS NM

The primary particle sizes for the SAS NMs as resulting from the analyses performed by different institutions are given in Table 44. As seen from the data, some variations are observed.

Table 44. Primary particle size of the SAS NMs analysed by different institutes.

Material	ECD (nm) ± SD ($N^{\$}$); CODA-CERVA	ECD (nm) ± SD ($N^{\$}$); INRS	Diameter (nm); IMC-BAS
NM-200	14 ± 7 (1876)	23 ± 8 (100)	18
NM-201	17 ± 8 (1726)	19 ± 4 (100)	18
NM-202	15 ± 7 (401)	18 ± 3 (105)	20
NM-203	13 ± 6 (448)	16 ± 3 (105)	45
NM-204	10 – 15*		19

* Manual measurement. $^{\$}$ is the number of particles used for the assessment

12.9. TEM: Quantitative analysis of aggregated and agglomerated NMs

12.9.1. Classes of parameters by principle component analysis

Principal component analysis (PCA) of the dataset consisting of the twenty-three parameters obtained by quantitative TEM analysis, see Table 31, allowed classifying the parameters in three uncorrelated principle components (PC) explaining approximately 93% of the variability in the samples see Table 45. Examination of the component pattern profiles of this PCA, see Figure 63, shows that PC 1 basically consists of direct size measures and 2D size measurements. The direct size measures include the Feret max, Feret mean, Feret min, central distance max, central distance mean, diameter max, diameter mean and diameter min. The 2D size measurements include area, convex area, rectangle max, rectangle mean, rectangle min, ECD, convex perimeter and perimeter. PC 2 is importantly determined by the aspect ratio, elongation and sphericity, which reflect the shape of the particles. PC 3 is mostly determined by the convexity and shape factor, parameters reflecting the surface topology of the particles.

One representative parameter was selected from each of the classifications based on PCA to describe and compare the SAS NMs. The mean diameter was chosen as a size measure,

the sphericity was chosen as a shape measure and the shape factor was chosen as a measurand for surface topology.

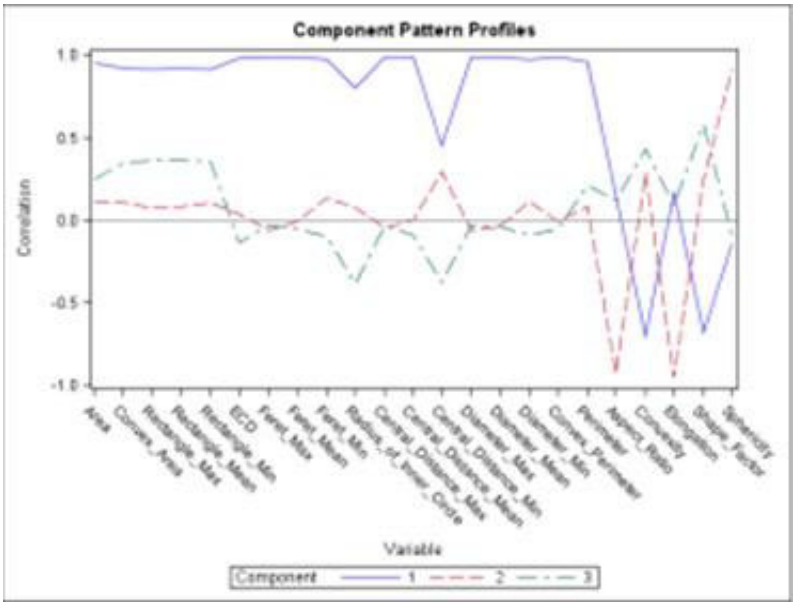

Figure 63 Representative examples of component pattern profiles of quantitative TEM analysis of NM-202 (A) categorized into three principle components (blue line, red dashed line and green dashed line).

Table 45. Representation of the proportion of the eigenvalues of the correlation matrix in each principle component.

	PC1 [x]	PC2 [x]	PC3 [x]	Cumulative [x]
NM-200	73,4 ± 0,7 %	13,5 ± 0,1 %	6,6 ± 0,5 %	93,6 ± 0,3 %
NM-201	73,7 ± 0,4 %	13,7 ± 0,1 %	6,8 ± 0,1 %	94,2 ± 0,5 %
NM-202	73,5 ± 0,3 %	12,9 ± 0,2 %	6,5 ± 0,2 %	92,9 ± 0,2 %
NM-203	74,1 ± 0,4 %	12,9 ± 0,1 %	6,4 ± 0,1 %	93,0 ± 0,3 %

[x] Mean values of medians ± SD are represented for 3 independent analyses

12.9.2. Characterisation based on quantitative measures

Table 32, Table 35, Table 37, Table 40 and Table 42 give the descriptive statistics of the measured 23 parameters of the SAS NMS based on TEM micrographs.

TEM analysis showed that the general morphology of the silicon dioxide nanomaterials was quite comparable, see Table 47. All samples consist of highly porous nanostructured

materials, which may be considered aggregates of primary silicon dioxide particles. However, when looking into the detail, the thermal SAS (NM-202 and NM-203) may have a more complex and branched structure than the precipitated SAS (NM-200 and NM-201). These differences were very clear in the quantitative morphology analysis, which showed much higher angularity of spheroidal silicon dioxide aggregates in NM-202 and NM-203 compared to NM-200 and NM-201. Based on the number-based distributions of the mean diameter (see Figure 64A) and on the comparison of the median mean diameters of the aggregates and agglomerates, the precipitated silicon dioxide (NM-200 and NM-201) cannot be unambiguously distinguished from the thermal silicon dioxide (NM-202 and NM-203). The number-based size distribution of NM-200 is different from those of NM-202 and NM-203, and the NM-200 median mean diameter is significantly different from those of NM-202 and NM-203; however the number-based size distribution of NM-201 is comparable to the curves of NM-202 and NM-203, and the NM-201 median mean diameter is not significantly different from those of NM-202 and NM-203.

Figure 64B and Figure 64C show that the number-based sphericity and shape factor distributions of the precipitated NM-200 and NM-201 are very similar, as are the corresponding distributions of the thermal NM-202 and NM-203. However, the curves of the precipitated and thermal NM tend to diverge. Table 46 confirms that the median sphericities and shape factors between the thermal and precipitated NM are significantly different, whereas within the precipitated and thermal NM no significant differences were found.

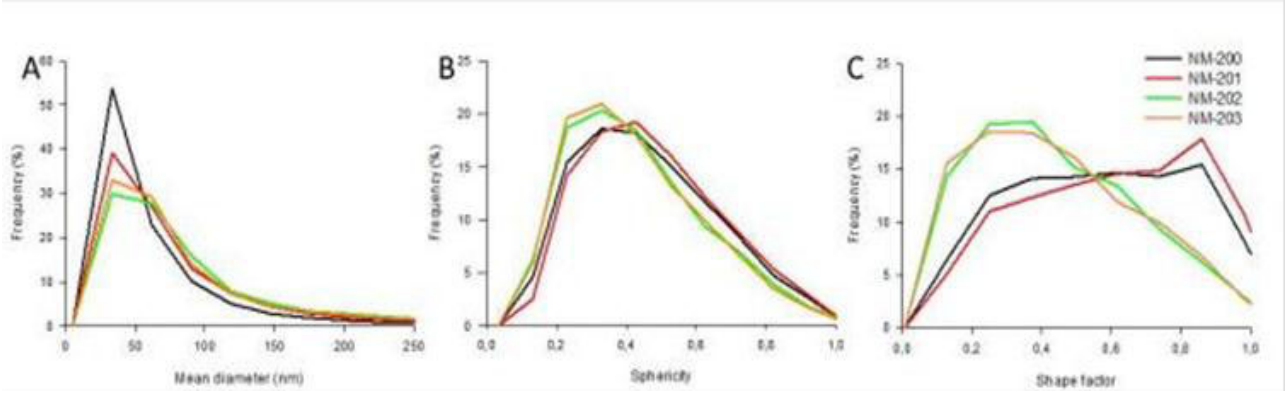

Figure 64. Number-based distributions of the mean diameter (A), sphericity (B) and shape factor (C) of agglomerates and aggregates of SAS NMs. The frequency of the agglomerates / aggregates of SAS NM are represented as a function of mean diameter, sphericity and shape factor.

Table 46. Characterization of aggregated SiO_2 (NM-200 to NM-203) by quantitative TEM.

	Mean diameter (nm)[x]	Sphericity [x]	Shape factor [x]	% < 100 nm [x,y]
NM-200	31 ± 3 [a]	0,39 ± 0,01 [a]	0,51 ± 0,02 [a]	94 ± 1 [a]
NM-201	43 ± 4 [a,b]	0,4 ± 0,01 [a]	0,56 ± 0,05 [a]	91 ± 2 [a,b]
NM-202	53 ± 9 [b]	0,36 ± 0,01 [b]	0,35 ± 0,01 [b]	87 ± 2 [b]
NM-203	48 ± 4 [b]	0,35 ± 0,02 [b]	0,35 ± 0,02 [b]	88 ± 2 [b]

[x] Mean values of medians ± SD are represented for 3 independent analyses
[y] The percentage of particles with a minimal Feret diameter smaller than 100 nm is represented.
[a, b] Different letters indicate significantly different mean values by One Way Analysis of Variance and pairwise compared with Tukey test.

Table 47. Summarizing table describing the morphology of aggregates/agglomerates of NM-200 to NM-203 according to Krumbein and Schloss (1963).

Material	Sphericity	Shape factor	General morphology
NM-200	Low to medium sphericity	Sub-angular to rounded	Sub-rounded, low to medium sphericity
NM-201	Medium sphericity	Rounded to well-rounded	Rounded, medium sphericity
NM-202	Low sphericity	Very angular to sub-angular	Angular, low sphericity
NM-203	Low sphericity	Very angular to sub-angular	Angular, low sphericity

12.10. Transmission Electron Tomography

The method to characterize SAS NMs by electron tomography (ET) is described in detail in van Doren et al. (2011). Briefly, particle coated grids, mounted in a tomography holder were analyzed using a Tecnai™ G2 Spirit microscope (FEI, Eindhoven, The Netherlands) with a BioTWIN lens configuration and a LaB6-filament operating at an acceleration voltage of 120 kV. Series of micrographs (tilt-series) were recorded semi-automatically over a tilt range of at least 65°, or highest angle possible, at intervals of 1 degree. Shift and focus changes were corrected at every interval. Electron micrographs were acquired with a 4*4 k Eagle CCD-camera (FEI) at magnifications of 26,500 times. The tilt series were aligned by iterative rounds of cross correlation. Reconstructions were made using the Simultaneous Iterative Reconstruction Technique (SIRT) algorithm. For visualization in 3D, isosurface rendering and pseudo-coloring was used to visualize the NM surface. This allowed measurement of the surface area of the reconstructed 3D objects and of their enclosed volume.

12.10.1. Three dimensional visualisation and measurement of SAS NMs using ET

In preliminary experiments (not shown) spherical and branched SAS were visualized in three dimensions. From the isosurface based volume rendering of the ET reconstructions, the total surface area and volume of their composing gold particles could be measured, so that VSSA could be calculated. A high correlation between the calculated and measured volume and surface area was found.

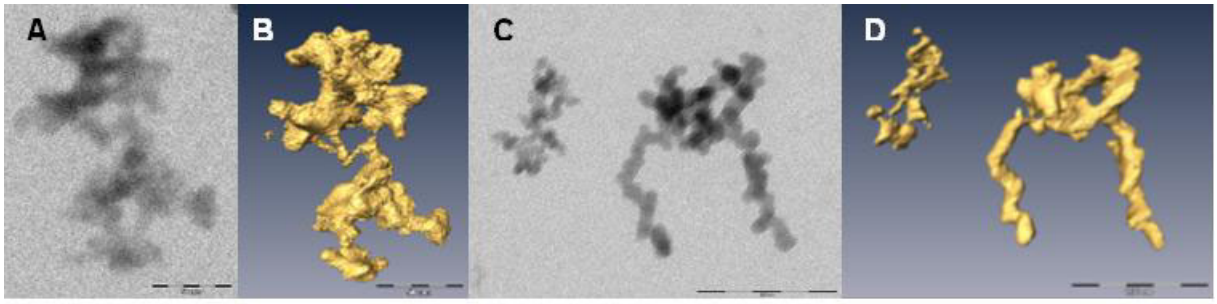

Figure 65. Electron tomographic analyses of NM-200 and NM-203. The micrographs, taken at 0°, show one (Figure 65A) and two aggregates (Figure 65C) consisting of multiple primary subunits of NM-200 and NM-203, respectively. Figure 65B and Figure 65D show the corresponding ET reconstructions. Bars: 200 nm.

It is not evident to visualise the structure of the materials NM-200 and NM-203 appropriately by conventional BF TEM (Figure 65A and Figure 65C). Their relatively low molar mass results in a low contrast, while their complex morphology results in blurring of ultrastructural details due to superposition of projected features. Electron tomographic reconstruction in three dimensions circumvents these difficulties. Figure 65B and Figure 65D, illustrate that both the precipitated NM-200 and the pyrogenic NM-203 consist of aggregates of very complex morphology composed of a variable number of interconnected primary subunits. Although the site where an aggregate interacts with the grid can be found in the 3D reconstruction as a relatively flat surface, structures of primary subunits remain extended in the z-direction, resulting in similar dimensions along the three axes. This suggests a limited flexibility of the material.

Table 48. Mean volume specific surface area of NM-200 and NM-203 based on electron tomographic reconstructions

Type of nanomaterial	n	Volume specific surface area (VSSA) (m^2/cm^3)[a]
Precipitated Silicon Dioxide (NM-200)	5	342 ± 36
Pyrogenic Silicon Dioxide (NM-203)	5	219 ± 23

[a] *Values represent mean VSSA ± standard error of mean*

Measurements in 3D showed that individual aggregates for both NM-200 and NM-203 are composed of similarly sized primary subunits. The size of the subunits of the aggregates of

NM-200 is relatively constant: they measure approximately 20 nm in diameter. The size of the subunits of different aggregates of NM-203 is variable: e.g. the subunits of the left aggregate shown in Figure 65D measure 8 to 12 nm in diameter, while the subunits of the right aggregate measure approximately 20 nm in diameter. In any of the tilt series of NM-200 and NM-203, diffraction contrast was observed, confirming their amorphous structure. The surface area and volume of NM-200 and NM-203 were measured for five ET reconstructions and the VSSA was calculated (Table 48). For both materials, the mean VSSA was significantly different ($P<0.05$) from 60 m^2/cm^3.

12.10.2. Combination of the results of quantitative AFM and TEM analyses

TEM analysis was done as previously described and the sample was prepared according to the NANOGENOTOX dispersion protocol. For Atomic Force Microscopy (AFM) measurements at CEA, stock suspensions were prepared differently by 20 min sonication at 40 % amplitude of suspensions of 6.82 g/L NM in Millipore water for SAS NMs. For the SAS NMs, mica sheets were preliminary coated with Alcian blue before dipping in suspension (25-fold diluted, 2 to 5 min).

Results of quantitative AFM and TEM analyses are highly complementary. Quantitative TEM allows determining the minimal and maximal size of aggregates in the X-Y plane, measured as Feret Min and Feret Max. AFM estimates the third dimension of a NM, measured as Z-max (Figure 66D, Figure 67D, Figure 68D and Figure 69D), giving indications on a statistical ”third dimension”, so that combining the two techniques allows to better characterize the aggregates in 3D. A direct link can be made between the Feret Min and Feret Max on a per particle level. Their ratio, as the aspect ratio, is a measure for aggregate morphology.

Figure 66C, Figure 67C, Table 49 and Table 50 show that the aggregates of the precipitated NM-200 and NM-201 have similar height (Z-max) and width (Feret min) and are 50 % longer than wide (Figure 66B and Figure 67B). Combining the AFM result (Figure 66A and Figure 67A) with primary particle dimensions (Table 34) confirms the observation (Figure 66C and Figure 67C) that most of these aggregates are approximately 1.5 primary particles thick.

Figure 68C and Figure 69C show that the aggregates of the pyrogenic NM-202 and NM-203 are fractal-like while the primary particle size between aggregates is highly variable. Combining the AFM results (Figure 68A and Figure 69A, Table 51 and Table 52) with primary particle dimensions (Table 39) confirms the observation (Figure 68C and Figure 69C) that most of these aggregates are approximately 1.5 primary particles thick. The

aggregates of NM-202 are as high (Z-max) and longer (Feret max) than wide (Feret min). The aggregates of NM-203 are wider (Feret min) than high (Z-max) and longer (Feret max) than wide (Feret min) (Table 37, Table 40, Figure 68B and Figure 69B).

For SAS NMs, the suspension preparation protocols for AFM and TEM were very similar (the only difference is 16 min sonication Vs. 20 min sonication which should not be of great influence since NM are already well dispersed after 16 min sonication), and nanoparticles interact with a surface coated with alcian blue in both cases. This explains the very good correspondence between AFM and TEM values, and validate the comparison.

Particles which are unequiaxial have a preferential orientation versus the carrier grid, as was observed for NM-200 and NM-203 by electron tomography.

Table 49. Characterization of SAS NM-200 in three dimensions.

Laboratory	Technique	Parameter	Median (N*)
CEA	AFM	Z max	21,9 (1382)
CODA-CERVA	TEM	Feret Min	21,9 (8005)
CODA-CERVA	TEM	Feret Max	34,5 (8005)

*N is the number of particles measured

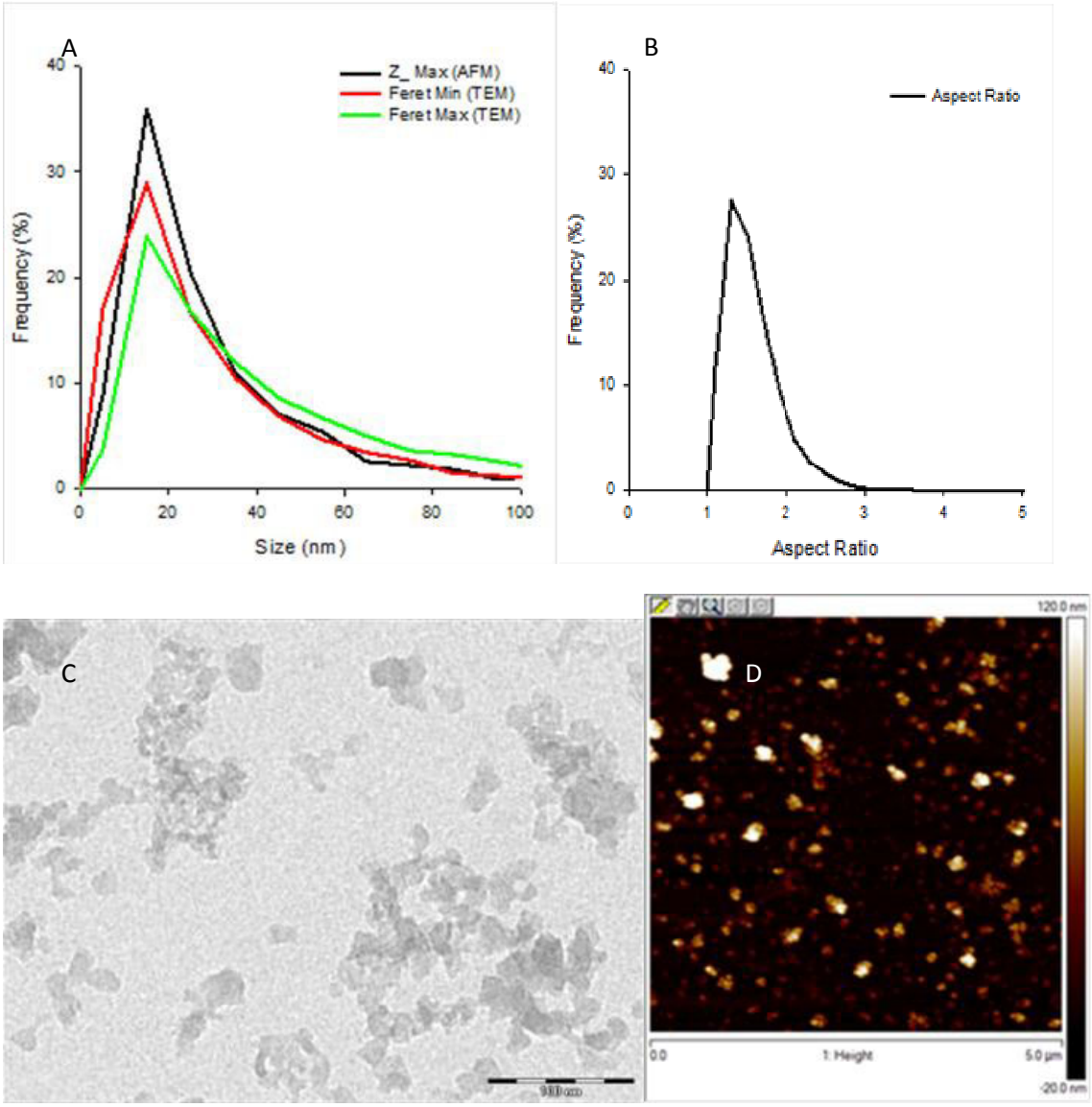

Figure 66. Characterization of the aggregates of NM-200 in three-dimensions by combination of TEM and AFM. A) Number based size distributions of Feret Min, Feret max and Z_max. B) Number based distribution of the aspect ratio. C) Representative TEM and D) AFM micrographs visualizing the morphology of the aggregates.

Table 50. Characterization of NM-201 in three dimensions.

Laboratory	Technique	Parameter	Median (N*)
CEA	AFM	Z max	33,5 (1275)
CODA-CERVA	TEM	Feret Min	25,4 (5311)
CODA-CERVA	TEM	Feret Max	38,5 (5311)

*N is the number of particles measured

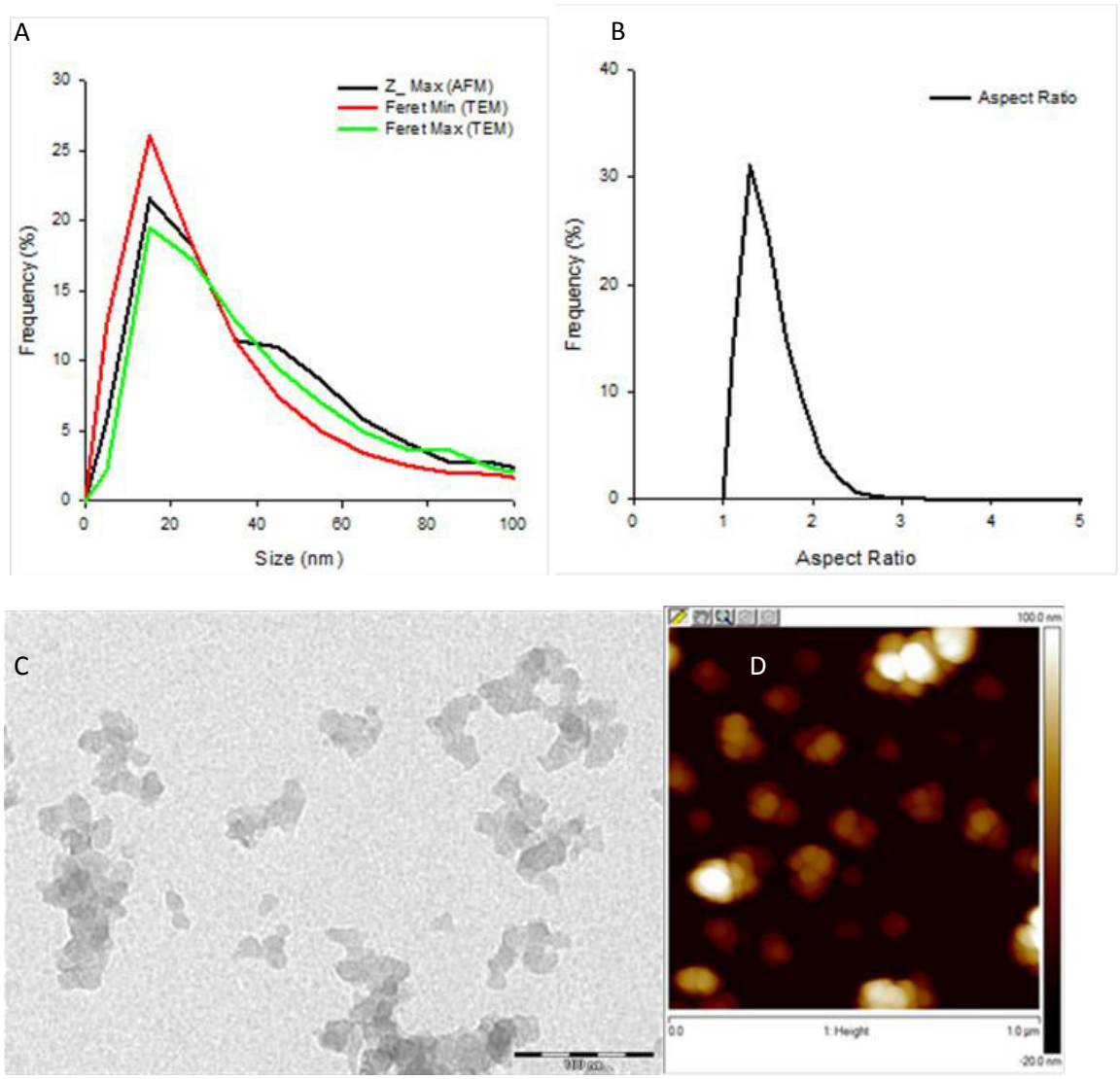

Figure 67. Characterization of the aggregates of NM-201 in three-dimensions by a combination of TEM and AFM. A) Number based size distributions of Feret Min, Feret max and Z_max. B) Number based distribution of the aspect ratio. C) Representative TEM and D) AFM micrographs visualizing the morphology of the aggregates.

Table 51. Characterization of SAS NM-202 in three dimensions.

Laboratory	Technique	Parameter	Median (N*)
CEA	AFM	Z max	38,2 (1103)
CODA-CERVA	TEM	Feret Min	37,2 (4248)
CODA-CERVA	TEM	Feret Max	58,4 (4248)

*N is the number of particles measured

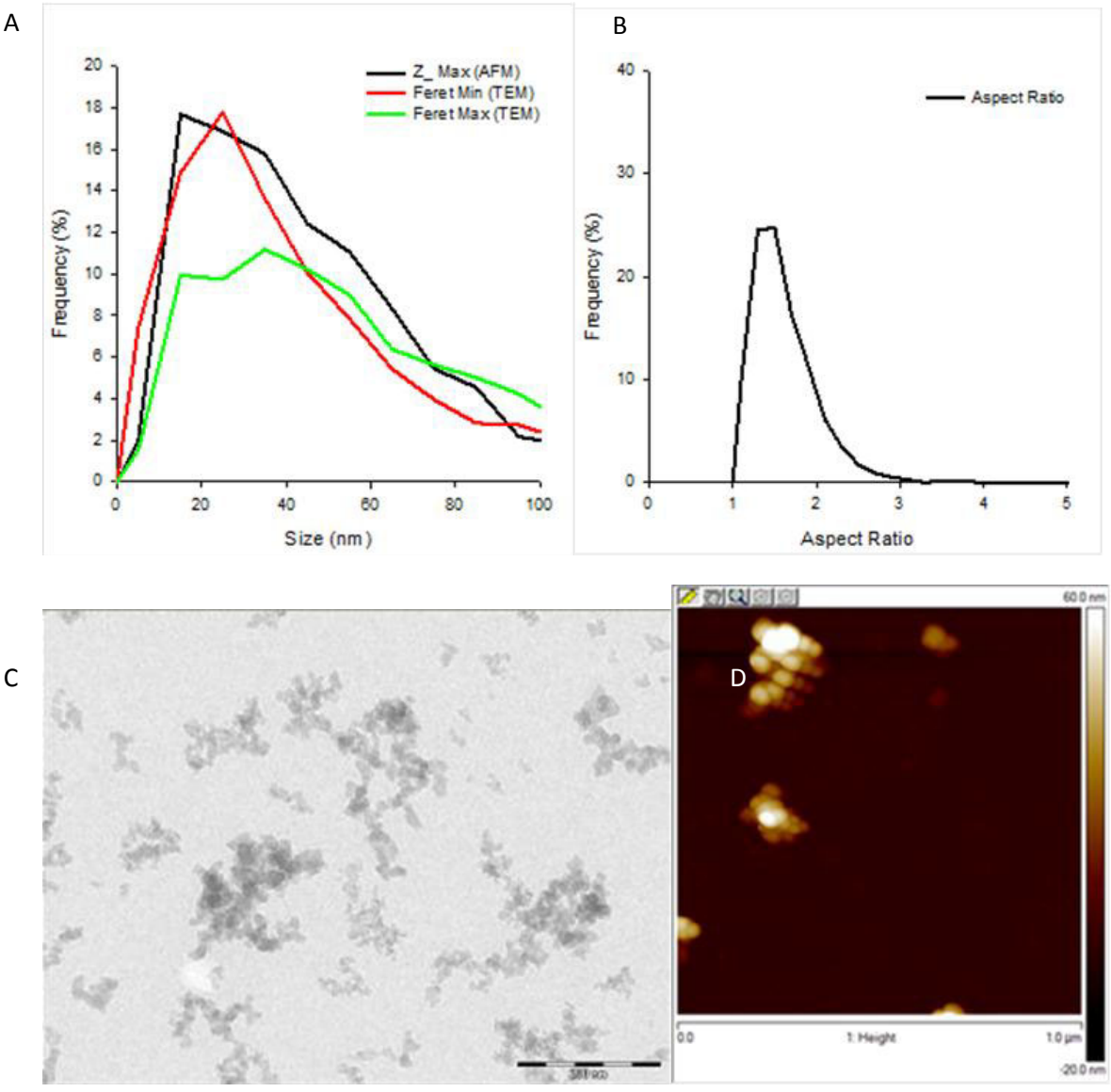

Figure 68. Characterization of the aggregates of NM-202 in three-dimensions by a combination of TEM and AFM. A) Number based size distributions of Feret Min, Feret max and Z_max. B) Number based distribution of the aspect ratio. C) Representative TEM and D) AFM micrographs visualizing the morphology of the aggregates.

Table 52. Characterization of NM-203 in three dimensions.

Laboratory	Technique	Parameter	Median (N*)
CEA	AFM	Z max	24,2 (593)
CODA-CERVA	TEM	Feret Min	33,5 (4889)
CODA-CERVA	TEM	Feret Max	53,2 (4889)

*N is the number of particles measured

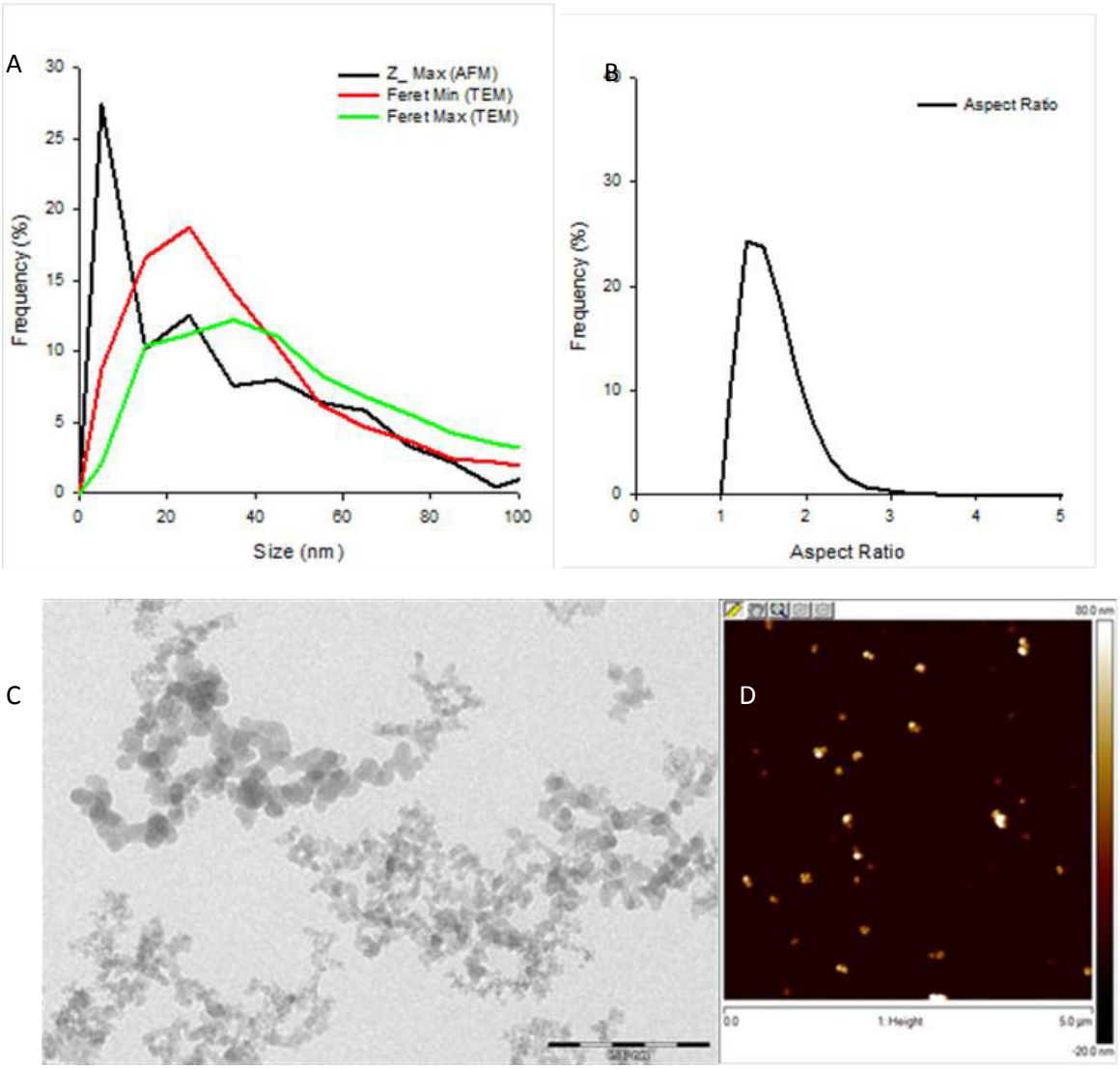

Figure 69. Characterization of the aggregates of NM-203 in three-dimensions by a combination of TEM and AFM. A) Number based size distributions of Feret Min, Feret max and Z_max. B) Number based distribution of the aspect ratio. C) Representative TEM and D) AFM micrographs visualizing the morphology of the aggregates.

12.11. Discussion of TEM results

12.11.1. Sample preparation

To characterize a NM sonication is recommended as a standard preparatory step to disperse large aggregates and agglomerates (OECD, 2012). The sonication energy required to prepare a SAS NM sample in its most disperse state was determined as suggested by Powers et al. (2006). This allowed optimization of the attachment of the NM to the grid.

To examine the intrinsic properties of SAS NM, samples were diluted in double distilled water as this medium allowed maximal adsorption of the fraction of nano-sized particles to the grid surface. Moderate salt concentrations as well as proteins resulted in a reduced number of particles per surface area, possibly indicating precipitation of NM-200. This is in agreement with the findings of Jiang et al. (2009).

12.11.2. Qualitative and quantitative analyses based on TEM micrographs

The general guidelines for image acquisition and analysis proposed by Pyrz and Buttrey (2008) were adapted to the analysis of NMs. TEM imaging conditions were chosen such that a compromise is reached that combines a sufficient number of particles per image with a resolution providing an acceptable number of pixels per image, while the useful range contained the large majority of the particles.

The pre-processing of images remains limited, only N x N averaging was essential, and is appropriate for all examined SAS NMs. This avoids loss of information and addition of artifacts associated with significant processing reducing errors into the analysis. Automation allows measuring multiple and arithmetically complex parameters, described in Table 31, on a high number of detected particles. It reduces operator-induced bias and assures a statistically relevant number of measurements avoiding the tedious repetitive task of manual measurement. Primary particle measurements remained labour intensive and only 4 parameters could be measured.

Since this method contains no material specific steps, it can readily be adapted to characterize aggregates and agglomerates of a variety of NMs, provided that they can be coated quantitatively to the EM-grid and distinguished from the background. For most metal oxides and for metallic NMs, the latter poses no problem.

Access to multiple parameters allows selecting the optimal parameter in function of a specific material or purpose as exemplified hereafter. The mean diameter, and Feret mean (Riley et al., 2003, Podczeck and Mia, 1996) are the result of multiple diameters measured under different angles. Therefore, they can be used to estimate the size of particles with complex surface topology, like SAS, more precisely than simple parameters, such as Feret min, Feret max, diameter min and diameter max. The measurement of the equivalent circle diameter (ECD), calculated from the projected surface area, assumes a spheroidal particle morphology like most separation and light scattering based techniques. Hence, ECD suits comparison of results obtained by techniques such as disc centrifugation and dynamic light scattering. To define a material as a NM, the percentage of aggregates smaller than 100nm can be calculated from the number-based distribution of Feret min, an estimate for minimal size in one dimension. In the examined sonicated SAS, these percentages were much higher than 50% (Table 46), defining them as NM according to (EC, 2011). Since stricto senso not the aggregate size, but the size of the primary particles complying with this condition, the actual percentage can be assumed much higher (Table 34 and Table 39). The standard deviation of this measure ranging from 1 to 2% for SAS NMs suggests that this method can also be useful in specific cases where, warranted by concerns for environment, health, safety or competitiveness, the number size distribution of 50% may be replaced by a threshold between 1 and 50% (EC, 2011). Size measures like the aggregate projected area (Area) and the aggregated maximum projected length (Feret Max) are suitable to assess fractal like NM comprising precipitated and pyrogenic silicon dioxides NM (Boldridge, 2009; Bau et al. 2010). Combined with the size and overlap coefficient of primary particles, the fractal dimensions can be inferred from these specific aggregate size measures according to Brasil et al., 1999. These fractal dimensions are used to explain different phenomena in physics, chemistry, biology and medicine Nel et al., 2009.

Principle component analysis demonstrated that the measured twenty-three parameters could be subdivided objectively for all SAS NMs into three orthogonal classes representing size, shape and surface topology. Barrett (1980) proposed a fourth parameter for NM characterization, namely the surface texture. According to ISO (2008), this parameter could be estimated from fractal dimension of the particles.

The characterization of a NM by at least one parameter of each of the three classes based on PCA is in line with the guidelines in (SCENIHR, 2010; EFSA 2011; OECD, 2010) that parameters of these classes are essential for the characterization and identification of a NM, e.g. in the context of the risk assessment of the application of NMs in the food and feed chain. The findings of Chu et al. (2011) corroborate this, showing that the size, physical form

and morphology parameters determine the access of NM to human cells and cell organelles. In this context, the properties of individual particles measured in two dimensions can be more meaningful than one-dimensional parameters. Certain subpopulations cannot be distinguished based on one parameter but can be distinguished based on combinations of parameters for size, shape and surface topology, as described earlier by Barett (1980).

As illustrated for thermal and precipitated SAS NM, differences in the production processes of SAS can result in differences in polydispersity, sphericity and shape factor. Boldrige (2010) proposed that for pyrogenic silicon dioxide the temperature variations occurring near the flame on a microscopic scale result in a greater variability in primary particle size as opposed to precipitated silicon dioxide where the primary particle size is more homogeneous.

12.11.3. Transmission electron tomography

As a proof of principle, it was shown that application of conventional BF ET allows 3D visualization of SAS NM. The examined SAS NMs were shown to be amorphous and the dominant contrast mechanism is weak scattering depending on their mass thickness. The BF images of the tilt series are thus essentially projections on which tomographic reconstructions can be based (Friedrich et al., 2009).

For SAS NMs, BF ET allows measuring their surface features and VSSA. This approach can hence contribute to a method relevant for measurements for the second and third condition of the definition of a nanomaterial proposed by the EC (EC, 2011)]. Recent technical developments promise for the near future the possibility to analyse large numbers of particles (Lengyel et al., 2008) representative for the sample, a better reconstruction (Batenburg et al., 2009), less influence of missing wedge artifacts (Lengyel et al., 2008; Penczek et al., 1995; Mastronarde, 1997; Tong et al. 2006] such that the characterization of nanomaterials by transmission electron tomography can become more precise and less time-consuming.

13. Dustiness

Dustiness is defined as the propensity of a material to emit dust during agitation. A European standard (EN15051) has been established containing two methods (the rotating drum and continous drop methods). However, EN15051 is not fully suitable for nanomaterials, as also stated in EN 15051. Other procedures are therefore currently under investigation. In this study dustiness was tested using two different agitation methods: a downscaled EN15051 rotating drum (the small rotating drum (SD)) method and the Vortex shaker (VS) method.

It is important to note that dustiness is not an intrinsic physical or chemical defined property of a powder. Its level depends on e.g. characteristic properties of the powders and the activation energy in the simulated handling, and thus different values may be obtained by different test methods.

Among the reasons for EN 15051 not applying to nanomaterials are that it:

- uses relatively bulky experimental setups, which limit their use in collective protection equipment such as fume cupboards.

- requires a large amount of material, typically above 500 g.

- is associated with mass-based protocols that give no indication of:

    * the determinants of expected potential toxicity such as the number of particles, their size distribution, their shape.

    * the presence or absence of particles smaller than 100 nm, or submicron particles.

The SD method, is a miniaturized version of the EN15051 drum developed by NRCWE (Schneider and Jensen, 2008). Test comparisons of respirable dustiness have shown strong agreement between the SD and the EN15051 standard drum (Jensen et al., 2012).

The Vortex shaker method, or VS method, consists of a centrifuge tube continuously agitated by vibration in which the test powdered material is placed. Originally proposed by Baron et al. (2002), this method was also used later by Isamu et al. (2009). More recently, INRS has developed this approach, particularly in the context of a collaborative project within the network PEROSH (Witschger et al., 2011).

Among the useful features of the SD and the VS methods are that only little material (between less than 0.1 and 6 grams) is needed for a test compared to the traditional methods described in the EN15051 standard (several hundred grams). In addition, the smaller size equipment is easier to place in an approved fume cupboard or safety cabinet, greatly improving the safety of the experimenters.

The SD and VS methods' determination of dustiness in respirable size-fractions were combined with number concentration and size-distribution analysis of the dust particles for both SD and VS methods. In addition, as possible in the existing SD method protocol, the inhalable fraction was systematically measured. For few of the tests conducted with the VS method, electron microscopy (EM) observations were performed.

Finally, particle-size distributions data are reported from measurements using Electrical Low-Pressure Impactor (ELPI^{TM} Classic) for the VS method, and Fast Mobility Particle Sizer (FMPS) and Aerodynamic Particle Sizer (APS) for the SD method. This difference arose as the two institutions did not have the same equipment for testing the NM samples.

The objective of this study is to analyse the propensity of the SAS NMs to generate fine dust during simulated agitation of raw powder. The nanomaterials powders were compared with each other according to their index of dustiness. Two indexes have been defined, one based on the number of particles emitted, and the other according to the mass of particles emitted. In addition, we were able to compare the results between the two fundamentally different methods, SD and VS, since SAS NM powders were tested with both methods.

13.1. Experimental Setup and Results

13.1.1. Small rotating drum method

The small rotating drum, Figure 70 was designed by NRCWE as a downscaled version of the EN 15051 rotating drum while maintaining important test parameters. Reduction in size was made to reduce sample size (≤6g per run) and to improve safety in handling by enabling placement in a regular-size fume hood. The drum consists of a cylindrical part [internal diameter 16.3 cm, length 23.0 cm, volume 4.80 l] with a truncated cone at each end (half angle 45°, length 6.3 cm, volume of two cones 1.13 l). The total volume of the drum is 5.93 l. The drum was made of stainless steel and all inside surfaces were polished to 450 ± 50 gloss units to minimize surface adhesion and to facilitate cleaning. The drum was electrically grounded as prescribed by EN 15051. The drum contains three lifter vanes (2 x 22.5 cm). Experiments were conducted at 11 rpm to obtain the same number of powder parcels falling per minute as in the EN 15051 test (Schneider and Jensen, 2008). The 11 lpm inlet air to the drum was controlled at 50 % relative humidity (RH) and HEPA-filtered to ensure no particle background.

Figure 70. Photograph showing the high-gloss polished inside of the dustiness drum. Also note the three lifter vanes marked a, b, and c at each 120° in the drum.

In the applied set-up, respirable dust is collected by a GK2.69 respirable dust sampler at 4.2 lpm (BGI, UK) and dust particle size-distributions are measured using the Fast Mobility Particle Sizer (FMPS 3091, TSI), with a range of 5.6 to 560 nm and providing a size distribution expressed in electric mobility equivalent diameter, and the Aerodynamic Particle Sizer (APS 3321, TSI) with a range of 0.5 to 20 µm and providing a size distribution expressed as the equivalent aerodynamic diameter, see Figure 71. A GRIMM CPC may be connected for simultaneous number-concentration measurements, but not used in this study.

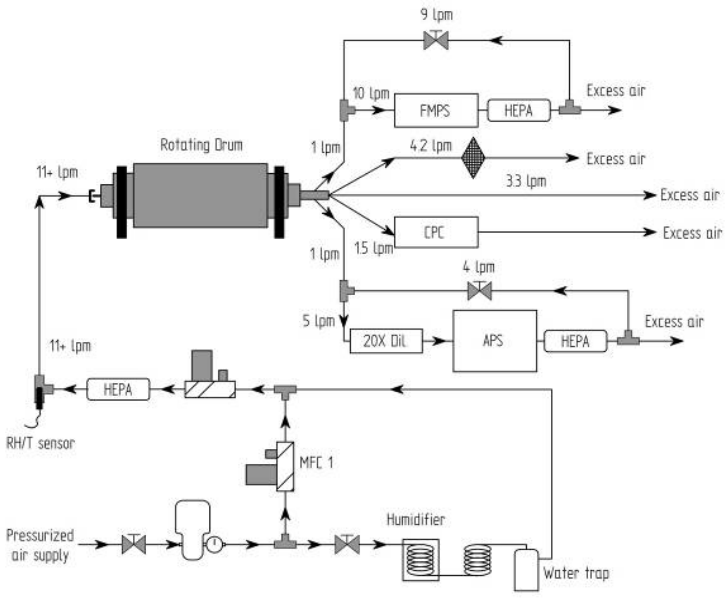

Figure 71. Small rotating drum setup at NRCWE in the standard set-up for sampling respirable dust simultaneously with online size distribution analyses by FMPS, APS and number concentration by CPC.

The dustiness test was conducted in triplicates for each NM after a so-called saturation run completed to coat all inner surfaces of the system with dust. The saturation test was

performed using 2 grams of powder and rotation for 60 s. Then the actual triplicate tests were completed using 6 grams of test material per run. After each run the drum was emptied by pouring out the residual powder and gently tapping the drum three times with a rubber hammer. When loading the powder was carefully placed centrally in the drum on the upwards moving side of a lifter vane placed vertical at bottom position. Then the drum was sealed, followed by 60 s of background measurements to ensure a particle free test atmosphere and perform zero-measurements for the online instruments. The experiment was then initiated by rotating the drum for 60 s during which particles were emitted and led through the airflow to the sampling train. After the drum was stopped, measurements and sampling was continued for additional 120 s to catch the remaining airborne particles in the dust cloud. Thus, the total time during for measurement is 180 s. The drum and sampling lines were thoroughly cleaned between each powder type using a HEPA-filter vacuum cleaner designed for asbestos cleaning and wet-wiping. Then the drum was left to air-dry before testing the next powder.

The mass of collected respirable dust was determined after conditioning the filters and controls in a weighing room (22°C; 50 %RH) using a Sartorius microbalance (Type R162 P; Sartorius GmbH, Göttingen, Germany). The mass is used to categorize the dustiness levels of the powders according to EN15051. Calculations of Dustiness Indexes, DI_{mass}, were done according to:

$$DI_{mass} = \frac{Q_{drum} \cdot m_{filter}}{Q_{cyclone} \cdot m_{drum}}$$

Q_{drum} and $Q_{cyclone}$ are the flows through the drum and cyclone respectively, m_{filter} is the blind-filter corrected filter mass in mg and m_{drum} is the powder mass loaded into the drum in kg.

In addition to the mass-based dustiness index, DI_{number}, an index for the total number of particles generated per mg of material during the 60 s of rotation and the following 120 s were calculated as:

$$DI_{Number} = \frac{Q_{drum}}{m_{drum}} \cdot \sum_{t=0}^{180s} N_t^{cpc}$$

where m_{drum} is the used mass of powder in mg and N_{cpc} is the CPC count in particles/cm^3.

Number size distributions were calculated as the summed up numbers over the 180 s as measured by FMPS and APS.

Table 53. Number of dust particles and mass-based dustiness indexes of SAS NMs. As explained in the text experimental data with the SD method are obtained over a test time of 180 s.

NM-20X	Test mass (g)	Dustiness index		
		Number (1/mg) **CPC**	**Inhalable**	**Mass** (mg/kg) **Respirable**
NM-200	4	6.16E+06	6459 (±273)	293 (±193)
NM-201	4	5.82E+06	6034 (±199)	218 (±24)
NM-202	4	4.13 E+06	4988 (±1866)	91 (±11)
NM-203	1.5	6.30E+06	5800 (±1488)	354 (±6)
NM-204	2	8.25E+06	24969 (±601)	1058 (-)

Figure 72 shows the particle number size distributions of aerosols generated during rotating drum dustiness testing of the SAS NMs. The SAS powders generate fine aerosol with an electrical mobility equivalent peak diameter typically between 200 and 300 nm. Larger µm-size-modes are present in all samples, but none of the coarse mode particle concentrations exceed the 200-300 nm mode-size particle concentrations. NM-203 produces the lowest number of particles, but also generates the finest dust particles measured by FMPS as seen by smallest peak sizes and a shoulder mode around 60 nm.

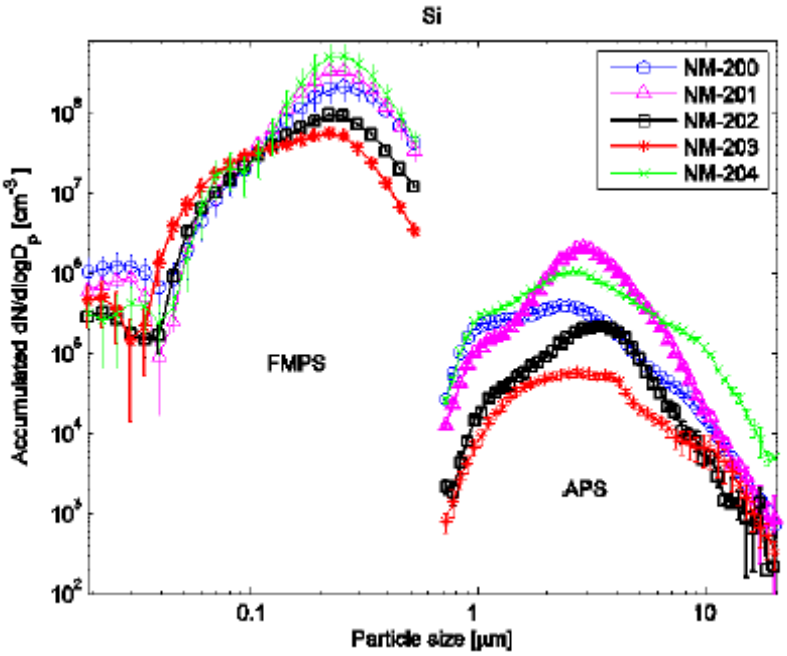

Figure 72. Particle number size distributions for SAS NM. All distributions are presented as given by the FMPS (electrical mobility equivalent diameter) and APS (aerodynamic equivalent diameter).

Figure 73 and Figure 74 show respectively the dustiness ranking of inhalable and respirable dust for SAS NMs. Compared to conventional mass-based dustiness indexing of the EN

15051 standard the SAS nanomaterials, the index are only categorized with high dustiness indices. However, there appears to be a larger variation in respirable dustiness ranking than for inhalable dust where NM-204 is observed to have very high dustiness levels.

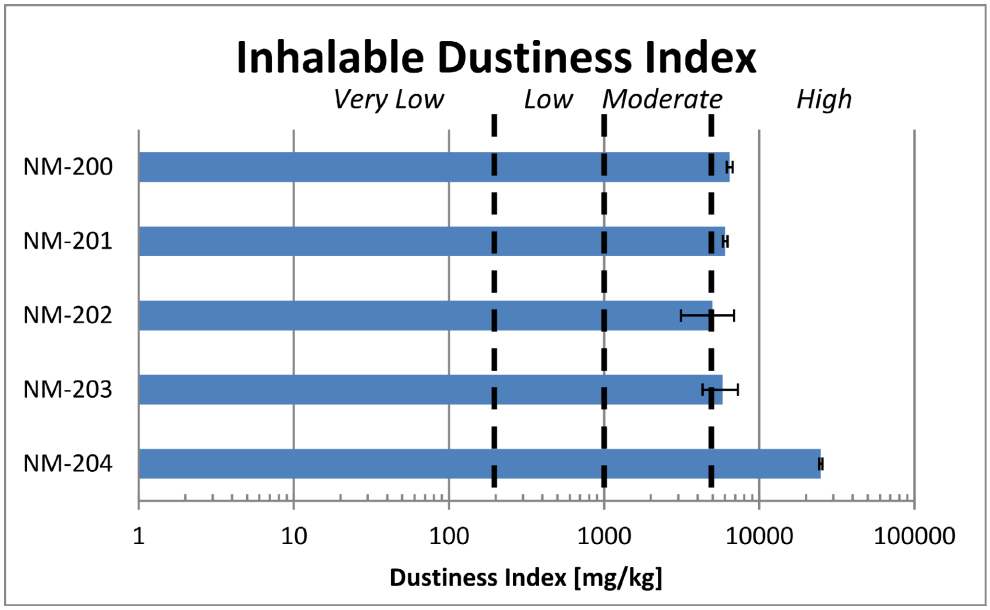

Figure 73. Dustiness ranking of <u>inhalable</u> dust for and SAS NMs as obtained with the small rotating drum method at NRCWE.

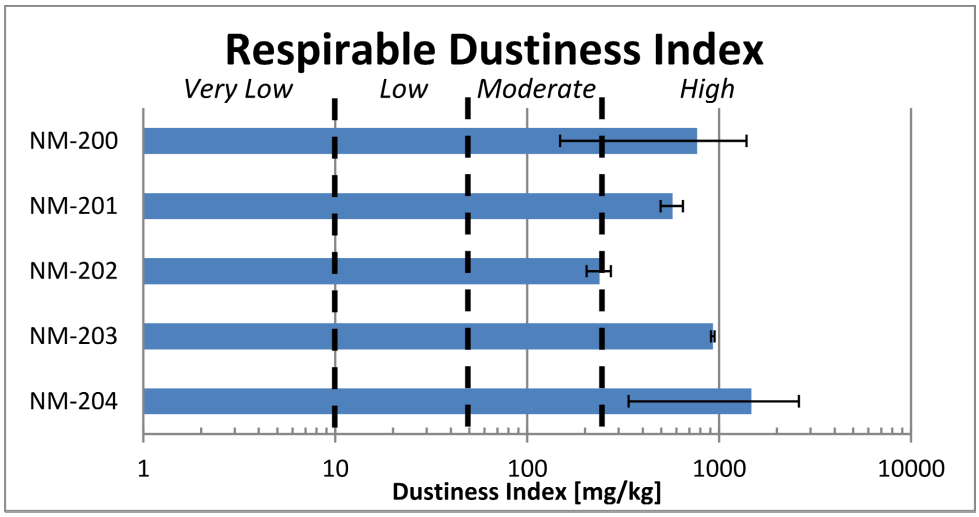

Figure 74. Dustiness ranking of <u>respirable</u> dust for SAS NMs as obtained with the small rotating drum method at NRCWE.

13.1.2. Vortex shaker method

The vortex shaker method consists of a centrifuge stainless tube agitated by a vortex in which the test powdered material is placed together with 100 µm diameter bronze beads. These are used to help the deagglomeration of powders. HEPA filtered air, controlled at 50%

RH, pass through the tube in order to transfer the released aerosol to the sampling and measurement section. The protocol developed for the experiments performed within this project at INRS used two different versions of the sampling and measurement section.

All tests conducted with VS method used approximately 0.5 ml powder, which was placed in the sample vial together with 5 g bronze beads (100 µm), used to agitate and de-agglomerate the powder. The sample is allowed conditioning in the 50% RH before the shaker for a powder agitation period of 3600 s (60 min).

The first version of the sampling and measurement was devoted for real-time measurement using ELPI^{TM} Classic (Electrical Low Pressure Impactor) (10 lpm, Dekati) for size distributions according to the equivalent aerodynamic diameter and Condensation Particle Counter (CPC. Model 3786 UWCPC, TSI) for number concentrations. This version was also devoted for collecting airborne particles for subsequent electron microscopy observations. Tests were completed in triplicates for each NM.

The CPC used was the Model 3785 Water-based CPC (TSI, USA). This CPC detects particles from 5 to >3000 nm. It provides a wide, dynamic, particle-concentration range, an essential characteristic for the tests considered. Featuring a single-particle-counting mode with continuous, live-time coincidence correction and a photometric mode, the CPC measures particle number concentrations at $<10^7$ particles/cm^3.

ELPI™ is an instrument to measure airborne particle size distribution and concentration in real-time. It operates in the size range of 7 nm – 10 µm in its standard configuration. Because of its wide particle size range and rapid response (< 5 s), the ELPI™ has been considered an ideal measurement instrument for the analysis of the unstable concentrations and size distributions, or the evolution of size distributions that could be observed in these tests. To prevent particle bounce and charge transfer during the tests, all collection substrates (PVC GELMAN GLA-5000 5µm / 25 mm) were greased.

The results of the tests performed with this first version of the VS method leads to the determination of:

- Dustiness indices expressed as the total number of particles emitted (based on data from CPC).

- Particle size-distribution of the aerosol (based on data from ELPITM Classic in its standard configuration).

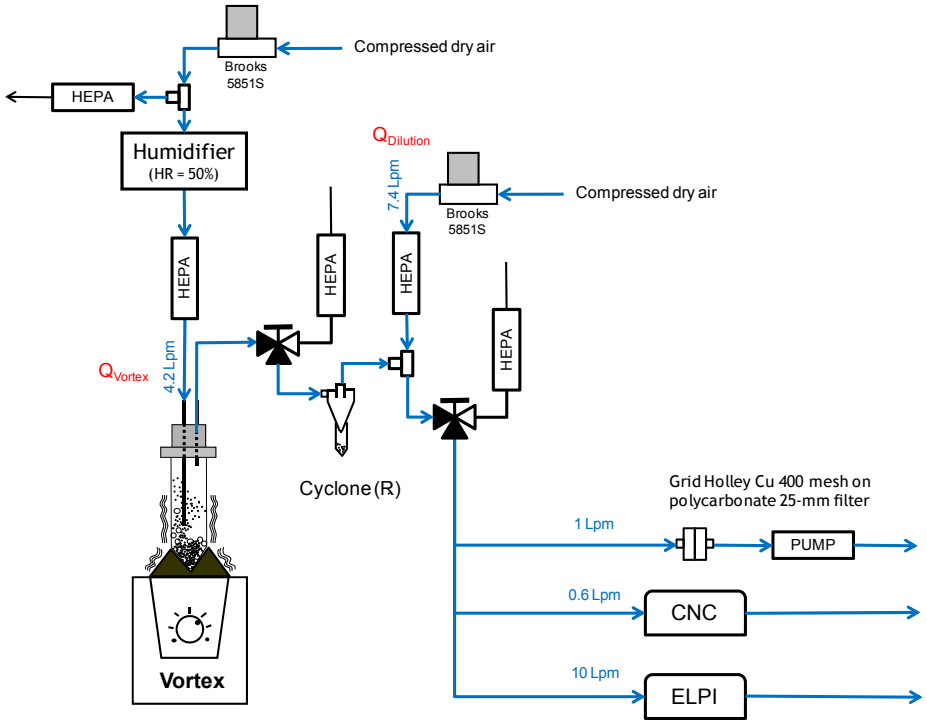

Figure 75. Experimental set-up of the vortex shaker method for measuring number concentrations and particle-size distributions, and for collecting airborne particles for subsequent EM observations.

In the ELPI the measured current signals are converted to (aerodynamic) size distribution using particle size dependent relations describing the properties of the charger, the impactor stages, and the effective density of the particles. The particle effective density provides a relationship between mobility and aerodynamics sizes. Effective density is a parameter which is complex to measure (Olferta et al., 2007), and values for samples used in the project are not available in the literature. Therefore, the following assumption has been made for the data from the ELPI: spherical particle with a density equal to the density of the condensed phase of the material constituting the NM. Densities used were 2.2 g/cm^3 for all SAS NMs based on Kim et al. (2009). If this assumption is questionable, there is no robust method that can be applied to polydispersed aerosols over a wide size range, such as those used here. However, to assess the effect of this parameter on the results, the number size distributions were also calculated for a density of 1 g/cm^3.

$S_{Vortex}^{Number(CNC)}$ is the total number of generated particles from the Vortex tube and it was calculated as:

$$S_{Vortex}^{Number(CNC)} = [Q_{Vortex} + Q_{Dilution}] \cdot \Delta t \cdot \sum_{i=0}^{\frac{T}{\Delta t}} C_{CNC}(t_0 + i \cdot \Delta t)$$

Where:

- T is the time over which the total number of particles is calculated. This time is between 5 and 3600s, the latter is the test duration in the original protocol of the VS method.

- Δt is the step time of the CNC (for all tests it was set as 5 s)
- $C_{CNC}(t_o+i\cdot\Delta t)$ is the number concentration measured during the time interval
- Q_{Vortex} is the total air flow rate passing through the vortex tube (4.2 lpm)
- $Q_{Dilution}$ is the flow rate of dilution air (7.4 lpm).

$DI_{Number(CNC)}$ is the dustiness index in number of particles per gram, and it was calculated as the total number of generated particles divided by the total mass of the test NM sample in milligrams (unit 1/mg):

$$DI_{Number(CNC)} = \frac{S_{Vortex}^{Number(CNC)}}{m_{NM}}$$

To get information on particle morphology of the emitted aerosol, a simple but specific sampling set-up has been designed (not shown here). Transmission electron microscope (TEM) copper grids were taped onto 25 mm diameter polycarbonate membrane filters (0.4 or 0.8µm). Fibre backing filters were used to support the polycarbonate filters. Air flow was driven by a personal sampling pump at a flow rate of 1 L/min. The duration of the sampling was set to 1 hour. The sampling period was set equal to the duration of a test (1 hour). For some test, the sample was accumulated over two trials in order to have enough particles to observe. Different TEM copper grids having different carbon films have been used (Carbon film, Quantifoil Holey Carbon Films or Holey Carbon Support Film).

It is important to note that the duration of the test is a relevant test parameter as the process is dynamic. In the original INRS protocol developed, the duration of a test was set equal to 3600 s. But in the first version of the set-up (Figure 75), as the instruments measure in real time, it is possible to perform the calculation for different durations between 0 and 3600 s. In this report, the calculations based on the condensation nuclei counter CNC data were performed for two durations: 180 s and 3600 s. The first duration (180 s) was chosen to be consistent with the SD method. For the second version of the setup, the duration of the test was set to 3600 s, which corresponds to the original protocol of the VS method.

The second version of the setup (Figure 76) is used for collecting respirable mass fraction of the emitted aerosol. The respirable mass fraction is obtained by sampling with a GK2.69 cyclone (BGI, UK). The filters have been preweighed and post-weighed following the recommendations of the ISO 15767:2009 on the same analytical balance. Only one test was performed with this setup due to time constraints. Therefore the results are not presented with a confidence interval based on reproducibility. However, measurement uncertainty has been calculated for each measurement performed.

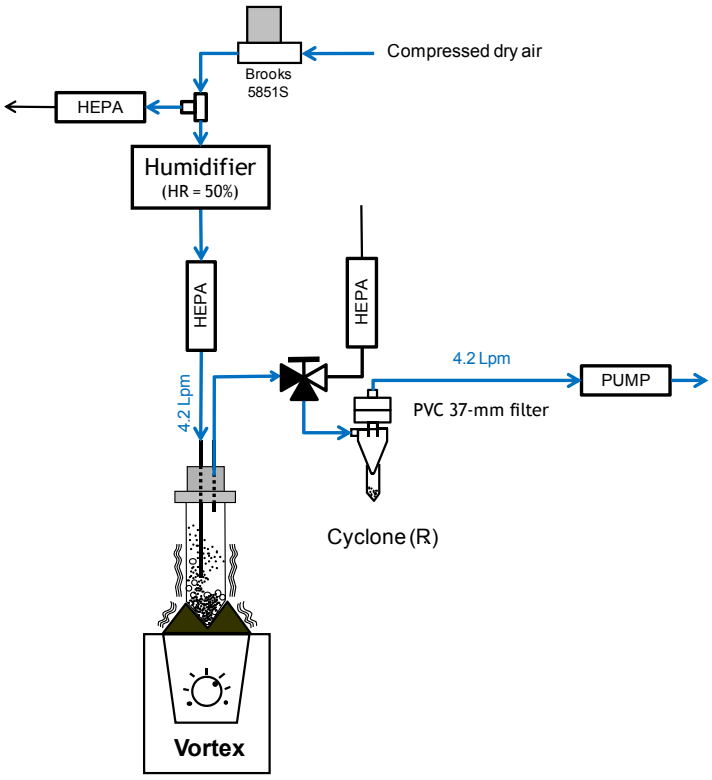

Figure 76. Experimental set-up of the vortex shaker method for collecting respirable mass fraction of the emitted aerosol.

$DI_{Mass(GK2.69)}$ is the dustiness index in respirable mass (mg) of particles per kilogram and it was calculated as the respirable mass of generated particles in milligrams divided by the total mass of the test NM sample in kilograms:

$$DI_{Mass(GK2.69)} = \frac{S_{Vortex}^{NumMass(GK2.69)ber(CNC)}}{m_{NM}}$$

The recommendations of the standard ISO 15767:2009 were followed to determine the LOD of the weighing procedure for the filters used for sampling respirable mass of particles during this project. The LOD for the PVC GELMAN GLA-5000 (5 µm/37 mm) filters was equal to 20ng. This value is used to determine the LOD expressed in dustiness index.

The preparation of NM samples for VS testing included: 1) to take a series of 7 samples of 0.5 cm^3 from the vial containing the nanomaterial, 2) to accurately weigh the samples. Three samples are devoted for testing with the first version of the set-up, one for the second version (respirable mass fraction measurement) and three for the gravimetric water content measurement. The gravimetric water content was performed using a HR83 Halogen Moisture Analyzer (Mettler Toledo) and following a drying program defined specifically for small quantities of used NM (Temperature = 160°C; duration = 170 s).

The weighing of the NM samples was performed with a XP205 analytical balance (10 µg readability, Mettler Toledo) while the weighing of the 37-mm filters from the respirable sampler was performed with a MX5 microbalance (1 µg readability, Mettler Toledo).

Particular attention was given to cleaning the experimental device between successive tests. All pipes and other connections were systematically cleaned with water and/or ethanol and dried in an oven, or eventually changed. The checking of the airflows was performed using a primary flow bubble calibrator (Gillian® Gillibrator 2). Prior to each test, the cleanliness of the air was assessed on the basis of measurements made using the condensation nuclei counter. In the case of a non-compliant result, the cleaning was performed again or pipes and other connections changed. The validation of a test depends on several factors such as: 1) the stability of the parameters during the test, 2) a good reproducibility of measured number concentrations, 3) the sequence of steps for the respirable aerosol sampling etc.

The entire set-up was located inside a variable volume fume hood to prevent exposure of the operator. Similarly, all operations like weighing, water content measurement and sample preparation were carried out in a specific containment system that has a unique turbulent-free, low flow design which allows our sensitive balance to operate without fluctuation and protects the operator from exposure to airborne particles that could be released when handling and weighing NM samples.

13.1.3. Results for the Vortex Shaker Method

Table 54 lists the gravimetric water content (expressed in weight percent) and bulk density of the nanomaterials in powders. The results were obtained in tests conducted by INRS.

Table 54. Gravimetric water content and bulk density of the SAS NMs.

Material	Sample mass (mg)	Water content (wt % dry)	Bulk density (g/cm^3)
NM-200	121	8%	0.12
NM-201	195	8%	0.28
NM-202	147	1%	0.13
NM-203	119	1%	0.03
NM-204	134	6%	0.16

Experimental data obtained with the VS method are summarized in Table 55. Number-based data with the VS method are calculated from the time profiles with two test durations 180 s and 3600 s. The first duration (180 s) was chosen to correspond to the test duration of the

SD method. The mass-based data, obtained with a test duration of 3600 s, correspond to the respirable fraction only as the inhalable fraction was not part of the VS original protocol.

Table 55. Number-based and mass-based dustiness indexes SAS NMs.

NM-20X	Test mass (mg)	Dustiness Index			
		Number (1/g)			Mass (mg/kg)
		T = 180 s		T = 3600 s	
		CPC $_{(S.D)}$[b]	ELPI[a] $_{(S.D)}$[b]	CPC $_{(S.D)}$[b]	Respirable $_{(S.D)}$[c]
NM-200	60.2	2.9E+06 (2.9E+05)	1.1E+07 (6.0E+06)	8.2E+06 (1.3E+06)	3.4E+04 (3.04E-02)
NM-201	140.0	4.6E+04 (1.3E+04)	9.3E+04 (4.2E+04)	8.6E+05 (1.1E+05)	6.5E+03 (5.814E-03)
NM-202	62.6	5.6E+04 (1.3E+04)	2.1E+05 (2.0E+04)	1.6E+06 (9.9E+05)	1.7E+04 (1.54E-02)
NM-203	14.3	4.1E+05 (1.1E+04)	1.6E+06 (2.0E+05)	2.1E+07 (1.1E+07)	5.1E+04 (4.55E-02)
NM-204	79.4	1.3E+06 (1.5E+05)	2.6E+06 (3.9E+05)	3.0E+06 (5.2E+05)	1.4E+04 (1.22E-02)

a The assumption for calculating the number of particles emitted from the data from the ELPI is: spherical particle with a density equal to the density of the condensed phase of the material constituting the NM. Densities used were 2.2 g/cm3 for all NM-20x; based on Kim et al. (2009).
b standard deviation calculated over 3 repeats
c measurement uncertainty as there was no repeat for this tests

13.1.4. Comparison of the SD and VS methods

Figure 77 shows the respirable mass dustiness indices obtained by the SD and VS methods.

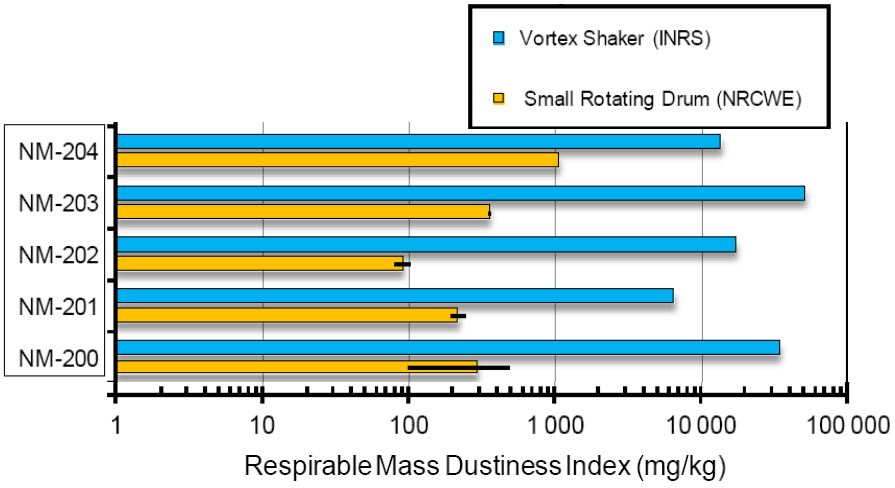

Figure 77. Comparison between respirable mass dustiness indices obtained with the small rotating drum and vortex shaker method. Errors bars on the SD values correspond to the reproducibility over 3 repeats.

The comparison between the small drum and Vortex shaker results shows that no significant correlation between these two methods can be found. Further evaluation of the VS method is needed in order to link it to the standardized Rotating Drum method. As already stated,

dustiness is not an intrinsic physical or chemical defined property of a powder, but its level depends on both characteristic properties of the powders and the activation energy in the simulated handling. Therefore different values may be obtained by different test methods (test apparatus, operation procedure, sampling and measurement strategy, etc.). Hence, direct comparability is not expected between the SD and the VS. Morover, the absence of a harmonized approach for the measurement strategies and techniques, metrics and size ranges and the procedures for data analysis and reporting may additionally limits the comparison of the results obtained by the two dustiness methods.

14. Conclusions

The JRC established the repository for representative nanomaterials. The work started in 2008 and the repository was launched in February 2011, hosting more than 20 different types of nanomaterials at the JRC Ispra (Italy) site. The nanomaterials in the repository have the following code: NM-XXX, where XXX is a digital identifier unique to one material.

The NM-series of representative test nanomaterials was introduced by the JRC to support the OECD Working Party on Manufactured Nanomaterials' programme "Safety Testing of a Set of Representative Manufactured Nanomaterials", established in November 2007, as well as national and international research projects within and outside the EU. More than 10,000 individual test samples have been distributed to national authorities, research institutions, industrial reserachers and scientific stakeholders.

The OECD WPMN recommended to test selected nanomaterials for a series of end-points in the OECD nanomaterials testing programme. The synthetic amorphous silicon dioxides, NM-200, NM-201, NM-202, NM-203 and NM-204 are some of the key materials of the OECD WPMN programme, and information on physico-chemical characterisation as well as stability and homogeneity for NM-200 and NM-203 is presented in the current report with special regard to its use and appropriateness as representative nanomaterial.

Also outside the OECD WPMN, characterisation of nanomaterials and applicable methods are intensively studied to understand naomaterials both in a regulatory and a scientific context. For example, the JRC published recently a report regarding "Requirements on measurements for the implementation of the European Commission definition of the term "nanomaterial" (see Linsinger et al. 2012) that also evaluates the limits and advantages of the existing methods for characterisation of nanomaterials, and the reader is referred to it for additional information on the applicability areas of the methods.

The physico-chemical characterisation of SAS NMs was performed within the NANOGENOTOX project, and by the JRC. Chapter 14.2 gives an overview of the outcome of the physico-chemical characterisation of each of the 5 SAS NMs and the measurement methods applied.

In the NANOGENOTOX project a dispersion protocol was developed which was used for the in vitro and in vivo experiments with the 3 types of materials, TiO_2, SiO_2 and MWCNT, investigated and such a protocol is obviously not optimised for the single material type, let alone the individual experiments. For the dispersion protocol the NMs are dispersed into the

media using sonication and the sonicator seems to have an important influence on the degree of dispersion and final particle size distribution in the medium. A part of the physico-chemical characterisation was done using the NANOGENOTOX protocol, but for investigating the inherent properties also other dispersion protocols were relevant.

After preparation of the dispersion of the test item, analysis should always be performed to ensure dispersion stability, as successful (liquid) sample splitting can only be conducted if a homogeneous dispersion has been achieved, otherwise a much higher sampling error will be introduced. Dispersion can be assessed using for example light scattering techniques such as Dynamic Light Scattering (DLS) or optical microscopy. Each characterisation method has limitations, which operators must be aware of. For example, DLS is not suitable to resolve a broad particle size distribution, as potentially larger particles can mask the signal of the smaller nanoparticles. In order to resolve multi-modal particle distribution, techniques that have a separation mechanism element integrated in the analytical tool will be more suitable, such as a CLS disc centrifuge. In addition to errors incurred from sub-sampling steps, stability of the dispersion is important for nanoparticle characterisation, as only stable dispersions give reliable characterisation data.

14.1. Characterisation

Almost all of the OECD endpoints on physical-chemical testing have been completed for the principal OECD WPMN material, NM-200. Also the alternate materials, NM-201, NM-202, NM-203 and NM-204 have been extensively characterised. The determination of the octanol water coefficient is not feasible for nanomaterials, as discussed at an OECD workshop in Mexico, March 2013, and was considered to be not relevant for insoluble and sparingly soluble nanomaterials. The photocatalytic activity was considered to be not relevant for SAS. Analysis of intrinsic hydroxyl radical formation capacity, using the Benzoic acid probe for quantification, gave no detectable radical after 24 and 48-hour incubation.

The **homogeneity** within and between vials was investigated for NM-200 and NM-203, as was the reproducibility of results between laboratories. The method used was DLS. Both for NM-200 and for NM-203 the intra-vial reproducibility seemed to be very dependent both on the mesurand and the laboratory. At INRS, the variability of data from the cumulant analysis (Z-average and PdI) is only a few percent, whereas it is much higher for the position of the peak obtained from Padé-Laplace analysis. At CEA, the variability intra-vial observed is about 6 to 10 percent. When comparing the 3 vials tested at NRCWE, the inter vial homogeneity seemed very good (2-3%) even better than the intra-vial homogeneity observed at CEA. However, for both NM-200 and NM-203 the particle size measured by each

institution was quite different, so when comparing results of the testing of vials in the 3 laboratories, the variability was higher than 10%. Given the consistency of the results obtained from each institution, the vials are thought to be rather homogeneous and the variations are considered to originate from a systematic difference of sample preparation caused e.g. by the different types of sonicator. However, the homogeneity study was performed using DLS to investigate and, as the results from the DLS method do not always reflect the underlying size distribution of the dispersed particles (Calzolai et al., 2011), a validation of the results would be relevant.

In general, results indicate high zeta-potential values for SAS NMs that are dispersed either in pure DI water or in DI water with 5 mM NaCl, and thus confer stability in such media. Results show values of zeta-potential measured were lower when the NMs were dispersed in an ecotoxicology media indicating much poorer dispersion stability in such media.

The elemental analysis showed that the SAS NMs are rather pure, consisting of between 96.0 to 99.2 %wt silicon dioxide. The SAS NMs were analysed using several techniques: EDS, ICP-OES, TGA and DTA. In addition also XRD gave information about crystalline impurities. The three precipitated SAS, NM-200, NM-201 and NM-204 contain slightly more impurities than the pyrogenic materials, NM-202 and NM-203, as they contain sodium sulphate from the starting materials. All the SAS NMs appear to contain some aluminium (see Table 10) and in addition traces of other elements were identified for the precipitated NMs (see Table 11). The TGA analysis indicated that the three precipitated NMs all had some weight loss below 100 °C which may be ascribed to water adsorbed on the surface. The TGA for both of the pyrogenic NMs had a weight change due to buoyancy, and in addition a phase transition was identified for NM-203 at 324°C. Thus, the elemental analyses performed were indicative, and the outcomes reflect also that the materials have an industrial origin, as within one NM not all samples contain the same impurities, and sub-samples of one vial may be of slightly different composition. More information regarding the nature of the impurities should be generated for the future.

Material	Calculated indicative content of SiO_2* (%wt)	Major impurities identified by EDS	Major impurities identified by XRD
NM-200	96	Na, Al, S, Ca	Na_2SO_4, böhmite
NM-201	97	Na, Al, S, Ca	Na_2SO_4, böhmite
NM-202	99		böhmite
NM-203	99		böhmite
NM-204	98	Na, Al, S	no impurities detected

*The calculation is based on the silicon content given in Table 10 and the ratio of the molar weight of one Si atom (23.0 g/mol) to two oxygen atoms (32.0 g/mol).

All the SAS NMs were analysed by XPS, a technique that gives information on the elemental surface composition of the materials down to a depth of 10 nanometres. The analysis indicated presence of carbon in all materials and this was largely attributed to carbon contamination on the surface of the particles. In addition, presence of sodium was identified in NM-200, NM-201 and NM-204, and for NM-200 and NM-201 sulphur was detected. The XRD analysis is conformative with the presence of sodium sulphate and the elemental analysis identifies the presence of sodium and sulphur so these results confirm each other.

The combined results of homogeneity analysis and elemental analysis indicate that these materials may work well as representative nanomaterials, but the volume at which repeatability can be reached needs to be established; possibly involving additional sub-sample homogenization, or other treatments to enable use as as reference materials

The TEM analysis showed the SAS-NMs consist of highly agglomerated and aggregated primary particles. The SAS NMs are produced by two methods: by precipitation process or a pyrogenic process. The TEM micrographs indicate that the SAS NMs have a polydisperse particle size distribution; the average value of the primary particle size was estimated to be below 20 nm for all SAS NMs (except NM-203, as measured by IMC-BAS). The shape of the particles was statistically analysed and the results are given in the table below that summarises the morphology of aggregates/agglomerates of SAS NMs according to Krumbein and Schloss (1963). Table 46 confirms that the median sphericities and shape factors between the thermal and precipitated NM are significantly different, whereas within the precipitated and thermal NM no significant differences were found.

Material	Sphericity	Shape category	General morphology
NM-200 (precipitated)	Low to medium sphericity	Sub-angular to rounded	Sub-rounded, low to medium sphericity
NM-201 (precipitated)	Medium sphericity	Rounded to well-rounded	Rounded, medium sphericity
NM-202 (pyrogenic)	Low sphericity	Very angular to sub-angular	Angular, low sphericity
NM-203 (pyrogenic)	Low sphericity	Very angular to sub-angular	Angular, low sphericity

Analysis of TEM micrographs showed that the general morphology of the nanomaterials was quite comparable (Table 47). All samples consist of highly porous nanostructured materials, which may be considered aggregates of primary silicon dioxide particles. However, when looking into the detail, the thermal SAS (NM-202 and NM-203) may have a more complex and branched structure than the precipitated SAS (NM-200 and NM-201). These differences

were very clear in the quantitative morphology analysis, which showed much higher angularity of spheroidal silicon dioxide aggregates in NM-202 and NM-203 compared to NM-200 and NM-201. Based on the number-based distributions of the mean diameter (Figure 64A) and on the comparison of the median mean diameters of the aggregates and agglomerates, the precipitated NM-200 and NM-201 cannot be unambiguously distinguished from the thermal NM-202 and NM-203. The number-based size distribution of NM-200 is different from those of NM-202 and NM-203, and the NM-200 median mean diameter is significantly different from those of NM-202 and NM-203; however the number-based size distribution of NM-201 is comparable to the curves of NM-202 and NM-203, and the NM-201 median mean diameter is not significantly different from those of NM-202 and NM-203.

The number-based sphericity and shape factor distributions of the precipitated NM-200 and NM-201 are very similar (Figure 64B and Figure 64C), as are the corresponding distributions of the thermal NM-202 and NM-203. However, the curves of the precipitated and thermal NM tend to diverge.

TEM micrographs also allowed an analysis of the primary particle size of the SAS NMs, see the table below. The primary particle size is in good agreement both between laboratories using the same technique.

Material	ECD (nm) ± SD ($N^{\$}$) CODA-CERVA (TEM)	ECD (nm) ± SD ($N^{\$}$) INRS (TEM)	Diameter (nm) IMC-BAS (TEM)
NM-200	14 ± 7 (1876)	23 ± 8 (100)	18
NM-201	17 ± 8 (1726)	19 ± 4 (100)	18
NM-202	15 ± 7 (401)	18 ± 3 (105)	20
NM-203	13 ± 6 (448)	16 ± 3 (105)	45
NM-204	10 – 15*		19

* Manual measurement. $ is the number of particles used for the assessment

The CLS curves for precipitated SAS (NM-200 NM-201 and NM-204) are similar to each other, and the CLS curves for pyrogenic SAS (NM-202 and NM-203) are similar to each other. The two sets of CLS measurement curves are different in shape and the precipitated NMs have a broader size distribution and contain a fraction of very large particles, whereas the pyrogenic SAS have a narrower particle size distribution and do not contain very large agglomerates/aggregates.

Based on the CLS measurements, the size (position of the peak), the CLS derived polydispersity index (D_n/D_w, i.e. the diameter calculated based on number divided by the diameter based on weight) and the half width were estimated (Table 22). The peak was below 100 nm for all SAS NMs and the SAS NMs were polydisperse.

CLS measurements cannot distinguish between individual particles and aggregates. The particle size measured by CLS is consistently smaller than the particle size measured by DLS (nor this technique can distinguish individual particles and aggregates) which may be due to the CLS separation of particles according to sizes that promotes a better visibility of smaller particles. However, sample preparation steps for both DLS and CLS involve sonication which probably produces true breaking of aggregates due to the brittle nature of amorphous silicon dioxide. This could be investigated further by performing both types of measurements on the same prepared sample to investigate the influence from the sonication step on the two particle size distributions.

The solubility of the SAS NMs in the BSA/water (i.e. the NANOGENOTOX dispersion protocol), Gambles solution and Caco2 medium was investigated; the solubility in pure water was not included. The SAS NMs dissolve partly in all three media and are least soluble in the BSA/water solution applied in the NANOGENOTOX project.

The pH and O_2 reactivity of the SAS dispersed in BSA/water, Gambles solution and Caco2 medium were assessed using a commercial Sensor Dish Reader system that enables in situ measurement of pH and O_2 concentration at 1 s resolution. In all experiments the pH and O_2 evolution was investigated over 24 hours as compared with the evolution in the pure media. All experiments were conducted in a cell incubator and all dispersions were prepared following the generic BSA/water NANOGENOTOX dispersion protocol. The experiments showed limited pH reactivity, but a burst in O_2 was usually observed. Interestingly, the reactivity may not be exerted to similar degree in the different media. It appears as though the reactivity for the SAS NMs often is less pronounced in the BSA medium than in the Gambles solution and Caco 2 media. However, NM-200 had negligible reaction in Caco-2 medium and NM-204 was only slightly reactive in all three media tested. The maximum O_2 change was in the order of 40 µmol/ml corresponding to more than 1 µmol O_2/mg. The use of the SDR system is still at experimental level and clear data interpretation is not yet possible. It is, however, very evident that the MN's do react and have influence on the O_2 concentrations in the dispersions. It is currently assumed that the O_2 variebility indicates tha the SAS MN's are redox-active due to direct electron transfer processes or due to dissolution-related reactions. However, combined with data using benzoic acid probe, suggests that the reactivity does not result in production for hydroxyl radicals.

Specific surface area measurements using BET show specific surface area values of the same order of magnitude for the SAS NMs, from 136.6 (NM-204) to 204.1 (NM-202) m^2/g. The SAS NMs have some microporosity, except NM-203, as well as some micro surface

area, i.e. in addition to particle size and shape also internal porosity contributes to the specific surface area.

For dustiness the small rotating drum (SD) and the Vortex shaker (VS) methods were applied and are currently proposed as standardised test methods for nanomaterials as the dustiness methods in EN15051 do not directly apply to nanomaterials. Both methods are based on agitation, and for both the determination of dustiness in respirable size-fractions were combined with number concentration and size-distribution analysis of the dust particles. In addition, as it was possible in the SD method protocol, the inhalable fraction was systematically measured. For a few of the tests conducted with the VS method, electron microscopy (EM) observations were performed. Finally, particle-size distributions data were reported from measurements using Electrical Low-Pressure Impactor (ELPI^{TM} Classic) for the VS method, and Fast Mobility Particle Sizer (FMPS) and Aerodynamic Particle Sizer (APS) for the SD method. The comparison between the small drum and Vortex shaker results shows that no significant correlation between these two methods can be found. Further evaluation of the VS method is needed in order to understand the most appropriate test conditions and metrics and potentiallt link the results to results using the SD.

14.2. Summary of the characterisation of each SAS NM

Table 4 gives an overview of the physico-chemical characterisation performed, the methods used and the institutions involved in the testing. Table 56 to Table 60 summarise the results obtained in for the 5 different synthetic amorphous silicon dioxides.

14.2.1. NM-200, summary of physico-chemical characterisation

Table 56. Overview of results from the physico-chemical characterisation of NM-200.

Method	Institution	Results
Homogeneity		
DLS	CEA, INRS, NRCWE	Repeated DLS studies were performed between the vials and within the vial. The observed variability between the vials is very low (2-3%) but intra-vial is much higher: 6-10%.
Agglomeration / aggregation		
SAXS	CEA	Structure and size parameters extracted from SAXS data. Gyration radius of primary particles and aggregates $2xRg_1$: 18 nm and $2xRg_2$: 440 nm, fractal dimension D_f: 2.45 and number $N_{part/agg}$ of particles per aggregate: 3600
DLS	CEA	• Ultra-pure water dispersion (intra vial study) Z-average (nm): 207.1±12.3, PdI: 0.390±0.041

		• Ultra-pure water dispersion (inter vial study) Z-average (nm): 195.3, PdI: 0.378
	NRCWE	• Ultra-pure water dispersion (inter vial study) Z-average (nm): 181.5±4.3, PdI: 0.238±0.006
	INRS	• Ultra-pure water dispersion (intra vial study) Z-average (nm): 240.5±2.3, PdI: 0.248±0.006
	JRC	• miliQ water dispersion. Z-average (nm): peak 1: 136, peak 2: 376, PdI: 0.524 • culture media dispersion Z-average (nm): peak 1: 144.4, peak 2: 2611, PdI: 0.492 • PBS dispersion Z-average (nm): peak 1: 187.2, peak 2: 712.7, PdI: 0.532
TEM	CODA-CERVA, IMC-BAS	High porosity nanostructured material which may be considered aggregates of primary particles. Mean diamater (nm): 31±3. Feret min: 21.9 nm (median of 8005) Feret max: 34.5 nm (median of 8005) Morphology of aggregates/agglomerates: low to medium sphericity, sub-angular to rounded.
TEM-tomography	CODA-CERVA	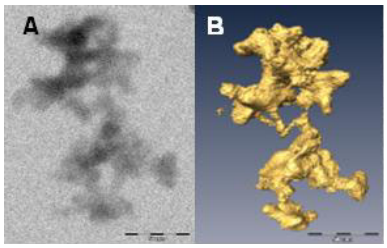 Aggregates of very complex morphology composed of a variable number of interconnected primary subunits.
AFM	CEA	Third dimension of the agglomerates/aggregates: median (of 1382): 21.9 nm
Water Solubility		
24-hour acellular *in vitro* incubation test	NRCWE	The 24-hour dissolution ratio of NM-200 was measured in three different media: 0.05% BSA in water, Gambles solution and Caco 2 media. Both NM-200 and the Al impurities are partially soluble in all media but amounts vary considerably with medium, as does the relative amounts of dissolved Al impurities compared with dissolved Si, suggesting that the solubility behaviour of the Al impurity and NM-200 depends on the medium.
Crystalline phase		
XRD	JRC	Synthetic amorphous silicon dioxide. Peaks supporting the presense of crystalline material, consistent with Na_2SO_4 were seen.
	NRCWE	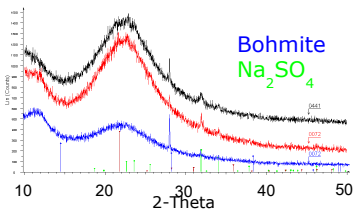 Synthetic amorphous silicon dioxide; impurities of Na_2SO_4, and Böhmite (γ-AlO(OH)) were detected.

	IMC-BAS	Synthetic amorphous silicon dioxide.
Dustiness		
Small Rotating Drum	NRCWE	Inhalable dustiness index (n=3) 6459±273 Respirable dustiness index (n=3) 293±193
Vortex Shaker Method	INRS	Respirable dustiness index (n=1) 34000
Crystallite size		
SAXS	CEA	Amorphous material. Primary particle size: Equivalent diameter for spheres: 22nm, 2xRg$_1$ is 18nm
XRD	JRC	Synthetic amorphous silicon dioxide. Traces of crystalline material seen around 2-Theta equal to 32° and 34°, which is consistent with the suggested presence of Na_2SO_4
	NRCWE	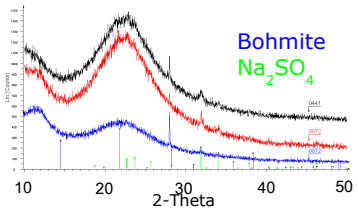 Synthetic amorphous silicon dioxide. Crystalline impurities of Na_2SO_4 and Böhmite (γ-AlO(OH))
	IMC-BAS	Synthetic amorphous silicon dioxide
Representative TEM picture(s)		
TEM	CODA-CERVA, IMC-BAS	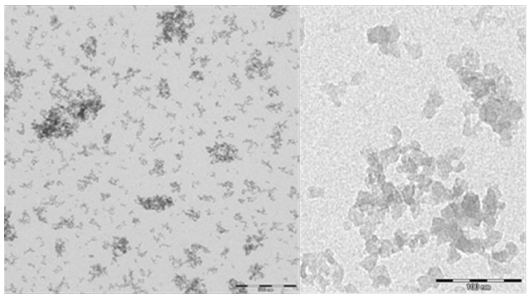 Aggregates with dense, complex structure
Particle size distribution		
SAXS	CEA	Primary particle size: Equivalent diameter for spheres: 22 nm, 2xRg$_1$ is 18nm
TEM	CODA-CERVA	Primary particle size: 14±7 nm
	IMC-BAS	Primary particle size: 18nm
	INRS	Primary particle size: 23±8 nm
TEM	CODA-CERVA, IMC-BAS	Number (expressed in %) of SAS NM particles smaller than 100 nm, 50 nm and 10 nm <100 nm - 88.7%, <50 nm - 69.8% <10 nm - 1.7%
DLS	CEA	The material is polydisperse.

		The intensity size distribution, which consists of two main peaks is very broad and revels the presence of large aggregates of few microns. • Ultra-pure water dispersion (intra vial study) Z-average (nm): 207.8±11.9, PdI: 0.388±0.036, FWHM peak width(nm): 160.4±43.4 • Ultra-pure water dispersion (inter vial study) Z-average (nm): 195.3±12.3, PdI: 0.378±0.041, FWHM peak width (nm): 222.4±50.1
	JRC	The material is polydisperse. The intensity size distribution, which consists of two main peaks is very broad and revels the presence of large aggregates of few microns. • miliQ water dispersion. Z-average (nm): peak 1: 136, peak 2: 376, PdI: 0.524, • culture media dispersion Z-average (nm): peak 1: 144.4, peak 2: 2611, PdI: 0.0.492 • PBS dispersion Z-average (nm): peak 1: 187.2, peak 2: 712.7, PdI: 0.532
	NRCWE	The material is polydisperse. • Ultra-pure water dispersion (inter vial study) Z-average (nm): 181.5±4.3, PdI: 0.238±0.006, main peak (nm): 116.7±8.3
	INRS	The material is polydisperse. • Ultra-pure water dispersion (intra vial study) Z-average (nm): 240.5±2.3, PdI: 0.248±0.006
CLS	JRC	Peak (nm): 75-95, CLS PdI: 10.18
Specific Surface Area		
BET	IMC-BAS	189.16 (m^2/g)
SAXS	CEA	123.3±4.9 (m^2/g)
TEM-topography	CODA-CERVA	342±36 (m^2/cm^3) (Volume specific surface area)
Zeta Potential (surface charge)		
Zetametry	CEA	NM-200 forms a stable suspension, with negatively to neutral charged nanoparticles. The zeta potential, however, varied greatly as function of pH and reached -45 mV around pH 7. IEP <2
	JRC	Zeta potential at pH 7, milliQ water: -47.5 (mV). Zeta potential at pH 7.1, PBS: -18 (mV)
Surface Chemistry		
XPS	JRC	The following elements were identified in the surface of NM-200: O (70.8 at%), Si (24.7 at%), C (4.1 at%), Na (1.0 at%) and S (0.1 at%). The presence of C is considered to be due to surface contamination.

TGA	NRCWE	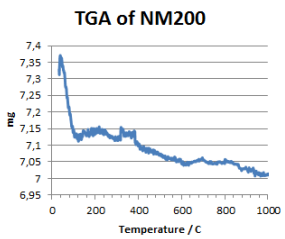	Significant mass loss was observed below 100°C (water). A 3 wt% gradual mass loss was observed above 110°C and may indicate some associated organic compounds.
Photo-catalytic activity			
End-point not relevant for SAS			
Pour-density			
Weighing	INRS	0.12 g/cm^3 (8 wt% water content)	
Porosity			
BET	IMC-BAS	Micropore volume (mL/g): 0.01181	
Octanol-water partition coefficient,			
End-point not relevant			
Redox potential			
OxoDish fluorescent sensor plate for O_2 detection	NRCWE	The evolution of O_2 level during 24-hour incubation was measured in three different media. Different dO_2 values were observed for all applied media. In the 0.05% BSA-water and Gambles solution NM-200 showed negligible reactivity. In Caco 2 media, a negative dose-reponse relation was observed with decreasing dO_2 level with increasing concentration of NM-200. The results suggest that NM-200 is inactive or reductive in the different incubation media.	
Radical formation			
HPLC + UV	NRCWE	Using the benzoic acid probe to form 4 hydroxy benzoic acid in a phosphate buffered hydrous solution gave no detectable concentration OH radicals.	
Composition			
ICP-OES	IMC-BAS	Na-8800 ppm, Al- 4600 ppm, S- 8700 ppm, Si -44.77 (wt %), O (wt%) calculated- 53.02	

14.2.2. NM-201, summary of physico-chemical characterisation

Table 57. Overview of results from the physico-chemical characterisation of NM-201.

Method	Institution	Results
Homogeneity		
DLS		Study not performed
Agglomeration / aggregation		
SAXS	CEA	Structure and size parameters extracted from SAXS data. Gyration radius of primary particles and aggregates $2xRg_1$: 20 nm and $2xRg_2$: 180 nm, fractal dimension D_f: 2.45 and number $N_{part/agg}$ of particles per aggregate: 457
DLS	CEA	• Ultra-pure water dispersion (intra vial study) Z-average (nm): 208.1±34.5, PdI: 0.352±0.028 • Ultra-pure water dispersion (inter vial study) Z-average (nm): 197.0±15.7, PdI: 0.337±0.020
	JRC	• miliQ water dispersion. Z-average (nm): peak 1: 161, peak 2: 968, PdI: 0.420
TEM	CODA-CERVA, IMC-BAS	High porosity nanostructured material which may be considered aggregates of primary particles. Mean diamater (nm): 43±4. Feret min: 25.4 nm (median of 5331) Feret max: 34.5 nm (median of 5331) Morphology of aggregates/agglomerates: Medium sphericity, rounded to well--rounded. % of aggegates <100 nm: 91±2
AFM	CEA	Third dimension of the agglomerates/aggregates: median (of 1275): 33.5 nm
Water Solubility		
24-hour acellular *in vitro* incubation test	NRCWE	The 24-hour dissolution ratio of NM-201 was measured in three different media: 0.05% BSA in water, Gambles solution and Caco 2 media. Both NM-201 and the Al impurities are partially soluble in Gambles Solution and Caco2 media but amounts vary considerably with the medium. In 0.05% BSA in water only the Al impurities were partially soluble, Si was below the detection limit. The relative amounts of dissolved Al impurities and dissolved Si were different depending on medium, which suggests different solubility behaviour of the Al impurity and NM-201 depending on the medium.
Crystalline phase		
XRD	JRC	Synthetic amorphous silicon dioxide. Traces of crystalline material seen around 2-Theta equal to 32° and 34°, which is consistent with the suggested presence of Na_2SO_4

	NRCWE	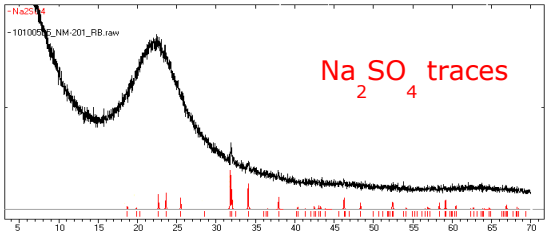 Synthetic Amorphous silicon dioxide; impurities of Na_2SO_4, Böhmite (γ-AlO(OH)).
	IMC-BAS	Synthetic amorphous silicon dioxide.
Dustiness		
Small Rotating Drum	NRCWE	Inhalable dustiness index (n=3) 6034±199 Respirable dustiness index (n=3) 218±24
Vortex Shaker Method	INRS	Respirable dustiness index (n=1) 65000
Crystallite size		
SAXS	CEA	Amorphous material. Equivalent diameter for spheres: 22 nm, gyration radius $2xRg_1$ = 20 nm
XRD	JRC	Synthetic amorphous silicon dioxide. Traces of crystalline material seen around 2-Theta equal to 32° and 34°, which is consistent with the suggested presence of Na_2SO_4
	NRCWE	Synthetic amorphous silicon dioxide. Crystalline impurities of Na_2SO_4, Böhmite (γ-AlO(OH).
Representative TEM picture(s)		
TEM	CODA-CERVA, IMC-BAS	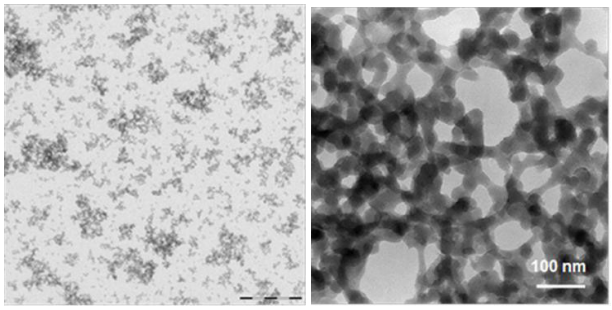 Aggregates with complex, open network structure.
Particle size distribution		
SAXS	CEA	Equivalent diameter for spheres: 22 nm, gyration radius $2xRg_1$ = 20 nm
TEM	CODA-CERVA	Primary particle size: 17±8 nm
	IMC-BAS	Primary particle size: 18
	INRS	Primary particle size: 19±4 nm
TEM	CODA-CERVA,	Number (expressed in %) of SAS NM particles smaller than 100 nm, 50 nm and 10 nm

	IMC-BAS	<100 nm - 81.5%, <50 nm – 55.3% <10 nm – 1.1%
DLS	CEA	The material is polydisperse. The intensity size distribution, which consists of two main peaks is very broad and revels the presence of large aggregates of few microns. • Ultra-pure water dispersion (intra vial study) Z-average (nm): 208.1±34.5, PdI: 0.352±0.028, FWHM peak width(nm): 140.4±105.7 • Ultra-pure water dispersion (inter vial study) Z-average (nm): 197.0±15.7, PdI: 0.337±0.020 FWHM peak width(nm): 105.6±49.3
	JRC	The material is polydisperse. The intensity size distribution, which consists of two main peaks is very broad and revels the presence of large aggregates of few microns. • miliQ water dispersion. Z-average (nm): peak 1: 161, peak 2: 968, PdI: 0.420
CLS	JRC	Peak (nm): 88, half width: 136, CLS PdI: 2.65
Specific Surface Area		
BET	IMC-BAS	140.46 (m^2/g)
SAXS	CEA	123.3±8.3 (m^2/g)
Zeta Potential (surface charge)		
Zetametry	CEA	NM-201 forms a stable suspension, with negatively to neutral charged particles. The zeta potential, however, varied greatly as function of pH and reached -40 mV around pH 7 . IEP <2
	JRC	Zeta potential at pH 6.9, milliQ water: -51.7 (mV).
Surface Chemistry		
XPS	JRC	The following elements were identified in the surface of NM-201: O (70.3 at%), Si (23.6 at%), C (4.5 at%), Na (1.5 at%), Ce (0.25 at%) and S (0.01 at%).The presence of C is considered to be due to surface contamination.
TGA	NRCWE	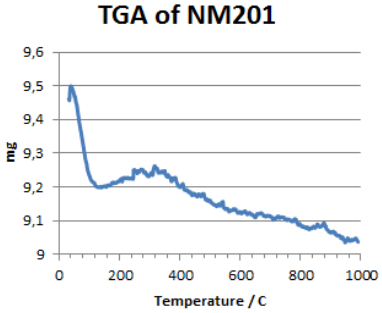 A significant mass loss is observed below 100°C (water). Gradual 3 wt% mass loss was observed above 110°C and may indicate some associated organic compounds.
Photo-catalytic activity		
End-point not relevant for SAS		
Pour-density		
Weighing	INRS	0.28 g/cm^3 (8 wt.% water content)
Porosity		
BET	IMC-BAS	Micropore volume (mL/g): 0.00916

Octanol-water partition coefficient,		
End-point not relevant		
Redox potential		
OxoDish fluorescent sensor plate for O_2 detection	NRCWE	The evolution of O_2 level during 24-hour incubation was measured in three different media. Different dO_2 values were observed for all applied media. In the Gambles solution and Caco 2 media the concentration of dO_2 was the highest (increased ca. 40 µmol/l) for 0.16mg/ml concentration of NM-201. In the 0.05% BSA in water the dO_2 level increases along with the concentration of NM-201 The results suggest that NM-201 has oxidative behaviour in these incubation media.
Radical formation		
HPLC + UV	NRCWE	Using the benzoic acid probe to form 4 hydroxy benzoic acid in a phosphate buffered hydrous solution, gave no detectable concentration OH radicals.
Composition		
ICP-OES	CODA-CERVA	>0.01%: Al(>0.1%), Ca, Na(>0.1%), S; 00.5-0.01%: Zr; 0.001-0.005%: Fe, K, Mg
EDS	IMC-BAS	Na-4400 ppm, Al- 7400 ppm, S- 4600 ppm, Si -45.27 (wt %), O (wt%) calculated- 53.08

14.2.3. NM-202, summary of physico-chemical characterisation

Table 58. Overview of results from the physico-chemical characterisation of NM-202.

Method	Institution	Results
Homogeneity		
DLS		Study not performed.
Agglomeration / aggregation		
SAXS	CEA	Structure and size parameters extracted from SAXS data. Gyration radius of primary particles and aggregates Rg_1: 16 nm and Rg_2: 100 nm, fractal dimension D_f: 2.5 and number $N_{part/agg}$ of particles per aggregate: 200
DLS	CEA	• Ultra-pure water dispersion (intra vial study) Z-average (nm): 175.9±4.5, PdI: 0.355±0.001
	JRC	• miliQ water dispersion. Z-average (nm): peak 1: 156, peak 2: 200, PdI: 0.160
TEM	CODA-CERVA, IMC-BAS	High porosity nanostructured material which may be considered aggregates of primary silicon dioxide particles. Mean diamater (nm): 53±9. Feret min: 37.2 nm (median of 4248) Feret max: 58.4 nm (median of 4248) Morphology of aggregates/agglomerates: Low sphericity—very angular to sub-angular. % of aggregates <100 nm: 87±2
AFM	CEA	Third dimension of the agglomerates/aggregates: median (of 1103): 38.2 nm
Water Solubility		
24-hour acellular *in vitro* incubation test	NRCWE	The 24-hour dissolution ratio of NM-202 was measured in three different media: 0.05% BSA in water, Gambles solution and Caco 2 media. Both NM-202 and the Al impurities are partially soluble in all media but amounts vary considerably with medium as does the relative amounts of dissolved Al impurities compared with dissolved Si suggesting different solubility behaviour of the Al impurity and NM-202 depending on the medium.
Crystalline phase		
XRD	JRC	Synthetic amorphous silicon dioxide.
	NRCWE	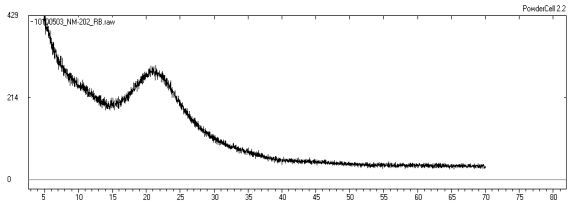 Synthetic amorphous silicon dioxide; impurities of Böhmite (γ-AlO(OH)).
	IMC-BAS	Synthetic amorphous silicon dioxide.
Dustiness		

Small Rotating Drum	NRCWE	Inhalable dustiness index (n=3) 4988±1866 Respirable dustiness index (n=3) 91±11
Vortex Shaker Method	INRS	Respirable dustiness index (n=1) 510000
Crystallite size		
SAXS	CEA	Amorphous material. Equivalent diameter for spheres: 22 nm, gyration radius $2xRg_1$ = 15 nm
XRD	JRC	Synthetic amorphous silicon dioxide.
	NRCWE	Synthetic amorphous silicon dioxide. Crystalline impurities of Böhmite (γ-AlO(OH)).
Representative TEM picture(s)		
TEM	CODA-CERVA, IMC-BAS	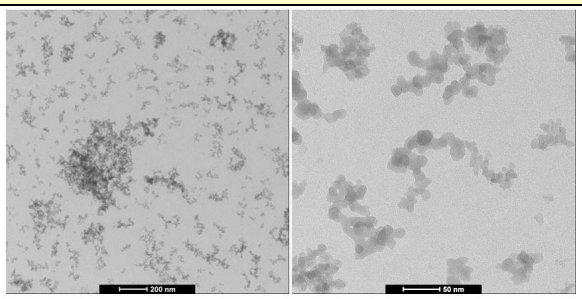 Aggregates with complex, open network structure.
Particle size distribution		
SAXS	CEA	Equivalent diameter for spheres: 22 nm, gyration radius $2xRg_1$ = 15 nm
TEM	CODA-CERVA	Primary particle size: 15±7 nm
	IMC-BAS	Primary particle size: 20 nm
	INRS	Primary particle size: 18±3 nm
TEM	CODA-CERVA, IMC-BAS	Number (expressed in %) of SAS NM particles smaller than 100 nm, 50 nm and 10 nm <100 nm - 80.4%, <50 nm – 55% <10 nm – 0.9%
DLS	CEA	The material is polydisperse. The intensity size distribution, which consists of two main peaks is very broad and revels the presence of large aggregates of few microns. • Ultra-pure water dispersion (intra vial study) Z-average (nm): 175.9±4.5, PdI: 0.355±0.001, FWHM peak width (nm): 56.2±2.9
	JRC	The material is polydisperse. The intensity size distribution, which consists of two main peaks is very broad and revels the presence of large aggregates of few microns. • miliQ water dispersion. Z-average (nm): peak 1: 156, peak 2: 200, PdI: 0.160
CLS	JRC	Peak (nm): 73, half width: 45, CLS PdI: 1.43
Specific Surface Area		

BET	IMC-BAS	204.11 (m^2/g)
SAXS	CEA	184±17.8 (m^2/g)
BET	JRC	Sample stored at 40°C: single point: 186.5392 (m^2/g); multi point: 191.9871 (m^2/g). Sample stored at -80°C: single point: 187.4781 (m^2/g); multi point: 192.9282 (m^2/g).
Zeta Potential (surface charge)		
Zetametry	CEA	NM-202 forms a stable suspension, with negatively to neutral charged particles. The zeta potential, however, varied greatly as function of pH and reached -40 mV around pH 7. IEP 2-4.
	JRC	Zeta potential at pH 6.5, milliQ water: -43.7 (mV).
Surface Chemistry		
XPS	JRC	The following elements were identified in the surface of NM-202: O (72.1 at%), Si (25.0 at%) and C (2.9 at%). The presence of C is considered to be due to surface contamination.
TGA	NRCWE	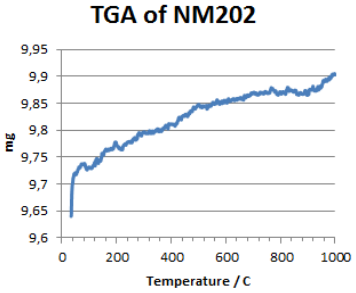 No mass loss observed. Observed mass-increase in graph is due to boyancy.
Photo-catalytic activity		
End-point not relevant for SAS		
Pour-density		
Weighing	INRS	0.13 g/cm^3 (1 wt.% water content)
Porosity		
BET	IMC-BAS	Micropore volume (mL/g): 0.0.00084
Octanol-water partition coefficient,		
End-point not relevant		
Redox potential		
OxoDish fluorescent sensor plate for O_2 detection	NRCWE	The evolution of O_2 level during 24-hour incubation was measured in three different media. Different dO_2 values were observed for all applied media. In the Caco 2 media the concentration of dO_2 was the highest for 0.16mg/ml concentration of NM-202. In the Gambles solution and in 0.05% BSA in water the dO_2 level increased along with the concentration of NM-202. Maximum increase of ca. 30 µmol/l was observed in 0.05% BSA water. The results suggest that NM-202 has oxidative behaviour in these incubation media.
Radical formation		

HPLC + UV	NRCWE	Using the benzoic acid probe to form 4 hydroxy benzoic acid in a phosphate buffered hydrous solution, gave no detectable concentration OH radicals.
Composition		
ICP-OES	CODA-CERVA	No impurities detected
EDS	IMC-BAS	Al- 4500 ppm, Ca- 1800 ppm, Si -46.23 (wt %), O (wt%) calculated- 53.14

14.2.4. NM-203, summary of physico-chemical characterisation

Table 59. Overview of results from the physico-chemical characterisation of NM-203.

Method	Institution	Results
Homogeneity		
DLS	CEA, INRS, NRCWE	Repeated DLS studies were performed between the vials and within the vial. The observed variability between the vials is very low (2-3%) but intra-vial is much higher ca. 20%.
Agglomeration / aggregation		
SAXS	CEA	Structure and size parameters extracted from SAXS data: Gyration radius of primary particles and aggregates Rg_1: and Rg_2: fractal dimension D_f and number $N_{part/agg}$ of particles per aggregate could not be calculated as parameters could not be fitted.
DLS	CEA	• Ultra-pure water dispersion (intra vial study) Z-average (nm): 172.9±9.2. PdI: 0.427±0.025 • Ultra-pure water dispersion (inter vial study) Z-average (nm): 176.9, PdI: 0.425
	NRCWE	• Ultra-pure water dispersion (intra vial study) Z-average (nm): 147.5±4.5. PdI: 0.244±0.017 • Ultra-pure water dispersion (inter vial study) Z-average (nm): 146.8±0.06, PdI: 0.229±0.015
	INRS	• Ultra-pure water dispersion (intra vial study) Z-average (nm): 245.7±37.2. PdI: 0.299±0.024
	JRC	• miliQ water dispersion. Z-average (nm): peak 1: 133, peak 2: 221, PdI: 0.490 • culture media dispersion Z-average (nm): peak : 94.5, PdI: 0.123 • PBS dispersion Z-average (nm): peak: 170.3, PdI: 0.202
TEM	CODA-CERVA, IMC-BAS	High porosity nanostructured material which may be considered aggregetes of primary silicon dioxide particles. Mean diamater (nm): 48±4 Feret min: 33.5 nm (median of 4889) Feret max: 53.2 nm (median of 4889). % of aggregates <100nm: 88±2. Morphology of aggregates/agglomerates: Low sphericity, angular.
TEM-topography	CODA-CERVA	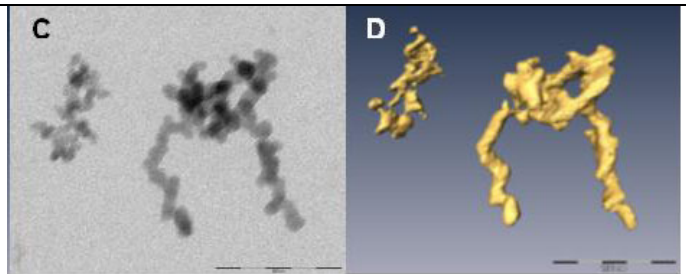 Aggregates of very complex morphology composed of a variable number of

		interconnected primary subunits.
AFM	CEA	Third dimension of the agglomerates/aggregates: median (of 593): 24.2 nm.
Water Solubility		
24-hour acellular *in vitro* incubation test	NRCWE	The 24-hour dissolution ratio of NM-203 was measured in three different media: 0.05% BSA in water, Gambles solution and Caco 2 media. Both NM-203 and the Al impurities are partially soluble in all media but amounts vary considerably with medium, as does the relative amounts of dissolved Al impurities compared with dissolved Si, suggesting that the solubility behaviour of the Al impurity and NM-203 depend on the medium.
Crystalline phase		
XRD	JRC	Synthetic amorphous silicon dioxide
	NRCWE	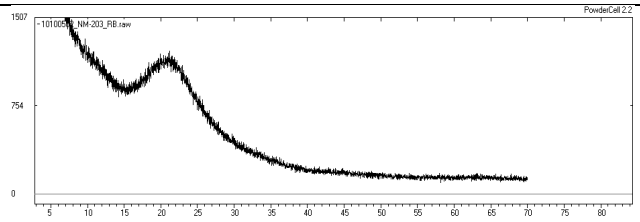 Synthetic amorphous silicon dioxide; impurities of Böhmite (γ-AlO(OH)).
	IMC-BAS	Synthetic amorphous silicon dioxide.
Dustiness		
Small Rotating Drum	NRCWE	Inhalable dustiness index (n=3) 5800±1488 Respirable dustiness index (n=3) 354±6
Vortex Shaker Method	INRS	Respirable dustiness index (n=1) 510000
Crystallite size		
SAXS	CEA	Parameters could not be fitted
XRD	JRC	Synthetic amorphous silicon dioxide
	NRCWE	Synthetic amorphous silicon dioxide. Crystalline impurities of Böhmite (γ-AlO(OH)
	IMC-BAS	Synthetic amorphous silicon dioxide
Representative TEM picture(s)		
TEM	CODA-CERVA, IMC-BAS	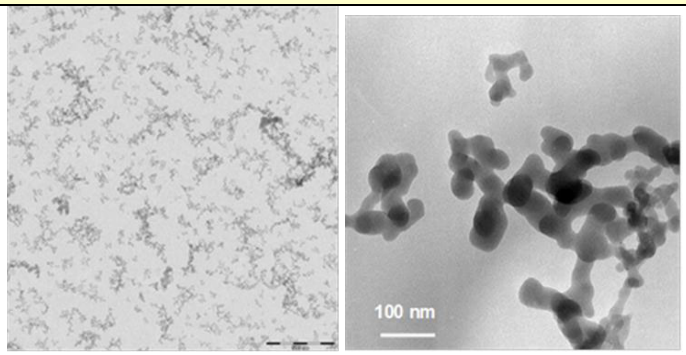 Aggregates with complex open structure.

Particle size distribution		
SAXS	CEA	Parameters could not be fitted.
TEM	CODA-CERVA	Primary particle size: 13±6 nm
	IMC-BAS	Primary particle size: 45
	INRS	Primary particle size: 16±3 nm
TEM	CODA-CERVA, IMC-BAS	Number (expressed in %) of SAS NM particles smaller than 100 nm, 50 nm and 10 nm <100 nm – 77.5%, <50 nm – 48.4% <10 nm – 0.3%
DLS	CEA	The material is polydisperse. The intensity size distribution, which consists of two main peaks is very broad and revels the presence of large aggregates of few microns. • Ultra-pure water dispersion (intra vial study) Z-average (nm): 172.9±9.2. PdI: 0.427±0.025, FWHM peak width: 82.5±11.3 • Ultra-pure water dispersion (inter vial study) Z-average (nm): 176.9, PdI: 0.425, FWHM peak width: 73.15
	JRC	The material is polydisperse. The intensity size distribution, which consists of two main peaks is very broad and revels the presence of large aggregates of few microns. • miliQ water dispersion. Z-average (nm): peak 1: 133, peak 2: 221, PdI: 0.490 • culture media dispersion Z-average (nm): peak : 94.5, PdI: 0.123 • PBS dispersion Z-average (nm): peak: 170.3, PdI: 0.202
	NRCWE	• Ultra-pure water dispersion (intra vial study) Z-average (nm): 147.5±4.5. PdI: 0.244±0.017, FWHM: 84.4±10.4 • Ultra-pure water dispersion (inter vial study) Z-average (nm): 146.8, PdI: 0.06, FWHM: 83.8±0.6
	INRS	The material is polydisperse. • Ultra-pure water dispersion (intra vial study) Z-average (nm): 245.7±37.2. PdI: 0.299±0.024
CLS	JRC	Peak (nm): 64, half width: 50, CLS PdI: 1.35
Specific Surface Area		
BET	IMC-BAS	203.92 (m^2/g)
SAXS	CEA	167.2±13.4 (m^2/g)
TEM-topography	CODA-CERVA	219±23 (m^2/cm^3) (Volume specific surface area)
BET	JRC	Sample stored at 40°C: single point: 192.4628 (m^2/g); multi point: 198.0809 (m^2/g). Sample stored at -80°C: single point: 189.8376 (m^2/g); multi point: 195.4241 (m^2/g).
Zeta Potential (surface charge)		

Zetametry	CEA	NM-203 forms a stable suspension, with negatively to neutral charged particles. The zeta potential, however, varied greatly as function of pH and reached -35 mV around pH 7. IEP 2-4
	JRC	Zeta potential at pH 6.6, milliQ water: -46.1 (mV). Zeta potential at pH 7.1, PBS: -18 (mV)
Surface Chemistry		
XPS	JRC	The following elements were identified in the surface of NM-203: O (71.7 at%), Si (26.0 at%) and C (2.31 at%). The presence of C is considered to be due to surface contamination.
TGA	NRCWE	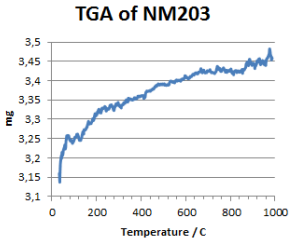 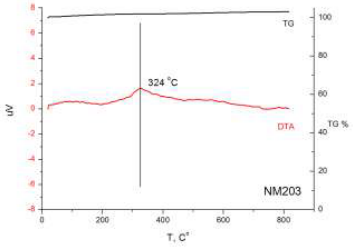 No mass loss detected Phase transtion detected at 324C (DTA). Observed mass-increase in TGA graph is due to boyancy.
Photo-catalytic activity		
End-point not relevant for SAS		
Pour-density		
Weighing	INRS	0.03 g/cm^3 (1 wt.% water content)
Porosity		
BET	IMC-BAS	Micropore volume (mL/g): 0.0
Octanol-water partition coefficient,		
End-point not relevant		
Redox potential		
OxoDish fluorescent sensor plate for O_2 detection	NRCWE	The evolution of O_2 level during 24-hour incubation was measured in three different media. Different dO_2 values were observed for all applied media however in all three media the level of dO_2 increases with increased concentration of NM-203. The most profound increases with up to ca. 30 µmol O_2/l were observed in the 0.05% BSA water and Caco2 medium. The results suggest oxidative reactivity of NM-203.
Radical formation		
HPLC + UV	NRCWE	Using the benzoic acid probe to form 4 hydroxy benzoic acid in a phosphate buffered hydrous solution, gave no detectable concentration OH radicals.
Composition		
ICP-OES	CODA-CERVA	00.5-0.01%: Na in one of the vials tested
EDS	IMC-BAS	Al: 4300 ppm, S: 400 ppm, Si: 46.32 (wt %), O (wt%) calculated: 53.21

14.2.5. NM-204, summary of physico-chemical characterisation

Table 60. Overview of results from the physico-chemical characterisation of NM-204.

Method	Institution	Results
Homogeneity		
DLS		Study not performed
Agglomeration / aggregation		
SAXS	CEA	Data regarding structure and size parameters not extracted from SAXS data.
DLS		Study not performed
TEM	CODA-CERVA, IMC-BAS	The amount of particles smaller than 100 nm is 71.2%. Quantitative study for aggregates/agglomerates not performed.
AFM		Study not performed
Water Solubility		
24-hour acellular *in vitro* incubation test	NRCWE	The 24-hour dissolution ratio of NM-204 was measured in three different media: 0.05% BSA in water, Gambles solution and Caco 2 media. Both NM-204 and the Al impurities are partially soluble in 0.05% BSA in water and Caco2 media but amounts vary considerably with medium. In Gambles solution only NM-204 is partially soluble. The relative amounts of dissolved Al impurities compared with dissolved Si differ depending on medium, which suggests different solubility behaviour of the Al impurity and NM-204 depending on the medium.
Crystalline phase		
XRD	JRC	Synthetic amorphous silicon dioxide
	NRCWE	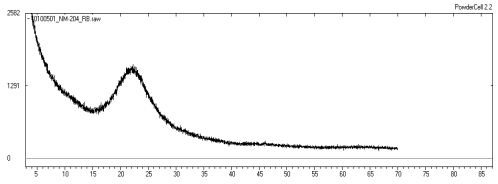 Synthetic amorphous silicon dioxide
	IMC-BAS	Synthetic amorphous silicon dioxide
Dustiness		
Small Rotating Drum	NRCWE	Inhalable dustiness index (n=3) 24969±601 Respirable dustiness index (n=3) 1058
Vortex Shaker Method	INRS	Respirable dustiness index (n=1) 140000
Crystallite size		
SAXS	CEA	Amorphous material.

XRD	JRC	Synthetic amorphous silicon dioxide
	NRCWE	Synthetic amorphous silicon dioxide
	IMC-BAS	Synthetic amorphous silicon dioxide
Representative TEM picture(s)		
TEM	CODA-CERVA, IMC-BAS	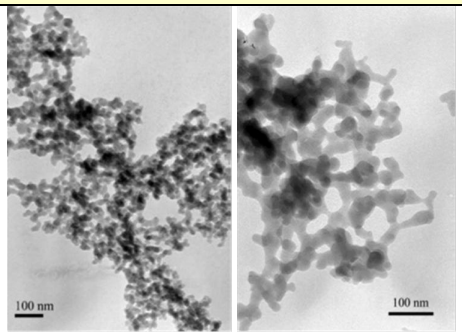 Aggregates with complex, open structure.
Particle size distribution		
SAXS	CEA	Equivalent diameter for spheres: 21nm (Primary particle size)
TEM	CODA-CERVA	Primary particle size: 10-15 nm (manual measurements)
	IMC-BAS	Primary particle size: 19
TEM	CODA-CERVA, IMC-BAS	Number (expressed in %) of SAS NM particles smaller than 100 nm, 50 nm and 10 nm <100 nm - 71.2%, <50 nm - 36.4% <10 nm - 0.3%
DLS		Study not performed
CLS	JRC	Peak (nm): 98, half width: 203, CLS PdI: 2.99
Specific Surface Area		
BET	IMC-BAS	136.6 (m^2/g)
SAXS	CEA	131±22.9 (m^2/g)
BET	JRC	Sample stored at 40°C: single point: 131.7462 (m^2/g); multi point: 134.3128 (m^2/g). Sample stored at -80°C: single point: 132.057 (m^2/g); multi point: 134.6187 (m^2/g).
Zeta Potential (surface charge)		
Zetametry		Study not performed
Surface Chemistry		
XPS	JRC	The following elements were identified in the surface of NM-204: O (71.9 at%), Si (23.2 at%), Na (0.5 at%) and C (4.3 at%). The presence of C is considered to be due to surface contamination.

TGA	NRCWE	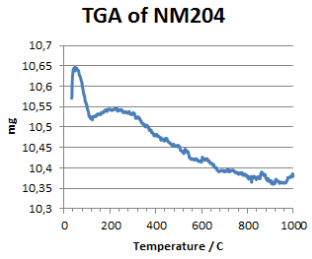 Significant mass loss below 100°C (water). A 0.5 wt% gradual mass-loss above 110°C may indicate organic coating
GC-MS	NRCWE	GC-MS analysis results (retention time in min.): Tetramtehyl silicate:4.9; Hexadecanoic acid methyl ester: 33.4; Hexadecanoic acid: 33.9; Octadecanoic acid: 35.8
Photo-catalytic activity		
End-point not relevant for SAS		
Pour-density		
Weighing	INRS	0.16 g/cm^3 (6 wt.% water content)
Porosity		
BET	IMC-BAS	Micropore volume (mL/g): 0.00666
Octanol-water partition coefficient,		
End-point not relevant		
Redox potential		
OxoDish fluorescent sensor plate for O_2 detection	NRCWE	The evolution of O_2 level during 24-hour incubation was measured in three different media. Different dO_2 values were observed for all applied media however in 0.05% BSA in water and Gambles solution, for all three different concentration of NM-204, the same behaviour of dO_2 was observed. In case of Caco2 media a clear increment in dO_2 level was only observed at lowest dose suggesting O_2.The maximum O_2 changes observed for NM-204 is on the order of 30 µmol/ml. The results suggest that NM-204 generally has negligible redox activty.
Radical formation		
HPLC + UV	NRCWE	Using the benzoic acid probe to form 4 hydroxy benzoic acid in a phosphate buffered hydrous solution, gave no detectable concentration OH radicals.
Composition		
ICP-OES	CODA-CERVA	>0.01%: Al, Na(>0.1%), S 00.5-0.01%: Ca, 0.001-0.005%: Fe, Zr
EDS	IMC-BAS	Na-1800 ppm, Al- 4800 ppm, S- 2100 ppm, Si -45.96 (wt %), O (wt%) calculated- 53.17

15. References

Baron P.A., Maynard A.D. and Foley M. (2002) Evaluation of Aerosol Release During the Handling of Unrefined Single Walled Carbon Nanotube Material. NIOSH DART-02-191 December 2002

Barrett P.J. (1980) The shape of rock particles, a critical review. Sedimentology, 27(3):291-303.

Batenburg K.J., Bals S., Sijbers J., Kubel C., Midgley P.A., Hernandez J.C., Kaiser U., Encina E.R., Coronado E.A. and Van Tendeloo G. (2009) 3D imaging of nanomaterials by discrete tomography. Ultramicroscopy, 109(6):730-740.

Bau S., Witschger O., Gensdarmes F., Rastoix O. and Thomas D. (2010) A TEM-based method as an alternative to the BET method for measuring off-line the specific surface area of nanoaerosols. Powder Technology, 200(3):190-201.

Boldridge D. (2010) Morphological Characterization of Fumed Silica Aggregates. Aerosol Science and Technology, 44(3):182-186.

Brasil A.M., Farias T.L. and Carvalho M.G. (1999) A recipe for image characterization of fractal-like aggregates. Journal of Aerosol Science, 30(10):1379-1389.

Briggs D. and Seah M.P. (1983) Practical surface analysis, 2nd ed, vol1, Wiley, New York.

Brunauer S., Emmett P. H. & Teller E. (1938) Adsorption of gases in multimolecular layers. J. Am. Chem. Soc. 60, pp. 309-319

Calzolai L., Gilliland D., Garcia C.P. and Rossi F. (2011) Separation and characterization of gold nanoparticle mixtures by flow-fioeld-flow fractionation. Journal of Chromatography A,1218 (27), pp. 4234-4239.

Cedervall T., Lynch I., Lindman S., Berggård T., Thulin E., Nilsson H., Dawson K.A. and Linse S. (2007) Understanding the nanoparticle–protein corona using methods to quantify exchange rates and affinities of proteins for nanoparticles. The National Academy of Sciences of the USA, PNAS vol. 104 no.7 pp. 2050-2055.

Christensen V.R., Jensen S.L., Guldberg M. and Kamstrup O. (1995) Effects of chemical composition of man-made vitrous fibers on the rate of dissolution in vitro at different pHs. Environmental Health Perspectives 102/5, 83-86.

Cho W.-S., Duffin R., Howie S.E.M., Scotton C.J., Wallace W.A.H., MacNee W., Bradley M., Megson I.L. and Donaldson K. (2011) Progressive severe lung injury by zinc oxide nanoparticles; the role of Zn^{2+} dissolution inside lysosomes. Particle and Fibre Toxicology 2011, 8:27

Chu Z., Huang Y., Tao Q. and Li Q. (2011) Cellular uptake, evolution, and excretion of silica nanoparticles in human cells. Nanoscale, 3(8):3291-3299.

De Temmerman, P.-J., van Doren E., Verleysen E., van der Stede Y., Francisco M.A.D. and Mast J. (2012) Quantitative characterization of agglomerates and aggregates of pyrogenic and precipitated amorphous silica nanomaterials by transmission electron microscopy. Journal of Nanobiotechnology 2012, **10**:24

Dick C.A.J., Brown D.M., Donaldson K. and Stone V. (2003) The role of free radicals in the toxic and inflammatory effects of four different ultrafine particle types. Inhalation toxicology 15/1, 39-52

EC (European Commission) (2011) Commission Recommendation of 18 October 2011 on the definition of nanomaterial (2011/696/EU). OJ L 275, 20.10.2011, 38-40

EFSA (2011) Guidance on the risk assessment of the application of nanoscience and nanotechnologies in the food and feed chain [http://www.efsa.europa.eu/en/efsajournal/doc/2140.pdf]

Friedrich H., de Jongh P.E., Verkleij A.J., de Jong K.P. (2009) Electron tomography for heterogeneous catalysts and related nanostructured materials. Chem Rev, 109(5):1613-1629

Förster H. and Tiesler H. (1993) Contribution to comparability of in vitro and in vivo man-made mineral fibre (MMMF) durability experiments. Glastechnology Bereitung 66/10, 255-266.

Hill R.J. and Madsen I.C. (1986) The effect of profile step width on the determination of crystal structure parameters and estimated standard deviations by X-ray Rietveld analysis. Journal of Applied Crystallography 19, 10-18. DOI: 10.1107/S0021889886090076

ISO (2004) ISO 13322-1: Particle size analysis -Image analysis methods-. In: Part 1: Static image analysis methods.

ISO (2008) ISO 9276-6: Part 6: Descriptive and quantitative representation of particle shape and morphology. In: Representation of results of particle size analysis. Geneva.

Jensen K.A et al. (2012). Presentation. "Nanomaterial dustiness. A comparison between three different methods" http://www.nanosafe.org/home/liblocal/docs/Nanosafe2012/presentations%20orales/Session%205/O5c1%20Jensen%20et%20al_Dustiness%203%20Methods%20Comparison_NANOSAFE2012%20vs2%20[Mode%20de%20compatibilit%C3%A9].pdf

Jiang J., Oberdörster G. and Biswas P. (2009) Characterization of size, surface charge, and agglomeration state of nanoparticle dispersions for toxicological studies. Journal of Nanoparticle Research, 11(1):77-89.

Kim S.H., Mulholland G.W. and Zachariah M.R. (2009) Density measurement of size selected multiwalled carbon nanotubes by mobility-mass characterization. Carbon, 47, 1297-1302.

Krumbein W.C. and Sloss L.L. (1963) Stratigraphy and Sedimentation. San Francisco

Lengyel J.S., Milne J.L. and Subramaniam S. (2008) Electron tomography in nanoparticle imaging and analysis. Nanomedicine (London), 3(1):125-131.

Linsinger T, Roebben G., Gilliland D., Calzolai L., Rossi F., Gibson N. and Klein C. (2012) Requirements on measurements for the implementation of the European Commission definition of the term 'nanomaterial'. 52 pp. EUR 25404 EN

Mastronarde D.N. (1997) Dual-axis tomography: an approach with alignment methods that preserve resolution. J Struct Biol, 120(3):343-352.

Masuda H. and Gotoh K. (1999) Study on the sample size required for the estimation of mean particle diameter. Advanced Powder Technology, 10(2):159-173.

Merkus H.G. (2009) Particle Size Measurements. 1 edn. Pijnacker: Springer.

Nel A.E., Madler L., Velegol D., Xia T., Hoek E.M., Somasundaran P., Klaessig F., Castranova V. and Thompson M. (2009) Understanding biophysicochemical interactions at the nano-bio interface. Nature Materials, 8(7):543-557.

Nobbman U., Connah M., Fish B., Varley P., Gee C., Mulot S., Chen J., Zhou L., Lu Y., Sheng F., Yi J. and Harding S.E. (2007) Dynamic light scattering as a relative tool for assessing the molecular integrity and stability of monoclonal antibodies. Biotechnology and Genetic Engineering Reviews 24: 117-128

Nordstöm, D.K. and Munoz, J.L. (1994) Geochemical Thermodynamics. Second edition. Blackwell Scientific Publications. 493 pp.

OECD (2010). ENV/JM/MONO(2009)20-REV-ENG. Guidance Manual for Sponsors, OECD, Paris.

OECD (2012). ENV/JM/MONO(2012)40. Guidance on sample preparation and dosimetry for the safety testing of manufactured nanomaterials, OECD, Paris.

Olferta J.S., Symonds J.P.R. and Collings N. (2007) The effective density and fractal dimension of particles emitted from a light-duty diesel vehicle with a diesel oxidation catalyst. Journal of Aerosol Science, 38, 69-82.

Oosthuizen L., Swart H. C., Viljoen P. E., Holloway P. H. and Berning G. L. P. (1997) Applied Surface Science, 120, 9.

Penczek P., Marko M., Buttle K. and Frank J. (1995) Double-tilt electron tomography. Ultramicroscopy 60(3):393-410.

Podczeck F. and Mia Y. (1996) The influence of particle size and shape on the angle of internal friction and the flow factor of unlubricated and lubricated powders. International Journal of Pharmaceutics, 144(2):187-194.

Powers K.W., Brown S.C., Krishna V.B., Wasdo S.C., Moudgil B.M. and Roberts S.M. (2006) Research Strategies for Safety Evaluation of Nanomaterials. Part VI. Characterization of Nanoscale Particles for Toxicological Evaluation. Toxicol Sci, 90(2):296-303.

Pyrz W.D. and Buttrey D.J. (2008) Particle Size Determination Using TEM: A Discussion of Image Acquisition and Analysis for the Novice Microscopist. Langmuir, 24(20):11350-11360.

Riley C.M., Rose W.I. and Bluth G.J.S. (2003) Quantitative shape measurements of distal volcanic ash. Journal of Geophysical Research, 108(B10):2504.

Roebben, G., Rasmussen, K., Kestens, V., Linsinger, T. P. J., Rauscher, H., Emons, H., Stamm, H. (2013) Reference materials and representative test materials: the nanotechnology case. Journal of Nanoparticle Research, Vol. 15, pp. 1455-1468.

SCENIHR (2009). Scientific Committee on Emerging and Newly Identified Health Risks (SCENIHR), Opinion on “Risk Assessment of Products of Nanotechnologies”, Brussels.

SCENIHR (2010) Scientific Basis for the Definition of the Term “Nanomaterial” [http://ec.europa.eu/health/scientific_committees/emerging/docs/scenihr_o_030.pdf]

Schneider T. and Jensen K.A. (2008) Combined single drop and rotating drum dustiness test of fine to nanosized powders using a small drum. Annals of Occupational Hygiene 52/1: 23-34.

Schneider T. and Jensen K.A. (2009) Relevance of aerosol dynamics and dustiness for personal exposure to manufactured nanoparticles. J Nanopart Res 11:1637–1650

Sebastian K., Fellman J., Potter R., Bauer J., Searl A., de Meringo A., Maquin B., de Reydellet A., Jubb G., Moore M., Preininger R., Zoitos B., Boymel P., Steenberg T., Madsen AL., Guldberg

M. (2002) EURIMA test guideline: In vitro acellular dissolution of man-made vitrous silicate fibres. Glass Science Technology 75/5, 263-270.

Tong J., Arslan I. and Midgley P. (2006) A novel dual-axis iterative algorithm for electron tomography. J Struct Biol 2006, 153(1):55-63.

Van Doren E., De Temmerman P.-J., Francisco M and Mast J. (2011) Determination of the volume-specific surface area by using transmission electron tomography for characterization and definition of nanomaterials. Journal of Nanobiotechnology, 9(1):17.

Wiecinski, P.N., Metz K.M., Mangham, A.N., Jacobson, K.H., Hamers, R.J., Pedersen, J.A (2009) Gastrointestinal biodurability of engineered nanoparticles: Development of an in vitro assay Nanotoxicology Volume: 3 Issue: 3 Pages: 202-U66

Witschger O., Brouwer D., Jensen K.A., Koponen I.K., Berges M., Jankowska E., Dahman D., Burdett G. and Bard D. (2011) DUSTINANO: A PEROSH initiative towards a harmonized approach for evaluating the dustiness of nanopowders. 5th International Symposium on Nanotechnology, Occupational and Environmental Health August 9 - August 12, 2011 — Boston, MA, USA, in abstract book, p.178

Xia T., Kovochich M., Brant J., Hotze M., Sempf J., Oberley T., Sioutas C., Yeh J.I., Wiesner M.R., Nel, A.E. (2006) Comparison of the abilities of ambient and manufactured nanoparticles to induce cellular toxicity according to an oxidative stress paradigm, Nano Letters 6/8, 1794-1807

A. Appendix. SOP: Dynamic Light Scattering Measurements and Data Treatment

General description of scientific background

Dynamic Light Scattering (DLS), also called Photon Correlation Spectroscopy (PCS) or Quasi-Elastic Light Scattering (QELS), is a technique of characterization of colloidal systems based on the scattering of visible light resulting from the difference in refractive index between the dispersed colloids and the dispersion medium. The method may be applied for sizing particles suspended in a liquid in the range from about 0.6 nm to about 6 μm depending on the optical properties of the material and medium.

The principle in DLS is measurement of fluctuations in laser light scattered by vibrating particles suspended in a liquid as function of time. The vibration is due to Brownian motion caused by collision with solvent molecules of the liquid. The Brownian motion varies as a function of particle size and causes variation in the intensity of scattered light as function of time. A correlator compares the signal measured at a time t_0 with different very short time delays *dt* (autocorrelation). As the particles move, the correlation between t_0 and subsequent *dt* signals decreases with time, from a perfect correlation (1) at t_0, to a complete decorrelation (0) at infinite time (order of milliseconds). In the case of big particles, the signal changes slowly and the correlation persists for a long time, whereas small particles have high Brownian movement causing rapid decorrelation.

A DLS instrument measures the velocity of Brownian motion, defined by the translational diffusion coefficient *D* of the particles. The particle size, or more precisely its hydrodynamic diameter d_h, is then estimated using the Stokes-Einstein equation assuming spherical shape:

$$d_h = \frac{kT}{3\pi\eta D}$$

k: Boltzmann's constant
D: translational diffusion coefficient
T: absolute temperature
η: viscosity

It should be noted that even if a particle is really spherical, the spherical DLS size is fundamentally different from the physical spherical size. The hydrodynamic size includes the double-layer of highly polarized water molecules around the physical particle. When the particle morphology is highly non-spherical, the hydrodynamic size should be understood as the equivalent hydrodynamic spherical size. Establishment of mean hydrodynamic size and

size distributions (intensity, number, volume) is reached by DTS software algorithms, by fitting the correlation function in the data treatment.

Chemicals and equipment

- Test material or chemical
- Dispersion medium
- Ultrasonic probe equipped with a standard 13 mm disruptor horn
- Dynamic Light Scattering apparatus
- Viscosimeter (e.g, Malvern Inc., SV-10 Vibro Viscometer) *Optional for measurement of true viscosities*
- Pipette and pipette tips
- Syringes and syringe filters or filter paper

Specificities for Zetasizer NanoZS from Malvern Instruments

DLS measurements rely on non-invasive back scatter (NIBS®) technology developed by Malvern Instruments, in which the signal is detected at 173°. The signal is treated by a digital correlator, and transmitted to the computer. DTS software enables the fitting of correlation data either by a monomodal mode, called the cumulant analysis (as defined by ISO 13321 Part 8) to obtain a mean size (Z-average diameter) and a polydispersity index (PdI), or by a multiple exponential known as the **CONTIN method** to obtain a distribution of particle sizes.

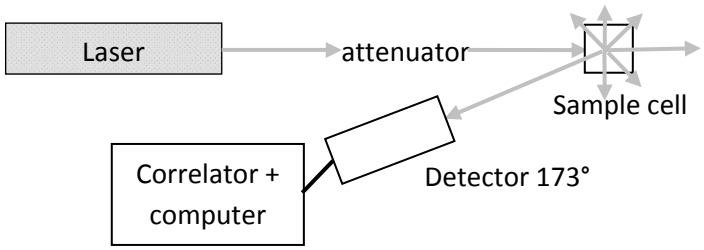

Figure A1. Simplified sketch of the optical configuration for DLS measurement on Zetasizer Nano ZS

Specificities for Vasco Cordouan

The VASCO™ has an original design of the sample cell (thin layer technology) and optics arrangement. The configuration allows also the photo-detector to collect the back-scattered light signal at an angle of 135° (Figure C.2 below). In addition, the cell is hermetically closed by a mechanical system that includes a mobile glass rod with a photon trap. This rod can

both absorb the excess of transmitted light and control the sample thickness, down to few tens of microns. Decreasing the thickness of the sample (and then volume of analysis) reduces significantly the probability for a photon to be scattered several times. Thus, the multiple-scattering artifact is well reduced using this unique design. Also the thin layer technology prevents the sample from local heating.

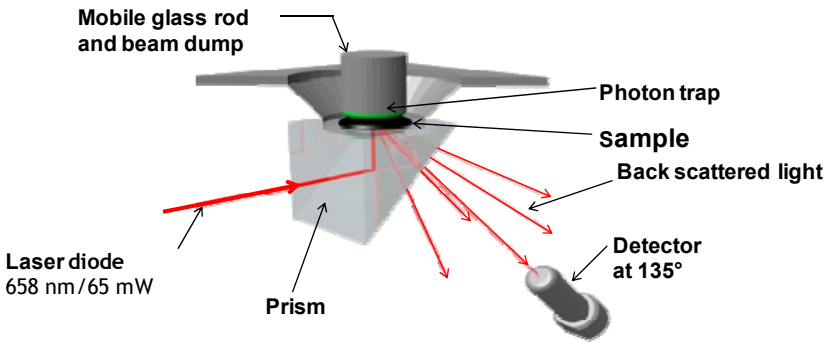

Figure A2. Configuration for DLS measurements on VASCO™

The NanoQ™ software proposes two acquisition modes:

- **Continuous mode where the data acquisition is stopped by the user.**
- Statistical mode where successive data acquisitions are performed automatically following a pattern set by the user (e. g. 15 successive acquisitions of 60s each).

The NanoQ™ software supports two different algorithms for data analysis:

- **Cumulant method** (according to ISO 13321) for mono-disperse samples. The monomodal analysis of the autocorrelation function provides only a mean size value (light scattering intensity-averaged diameter also named as Z-averaged diameter) and a measure of the broadness of the distribution through the polydispersity index.
- **Padé-Laplace** method for polydisperse samples, which does not make any hypothesis for the number of components for multi-exponential analysis. The method gives as a result a discrete density of intensities (histogram), each of them corresponding to a given hydrodynamic diameter. Volume and number histograms are also available based on the Pade-Laplace analysis combined with a Mie algorithm. The NanoQ™ does not provide results expressed as continuous distribution curves for polydisperse samples.

Sample preparation

Dispersions for analysis are prepared by mixing particulate material into a dispersion medium. A sub-sample of a suitable concentration is added to suitable measurement

cuvettes. Dispersions are typically produced by sonication in a dispersion medium; SOPs were developed for dispersing the NMs, see e.g. http://www.nanogenotox.eu. The dispersion medium must be filtrated before use to avoid any dust contamination. This can be done by using syringe filters or filter paper with high efficiency. Usually filters with a 0.2 to 0.45 μm pore-size are sufficient for filtration of dispersion media.

The concentration required for analysis depends e.g. on the relative refractive index between particles and dispersion medium, the particle size and polydispersity and the sample absorption. Malvern apparatus is designed to measure samples over a large range of concentration and size of particles. Specifications of sample properties (concentration range, size of nanoparticles, medium) is found in the documentation from Malvern Instrument on their website. The dispersion must be stable during the measurement.

Measurements

Summary

Measurements are performed at ambient temperature according to the procedure appropriate for each type of apparatus. Sample properties such as material and dispersant refractive indices and viscosity are entered in the software for analysis. Number and duration of run and optical configuration are automatically optimized by the software for Malvern apparatus. For Cordouan apparatus, 15 runs of 60s are performed.

About ZetaSizer NanoZS from Malvern Instrument

DLS measurements can be performed in disposable polystyrene cuvettes (optical path 1 cm, volume 1 mL) or alternatively glass cuvettes (at NRCWE) or in semi micro polystyrene disposable cuvettes (optical path 1 cm, volume 500 µL) or in clear disposable zeta cells DTS1061 just before zeta potential measurements (at CEA). The measurements are repeated 3 (CEA) or 6 (NRCWE) times with automatic determination of duration and number of runs, and averaged. The repeated analyses are conducted to enable omission of measurements with poor correlation data or abnormal solutions to the correlation function (must be carefully considered).

The following standard procedure is recommended as the general approach for DLS measurement of NM dispersions:

- Turn on the computer and DLS instrument
- Allow the instrument to warm up according to the manufacturer's recommendation (30 min).

- *Optional: Complete viscosity measurement using the SV-10 Vibro Viscometer mounted with the 10 ml flow-reactor placed in a thermostated water jacket. The measured dynamic viscosity is used as input data for the specific dispersion measured in the DTS software.*
- Upload the DTS software and the "Measurement" window for entering material specific data on dispersion medium, test material and specific analytical settings:
    - Refractive index and absorption values for dispersant and NM.
    - Temperature conditions (25°C) and equilibration time for measurement.
    - The General purpose model is selected for initial evaluation of data and is the most generic model for calculation of size.
- Select a sample cuvette, ensure that it is dustfree and has no defects or scratches in the measurement area of the cuvette. Some producers have been found to deliver cuvettes with scratches or folding structure in the measurement area at one side of the cuvette. Dust may be cleaned out by rinsing the cuvette in dispersion medium.
- Fill in a suitable volume of dispersion into a measurement cuvette using a pipette.
- Place the sample cuvette in the sample holder in the DLS instrument.
- Run analysis (click "play" on the measurement window).
- The size analysis may be immediately accepted if the DTS Expert advice denotes the result quality as "Good". If the result is not of good quality, the sample should be further analyzed for presence of dust, cuvette errors, large particles, sedimentation, wall-deposition etc.
- If the sample contains particles with large spread in size distribution, one may consider filtering the sample through different syringe filters to investigate presence of small nm-size particles. Small nm-size particles may not be fully resolved when larger particles are present due to the large drop (10^6 per factor of ten in size ratio) in scattered light intensity with size.
- If parameters such as refractive indexes, absorption coefficient or viscosity were wrong or unknown at the measurement time, the correction can be made afterwards using the command Edit (right click on the measurement) in the DTS software.

The measurement conditions generally used at CEA and NRCWE are listed in Tables A1 and A2, respectively. The viscosity considered for measurement is generally the one of pure water, 0.8872 cP, but the data can be corrected afterwards for the values measured.

At CEA, the viscosity of water is considered for all samples prepared without addition of BSA or in the pH-adjusted protocol. For suspensions prepared according to the validated NANOGENOTOX protocol, all data were corrected considering the real viscosities measured by NRCWE (usually around 0.99 cP – 1 cP).

Table A1. Conditions used at CEA, refractive index (R_i), absorption or imaginary part (R_{abs}) and dynamic viscosity.

	Water (STP)	$SiO_{2(amorphous)}$
R_i	1.33	1.50
R_{abs}		0.01
Viscosity [cP]	0.8872	-

Table A2. Conditions used at NRCWE, refractive index (R_i), absorption or imaginary part (R_{abs}) and dynamic viscosity.

	Water (STP)	$SiO_{2(amorphous)}$
R_i	1.33	1.544
R_{abs}		0.20
Viscosity [cP]	0.8872	water

DLS measurements for stability over time

DLS measurements for stability over time were performed on 500 µL suspension in semi micro polystyrene cuvette (CEA) or 1 mL in standard disposable cuvette (NRCWE). The first measurement at t_0 is performed as usual DLS measurements (described above) with automatic determination of parameters. The number of the run, duration, position and choice of attenuator are then recorded and used for the following measurements, which are scheduled over a period of approximately 16 h, usually every 30 min.

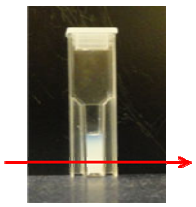

Figure A3. Semi micro cuvette used at CEA for DLS measurements over time. The arrow represents the position of the laser beam probing the suspension.

On Vasco™ from Cordouan Technologies

The following procedure was used and is recommended:

- Turn on the Vasco™ 30 minutes before starting a measurement.
- Run the NanoQ™ software, enter the material specific data on dispersion medium and test nanomaterial as well as specific analytical settings (see table below). Temperature is set to 21 °C.
- Prior to any measurement, it is strongly recommended to carefully clean the cell to avoid pollution from previous measurements. The cleaning operation has to be made gently according to the manufacturer's recommendations.
- Once the cell is perfectly clean, introduce the sample to analyse. For that, use a plastic pipette to extract a sample from the suspension to analyse and drop off a small volume (≈ 2 µl) in the centre of the cell as shown on the picture below. In order the perform measurements under good conditions, the suspension to be analysed should cover entirely the bottom of the cell, as this correspond to the upper surface of the glass prism guiding the laser beam. For the suspensions analysed in NANOGENOTOX, the thickness of the liquid was set to about 1.5mm (position "up" of the dual thickness controller). After closing the mechanical system, measurements can begin.

- Run the analysis.
- Process the data.

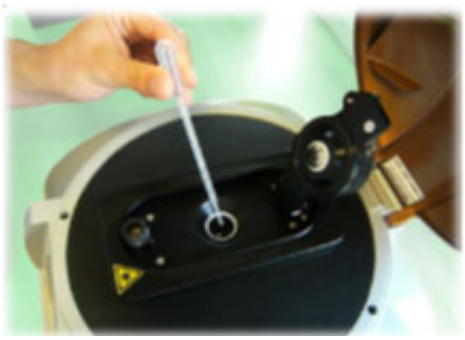

Figure A.4. Illustration of sample deposition on Vasco™ apparatus.

The conditions used at INRS for the analysis with the Vasco™ are reported in Table A3.

Table A3. Conditions used at INRS, refractive index (R_i), absorption or imaginary part (R_{abs}) and dynamic viscosity.

	Water	$SiO_{2(amorphous)}$
R_i	1.33	1.54
R_{abs}		0.2
Viscosity [cP]	0.97	0.97

For all measurements performed with the Vasco™ in the NANOGENOTOX project, the "statistical mode" was used, i.e. 15 successive measurements, each with a duration of 60 seconds.

Data treatment

Summary

A monomodal model, the cumulant analysis is used to treat the raw data correlograms (decaying as exponential). It determines a Z-average (diameter of particles scattering with higher intensity) and a polydispersity. Since these samples are quite polydisperse, more sophisticated models, such as the CONTIN method, are applied as multimodal analysis to reveal size distributions.

About ZetaSizer NanoZS from Malvern Instrument

The actual raw data obtained from a dynamic light scattering experiment is the autocorrelation function, which is an exponential decay with a characteristic time related to the size of the diffusing object. An example of correlation data is shown on Figure A5 for two NM104 samples (0.5 g/L TiO_2, 0.036 mol/L of monovalent salt), one stable suspension at pH 2.8 (red curves) and the supernatant of an aggregated sample at pH 10.1 (green curves). The data used are the averaged data for 3 consecutive measurements.

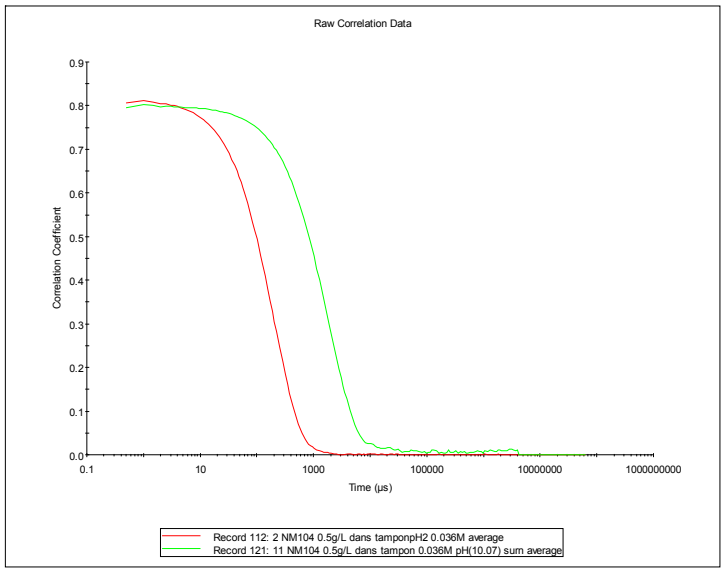

Figure A5. Example of raw correlation data for two NM104 samples (0.5 g/L TiO_2 in 0.036 mol/L ionic buffer), one stable suspension of relatively dispersed particles at pH2.8 (red curve), and one unstable sample of big aggregates at pH10.1 (green curve, measure on supernatant).

The raw correlation data are analysed to extract information on size and distribution. Various algorithms can be used and the simplest is the *Cumulants analysis* which fits the data by approximating the single exponential decay by a degree 2 Taylor development function. This provides a Z-average mean value, which corresponds to the particle size diffusing with the highest intensity, and a polydispersity index (PdI) for this monomodal distribution. In the DTS software, the corresponding graph is entitled “Cumulants fit”. The method applies to monomodal distributions with polydispersity lower than 0.25, and is in agreement with ISO 13321 standard. For higher polydispersity, the two parameters Z-average and PdI alone do not accurately describe the sample size distribution and a multimodal analysis is necessary.

Some examples of Cumulant fits analysis applied to NM-104 (TiO_2) are shown in Figure A6. The high PdI obtained for the sample at pH 10 indicates that this model is not advanced enough to determine an accurate size distribution for this sample.

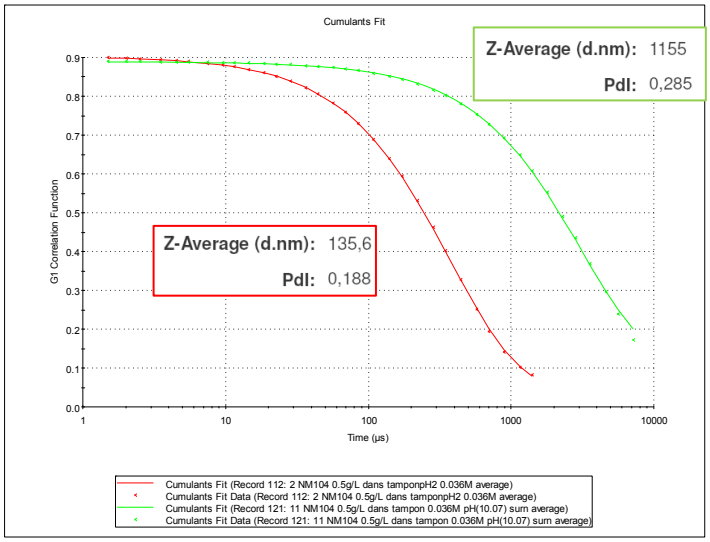

Figure A6. Example of data and fits by the Cumulant method, together with calculated values of Z average and polydispersity, for two NM-104 (TiO_2) samples (0.5 g/L TiO_2 in 0.036 mol/L ionic buffer, stable suspension at pH2.8 in red and unstable sample of big aggregates at pH10.1 in green).

For polydispersity indices between 0.08 and 0.5, the correlation data can be better analyzed by the *CONTIN method*. It fits the correlation data to the best combination of a set of 24 exponential functions, giving rise to a size distribution over 24 granulometric classes. In DTS software, this fit is denominated as “distribution fit”, “data fit” or “size fit” (Figure A7).

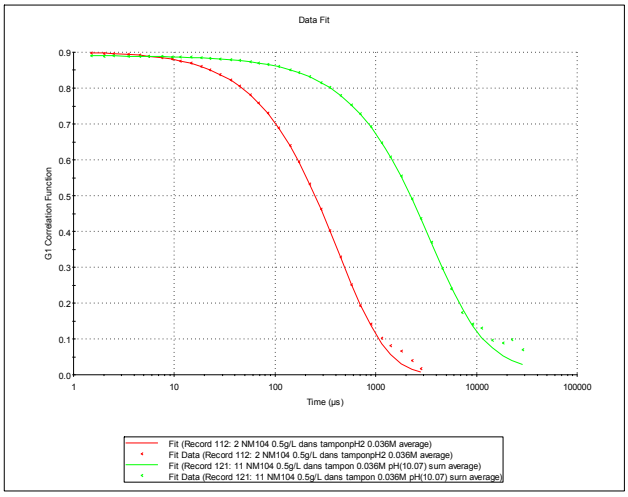

Figure A7. Example of data and fits by the CONTIN method, for two NM-104 (TiO_2) samples (0.5 g/L TiO_2 in 0.036 mol/L ionic buffer, stable suspension at pH2.8 in red and unstable sample of big aggregates at pH10.1 in green).

Taking into account the refractive indices of material and dispersant, Mie Theory can be applied to represent size distribution in volume. The number size distribution can then be calculated from simple geometrical considerations (Figure A8). Distribution data can be

retrieved from DTS software in the form of tables of diameter, percentage and width for the three main peaks.

It should be noted that for 2 particles with a size ratio of 10, the bigger particle contributes 10^3 times more than the smaller one to the volume distribution, and 10^6 times more to the distribution by intensity. Since DLS measurements are based on intensity, this means that the light scattered by a few large particles may totally cover the signal from the smaller ones.

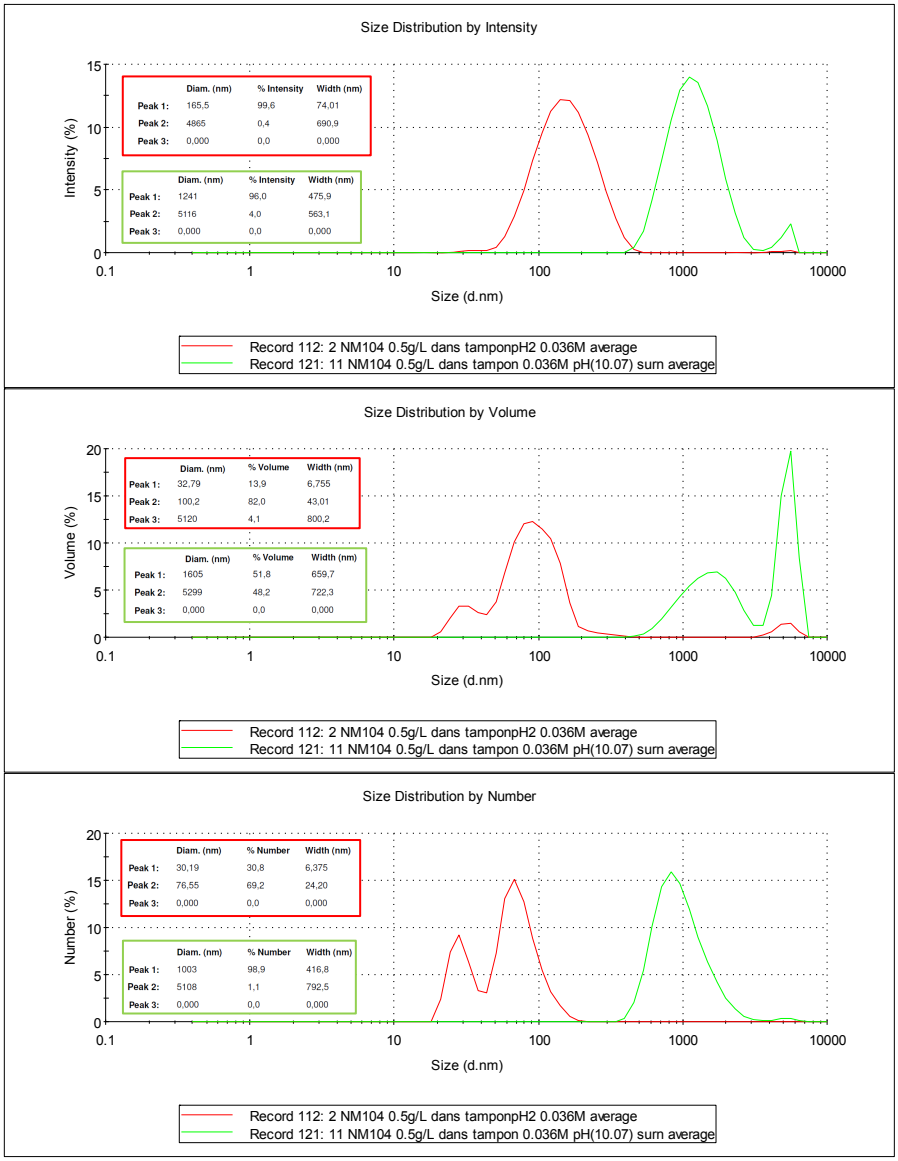

Figure A8. Example of size distributions by intensity, by volume and by number, together with tables of numerical values for the three main peaks of each distribution, for two NM-104 (TiO_2) samples (0.5 g/L TiO_2 in 0.036 mol/L ionic buffer, stable suspension at pH2.8 in red and unstable sample of big aggregates at pH10.1 in green).

After controlling correlation data and fits, an average measurement is calculated with the software. As an example, the main graphs observed for the 3 initial measurements of a

sample of NM-104 at pH 2.8 (0.5 g/L TiO_2, 0.036 mol/L of monovalent salt) are displayed on Figure A9. Since the correlation data are good, all 3 measurements are taken into consideration for the averaged data.

The main parameter reported in the results section is *"Z-average"*, which represents the mean size contributing to the major part of the signal **in intensity**. For polydisperse samples, this value mostly gives a hint about the aggregation state of the particles but does not reflect the hydrodynamic size of most of the dispersed particles (in number), which of course is much lower. When Z-average is higher than approximately 500 nm, it can only be deduced that there are big aggregates in suspension but the numerical value is usually meaningless.

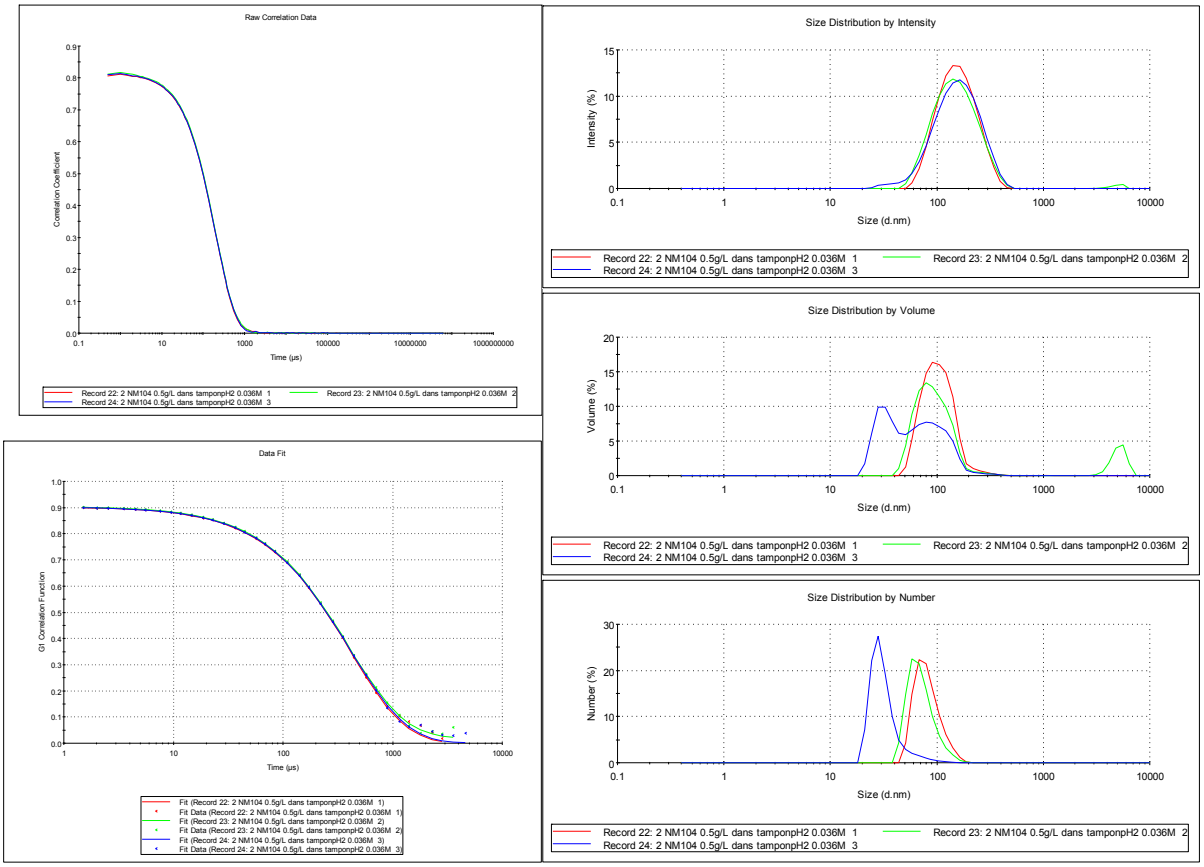

Figure A9. Main graphs reported by DTS software for 3 consecutive measurements of a NM-104 (TiO_2) sample (pH 2.8, 0.5 g/L TiO_2 in 0.036 mol/L aqueous ionic medium)

On Vasco™ from Cordouan Technologies

As for the Zetasizer NanoZS, the raw data obtained from Vasco™ is the autocorrelation function, which is an exponential decaying function with a characteristic time related to the size of the diffusing object.

Comments on use and applicability

DLS is very suitable for size and stability analysis of particles in liquid dispersions. However, great care should be taken in interpretation of data; especially when the sample contains both μm- and small nm-size particles.

For better accuracy of size-determination, it is important to obtain true values of the optical properties and viscosity of the dispersion liquid.

References

Support documents can be downloaded from http://www.malvern.com, application library section.

B. Appendix. The Sensor Dish Reader System

The hydrochemical reactivity was assessed regarding acid-base reactivity and influence on the oxygen balance using a recently developed 24-well SDR (Sensor Disc Reader) system (PreSens Precision Sensing GmbH, Germany) intended for use for in vitro assays (Figure B1). Determination of the acid-base reactivity is particularly important in cell media, where a buffer usually is applied to ensure pH stability in the bioassay. However, if a NM is particular reactive, this pH buffer may be insufficient at sufficiently high NM doses. The O_2 reactivity may another important parameter and relates to hydrochemical reactions that consume or liberate oxygen. Deviations in the O_2-balance can be caused by different reactions including redox-reactions, protonation and deprotonation in the dispersion. These phenomena may be caused by catalytic reactions, but also dissolution, transformation of molecular speciation and precipitation in the medium under investigation.

Figure B1. Sensor Dish Reader, examples of sensor products and illustration of the SDR measurement principle. In this study we used the 24-well Oxy- and HydroDish for O_2 and pH monitoring. Source: PreSens Precision Sensing GmbH, Germany.

The pH variation was measured using the HydroDish® fluorescent sensor plate for pH detection with up to ± 0.05 pH resolution for pH 5 to 9. Measurement is not possible outside of this range.

The O_2 variation was measured using the OxoDish® fluorescent sensor plate for O_2 detection with ± 2 % air saturation resolution. The OxoDish® sensor can measure O2 concentrations between 0 and 250% saturation, corresponding to 0 to 707.6 µmol/l.

In brief, the fluorescent sensor spots are placed at the bottom of each wells in the dishes. For our study, we used 24 well plates. The sensor spot contains a luminescent dye. It is excited by the SensorDish® Reader using a laser diode, placed below the multidish, which is only active when analyses are done, and the sensor luminescence lifetime is detected through the transparent bottom. The luminescence lifetime of the dye varies with the oxygen partial pressure (OxoDish®) and the pH of the sample (HydroDish®), respectively. This signal is converted to oxygen and pH values by the instrument software. The sensor plates are pre-calibrated and the calibration data are uploaded and used for the specific plates used.

Experimental Procedure

Samples were prepared by prewetting the NMs with 0.5% v/v ethanol and dispersion in 0.05% w/v BSA water by probe-sonication following the generic NANOGENOTOX dispersion protocol. Chemically pre-analyzed and approved Nanopure filtered water was used for the batch dispersion to ensure minimum background contamination in the test.

The incubation media included 0.5% BSA-water, low-Ca Gambles solution and Caco 2 medium. The BSA water was included in the study to assess the behavior of the NMS in the batch dispersion medium, which is the first stage in all the biological tests in NANOGENOTOX. The reactivity was tested at doses 0.32, 0.16, 0.08 and 0 mg/ml and a total volume of 2 ml was entered into each well of the SDR plates. Figure B2 illustrates the general procedure.

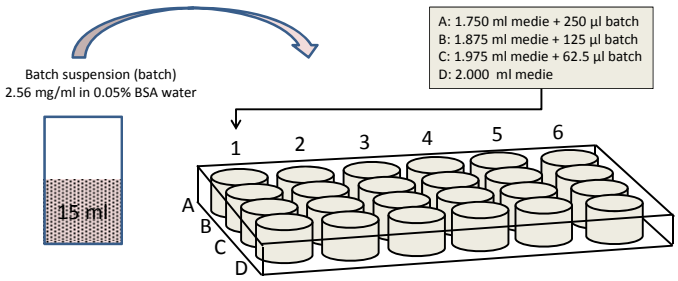

Figure B2. Principal sketch of the dosing into the SDR plates resulting in 2 ml test medium in each well. In this way six dose-response measurements can be made in one test round.

After 24-hours incubation, the maximum dose and control media from the pH and O_2 wells were retrieved by pipette, filtered through a 0.2 µm CAMECA syringe filter and centrifuged in Eppendorf tubes for 60 minutes at 20,000xG RCF using a Ole Dich table top centrifuge. NM samples were placed in the outer ring and pure reference media in the inner ring. Then the upper 1.25 ml of each filtrate from the pH and O_2 wells were sampled, pooled (2.5 ml) in Eppendorf tubes and stabilized with 1 ml 2% HNO_3 water (sample diluted 5/7). The liquids

were then stored in darkness until sent for analyses. All vials were washed and rinsed in acid before use.

Data Treatment and Evaluation

The reactivity of each NM was evaluated qualitatively from the evolution of the pH and O_2 over time for each NM at the four dose levels, including the blank control. The SDR pH-values were plotted directly as function of time. The data were then evaluated visually comparing the SDR values of exposed wells with that of the un-exposed control media as well the readings from the initial medium readings in each of the wells to assess if there would be any systematic off-set in some of the sensors. This sensor-evaluation was always done using the blank control as the assumed correct internal reference value.

For the O_2 analyses, the difference between time-resolved readings from ”exposure doses” and the medium control ($dO_2 = (O_{2,dose} – O_{2,medium\ control})$) were plotted as function of time.

For both pH and O_2, if the SDR readings from the dosed media showed no difference or followed the same trend as the reference media, the NM was assumed to have negligible pH reactivity or influence on the oxygen balance through redox reactivity or dissolution.

Nanomaterial dissolution and biodurability

The NM dissolution and biodurability was assessed from elemental analyses of the solute adjusted for background concentrations in the three test media. It was assumed that maximum dissolution would be observed at the 0.32 mg/ml dose and that equilibrium was reached in 24 hours. Consequently, if the elemental composition of the test materials is given, the results enable calculation of the solubility limit as well as the durability (the un-dissolved residual) of the specific NM in the batch dispersion, the lung lining fluid and the Caco2 media. However, in this study, we have only semi-quantitative elemental composition data on the SAS.

Elemental analysis

The concentrations of dissolved Si elements in the media were analysed using Inductively Coupled Plasma-Optical Emission Spectroscopy. Ti, Al, Fe, Co, and Ni were determined by ICP Mass-spectrometry. Both element series were analysed as a commercial service by Eurofins, DK-6600 Vejen, Denmark. The elemental background concentrations in the three test media were determined on three doublet samples for each media. The elemental concentrations after dissolution were determined in two sub-samples for each NM.

C. Appendix. SOP for surface charge and isoelectrical point by zetametry

General description

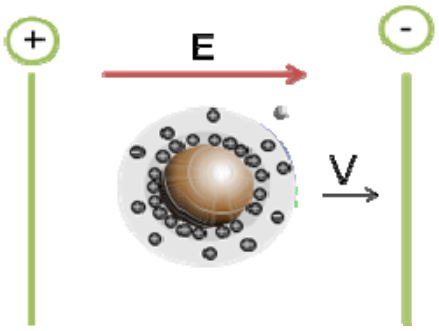

Figure C1. scheme of charged particle in electric field applied between electrodes of zeta cell

Dispersion state and stability of suspensions are governed by an equilibrium between attractive (mainly van der Waals) and repulsive (electrostatic or steric) interactions. A stable suspension is obtained if repulsive interactions overcome the attractive ones, which are responsible for aggregation and subsequent sedimentation. Zeta potential is a good indicator of the magnitude of repulsive interactions between charged particles. The charge at the very surface of the particles is not accessible and Zeta potential corresponds to the potential at the shear plane. This is the boundary between the bulk dispersant and the double layer of solvent and ions moving together with the particles, see Figure C1. The reciprocal Debye length, κ^{-1}, represents the thickness of this double layer. The zeta-potential varies with pH due to protonation-deprotonation of the material surface. From colloid science, a suspension of small particles is considered stable if the zeta-potential exceed |30| mV.

For low pH (acidic medium), the surface of metal oxide (MO) materials is protonated (MOH_2^+), i.e. positively charged. For high pH the deprotonation results in negatively charged particles (MO^-). The pH-value at which the charge is reversed determines the so-called isoelectric point (IEP) where the dispersion is unstable. IEP can be determined by titration, but can also be measured from manually prepared different dispersions displaying the same ionic strength for various pH. The zeta potential can be highly influenced by the properties of the medium, such as ionic strength (by compression of the double layer), or adsorbing molecules or ions (especially multivalent ions).

The zeta potential (ζ) is not directly measurable and is calculated from the measurement of electrophoretic mobility U_E using Henry's equation:

$$U_E = \frac{2\,\varepsilon\,\zeta\,f(\kappa a)}{3\eta}$$

ε: dielectric constant of medium
η: viscosity
κ: inverse of the Debye length, a: radius of a particle
$f(\kappa a)$ = 1.5 for aqueous suspensions in the Smoluchowski approximation

In practice, the sample is exposed to an electric field which induces the movement of charged particles towards the opposite electrode.

Chemicals and equipment

- HNO_3 (analytical grade)
- NaOH (analytical grade)
- $NaNO_3$ (analytical grade)
- Purified water (MilliQ or Nanopure water)
- Ultrasonic probe Sonics & Materials, VCX500-220V, 500 W, 20 kHz equipped with a standard 13 mm disruptor horn, or equivalent
- pH-meter with standard pH probe
- Zetasizer Nano ZS (e.g, Malvern Instruments), equipped with laser 633 nm
- Autotitrator (Malvern MPT-2) –*optional for automatic determination of IEP*
- Malvern computer software (DTS 5.03 or higher) to control the Zetasizer
- Clear, disposable zeta cells (DTS1061 - DTS1060C)

Sample preparation

Summary

Samples for zeta potential measurements are prepared as aqueous suspensions of 1 g/L for SiO_2 nanomaterials with constant ionic strength of 0.036 mol/L (monovalent salt) and controlled pH. They are prepared by dilution of concentrated sonicated stock suspensions of 10 g/L into pH and ionic strength controlled “buffers” prepared by addition of HNO_3, NaOH and $NaNO_3$ in various proportions.

Stock suspension preparation

20 mL of stock suspensions of 10 g/L NM in pure water are prepared as follows:

200 mg of NM are weighed and introduced in a 20 mL gauged vial (with protective gloves, mask and glasses, and damp paper towel around the weigh-scale).

- The 20 mL gauged vial is completed with ultrapure water (MilliQ®)
- The suspension is transferred into a flask suitable for sonication (a 40 mL large-neck glass flask of internal diameter 38 mm was used, height of 20 mL liquid 20 mm), making sure that all the settling material is recovered.
- The suspension is dispersed by ultrasonication for 20 min at 40% amplitude in an ice-water bath. Probe, sample and bath are placed in a sound abating enclosure, and in a fume hood.

Preparation of "buffer" solution

Denominated *"buffer"* solutions are aqueous ionic solutions of Na^+, H^+, NO_3^- and OH^-, designed to display the same ionic strength with a modulated pH.

- A first set of concentrated buffer solutions (0.1 mol/L of salt, various pH) are prepared by addition of HNO_3, NaOH and $NaNO_3$ in various proportions in ultrapure water.
- Then 20 mL of these concentrated buffers are poured into 50 mL gauged vials completed with ultrapure water, giving a new set of buffers with a salt concentration of 0.04 mol/L and a pH ranging from 1.5 to 12.5. The combination of the two buffers gives access to the necessary intermediate pH.
- By this procedure, acidic buffers contain 0.04 mol/L of NO_3^- and various ratios of Na^+/ H^+ as counter ions; likewise, basic buffers contain 0.04 mol/L of Na^+ and various ratios of NO_3^-/OH^-.

Preparation of suspensions for zeta potential measurements and determination of isoelectric point

In this SOP Zeta potential measurements are performed on 1 g/L suspensions for SiO_2 samples. 10 g/L suspensions of the SiO_2 samples are used right after sonication. Series of samples are prepared by addition of 400 µL of concentrated NM suspension and 3.6 mL of 0.04 mol/L buffer solutions in a 5 mL glass flask. This leads to samples of 1 g/L SiO_2 and a constant ionic concentration of 0.036 mol/L in monovalent salt.

For each NM, an additional sample is prepared in MilliQ or Nanopure water with the same NM concentrations, i.e. 400 µL of concentrated NM suspension and 3.6 mL of water.

Measurements and data treatment

Summary

For each suspension of known pH, fixed ionic strength and fixed NM concentration, the measurements for determining the zeta potential are performed on a general purpose mode with automatic determination of measurement parameters. Three measurements are performed and averaged for reporting. For unstable samples, measurements are performed on supernatants. Zeta potentials are then plotted against pH to determine the stability domains and isoelectric points (IEP).

Equilibrium pH of the suspensions are measured and considered as pH values for the reported results. The suspension to be characterized by zetametry are inserted in Malvern patented folded capillary cells with gold electrodes (volume 0.75 to 1 mL), DTS1061. Zeta

measurements (electrophoretic mobility) are performed on the "*general purpose"* mode at 25°C with automatic optimization of laser power, voltage settings, the number of runs (10 - 100) and run duration, and repeated 3 times with no equilibration time as the sample is already at ambient temperature.

The Smoluchowski model (F(κa)=1.5) was used, considering the high polarity of aqueous solvent, and hence a thin double layer around the particles. For the dispersant, the refractive index R_i, absorption R_{abs}, viscosity and di-electric properties considered are the ones of pure water and the table below lists the parameters used for dispersant and material properties.

Table C1. Properties of dispersant and material phases used for zeta potential measurements

	Water (STP)	**$SiO_{2(amorphous)}$**
R_i	1.33	1.5
R_{abs}		0.01
Viscosity [cP]	0.8872	-

Data treatment

Electrophoretic mobility is measured by a combination of laser Doppler velocimetry, a technique based on the phase shift of the laser beam induced by the movement of particles under an electric field, and phase analysis light scattering (patented M3-PALS technique). In this "mixed mode measurement" (M3), the measurement consists of the application of an alternative electric field in two modes, a fast field reversal mode, and a slow field reversal mode. The light scattered at an angle 17° is combined with the reference beam and the resulting signal is treated by the computer (Figure C2). During the fast field reversal mode, the electro-osmose effect is negligible, allowing to determine an accurate mean zeta potential, whereas the slow field reversal mode helps modelling the distribution of potentials.

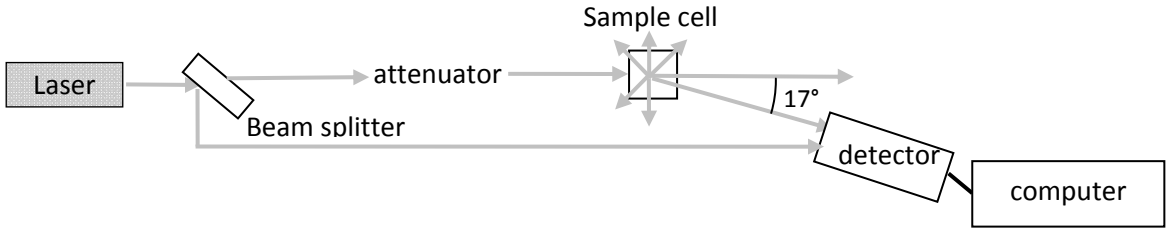

Figure C2. Simplified scheme of optical configuration for zeta potential measurement on Zetasizer NanoZS.

An example of the main data plots returned by DTS software from zeta potential measurements is shown on figure C3 (phase plot and corresponding electric field applied, mean zeta potential and zeta potential distribution).

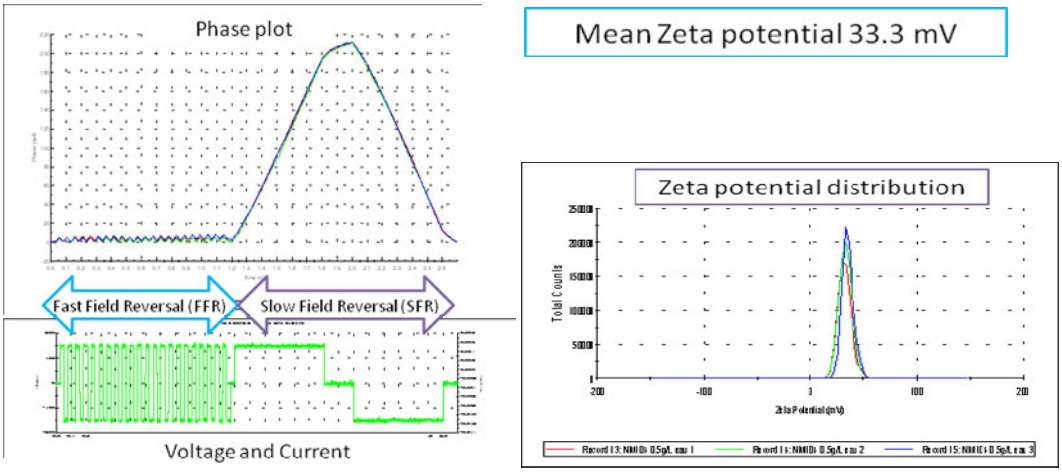

Figure C3. Data plots retrieved from zeta potential measurements on Nanosizer ZS, example of 3 consecutive measurements on a suspension of NM-104 (TiO_2) at 0.5 g/L in pure water.

More details on the results of zeta potential measurements with the M3-PALS technique are available in the documentation from Malvern Instruments and can be downloaded from http://www.malvern.com, application library section. The reported value is the average of zeta potential values from the 3 measurements (determined during the fast field reversal step), with possible exclusion of diverging data.

D. Appendix. SOP for Small Angle X-ray Scattering.

This appendix describes the general procedure applied at CEA/LIONS (Laboratoire Interdisciplinaire sur l'Organisation Nanométrique et Supramoléculaire) to perform Small Angle X-ray Scattering measurements and the data treatment to extract physico-chemical properties of materials. This procedure was applied to characterize the SAS NMs as powders and in aqueous suspension.

General description

Small-Angle X-ray Scattering is a technique based on the interaction between X-rays and electrons to probe the structure of materials. The processed data is the number of X-rays scattered by a sample as a function of angular position of a detector, see Figure D1.

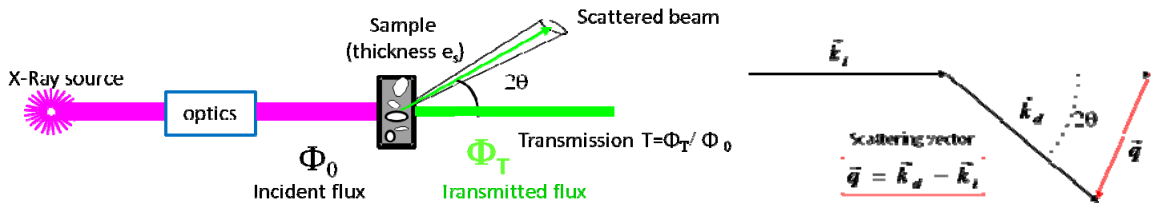

Figure D1. Schematic set up for SAXS and physical quantities

2D raw data images are converted into diffractograms displaying the **scattered intensity *I*** as a function of scattering vector *q* defined by:

$$q = \frac{4\pi \sin\theta}{\lambda}$$

λ : X-ray wavelength

The experimental scattering intensity is defined as the differential scattering cross-section per unit volume of sample and can be expressed as follows:

$$I(q) = \frac{1}{V}\frac{d\sigma}{d\Omega} = \frac{\eta_1 C_{ij}}{\eta_2 (\Phi_0 S T) dt}\frac{1}{\Delta\Omega}\frac{1}{e}$$

σ : scattering cross-section

V : volume of sample

C_{ij}: number of counts detected on a pixel ij during dt

η_1: detector quantum efficiency when measuring the direct beam

η_2: detector quantum efficiency for the count Cij

(φ_0ST): flux (in detector unit counts/s) integrated over the whole beam transmitted by the sample

T: transmission of the sample

$\Delta\Omega$: solid angle covered by one pixel seen from the center of the sample ($\Delta\Omega = p^2/D^2$ with p the pixel size and D the sample to detector distance)

The intensity is then expressed in **absolute scale** (in cm^{-1}) to be independent of the experimental set up parameters (X-ray wavelength, experimental background, time for acquisition, sample thickness, etc.).

General theorems of experimental physics have been developed to extract different properties of nanostructured material from the diffractograms, such as shape of nanoparticles, surface area, interactions occurring, etc. *I(q)* curves can also be theoretically calculated from assumed nanostructures to fit the experimental curves.

In the simple case of binary samples, the scattering intensity is proportional to:

- the electronic contrast, more precisely the square of scattering length density difference between the two materials $(\Delta\rho)^2$,
- the concentration of the scattering object (in volume fraction), in case of suspensions for example.

Ultra Small Angle X-ray Scattering (USAXS) measurements give access to X-ray scattering data for a range of smaller *q* and then complement the SAXS diffractograms. It requires a specific and very precise set-up, different from the one used for SAXS.

Equipment

The experimental set up (X-ray source, optical elements, detectors, etc.) and the procedure for absolute scaling of data has been thoroughly described by Zemb (Zemb et al., 2003) and Né (Né et al., 2000).

Apparatus

The main set up components used for SAXS and USAXS experiments at CEA/LIONS are listed below:

- X-ray generator : Rigaku generator RUH3000 with copper rotating anode (λ= 1.54 Å), 3kW
- Homemade optic pathways and sample holders (with two channel-cut Ge (111) crystals in Bonse/Hart geometry for USAXS set up (Lambard et al.,1992)
- Flux measurement for SAXS set up : pico amperemeter Keithley 615

- Flux measurement for USAXS set up : DonPhysik ionization chamber
- Detector for SAXS set up : 2D image plate detector MAR300
- Detector for USAXS set up: 1D high count rate CyberStar X200 associated to a scintillator/ photomultiplier detector.

All experimental parameters are monitored by computer by a centralized control-command system based on TANGO, and interfaced by Python programming. 2D images are treated using the software *ImageJ* supplemented with some specific plugging developed at CEA/LIONS by Olivier Taché (Taché, 2006).

Calibration

A sample of 3 mm of Lupolen® (semi crystalline polymer) is used for the calibration of the intensity in absolute scale, the maximum intensity being adjusted to 6 cm^{-1}.

A sample of 1 mm of octadecanol is used for the calibration of the q range (calculation of sample-to-detector distance), the position of the first peak standing at 0.1525 $Å^{-1}$.

Calibrations in intensity and in q range are performed before each series of measurements.

Sample preparation

Almost any kind of material can be analysed by SAXS, whether as a powder, a colloidal suspension, a gel, or even self-supported hybrid materials, as long as the sample prepared meets some requirements of transmission and scattering properties.

Depending on the X-ray absorption coefficient of the material and its scattering properties, the sample thickness has to be adjusted to get a transmission as close as possible to the target transmission of 0.3 (optimal absorption/transmission ratio).

The sample thickness *e* is directly linked to the transmission *T* by the following equation:

$$e = -\frac{1}{\mu}\ln(T)$$

μ: X-ray absorption coefficient of the material,

T: transmission, *T* = transmitted flux/ incident flux of the direct beam

If not self-supported (liquids, powders or gel), the material to be analysed is inserted in a cell, which can be made of glass (capillary), or X-ray transparent material such as Kapton® (polyimide). A measurement of the empty cell is performed and subtracted as a background for the sample measurement. See Figure D2 for examples of cells used at CEA/LIONS.

Powders

The absorption coefficient depends on the material and on the energy. For the Cu K-alpha emission (8 keV) used here, the coefficient, $\mu_{SiO2,}$ for SiO_2 is 77 cm^{-1} and the optimal sample thickness (equivalent thickness of dense material) to get a transmission of 0.3 is 150 µm.

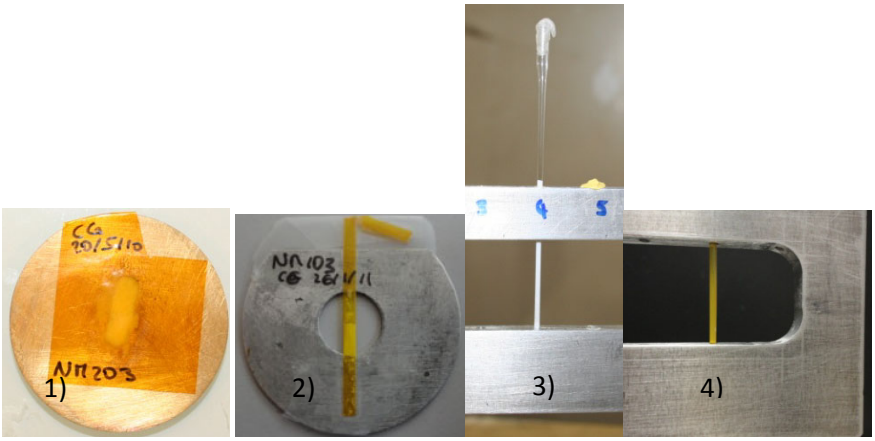

Figure D2. Examples of different type of cells used for SAXS measurements, 1) double sticky kapton® cell for powders, 2) 1.5 mm flattened polyimide capillary for powders, 3) 1.5 mm glass capillary for powder or liquid samples, 4) 1.5 mm polyimide capillary for powder or liquid samples.

The SiO_2 powder samples, except NM-203, were prepared in 1.5 mm glass capillaries leading to typical equivalent thickness of dense material from 100 to 200 µm. NM-203 powder is very sticky and was very difficult to insert into capillaries, so it was measured in a double sticky kapton® cell.

Aqueous suspensions

The usual thickness of aqueous samples for SAXS measurement is 1mm with an acquisition time of 1 hour. Dispersions for analysis are typically produced by sonication in a dispersion medium. The concentration required for analysis depends on the relative scattering length densities between particles and dispersion medium, and the density of materials. The sample must be stable within the time-frame of the measurement.

Typical concentration in oxide for NANOGENOTOX suspensions is 3 g/L. Since the scattering length density of silicon dioxide is relatively low, higher concentrations were used when possible.

Measurements

In order to calculate the sample transmission, the flux of incident and transmitted beam are measured and averaged over 200 s before running the SAXS measurement. The time of

acquisition necessary for SAXS experiment depends on the sample properties. For SiO_2 powders, two measurements were performed: one with a short time of 200 s or 150 s to get unsaturated data for small angles (low q), and one for a long time of 1800 s to get data in the high q region with low signal/noise ratio.

For aqueous suspensions prepared for NANOGENOTOX, SAXS measurements were performed in kapton capillaries of internal thickness 1.425 mm and run for 3600s, leading to transmissions of about 0.25. USAXS measurements were performed in 1 mm or 1.5 mm non-sticky double kapton cells, cell types are shown on Figure D2.

Data treatment

Raw data, translated into intensity as a function of the scattering vector q, are first normalized by parameters of the experiments such as acquisition time, sample thickness and calibration constants determined using reference samples, thus expressing data in absolute scale (cm^{-1}). Backgrounds are then subtracted. To get continuous diffractograms for the whole q range SAXS data obtained for short and long times are combined with USAXS data.

For powder samples, the Porod law is applied to extract specific surface areas of raw materials. Data from suspensions are fitted with a model describing fractal aggregates of primary particles. In this model, the whole q range is divided into sections reflecting different structural levels in the sample, and fitted by local Porod and Guinier scattering regimes. Intensity average parameters are then determined such as radius of gyration for the primaries and for the aggregates, and a fractal dimension for the aggregates. Invariants are calculated, which give a correlation between the sample concentration and the specific surface area obtained in suspension.

Raw data treatment

SAXS data

Radial averaging of 2D image (ImageJ)

2D images from the detector are converted into Intensity = f(scattering vector q) graphs by the software ImageJ together with SAXS plugging. The process follows mainly these steps:

- Determination of the centre coordinates (direct beam position)
- Application of a mask to remove pixels corresponding to the beam stop and around the photodiode

- Radial averaging of the intensity, knowing pixel size, sample-detector distance and wavelength (example of parameters in Figure D3), conversion of pixel position into scattering vector *q*, and creation of a .rgr file containing *I(q)* data.

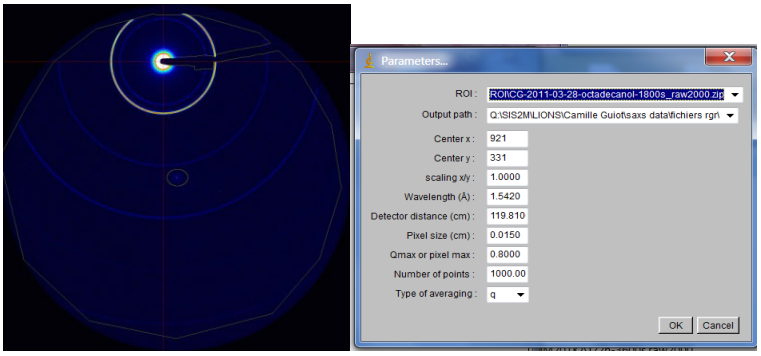

Figure D3. Example of raw 2D image (octadecanol) and parameters used for radial averaging with ImageJ

Absolute scaling of I(q) (pySAXS)

In order to scale the data to the absolute scale in cm^{-1}, *I(q)* data generated by *ImageJ* as .rgr files are treated by a homemade program called *pySAXS* and based on python programming.

The scaling involves a subtraction of the detector background and normalization by exposition time, sample transmission, sample thickness and K constant. The K constant is calibrated with Lupolen® sample and allows conversion of intensity in photons into absolute intensity in cm^{-1}. An example of parameters used for the scaling is shown on Figure D4.

The subtraction of the empty cell signal and normalization by the sample thickness can be done in a subsequent step.

USAXS data

Raw USAXS data are generated as intensity vs angle data in .txt files. Data treatment is achieved using *pySAXS* and involves the following steps:

- Subtraction of the “rocking curve” (signal with empty cell) normalized by the intensities at 0° (transmission).
- Desmearing, taking into account the effective size of the “punctual” detector (cf reference 0)
- Conversion of angle into q range
- Normalization by the sample thickness.

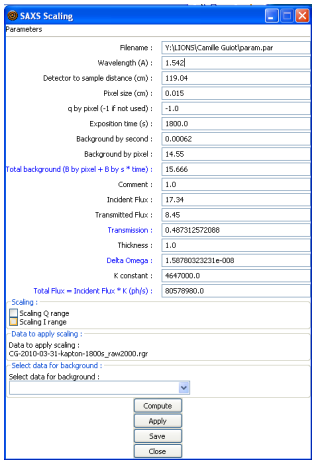

Figure D4. Example of SAXS scaling parameter file from PySAXS software

Data analysis

General theorems of X-ray scattering have been developed to analyze SAXS data. Here are presented some simple laws for **binary systems** (two phase samples) that may be of use in NANOGENOTOX framework.

Porod's Law

In the high q range, sample diffractograms display an intensity decreases in a q^{-4} trend, called the "Porod region". This region corresponds in the "real space" to the scale of the interfaces (for smooth interfaces).

Therefore, for a binary sample, the asymptotic limit of the so-called "Porod's plateau", when data are represented in Iq^4, is related to the total quantity of interface Σ (in m^2/m^3) between the two phases, as follows:

$$\Sigma\,[\mathrm{m}^{-1}] = \frac{\lim_{\text{plateau}} (I.q^4)}{2\pi(\Delta\rho)^2}$$

where $\Delta\rho$ is the difference in scattering length density between the two phases. For a binary sample of **known thickness**, the volume fraction of a material φ_A, its specific surface area S_A/V_A (surface developed/ volume of A in the binary sample) and Σ are linked by the following relation:

$$\Sigma\,[\mathrm{m}^{-1}] = \frac{S_A}{V_A}\varphi_A$$

For example, for a suspension of oxide in water, the determination of Porod plateau gives access to the concentration of the sample if the specific surface area of particles suspended is known (and vice versa).

Specific surface area determination from SAXS on powders

To treat raw SAXS data and get absolute intensities, the intensity by the thickness of the scattering material need to be normalised. However, for powder samples, the sample thickness is not well defined and cannot be precisely controlled as it depends on the powder compaction and the different scales of porosity, see Figure D5. To elude this problem, a model system is used, considering the effective thickness of material crossed by X-rays, called e_B, corresponding to an equivalent thickness if all the material would be arranged in a fully dense (no inner or outer porosity) and uniform layer.

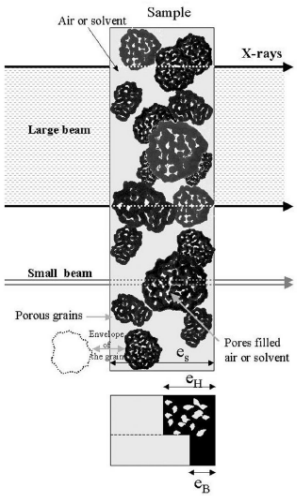

Figure D5. Schematic representation of a powder sample for SAXS measurement, and definitions of equivalent thicknesses e_H and e_B.

The sample transmission is related to this equivalent thickness by the following equation:

$$e_B = -\frac{1}{\mu}\ln\left(T_{exp}\right)$$

where μ is the material absorption coefficient for X-Ray (μ_{SiO2} = 77 cm^{-1}) and T_{exp} is the **experimental transmission** (transmitted flux Φ_T/ incident flux Φ_0), i.e. transmission of the sample with regard to the transmission of the empty cell (kapton® alone, empty capillary, etc). The intensity scaled by this thickness e_B is called I_1. The Porod's law can then be applied for I_1 to access the specific surface area of the powder.

Specific surface areas of powders are determined on the Porod plateau from the equation.

The values in m^{-1} are then converted into m^2/g taking into account the material density ρ_m:

$$\sum\left[\frac{m^2}{g}\right] = \frac{\Sigma[m^{-1}]}{\rho_m\left[\frac{g}{m^3}\right]}$$

If no uncertainty is considered for the material density, the relative uncertainty of the specific surface area calculated is directly linked to the determination of the Porod plateau:

$$\frac{\Delta\Sigma[\frac{m^2}{g}]}{\Sigma[\frac{m^2}{g}]} = \frac{\Delta\Sigma[m^{-1}]}{\Sigma[m^{-1}]} = \frac{\Delta \lim(I)_1 q^4}{\lim(I)_1 q^4}$$

However, if we consider a quantifiable uncertainty on the material density, it is passed on to the calculated sample thickness e_B and the theoretical scattering length density of the material. Finally, the relative uncertainty on the specific surface area is increased by the uncertainty on the material density:

$$\frac{\Delta\Sigma[m^{-1}]}{\Sigma[m^{-1}]} = \frac{\Delta \lim(I)_1 q^4}{\lim(I)_1 q^4} + \frac{\Delta\rho_m}{\rho_m}$$

The uncertainty on the material density even contributes twice when the specific surface area is expressed in m²/g:

$$\frac{\Delta\Sigma[\frac{m^2}{g}]}{\Sigma[\frac{m^2}{g}]} = \frac{\Delta \lim(I)_1 q^4}{\lim(I)_1 q^4} + 2\frac{\Delta\mu_m}{\rho_m}$$

All specific surface area results, together with their uncertainty calculations are presented below. Errors on the Porod's plateaus have been determined manually for each diffractogram, and the uncertainty on the material density is considered to be about 5%.

Invariant theorem

When *I(q)* can be extrapolated to zero values of *q* (no interaction at a large scale, i.e. a flat signal for low q) and at infinite *q* (usually with the Porod law), the following invariant theorem can be applied:

$$Q = \int_0^\infty I_{Abs}\, q^2 dq = 2\pi^2 \varphi(1-\varphi)(\Delta\rho)^2$$

This implies that the invariant Q is a constant for a defined composition, which gives access to the volume fraction φ, or to the evolution of interactions for a fixed composition.

Guinier regime

For dilute samples of monodisperse objects (negligible position correlation between scattering objects, i.e. structure factor 1), the intensity in the low q region ($qR_G<<1$) can be approximated to:

$$I(q) \approx A\left(1 - \frac{(qR_G)^2}{3} + Bq^3\right)$$

which gives access to the radius of gyration of the particles R_G with the slope of $\ln(I)=f(q^2)$.

Data fits

Assuming values of parameters such as volume fraction, size, shape and polydispersity of scattering objects for a model sample, it is possible to calculate theoretical curves of *I(q)*. Therefore, the adjustment of such parameters to fit experimental curves allows for the modelisation of the sample properties.

Unified model of aggregates in suspension for SAXS data treatment

A unified fitting approach, developed by Beaucage et al. (Beaucage et al., 1996; Kammler et al., 2004; Kammler et al., 2005) was used to treat X-ray scattering data from SiO_2 suspensions composed of aggregates of primary particles. In this model, the whole q range is divided into sections reflecting different structural levels in the sample, and fitted by local Guinier, fractal and Porod scattering regimes, see Figure D6.

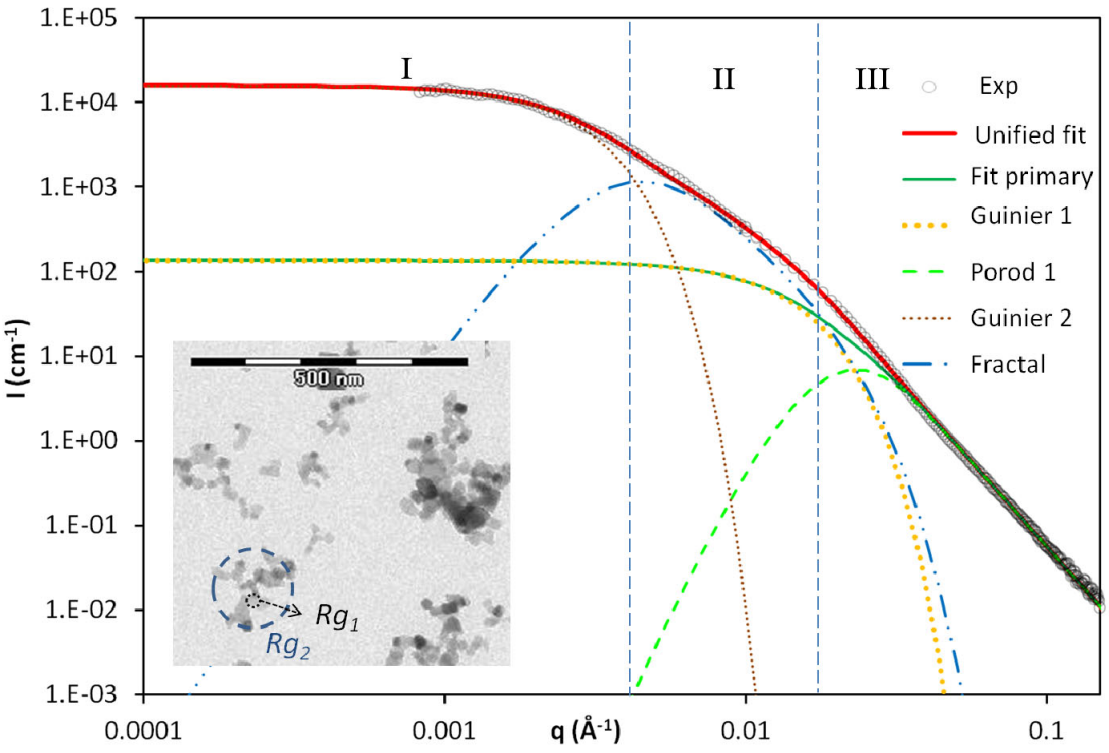

Figure D6. Example of SAXS diffractogram (NM-105, a TiO_2, suspension sonicated at pH 2 as circles) illustrating the unified fit (solid red line) and its components prevailing in each q-domain (dashed-dotted lines). Insert of TEM micrograph (by CODA-CERVA) illustrating the gyration radius of primary particles (Rg1) and aggregates (Rg2) used in the model. Exp = experimental data.

The scattering vector *q* is homogeneous to the reverse of a length, so large q values actually corresponds to small observation scale in the direct space.

For a smooth surface of primary particles, **at large q** (the scale of interfaces) the intensity decays as a power-law of q^{-4} defining the Porod regime:

$$I_{Porod\,1}(q) = B_1\, q^{-4}$$

The coefficient B_1 is directly linked to the specific surface area of the primary particles:

$$B_1 = 2\pi N(\Delta\rho)^2 S$$

with *N* and *S* respectively the number density and the average surface area of primary particles and $\Delta\rho$ the difference of scattering length density between scattering object (SiO_2) and medium (water).

This Porod regime is preceded **at lower q** by a Guinier regime, signature of the size of primary particles, and is described by:

$$I_{Guinier\,1}(q) = G_1 \exp\left(\frac{-q^2 {Rg_1}^2}{3}\right)$$

The sum of these two regimes (***Fit primary*** in Figure D6) would describe scattering intensity resulting from individual uncorrelated primary particles, *i.e.* if they were perfectly dispersed and non-aggregated. It prevails in the large q range (domain III, Figure D6). The upturn of the intensity at small q is due to the association of primary particles into aggregates of finite size.

These aggregates also present a finite size and inner structure. Thus, a second Guinier regime is associated with the structural size of aggregates and prevails in the domain I defined in the Figure D6:

$$I_{Guinier\,2}(q) = G_2 \exp\left(\frac{-q^2 {Rg_2}^2}{3}\right)$$

The coefficients G_1 and G_2 are defined by:

$$G_i = N_i(\Delta\rho)^2 V_i^2$$

where N_i and V_i are respectively the number density and volume of object i (primary particle or aggregate).

These two Guinier regimes give access to the radii of gyration of the primary particles, Rg_1 and of the aggregates, Rg_2.

The ratio of G1 to B1 is a measure of the anisotropy of the primary particles since

$$\frac{G_1}{B_1} \alpha \frac{V^2}{2\pi S}$$

with V the volume of the particles and S their surface.

For intermediate q range between the scale of aggregates and the scale of primary particles (domain II in Figure D6), the intensity decays with a slope typical for the fractal regime of an aggregate and described by a power-law linked to the mass-fractal dimension D_f:

$$I_{Fractal}(q) = B_2 \, q^{-D_f}$$

The coefficient B_2 is linked to D_f, G_2 and Rg_2 by:

$$B_2 = \frac{G_2}{Rg_2^{D_f}} D_f \Gamma\left(\frac{D_f}{2}\right)$$

Γ is the gamma function.

The fractal dimension D_f is a measure of the degree of ramification and density of aggregates (value between 1 and 3), see Hyeon-Lee et al., 1998.

An average number of primary particles per aggregate can be derived from the Guinier coefficients:

$$N_{part/agg} = \frac{G_2}{G_1}$$

The global unified fit is obtained by addition of the different terms, see Bushell et al., 2002.

To fit the experimental diffractograms, the total model curve

$$I(q) = I_{Porod\,1}(q) + I_{Guinier\,1}(q) + I_{Fractal}(q) + I_{Guinier\,2}(q)$$

is plotted and parameters (B_1, G_1, G_2, D_f, Rg_1 and Rg_2) are adjusted manually so that the model fits the best the experimental data. Three parameters are there to describe the primary particles, and three are also necessary to describe the aggregates structures of

primary particles. Also in TEM three independent parameters were required to describe the aggregates.

Some geometrical restrictions have to be respected ($D_f < 3$; volume of N primaries < volume of aggregate, total surface area of primaries cannot be smaller than the corresponding surface area for ideal spheres).

All SAXS data are treated to be represented in the absolute scale (intensity in cm^{-1}). Therefore quantitative measurements are accessible and through the use of the invariant theorem and it is possible to calculate the exact concentration of samples, and then correlate the specific surface area developed in the suspension to the specific surface area of raw materials obtained from powder samples.

References

1. T. Zemb, O. Taché, F. Né, and O. Spalla; “A high-sensitivity pinhole camera for soft condensed matter”; J. Appl. Crystal., 36, 800-805, **2003**.
2. F. Né, I. Grillo, O. Taché, and T. Zemb. ; “From raw image to absolute intensity: Calibration of a guinier-mering camera with linear collimation”; J. de Physique IV, 10(P10), 403-413, **2000**.
3. O. Spalla, S. Lyonnard, and F. Testard; “Analysis of the small-angle intensity scattered by a porous and granular medium”; J. Appl. Crystal., 36, 338-347, **2003**.
4. J. Lambard, P. Lessieur and Th. Zemb; “A triple axis double crystal multiple reflection camera for ultra small angle X-ray scattering”; J. de Physique I France, 2 , 1191-1213, **1992**. Lambard, J.; Lesieur, P.; Zemb, T., A triple axis double crystal multiple reflection camera for ultra small angle X-ray scattering. J. Phys. I France 1992, 2 (6), 1191-1213.
5. O. Taché ; « Une architecture pour un système évolutif de contrôle commande d'expériences de physique », Engineer thesis, **2006**, available at http://iramis.cea.fr/sis2m/lions/tango/tango-ds/memoire.pdf
6. Beaucage, G., Small-Angle Scattering from Polymeric Mass Fractals of Arbitrary Mass-Fractal Dimension. J. Appl. Crystal. **1996**, 29 (2), 134-146.
7. Kammler, H. K.; Beaucage, G.; Mueller, R.; Pratsinis, S. E., Structure of Flame-Made Silica Nanoparticles by Ultra-Small-Angle X-ray Scattering. Langmuir **2004**, 20 (5), 1915-1921.
8. Kammler, H. K.; Beaucage, G.; Kohls, D. J.; Agashe, N.; Ilavsky, J., Monitoring simultaneously the growth of nanoparticles and aggregates by in situ ultra-small-angle x-ray scattering. J. Appl. Physics **2005**, 97 (5), 054309-11.
9. Hyeon-Lee, J.; Beaucage, G.; Pratsinis, S. E.; Vemury, S., Fractal Analysis of Flame-Synthesized Nanostructured Silica and Titania Powders Using Small-Angle X-ray Scattering. Langmuir **1998**, 14 (20), 5751-5756.
10. Bushell, G. C.; Yan, Y. D.; Woodfield, D.; Raper, J.; Amal, R., On techniques for the measurement of the mass fractal dimension of aggregates. Advances in Colloid and Interface Science **2002**, 95 (1), 1-50.

11. Porod, G.; Glatter, O.; Kratky, O., General theory: Small-angle X-ray scattering. Academic Press ed.; Academic Press: New York, **1982**.

Title: Synthetic Amorphous Silicon Dioxide (NM-200, NM-201, NM-202, NM-203, NM-204): Characterisation and Physico-Chemical Properties

Authors: Kirsten Rasmussen, Agnieszka Mech, Jan Mast, Pieter-Jan De Temmerman, Nadia Waegeneers, Frederic Van Steen, Jean Christophe Pizzolon, Ludwig De Temmerman, Elke Van Doren, Keld Alstrup Jensen, Renie Birkedal, Marcus Levin, Signe Hjortkjær Nielsen, Ismo Kalevi Koponen, Per Axel Clausen, Yahia Kembouche, Nathalie Thieriet, Olivier Spalla, Camille Giuot, Davy Rousset, Olivier Witschger, Sebastian Bau, Bernard Bianchi, Boris Shivachev, Douglas Gilliland, Francesca Pianella, Giacomo Ceccone, Giulio Cotogno, Hubert Rauscher, Neil Gibson and Hermann Stamm

Luxembourg: Publications Office of the European Union

2013 – 200 pp. – 21.0 x 29.7 cm

EUR – Scientific and Technical Research series – ISSN 1831-9424

ISBN 978-92-79-32323-2

doi:10.2788/57989

Abstract

The European Commission's Joint Research Centre (JRC) provides scientific support to European Union policy including nanotechnology. Within this context, the JRC launched, in February 2011, a repository for Representative Test Materials (RTMs), based on preparatory work started in 2008. It supports both EU and international research projects, and especially the OECD Working Party on Manufactured Nanomaterials (WPMN). The WPMN leads an exploratory testing programme "Testing a Representative set of Manufactured Nanomaterials" for the development and collection of data on characterisation, toxicological and ecotoxicological properties, as well as risk assessment and safety evaluation of nanomaterials. The purpose is to understand the applicability of the OECD Test Guidelines for the testing of nanomaterials as well as end-points relevant for such materials.

The Repository responds to a need for nanosafety research purposes: availability of nanomaterial from a single production batch to enhance the comparability of results between different research laboratories and projects. The availability of representative nanomaterials to the international scientific community furthermore enhances and enables development of safe materials and products.

The present report presents the physico-chemical characterisation of the synthetic amorphous silicon dioxide (SiO_2, SAS) from the JRC repository: NM-200, NM-201, NM-202, NM-203 and NM-204. NM-200 was selected as principal material for the OECD test programme "Testing a representative set of manufactured nanomaterials".

NM-200, NM-201 and NM-204 (precipitated SAS) are produced via the precipitation process, whereas NM-202 and NM-203 (fumed or pyrogenic SAS) are produced via a high temperature process. Each of these NMs originates from one respective batch of commercially manufactured SAS. They are nanostructured, i.e. they consist of aggregated primary particles. The SAS NMs may be used as a representative material in the measurement and testing with regard to hazard identification, risk and exposure assessment studies.

The results for more than 15 endpoints are addressed in the present report, including physical-chemical properties, such as size and size distribution, crystallite size and electron microscopy images. Sample and test item preparation procedures are addressed. The results are based on studies by several European laboratories participating to the NANOGENOTOX Joint Action, as well as the JRC.

LB-NA-26046-EN-N

As the Commission's in-house science service, the Joint Research Centre's mission is to provide EU policies with independent, evidence-based scientific and technical support throughout the whole policy cycle.

Working in close cooperation with policy Directorates-General, the JRC addresses key societal challenges while stimulating innovation through developing new standards, methods and tools, and sharing and transferring its know-how to the Member States and international community.

Key policy areas include: environment and climate change; energy and transport; agriculture and food security; health and consumer protection; information society and digital agenda; safety and security including nuclear; all supported through a cross-cutting and multi-disciplinary approach.

ISBN 978-92-79-32323-2

Publications Office